

Dissertation
submitted to the
Combined Faculties for the Natural Sciences and for Mathematics
of the Ruperto Carola University of Heidelberg, Germany
for the degree of
Doctor of Natural Sciences

Put forward by
Dipl.-Phys. Joëlle Caroline Elisabeth Buxmann
Born in: Kilchberg bei Zürich

Oral examination: 25.07.2012

'Bromine and Chlorine Explosion' in a Simulated Atmosphere

Referees: Prof. Dr. Ulrich Platt
Prof. Dr. Thomas Wagner

Zusammenfassung

Als Brom und Chlor 'Explosion' (BE und CE) bezeichnet man die autokatalytische, heterogene Freisetzung von reaktiven Halogenverbindungen (RHV). Bei der Zerstörung von atmosphärischem Ozon und der Beeinflussung der HO_x und NO_x Chemie, spielen die RHV BrO und ClO eine grosse Rolle. In dieser Arbeit werden die ersten direkten Messungen des BrO aus der BE über einer künstlichen Salzpflanne in einer Smogkammer unter troposphärischer Lichteinstrahlung gezeigt. Zudem wurden ClO, OClO (aus der CE) und BrO aus künstlichem Seesalzaerosol freigesetzt, beobachtet. Ein White System in Kombination mit Differentieller Optischer Absorptions Spektroskopie (DOAS) und ein Ultraviolett-LED Resonator verstärktes DOAS Instrument wurden installiert, um diese RHV zu messen. Maximale BrO Konzentration von mehr als 6 ppb wurden bei einer relativen Luftfeuchte von 60 % gemessen. Die BrO Bildung war stark von der Luftfeuchte abhängig. Diese Abhängigkeit kann durch die Dicke der Flüssigkeitsschicht auf den Salzkristallen erklärt werden. Es stellte sich weiterhin heraus das sekundäres organisches Aerosol die BrO Bildung aus der Salzpflanne hemmt. Während der Salzaerosol Experimente bilden sich bis zu 17 ppb ClO, 6 ppb OClO und 1.6 ppb BrO bei hohen NO_2 und O_3 , was auf die Ansäuerung des Aerosols durch die Reaktion mit NO_2 zurückgeführt werden kann. Die Ergebnisse weisen darauf hin, dass OClO und wahrscheinlich OBrO wichtig für die Halogenfreisetzung sind. Während die BE in der Natur beobachtet wurde, bleibt die Frage, wie wichtig die CE für die Troposphäre ist, ungeklärt.

Abstract

Bromine and chlorine 'explosions' refer to auto catalytic, heterogeneous releases of reactive halogen species (RHS). ClO and BrO play a key role as RHS, in destruction of atmospheric ozone and influencing HO_x and NO_x chemistry. From a smog chamber under tropospheric light conditions, first direct observations of BrO from BE above a simulated salt pan are shown. Moreover, ClO, OClO (from CE) and BrO released from artificial sea salt aerosols were detected. A White system in combination with Differential Optical Absorption Spectroscopy (DOAS) and an ultraviolet LED cavity enhanced DOAS instrument were installed to measure RHS. Maximum BrO concentrations of more than 6 ppb were observed at 60 % relative humidity. BrO formation was strongly humidity dependent, possibly controlled by the liquid layer on salt crystals. Secondary organic aerosols appeared to inhibit BrO formation in salt pan experiments. In aerosol experiments, up to 17 ppb of ClO, 6 ppb of OClO, and 1.6 ppb of BrO were observed in the presence of high NO_2 and O_3 concentrations, possibly due to acidification of salt aerosols by reaction with NO_2 . These results suggest that OClO and possibly OBrO are important for the heterogeneous release process. While BE has been demonstrated to occur in nature, the question remains how important CE is in the troposphere.

Contents

1. Introduction	1
2. Chemistry and Kinetics of Halogen Species in the Troposphere	5
2.1. Important Oxidants in Tropospheric Chemistry	6
2.2. Bromine Chemistry	9
2.3. Chlorine Chemistry and Cross Reactions	12
2.4. Heterogeneous Processes of Halogen Species	15
2.5. Water Layers on Salt	18
2.6. Simple Reaction Kinetic Model	18
3. The Teflon Smog Chamber	21
3.1. Solar Simulator and Photolysis Rates	21
3.2. Further Analytical Instrumentation of the Smog Chamber	27
3.3. Generation of Aerosols in the Chamber	31
3.4. Salt Samples for the Salt Pan Experiments	32
3.5. Wall Effect of Ozone	34
3.6. Treatment of Heterogeneous Reactions in Smog Chambers	35
3.6.1. Comparison of Salt Pan and Aerosol Heterogeneous Interaction	41
4. Multi Reflection Systems used for Absorption Spectroscopy	43
4.1. Differential Optical Absorption Spectroscopy	43
4.1.1. Basics	44
4.2. The White-type Multi Reflection System	46
4.2.1. Light Propagation through the White System and Transfer	
Optics	46
4.2.2. The Xenon Lamp Radiation Source	49
4.2.3. Spectrograph and Detector	50
4.2.4. White System Mirror Coating	50
4.2.5. Stray Light	51
4.3. Data Analysis of the White-cell Measurements	53
4.3.1. Influence of Dielectric Coating on the Fit Range	57
4.3.2. BrO and OClO	65
4.3.3. ClO and O ₃	66
4.4. The CE-DOAS Instrument	66
4.4.1. The LED Radiation Source	66
4.4.2. Mirrors and Optics	68

4.4.3.	Spectrograph and Detector	68
4.4.4.	Peltier Cooling of the LED	69
4.5.	Cavity-Enhanced Differential Absorption Spectroscopy (CE-DOAS) .	70
4.5.1.	Continuous Data Collection	70
4.5.2.	Determination of the Average Light Path	71
4.5.3.	Correction of the Base Path-Length	71
4.5.4.	Correction for Light Path Reduction due to Extinction in the Cavity	72
4.5.5.	Correction of the Wavelength Dependence of the Average Light Path	73
4.6.	Data Analysis of the CE-DOAS-measurements	73
4.6.1.	Mirror Reflectivity and Path Length Calibration	73
5.	Results	81
5.1.	Inter Comparison of the Different Instruments	81
5.1.1.	Comparison of White System and CE-DOAS	82
5.1.2.	Comparison of White System and CE-DOAS with Ozone Mon- itor	83
5.1.3.	Comparison of White System and NO _x Monitor	88
5.1.4.	Comparison of White System and LOPAP	88
5.2.	Salt Pan Experiments	91
5.2.1.	Bromine Explosion Time Series	92
5.2.2.	Recovery of the BrO Source and Behavior of O ₃	93
5.2.3.	OH Radical Concentrations from Hydrocarbon Clock Data . .	97
5.2.4.	Chlorine Radicals	97
5.2.5.	Simple Reaction Kinetic Model for O ₃	100
5.3.	Sea Salt Aerosol Experiments	101
5.3.1.	Halogen Oxides from Sea Salt Aerosols at low NO _x	101
5.3.2.	Chlorine Explosion at high NO _x	108
5.4.	Influence of the Presence of SOA on the Halogen Release from the Simulated Salt-Pan	112
6.	Discussion	117
6.1.	White system and cavity enhanced DOAS	117
6.2.	Salt Pan Experiments	120
6.2.1.	Recovery of the BrO Source and Behavior of O ₃	120
6.2.2.	Bromine Release Mechanism	121
6.3.	Sea Salt Aerosol Experiments	125
6.3.1.	Comparison with Siekman Experiments	125
6.3.2.	Influence of NO _x and Chlorine Explosion	127
6.3.3.	Influence of Ozone and Ozone Model	128
6.4.	Interaction of RHS with Organics	128
6.5.	Atmospheric Relevance	130

7. Conclusions and Outlook	133
Bibliography	150
A. Abbreviations	151
Acknowledgements	154

1. Introduction

Even very low levels of reactive halogen species (RHS) in the order of parts per trillion (ppt) can significantly affect tropospheric chemistry. In particular bromine and chlorine species undergo catalytic reaction pathways to destroy ozone. In the troposphere, ozone is an important oxidant, acts as a green house gas [Solomon *et al.* 2007] and is a important source of the OH radical. The OH radical is a highly reactive compound, commonly known as the 'detergent' of the troposphere. It reacts with many pollutants, as well as with the greenhouse gas methane.

A drastic example of the effect of RHS in the troposphere is the depletion of boundary layer ozone. During polar spring ozone is consumed completely over the Arctic and Antarctic within days or hours. It is the result of catalytic cycles that appears to mainly involve bromine radicals (e.g. [Platt and Janssen 1996, Wennberg *et al.* 1998]). Recent studies in the Arctic at the Amundsen Gulf show that maximum BrO levels decrease linearly with ambient temperature (between -24°C and -15°C), providing indications for the conditions required for the release of RHS [Pöhler *et al.* 2010]. The temperature dependence was recently confirmed for early spring by sensitive evaluation of tropospheric BrO over the Arctic from satellites [Sihler 2012]. Bromine chemistry is also important at mid-latitudes. For example, high BrO mixing ratios compared to other regions of up to 200 ppt were detected at the Dead Sea in Israel (e.g. [Hebestreit *et al.* 1999, Tas *et al.* 2008]). Model calculations indicate that bromine release from salt aerosols and the lake surface is not sufficient as a source for BrO at the Dead Sea [Smoydzin and von Glasow 2009]. Only by increasing the source strength of the halogen species by direct degassing by a factor of 30 to 50, extremely high BrO mixing ratios were predicted by the model, which bring model and measurement into agreement. The more likely explanation for a larger total source strength, compared to the direct degassing, is a missing source [Smoydzin 2008]. This leads to the central question, which is addressed in this thesis:

What are the unknown release mechanisms not yet described by the current state of understanding of halogen chemistry?

In contrast to the Dead Sea where the model underestimates BrO, measurements from field campaigns in Namibia/Botswana, in Southern Russia and Mauritania showed one to two orders of magnitude lower BrO levels [Buxmann 2008a, Holla 2010] than expected, based on previous observations by Hebestreit *et al.* 1999 at other salt lakes. Based on limited field observations, conditions favoring halogen release are thought to be high salinity, a high bromide/chloride ratio [Behnke *et al.* 1999], and low pH [Fickert *et al.* 1999]. However, these conditions might not be

always necessary. Despite having one of the lowest bromine content in the world ($\text{Br}/\text{Cl} = 10^{-4}$), up to 20 ppt of BrO had been observed at Salar de Uyuni of Bolivia [Hönniger *et al.* 2004]. Low pH is needed for the auto catalytic release of BrO by the well-known 'bromine explosion' mechanism, referred to as BE in the following. Previous measurements also suggest that RH plays a role in the release of RHS. At the Great Salt Lake ($\text{pH} \approx 8$) in Utah, United States, 6 ppt of BrO and 15ppt of ClO were detected, after a period with light rain falls and relative humidities of 98% and 60% [Stutz *et al.* 2002].

To date, neither particular prerequisites for the systematic release of bromine from salt pans have been identified, nor have the contributions of the different possible processes been elucidated. More questions arise:

What triggers the halogen release processes?

Do the relative humidity and thus the water content of the halogen source play a major role?

In the field, varying environmental conditions make it difficult to separate the contributions of different possible triggering mechanisms to RHS release. Smog chambers offer the unique possibility to investigate the halogen release processes under controlled conditions of temperature, relative humidity, light, trace gases and halogen sources. Although the process of BE was suggested in the early 1990s [McConnell *et al.* 1992] and has been confirmed in smog chamber experiments [Behnke *et al.* 1999], the BrO radicals from this process have never been observed directly in smog chamber experiments. The Differential Optical Absorption Spectroscopy (DOAS), combined with multi reflection systems, is an elegant approach for the investigation of trace gases at low concentrations (ppb-ppt range) under spatially limited environments, such as in smog chambers.

DOAS is based on the characteristic absorption structures of the trace gases of interest. The technique has found widespread use for detection of halogen oxides, as well as NO_2 , O_3 and many other trace gases [e.g. Platt and Janssen 1995, Pöhler *et al.* 2010]. Within this thesis, two kinds of multi reflection systems for detection of halogen oxides have been used: a White-system [White 1942, White 1976] and a cavity-enhanced (CE) DOAS instrument [e.g. Washenfelder *et al.* 2008, Platt *et al.* 2009]. Both instruments were specially designed within the framework of this thesis. The teflon smog chamber in the Bayreuth Atmospheric Chemistry Research Laboratory provides an ideal setting for the investigation of tropospheric photochemistry, including halogen activation. Compared to glass or stainless steel, teflon is the better choice for avoiding uncontrolled reactions of the trace gases with the chamber walls. The aerosol simulation chamber in Bayreuth is placed in a spatially limited refrigerator laboratory, which makes the installation of the optical multi reflection systems, as well as later adjustment, a challenge. On the other hand, there are obvious advantages in terms of controlled conditions of temperature, as well as further analytical instruments such as O_3 , NO_2 and FID for indirect measurement of OH and Cl radicals. The challenge was undertaken!

To simulate the halogen release from salt flats/pans and partly dried salt surfaces (e.g. presently at the Dead sea), a new technique was applied: a salt sample was placed directly inside of the chamber on a teflon sheet. For comparison, halogen release from artificially created salt aerosols was also investigated. Furthermore, experiments under varying amounts of nitrogen oxides were conducted. The effects of oxides of nitrogen (in particular NO_2 , NO_3 , N_2O_5) on halogen release are still poorly understood and of great interest. A series of reactions including the air pollutants NO_2 , NO and partly oxidized organic species, is known to be the main source of tropospheric ozone. Recent studies suggest that nitrogen oxides play a key role in chlorine cycling at a land site in Boulder (Colorado) [Thornton *et al.* 2010]). The dependence on nitrogen dioxides was investigated in chamber studies before [e.g. Behnke *et al.* 1992, Zetzsch and Behnke 1992], but the question

Does the concentration of NO_x significantly affect the release of bromine or chlorine species?

still remains unknown. The investigation of these processes, under controlled conditions, in order to further increase our the knowledge in the underlying mechanisms is in one focus of this thesis. Moreover, model calculations predict about 3 ppt of BrO and about 30 ppt of ClO as a background over the open ocean [von Glasow and Salzmann 2012]. The model does not include interactions with organics, such as aldehydes and glyoxal, nor organic aerosols, as they are thought to be not relevant over the remote open ocean. Recently, amounts of up to 140ppt of glyoxal were detected over the open ocean [Sinreich *et al.* 2010]. This is surprisingly high, as glyoxal is very short lived (atmospheric life time ≈ 2 h) and highly water soluble. Therefore one may ask:

To which degree do organics possibly inhibit the release of the halogen oxides, including BrO and ClO ?

Indeed chlorine radicals react at a fast rate with most organics, and Br reacts with unsaturated or partly oxidized organics. Secondary organic aerosol, formed from gas phase precursors, could also well influence halogen chemistry [Ofner *et al.* 2012].

Outline of the Thesis

After the introduction, this thesis starts with a description of the chemistry and kinetics important for troposphere, and thus for the smog chamber experiments presented here. A short overview is given about the important oxidants in the tropospheric chemistry, such as O_3 , nitrogen oxides and the OH -radical. They influence the halogen chemistry and vice versa. The interaction of halogens with organics as a sink, is briefly explained, as it might be important for interaction with secondary organic aerosol (SOA). Gas phase reactions of both bromine and chlorine are described, and a simple chemical model based on the kinetic reaction constants is introduced.

In the third chapter, the unique smog chamber set-up in the Bayreuth laboratory

is explained in detail. A characterization of the driving force of photochemistry, the solar simulator, is given. The photolysis rates of the gas phase species, which are important in the scope of experiments are presented. The general conditions, as well as preparation methods of the used salt and aerosol samples, are explained. In addition, a theoretical approach describing the heterogeneous interaction of gas phase species with a surface, such as the teflon wall, salt surface or aerosol surface is given at the end of chapter 3.

After a brief description of the well established DOAS technique in chapter 4. The multi reflection systems developed within this thesis are described and characterized. First the optical properties of the White system (WS) as well as the general instrumental set-up are explained. Then the analysis settings for the White- system data are shown. In the second part of chapter 4, the novel UV- LED cavity enhanced (CE-)DOAS instrument set up is described, including a recently applied Peltier cooling of the LED. A short description of light path determination and extinction correction, as well as the general analysis settings is given at the end of that chapter.

In chapter 5, first a series of inter comparisons of the different instruments used for the smog chamber experiments is shown. The good agreement of the instruments is a basis for the chamber experiments. The second part of the results chapter shows several BE events, during simulated salt pan experiments, including a repetition experiment of four BEs from the same salt sample [Buxmann *et al.* 2012]. The third part shows the results of halogen release from salt aerosol droplets at two different NaBr/NaCl compositions, as well as varying conditions of hydrocarbons, ozone level and level of nitrogen oxides. At the end of the results chapter, the influence of the presence of SOA on the halogen release processes, which contributed to a paper of [Ofner *et al.* 2012], is shown.

In chapter 6, the results from our experiments are discussed, which leads to the conclusions in chapter 7. Based on the conclusions, an outlook for further research on this topic is given.

This work was conducted within a joint research project HALOPROC, which was designed to investigate the HALogenation PROCesses in the environment, atmosphere and soil. Naturally produced halogen compounds in the troposphere are the central subjects of HALOPROC, in which researchers from biogeosciences, geosciences and atmospheric science work together.

2. Chemistry and Kinetics of Halogen Species in the Troposphere

The halogens or halogen elements are a series of nonmetal elements from Group 17 IUPAC Style (formerly: VII, VIIA) of the periodic table, comprising of fluorine (F), chlorine (Cl), bromine (Br), iodine (I), and astatine (At). Halogens are highly reactive, because of their high electron negativity. They have seven electrons in the valence shell which means they lack just one electron to obtain the stable noble-gas configuration of octate. They are good oxidizing agents, which is of interest especially for atmospheric chemistry. For atmospheric processes in general bromine, chlorine and iodine are of interest. Chlorine is commonly used as disinfectant for drinking water and swimming pools, iodine for fresh wounds, spas, dishes, and surfaces.

The smog chamber experiments were focused on bromine and chlorine chemistry under simulated solar radiation similar to that of the troposphere. Therefore bromine and chlorine chemistry of the troposphere will be discussed in detail within this chapter. As the kinetics of halogens are one of the main foci of the chamber experiments, reaction rates and possibilities for simple reaction kinetic calculations are given as well.

There are several ways in which reactive bromine and chlorine species affect atmospheric chemistry. First pathway is their abilities to catalytically destroy ozone, which can lead to tropospheric (as well as stratospheric) ozone holes [e.g. *Platt and Lehrer* 1996; *Wennberg* 1999]. Furthermore RHS (reactive halogen species) can change the ratios of HO_2/OH and NO_2/NO in the troposphere [e.g. *Platt and Hönninger* 2003]. O_3 , OH and NO_x are important for the oxidizing capacity of the atmosphere. The first part of this chapter will provide a short overview of ozone, OH and NO_x chemistry and then describe in detail interaction with Halogen radicals. Oxidation of Dimethyl Sulfide [*von Glasow et al.* 2002, *Boucher et al.* 2003] and the deposition of elementary mercury[e.g. *Ariya et al.* 2002], are important effects of halogen chemistry, but not treated within this thesis. The term 'halogen' is originated from (hals) meaning 'salt' or 'sea', and (gen-) meaning (coming) from. An important source of halogens is sea salt, as well as salt flats and salt desserts. Heterogeneous reactions occurring at those sites and release mechanisms are described in the second part of this chapter. Parts of the bromine and chlorine chemistry as well as the simple kinetic model calculations, are already described and applied by

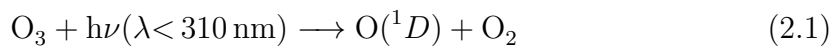
Buxmann et al. 2012.

2.1. Important Oxidants in Tropospheric Chemistry

The tropospheric chemistry of VOCs (volatile organic compounds) and oxides of nitrogen are known to be driven by a few key oxidants, especially O_3 , OH, and NO_3 [Finlayson-Pitts and Pitts 2000]. Chain reactions that oxidize organics and oxides of nitrogen and sulfur, as well as species such as CO, in air have been studied for more than five decades. Ozone formation and removal is central to the chemistry of the troposphere [Seinfeld and Pandis 2008]. Ozone is present at measurable levels during day and night and contributes to the oxidation of alkenes and some inorganics such as NO_2 (see below). Ground-level O_3 mixing ratios range from 20 to 60 ppb, but can exceed 100ppb in urban areas. In the 1960s, it became clear that in addition to O_3 , there must be some other highly reactive oxidizing species present in air that initiates organic oxidations starting at dawn. The hypothesis that the hydroxyl radical (OH) was the missing oxidant led to a large number of studies of the kinetics and mechanisms of oxidation of organics and inorganics by OH. This section will give a short overview of important reactions of OH, NO_x and ozone, as they are strongly connected to halogen chemistry in the troposphere as well as in the chamber. Very good and more detailed descriptions of the complex system of tropospheric kinetic and chemistry can be found in e.g. [Finlayson-Pitts and Pitts 2000, Seinfeld and Pandis 2008].

Ozone

O_3 photolysis, which produces ground state $O(^3P)$ and excited singlet $O(^1D)$ oxygen atoms is important in the troposphere:



The photolysis frequency of reaction 2.1 was calculated for our solar simulator to be $J_{O_3 \rightarrow O(^1D)} = 2.0 \cdot 10^{-5} s^{-1}$ and $J_{O_3 \rightarrow O(^3P)} = 2.1 \cdot 10^{-4} s^{-1}$. The UV filter of the solar simulator cuts off at wavelengths below 320nm (see chapter 3 and [Bleicher 2012]). Reaction 2.2 is possible in the Chappuis region (440-850 nm), as well as the Huggins bands (300-350nm), but the absorption coefficient is one to two orders of magnitude less than that below 250 nm [Finlayson-Pitts and Pitts 2000]. The photolysis reaction 2.2 is a null cycle as the ground state $O(^3P)$ combines rapidly with oxygen to regenerate O_3 :



Quenching of $O(^1D)$ to its ground state is possible under collision with N_2 or O_2 :



with reaction constants of $k_{N_2,2.5} = 260$ and $k_{O_2,2.5} = 400$. For atmospheric (and our chamber) mixture of $N_2 = 78\%$ and $O_2 = 20.9\%$, the value is $k_{2.5} = 290$. Second order rate constants are given here and below in units of $10^{-13} cm^3 \text{ molecule}^{-1} s^{-1}$ for a temperature of 298 K. Occasionally $O(^1D)$ collides with a water molecule and produces two OH radicals (reaction 2.6).

The OH Radical

The main source of OH radicals in the chamber experiments is the photolysis of ozone at wavelengths below 340 nm (reaction 2.1), followed by the reaction with water molecules:



with $k_{2.6} = 2200$ [Atkinson *et al.* 2004]. O_3 photolysis is the limiting reaction to OH formation here, since 90% of the $O(^1D)$ are quenched to its ground state by reaction 2.5 and reform O_3 via reaction 2.3. This depends on the H_2O concentration as well. Compared to that reaction 2.6 is very fast.

OH radicals can also be formed by photolysis of HONO; the latter can be formed by reaction of NO_2 with water:



with a photolysis frequency of $J_{HONO} = 1.3 \cdot 10^{-3} s^{-1}$ for our solar simulator. There are many inconsistencies and uncertainties in the kinetics and mechanism of reaction 2.7. While HONO is always produced, the formation of equivalent amounts of gaseous HNO_3 has not been observed. It is frequently argued that the nitric acid remains adsorbed to the walls of the reactor [Finlayson-Pitts and Pitts 2000]. This is reasonable given the high solubility of HNO_3 in water and aerosols. Formation of HO_2 from photolysis of formaldehyde is also possible:



with photolysis frequencies of $J_{HCHO,2.9} = 2,07 \cdot 10^{-5} s^{-1}$ and $J_{HCHO,2.10} = 1,28 \cdot 10^{-5} s^{-1}$ for our solar simulator. Formaldehyde is a first-generation product of CH_4 and, it turns out, of many other hydrocarbons [Seinfeld and Pandis 2008].

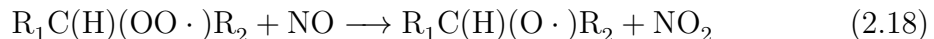
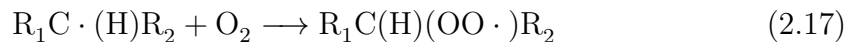
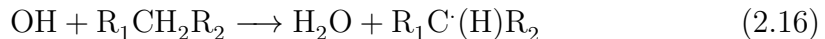
The OH radical is strongly connected with the HO₂ concentration via:



where $k_{2.13} = 0.73$ and $k_{2.14} = 0.002$ [Atkinson *et al.* 2004]. OH can also be recycled from HO₂ via the reaction with NO:



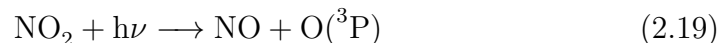
($k_{2.14} = 88$). The amount of HO₂ radicals is important as it is involved in the catalytic cycles including ClO and BrO (e.g. reaction 2.32). The hydroxyl radical oxidizes organics at reaction rates on the order of 10-100 (compare chapter 3). The alkyl peroxy (RO₂, with R indicating an organic rest in the general form C_nH_{2n+1} , $n \in \mathbb{N}$) or hydroperoxy (HO₂) radicals are formed and convert NO to NO₂:



Nitrogen dioxide formed in reaction 2.18 is photolyzed, generating ground-state oxygen atoms, O(³P), which then react with O₂ to form ozone (see reaction 2.19 and 2.20).

Nitrogen Oxides

In the presence of NO and NO₂ and radiation at wavelengths $< 424\text{nm}$, ozone formation occurs as a result of the photolysis of NO₂:



with $k_{2.20} = 0.15$. This is the main source of tropospheric ozone [Seinfeld and Pandis 2008]. NO₂ is regenerated, once O₃ reacts with NO at a rate of $k_{2.21} = 0.17$:



Assuming a photochemical stationary state between NO, NO₂ and O₃ this leads to the so-called Leighton ratio [Leighton 1961]:

$$\frac{[\text{NO}]}{[\text{NO}_2]} = \frac{J_{\text{NO}_2}}{k_{2.21}[\text{O}_3]} \quad (2.22)$$

Note that the steady state O₃ concentration is proportional to the [NO₂]/[NO] ratio, neglecting other sources or sinks.

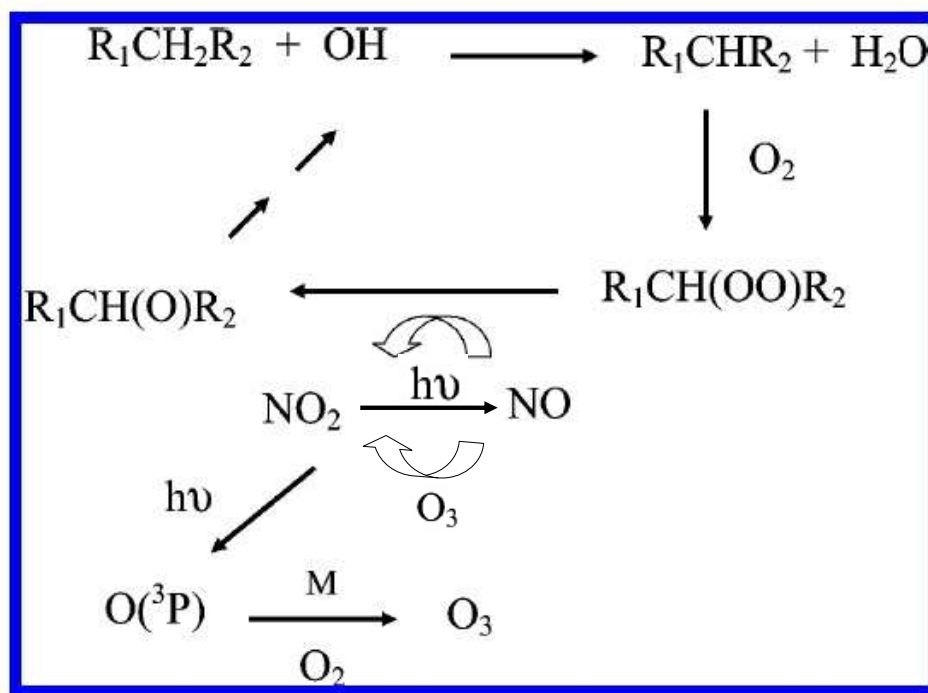


Figure 2.1.: Schematic of VOC-NO_x chemistry in the troposphere (adapted from [Finlayson-Pitts 2003]).

In the dark reaction of NO₂ with O₃, forming the nitrate radical, NO₃ becomes important as well:



The rate constant for this reaction at 298 K is relatively small, $k_{2.23} = 0.00032$ [DeMore *et al.* 1997], and in presence of light NO₃ photolizes rapidly. NO₃ also reacts with NO₂, forming dinitrogen pentoxide in a reversible equilibrium reaction:

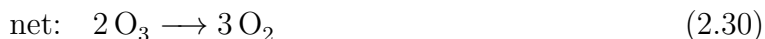
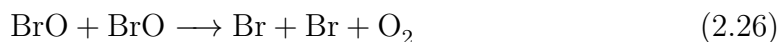


The recommended value of the equilibrium constant is $k_{2.24} = 190$ at 298 K [Atkinson *et al.* 2004]. N₂O₅ participates in heterogeneous release mechanisms, as explained later in section 2.4.

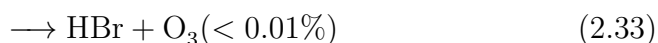
2.2. Bromine Chemistry

A more detailed description of bromine chemistry is given by e.g. Simpson *et al.* 2007 or von Glasow and Crutzen 2007. Reactive bromine species (e.g. Br, BrO,

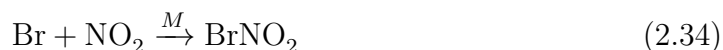
OBrO) can play an important role in tropospheric chemistry since even small concentrations can lead to ozone destruction through a catalytic cycle in the gas phase:



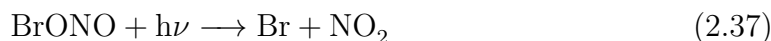
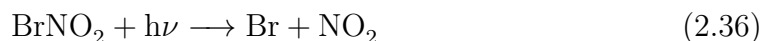
Second order rate constants and recommended values [Atkinson *et al.* 2007] for reactions 2.25-2.27 at 298 K are $k_{2.25}=12$, $k_{2.26}=27$ and $k_{2.27}=4.8$. Channel 2.28 is endothermic by 24 kJ/mol [Atkinson *et al.* 2007] and considered to be unimportant. The predominance of 2.26 over 2.27 has been confirmed in a recent study by Ferracci *et al.* [2011], who revised the temperature dependence of 2.27 and obtained $k_{2.26}=29$ and $k_{2.27}=6.2$ at 298 K. Ozone destruction may be limited by removal of Br and BrO via



with $k_{2.31}=17$ and an overall $k_{2.32} + k_{2.33}=240$ at 298 K [Atkinson *et al.* 2007]. Several studies (e.g. [Bedjanian *et al.* 2001]) have shown that the major product is HOBr. Mellouki *et al.* 1994 have determined that the yield of $\text{HBr} + \text{O}_3$ is negligible ($< 0.01\%$). However, once HOBr is taken up into the salty aqueous phase, Br_2 can be efficiently released into the gas phase (see section 2.4). As this process (i.e. reaction 2.32 followed by 2.77 in the liquid phase and return of Br_2 to the gas phase) can lead to an exponential growth in the BrO concentration, it earned the name 'Bromine Explosion' [Platt and Janssen 1996, Hönninger *et al.* 2004] (referred to as BE in the following). Br radicals as well as BrO react with NO_2 in the presence of a third body [M]:



The rate coefficients $k_{2.34}=270$ and $k_{2.35}=180$, are close to the high pressure limit ($[\text{M}] \longrightarrow \infty$) at 1000 mbar [Atkinson *et al.* 2007]. BrNO_2 is possibly first formed as bromonitrite, BrONO , in 2.34 and then thermalizes to nitryl bromide, BrNO_2 [Frenzel *et al.* 1998]. The absorption spectrum of BrNO_2 and BrONO have been reported by Scheffler *et al.* 1997, and photolysis is possible:



There are no experimental data on the primary photochemical processes for BrNO_2 , though the major dissociation pathway is most likely to be formation of Br and NO_2 [Atkinson *et al.* 2007]. The photolysis frequency was calculated to be $J_{\text{BrNO}_2} = 0,004\text{s}^{-1}$ for our solar simulator. The branching ratio of BrONO photolysis is unknown, both dissociation channels 2.37 and 2.38 are possible at an overall $J_{\text{BrONO}} = 0.01\text{s}^{-1}$.

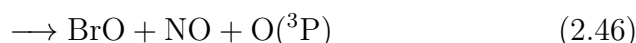
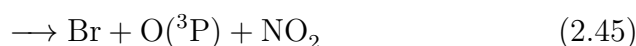
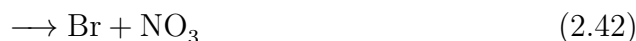
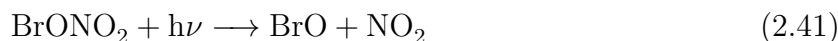
BrNO_2 is rather stable against hydrolysis [Frenzel *et al.* 1998] (compare section 2.4) as compared to BrONO_2 . We can suggested that a different isomer, BrOONO might be considered as an intermediate (by analogy to BrONO) that could rearrange to the possibly more stable bromonitrate, BrONO_2 ([Buxmann *et al.* 2012], compare 6. Nitrates either decompose thermally, photolyze, or react with water on surfaces. The rate expression of the thermal decomposition



is given by

$$k_{2.39}(T) = 2.79 \cdot 10^{13} [\text{s}^{-1}] e^{-103[\text{kJ/mole}]/RT} \quad (2.40)$$

by Orlando and Tyndall 1996. At $T=298\text{K}$ and $R = 8.314472\text{E-}03 \text{ kJ / mole K}$ this leads to $k_{2.39}=2.5 \cdot 10^{-5}\text{s}^{-1}$. There are several products of photolysis



with photolysis frequencies of $J_{\text{BrONO}_2,2.41} = 2 \cdot 10^{-4}\text{s}^{-1}$, $J_{\text{BrONO}_2,2.42} = 7 \cdot 10^{-4}\text{s}^{-1}$ and $J_{\text{BrONO}_2,2.44} = 6 \cdot 10^{-5}\text{s}^{-1}$ for our solar simulator. Photolysis rates are summarized in chapter 3. Heterogeneous uptake on liquid and/or salty surfaces will be discussed in section 2.4.

Additionally, BrO can react with NO with $k_{2.48}=210$:

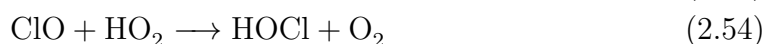


At NO_x levels comparable to HBr or even ten times smaller than BrO, reactions 2.34-2.48 could be competing reactions with reaction 2.26 and 2.32. They could



at a reaction rate coefficient of $k_{2.50} = 120$.

Reactions of Cl and ClO with HO_2 , similar to Br and BrO, but with different rate constants, can occur:

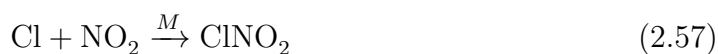


Recommended rate constant $k_{2.51}=340$, $k_{2.52}=93$ and an overall $k_{2.53}=440$ at 298 K, and branching ratios of 0.21 and 0.77 for reaction 2.51 and 2.52 [Atkinson *et al.* 2007]. The overall rate constant for reaction of ClO with HO_2 is given by $k_{2.54} + k_{2.55}=69$, and formation of HOCl is the dominant, if not sole, pathway [Atkinson *et al.* 2007].

Like BrO, ClO also reacts with NO,



with a rate constant of $k_{2.6} = 170$. And reactions with NO_2 and a third body [M]:



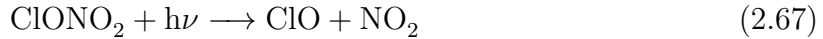
are important even at low NO_2 , as the rate coefficients, $k_{2.57}=1000$, $k_{2.58}=1000$ and $k_{2.59}=700$, are quite fast, close to the high pressure limit ($[\text{M}] \rightarrow \infty$) at 1000 mbar [DeMore *et al.* 1994, Atkinson *et al.* 2007]. Both ClONO and ClNO₂ are formed, with the former dominating. This has been explained by Chang *et al.* 1979. The thermal dissociation rate of



was measured by Anderson and Fahey 1989 at 298K to $k_{2.60}=3.2 \cdot 10^{-2}$, and the rate expression is given by

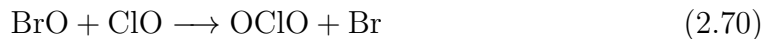
$$k_{2.60}(T) = 1.46 \cdot 10^{17} [\text{s}^{-1}] e^{-106[\text{kJ/mole}]/RT} \quad (2.62)$$

One important removal process for ClONO_2 , ClONO and ClNO_2 is known to be photolysis :

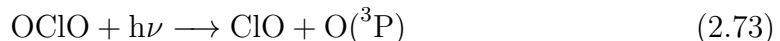


with photolysis frequencies of $J_{\text{ClNO}_2, 2.63} = 3 \cdot 10^{-5} \text{s}^{-1}$, $J_{\text{ClONO}_2, 2.67} = 2 \cdot 10^{-4} \text{s}^{-1}$ and $J_{\text{ClONO}_2, 2.68} = 4 \cdot 10^{-6} \text{s}^{-1}$ for our solar simulator. The production of $\text{O}(^3P)$ from reaction 2.64 is negligible. Oxygen atoms possibly formed via reaction 2.69 have been observed in several experiments, though some (or all) are formed by the decomposition of hot NO_3 radicals via reaction 2.68 [Atkinson *et al.* 2007]. Another sink, especially for BrONO_2 , could be the uptake on aerosols or salt surfaces, which can lead to acidification and heterogeneous chemistry (discussed in section 2.4). However, it is not clear up to date, which is the favored path way, and how the different mechanisms (including gas phase reactions, photolysis and aerosol uptake) influence the total ozone budget.

The ClO-ClO self reaction is slow ($k_{\text{ClO-ClO}} < 0.2$). Cl_2O_2 , the product of ClO-ClO reaction including a third body M , is unstable at temperatures of the lower troposphere and reforms two ClO atoms. But the reactions with BrO , which include the primary source of OClO , is :



The BrO-ClO cross reactions are important since the rate coefficients $k_{2.70} = 68$, $k_{2.71} = 62$, $k_{2.72} = 10$ [Atkinson *et al.* 2007] are fast. The direct oxidation of ClO by O_3 is not relevant, as $k_{\text{ClO}+\text{O}_3} < 0.00001$ is several orders of magnitude slower [Atkinson *et al.* 2007]. The destruction of OClO by O_3 oxidation is also slow ($k=0.000003$ [Atkinson *et al.* 2007]). The $\text{O}(^3P)$ atoms produced via the photo dissociation reaction

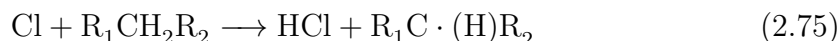


at a photolysis frequency of $J_{\text{OClO}} = 5.7 \cdot 10^2 \text{s}^{-1}$ might lead to new ozone formation.

Important reactions of Cl atoms are reactions with hydrocarbons. As methane is the most abundant hydrocarbon in the atmosphere the reaction



at a reaction rate of $k_{2.74} = 1.07$ (strong temperature dependence), becomes very important. The CH_4 mixing ratio in 2005 of about 1774 ppb is more than twice its pre-industrial values between 580 and 730 ppb. The increase by about 1000 ppb in the last two centuries, represents the fastest change in this gas over at least the last 80,000 years [Solomon *et al.* 2007]. Cl reacts with most hydrocarbons at reaction rates of 1000 (greater than those for OH), some examples are given in chapter 3. Reactions with aldehydes (e.g. with formaldehyde at $k_{\text{Cl-HCHO}} = 732$), are important as well. The formation of HCl can inhibit further reaction channels as it is highly soluble and is rapidly taken up into particles or undergoes deposition at the earth's surface. Due to this rapid removal of HCl, the comparably slow reaction with OH to generate chlorine atoms with $k_{\text{HCl+OH}} = 8$ is not important as a source of Cl. HCl can be assumed to be the dead end of chlorine formation. Once taken up into the aqueous phase HCl leads to acidification. On the other hand generation of alkyl, and subsequently alkylperoxy, radicals in reactions analogous to 2.16-2.18 for OH described earlier:



Ozone is then formed via reactions 2.18, 2.19 and 2.20. The total concentration of non-methane organic compounds varies with location, from a few ppb in remote regions to hundreds of ppb in polluted urban areas. Ozone concentrations fall approximately in the same range. Therefore Chlorine is expected to lead to ozone formation, rather than destruction, in the troposphere, regarding the reaction rates [Finlayson-Pitts 2003].

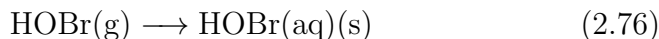
2.4. Heterogeneous Processes of Halogen Species

Heterogeneous reactions involve species that are distributed in different phases or are occurring at an interface, in contrast to homogeneous atmospheric reactions that take place in either the gas or the condensed phase. The interaction of gas phase molecules can occur at solid surfaces such as ice, acid hydrates and mineral dust and/or liquid surfaces including aqueous droplets, such as water, salt solutions (e.g., halide and sulphate), sulphuric acid, and semi volatile organics [Crowley *et al.* 2010]. The most widely used approach to describe the kinetics of heterogeneous processes is to use the uptake coefficient γ , which is the net probability that a molecule X undergoing a gas-kinetic collision with a surface is actually taken up at the surface.

Heterogeneous reactions (e.g. with nitrogen oxides, hypohalous acids HO_x ($x = \text{Cl, Br or I}$) and strong acids) are known to be involved in the release of inorganic halogen species from sea-salt aerosols. An excellent review on heterogeneous reactions on salts is given by [Rossi 2003] and the uptake coefficients are summarized in

[Crowley *et al.* 2010]. In this section the most important heterogeneous reactions are described, and the relevance to the salt pan and aerosol experiments will be discussed in chapter 7.

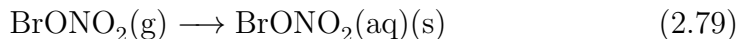
An auto catalytic production of reactive bromine species was proposed by Vogt *et al.* [1996], including the heterogeneous production of Br₂ and BrCl on sea salt aerosols. This is the 'bromine explosion' BE. HOBr produced from the gas phase reaction 2.32, which if absorbed into aerosols participates in the heterogeneous oxidation of bromide via:



Letters in brackets indicate the different phases (g),(aq),(s) as gas phase, aqueous phase and solid substrate, respectively. The uptake coefficient of HOBr on deliquescent NaBr aerosols was found to be clearly limited by the mass accommodation coefficient, which was calculated to be 0.6 ± 0.2 [Wachsmuth *et al.* 2002]. This is at least one order of magnitude higher than reported before e.g. [Fickert *et al.* 1999].

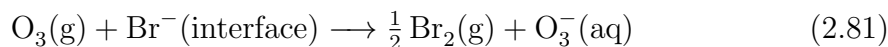
Fickert *et al.* (1999) examined the production of Br₂ and BrCl from the uptake of HOBr onto aqueous salt solutions in a wetted-wall flow tube reactor. The yield of Br₂ and BrCl was found to depend on the Cl⁻ to Br⁻ ratio, with more than 90% yield of Br₂ when [Cl⁻]/[Br⁻] (in mol l⁻¹) was less than 10³. The yield of Br₂ and BrCl is equal for [Cl⁻]/[Br⁻] ≈ 10⁴. With increasing [Cl⁻]/[Br⁻], BrCl is the main product. This is related to the rate constants of the intermediate reactions in the liquid phase. They also found a pH dependency of the out gassing of Br₂ and BrCl with greater release rates at lower pH, which was confirmed by model studies [von Glasow and Sander 2001]. The yield of Br₂ per HOBr was 50% at a pH between 7 and 8.

But other initial activation steps such as the reaction of bromine compounds with NO_x (NO + NO₂) and build-up of reactive BrONO₂ or BrNO₂ are also possible:



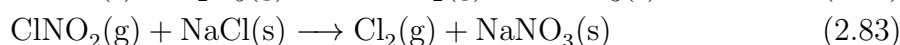
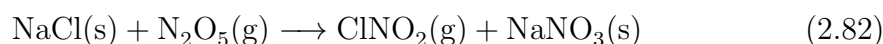
Aguzzi and Rossi [1999] investigated the reaction of BrONO₂ with solid alkali halides, such as NaCl, in a Teflon-coated Knudsen flow reactor at ambient temperature. They found the uptake coefficient for BrONO₂ on solid NaCl substrate to be 0.31. The primary product, BrCl, was detected in addition to Br₂ and HCl. Using bromide solutions, a fast initial loss rate of BrNO₂, approaching a steady state with slower loss rate, was observed by Frenzel and coworkers. This would lead to a fast build-up of Br₂. The uptake coefficient on an aqueous NaBr film of BrNO₂ is relatively small $> 1.2 \cdot 10^{-4}$ [Frenzel *et al.* 1998], compared to BrONO₂ and HOBr.

The initial step of halogen activation from the solid phase can be a reaction of O₃ with sea salt [Hunt *et al.* 2004].

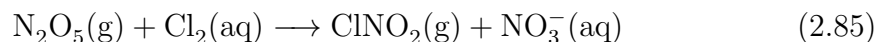
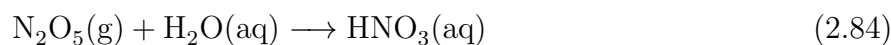


Hunt et al. 2004 reported halogen activation from a highly concentrated salt solution (close to saturation), where bromide is oxidized by ozone at the surface of deliquescent sea-salt aerosol to release Br_2 . They found an average probability of $(1.9 \pm 0.8) \cdot 10^{-6}$ of reaction 2.81, occurring for each collision of an O_3 molecule with the surface. Their results confirm observations from our laboratory on deliquescent aerosol [*Behnke et al.* 1999]. Additionally, *Clifford and Donaldson* 2007 showed direct experimental evidence for an enhanced heterogeneous reaction of ozone with bromide, although their experiments cannot address the issue of surface phase reactions under atmospheric conditions.

It was shown in 1989 by B.Finlayson-Pitts that reactions with N_2O_5 can lead to gas phase Cl_2 formation.



Reactions with NO_2 are a possible synthesis of NOCl , which has been postulated to occur under atmospheric conditions [*Finlayson-Pitts et al.* 1989]. In aerosol smog chamber studies [*Behnke et al.* 1993], those release mechanisms and the formation of Cl radicals has been confirmed, and it was shown that ClNO_2 yield depends on water and chloride concentrations within particles through the following competing reactions:



ClNO_2 production has an impact on NO_x and Cl budgets, both of which affect the troposphere's oxidizing capacity. Just recently a few hundred ppt of ClNO_2 have been measured in the middle of North America(Boulder, Colorado), whereas previous studies have been restricted to coastal or marine regions. Several estimates for the global $\text{Cl}\cdot$ source ClNO_2 range from 13 to 35 $\text{Tg Cl}\cdot \text{yr}^{-1}$ [*Platt et al.* 2004, *Allan et al.* 2007] to 8 to 22 $\text{Tg Cl}\cdot \text{yr}^{-1}$ [*Thornton et al.* 2010]. Some fraction of the $\text{Cl}\cdot$ from ClNO_2 may also be converted to temporary reservoirs, such as HOCl and ClONO_2 , possibly enhancing $\text{Cl}\cdot$ production not captured by model estimates [*Pechtl and von Glasow* 2007]. There is still an incomplete understanding of N_2O_5 [*Zhang et al.* 2007, *Bertram et al.* 2009] and of chloride partitioning across the particle distribution [*Moffet et al.* 2008]. The impact on the ozone destruction capacity is still very unclear, as Cl radicals react at a very fast rate with methane and other hydrocarbons present in the troposphere. It still remains unknown what triggers the initial steps and which is the favored reaction channel of the radical catalyzed reaction. A detailed description of chemistry involving halogens sources and sinks including the mechanisms is given in [*von Glasow and Crutzen* 2003].

2.5. Water Layers on Salt

A key variable in heterogeneous reactions involving halogens on sea salt is the relative humidity (RH), as it strongly influences the amount of available HO₂, which is necessary for the BE process. The RH also promotes the number of liquid micro layers on top of salt surfaces. A consequence is that the reaction area for heterogeneous processes is changed by varying the RH. An excellent summary of this dependence is given in a review by [Finlayson-Pitts 2003] and will be discussed below in view of our smog chamber results. The question is whether the bromine release processes are mainly limited by the chemical kinetics in the gas phase (e.g. of O₃, NO_x, HO₂, OH), by their heterogeneous interaction, or by the available sources of bromine species on top of the interaction area.

2.6. Simple Reaction Kinetic Model

In order to verify the ozone destruction by atomic bromine, it is possible to calculate the O₃ depletion at a certain time according to reaction cycle 2.25-2.29. In general the O₃ consumption can be written as:

$$\left(\frac{-d[O_3]}{dt}\right)_{Br} = k_{2.25}[Br][O_3] \quad (2.86)$$

This leads (for a given [Br]) to an exponential decay of the O₃ molecules.

$$[O_3] = [O_3]_0 \exp\left(-\frac{t}{\tau_{O_3}}\right) \quad (2.87)$$

The lifetime τ_{O_3} of O₃ can be calculated by using an exponential fit to the measured ozone time series (see chapter 5). The loss rate of ozone can be approximated as the rate-limiting step of the BrO-BrO self-reaction 2.26:

$$\left(\frac{-d[O_3]}{dt}\right)_{BrOBrO} = 2k_{2.26}[BrO][BrO] \quad (2.88)$$

At given (measured) BrO and the initial O₃ mixing ratios a time profile O₃(t) can be modeled.

In the presence of chlorine species other ozone destruction pathways can be important as well. The ClO-BrO crossreactions produce Br radicals via reaction 2.70 and 2.71, and through photolysis of BrCl from reaction 2.72, therefore:

$$\left(\frac{-d[O_3]}{dt}\right)_{BrOClO} = (k_{2.70} + k_{2.71} + k_{2.72})[BrO][ClO] \quad (2.89)$$

Since in some experiments no ClO was measured but Cl radicals and vice versa, an estimate of ClO can be made from the measured Cl radicals and vice versa. Since one ClO radical is formed via photo dissociation of OClO, reaction 2.70 does not

lead to a ClO concentration change. Therefore the steady state ratio of [ClO] to [Cl] is given by

$$\frac{[ClO]}{[Cl]} = \frac{k_{2.50}[O_3]}{k_{2.6}[NO] + (k_{2.71} + k_{2.72})[BrO]} \quad (2.90)$$

It is also possible to estimate an upper limit for the expected OClO concentration. As 2.71 and 2.72 do not contribute to OClO production and other losses of ClO are ignored, a photo stationary state between reaction 2.70 and can be assumed:

$$[BrO][ClO] \cdot k_{2.70} - [OClO] \cdot J_{OClO} = 0 \quad (2.91)$$

An upper limit for the OClO mixing ratio using the maximum calculated ClO concentration can be estimated:

$$[OClO] < \frac{[BrO][ClO]k_{2.70}}{J_{OClO}} \quad (2.92)$$

On the other hand if OClO is detected, it is possible to use equation 2.92, to calculate the expected ClO molecules.

The chlorine radicals destroy ozone very efficiently as well:

$$\left(\frac{-d[O_3]}{dt} \right)_{Cl} = k_{2.50}[Cl][O_3] \quad (2.93)$$

The different approximations for ozone destruction can now be summed up and a time profile $O_3(t)$ can be modeled. Further ozone loss can occur through wall reactions as well as photolysis, followed by reaction with water and OH production, which is shown in chapter 3. The different processes will be included in the 'simple model' for the results of the smog chamber experiments.

3. The Teflon Smog Chamber

A cylindrical chamber, made of Teflon film (FEP 200A, DuPont, thickness 0.05 mm) with a diameter of 1.33m and a volume of 3500l (as described by *Siekmann* [2008], *Bleicher* [2012] and *Buxmann et al.* [2012]), has been used. The set-up and instrumentation of the chamber will be described in this chapter, except the multi reflection systems used for detection of halogen oxides, which are part of chapter 4.

The chamber provides the capability to simulate various environmental conditions: e.g. defined injection of trace gases such as O_3 or controlled conditions of relative humidity and temperature. The temperature of the containment of the facility in the present experiments was set to $+20^\circ\text{C}$. But in general the teflon smog chamber is located in a temperature stabilized refrigerator laboratory and could achieve low temperature down to -20°C . The smog chamber facilities in the Atmospheric Chemistry Research Laboratory at the University of Bayreuth, allow us to simulate tropospheric photochemistry and aerosol simulation experiments similar to environment. The LOTASC (Low-Temperature Aerosol Simulation Chamber) facility is part of the EUROCHAMP project (Integration of EUROpean Simulation CHAMbers for Investigating Atmospheric Processes; <http://www.eurochamp.org/chambers/lotasc/>).

3.1. Solar Simulator and Photolysis Rates

A solar simulator is the heart of a smog chamber observing photochemistry, as the light is the driving force of the occurring reactions. The solar simulator used in the current set-up consists of 7 medium-pressure metal vapor (hydrargyrum medium-arc iodide, HMI Osram) lamps with 1.2 kW each (see figure 3.3) and is installed below the chamber. A borosilicate glass filter (Tempax, Schott) cuts the spectrum off at wavelengths $< 300\text{nm}$, similar to tropospheric conditions of radiation. Although still a small part of the UV-light ($< 2 \cdot 10^{11} \text{ photons cm}^{-2}\text{nm}^{-1}\text{s}^{-1}$) below 300nm remains. In order to prevent overheating of the glass and to remove part of the IR radiation we used an additional filter layer of distilled water, which was cooled by room air in a ventilated heat exchanger, similar to a car radiator. There were different set-ups used in former works, and as some of the results will be compared within the discussion section, they are included in figure 3.3.

Cl_2 actinometry was used to measure the actinic photon flux, which enables to determine photolysis rates for the applied solar simulator. For this purpose we injected the different hydrocarbons HC_i , summarized in table 3.3, (for observation of Cl radicals as described in section 3.2) and about 150 ppb Cl_2 into the chamber. After switching the solar simulator on, Cl_2 is photolyzed and the atomic Cl reacts,

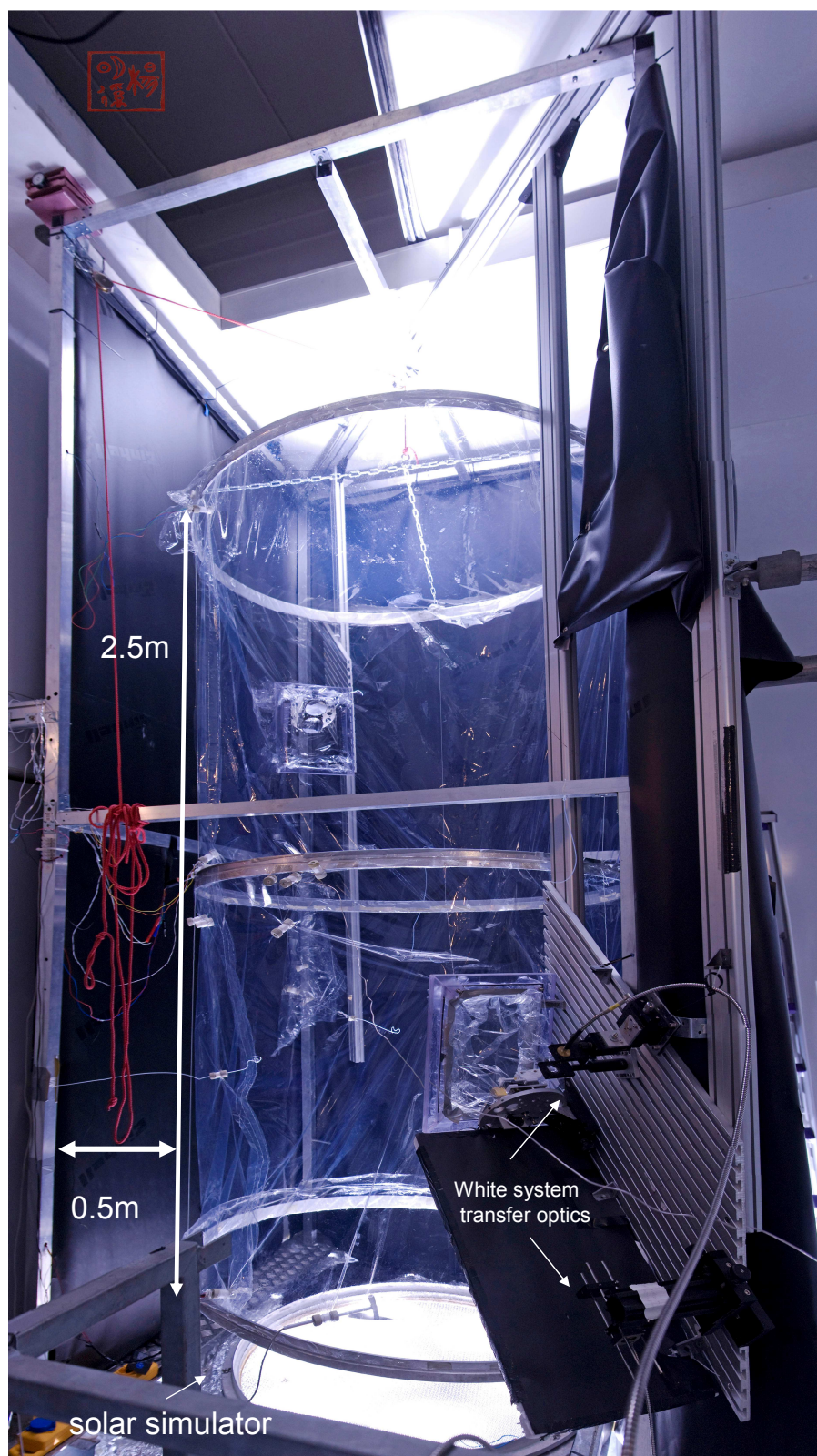


Figure 3.1.: Photography of the smog chamber with the White system. The solar simulator is switched on. The picture is a stack of 4 photographs (made by *Yang* [2010]).

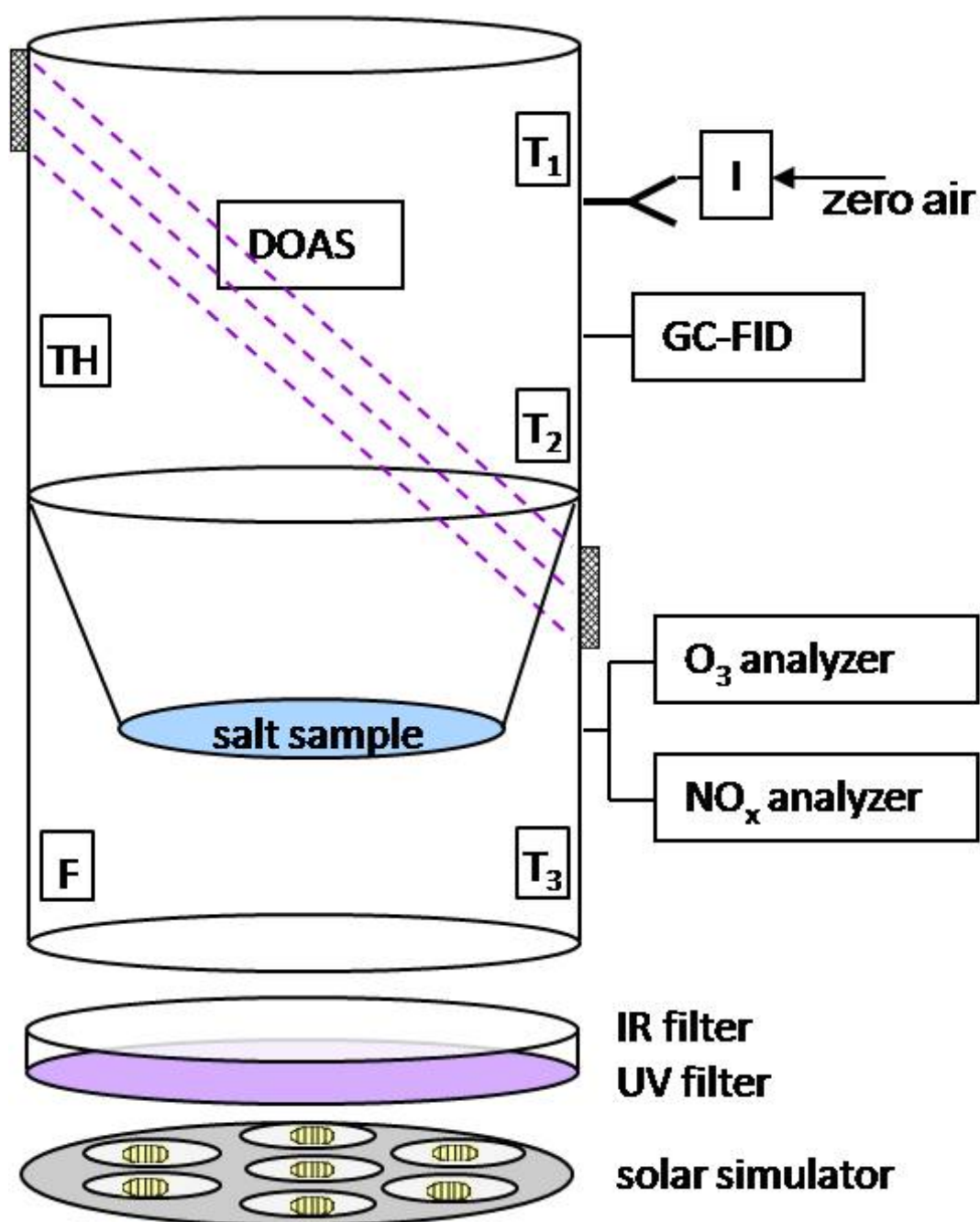


Figure 3.2.: set-up of the smog chamber with suspended fluorinated ethylene propylene (FEP)-sheet, salt sample and the analytical equipment: chemiluminescence (CL) analyzer for NO and NO_x , O_3 analyzer, gas chromatograph with flame ionization detector (GC-FID) for indirect detection of $Cl\cdot$ and $OH\cdot$ radicals, DOAS multi-reflection cell combination for direct detection of BrO , (I) impinger with a bypass inlet, (T_1, T_2, T_3) temperature sensors, (TH) temperature and humidity sensor, (F) fan (10 cm wing diameter, 0.4 W). A water layer on the UV filter serves as IR filter for the solar simulator that is mounted below. The photolytic frequency of NO_2 in the absence of the salt pan was determined to be $J_{NO_2} = 6.3 \cdot 10^{-3} s^{-1}$. (adapted from [Buxmann et al. 2012])

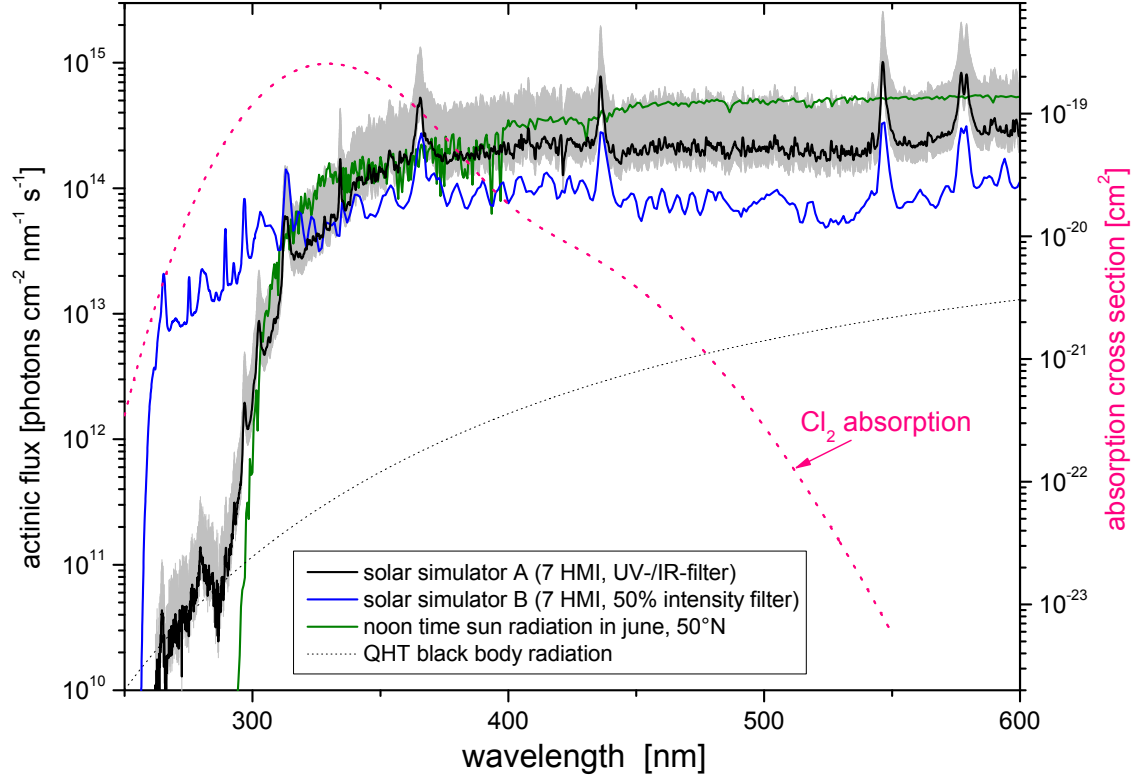


Figure 3.3.: Actinic flux of different solar simulators used in the teflon smog chamber. Solar simulator A was used in the experiments conducted within this thesis and is characterized by *Bleicher* [2012]. The grey shadow indicates the time degradation of the HMI lamps. Solar simulator B using an aluminum grid to reduce the intensity was applied by *Siekmann* [2008]. The absorption cross section of Cl_2 is shown in pink dashed line and the photolytic frequency of Cl_2 in the absence of the salt pan was determined to be $J_{\text{Cl}_2} = 1.55 \cdot 10^{-3} \text{ s}^{-1}$, using Cl_2 actinometry. Additionally a calibrated QTH (quartz tungsten halogen) lamp was used to proof the measured actinic flux. For comparison a typical noon time sun spectrum (june, 50°N), calculated using the system for transfer of atmospheric radiation (STAR)sci radiative transfer model is shown in green (adapted from [*Bleicher* 2012]).

consuming the HC_i . So it is possible to infer $[Cl](t)$. The relationship between $[Cl](t)$ and $[Cl_2](t)$ is expected to be linear after reaching the photo stationary state. $J_{Cl_2} = 1.55 \cdot 10^{-3} s^{-1}$ was obtained by considering the absorption cross sections of Cl_2 [Maric *et al.* 2005] and assuming a quantum yield of unity. J_{NO_2} was then calculated from the actinic flux, considering the cross sections of NO_2 [Burrows *et al.* 1998] and photolytic quantum yields of Gardner *et al.*, including the minor corrections by [Troe 2000]. The photolysis frequencies $NO_2 + h\nu \rightarrow NO + O$ for our solar simulator was determined to be $J_{NO_2} = 6.3 \cdot 10^{-3} s^{-1}$, based on Cl_2 actinometry.

Table 3.1.: List of photolysis frequencies [s^{-1}] for different light conditions, which are relevant for the smog chamber experiments. Values are rounded for the sake of clarity. The solar simulator consists of 7HMI lamps, a comparison with 1 HMI lamp and winter (December, Dec.) and summer (Junie) is shown. (adapted from [Bleicher 2012], and references therein.)

substance	7 HMI	1 HMI 50%	sun Juni	sun Dez.	exponent 10^{-x}
$O_3 \longrightarrow O(^1D)$	25	2000	25	2.5	6
$O_3 \longrightarrow O(^3P)$	2	3	5	3	4
H_2O_2	4	20	7	2	6
Cl_2	1.55	1.1	2.4	1	3
Br_2	17	7	35	22	3
$BrCl$	7	3	11	6	3
ClO	12	230	15	2	5
BrO	2	2	4	1	2
IO	11	5	20	10	2
$OCIO$	5	3	7	3	2
$OBRO$	20	8	50	35	2
$ClOOCl$	8	20	15	4	4
$HOCl$	17	20	28	9	5
$HOBr$	1.5	1	2	1	3
NO_2	6.7	3.8	9	4	3
$NO_3 \longrightarrow NO_2 + O(^3P)$	10	3	20	15	2
$NO_3 \longrightarrow NO + O_2$	11	2	23	18	3
$N_2O_5 \longrightarrow 2NO_2 + O(^3P)$	5	130	9	2	7
$N_2O_5 \longrightarrow NO_2 + NO_3$	2.5	8	4	1	5
$N_2O_5 \longrightarrow NO_3 + NO + O(^3P)$	1.5	500	-	-	8
$HONO$	15	10	20	7	
HNO_3	35	700	50	9	8
HNO_4	20	600	30	5	7
$ClNO_2$	20	40	35	10	5
$ClONO_2 \longrightarrow ClO + NO_2$	4	15	7.5	2	6
$ClONO_2 \longrightarrow Cl + NO_3$	3	3.5	4	1.5	5
$BrNO_2$	3.7	2.5	6.2	3.2	3
$BrONO_2 \longrightarrow BrO + NO_2$	2	2	3	1.5	4
$BrONO_2 \longrightarrow Br + NO_3$	7	6	11	5	4
$BrONO_2 \longrightarrow BrNO_2 + O(^3P)$	6	90	6	1	5
$HCHO \longrightarrow H + HCO$	10	40	30	5	6
$HCHO \longrightarrow H_2$	2	3	5	1	5

Table 3.2.: Overview of the instruments used and species measured during our smog chamber experiments with different halogen sources (SP=salt pan, SA=salt aerosol). Different kinds of Chemoluminescence monitors are used (CL^1 =Ecophysics CLD-700-Al, CL^2 =Ecophysics CLD-88p, CL^3 =Bendix-UPK8002).

Instrument	Species measured	Halogen source
GC-FID	n-butane, n-pentane, 2,2-dimethylbutane, 2,2,3,3-tetramethylbutane, toluene, n-perfluorohexane, and indirectly OH and Cl	SP and SA
WS DOAS	BrO, O ₃ , NO ₂ , HCHO, HONO, OCIO ClO	SP and SA SA
CE DOAS	BrO, O ₃ , NO ₂ , HCHO, HONO, OCIO	SP
CL ¹	NO, NO ₂ = NO _x -NO (molybdenum-converter)	SP
CL ²	NO, NO ₂ = NO _x -NO (blue light converter)	SA
CL ³	O ₃	SP
UV photometrie	O ₃	SA
EC + CNC	particle size and number	SA

3.2. Further Analytical Instrumentation of the Smog Chamber

Table 3.2 gives an overview of the instruments used and the species measured in our smog chamber.

Besides the analytical instrument for detection of trace gases and aerosols, the general conditions such as relative humidity, temperature, light and pressure are monitored as well. During all experiments the chamber was kept slightly overpressurized, in order to prevent leaking of room air into the system. During the salt pan experiments the over pressure was ensured using a bypass system. During the sea salt aerosol experiments a pressure sensor and a LabView program, to control the flow was applied (for details see [Bleicher 2012]). The LabView program simultaneously logs the NO, NO_x, O₃, RH, temperature and time as well. As illustrated in figure 3.2, there are three temperature sensors (LM35C, National Semiconductors) and a combined relative humidity/temperature sensor (DKRF 4001-P, Driesen und Kern) and a home-made fan to enforce mixing. A photo-UV-Diode (Infineon, BPX 65) with glass filters (Schott, UG11 and BG39), monitors at which time the solar simulator is switched on and off during an experiment. The temperature of the containment of the facility in the present experiments was set to +20°C. The temperature of the relative humidity sensor showed periodic fluctuations with an amplitude of about 2°C every 33 min before the solar simulator was started, changing to smaller fluctuations of 0.5°C every 6 min when it was switched on. The

Table 3.3.: Initial mixing ratios, C_0 , and rate coefficients for the reactions of the hydrocarbons with OH (k_{OH}) and Cl (k_{Cl}) used for the radical clock method (in Units of $10^{-13} \text{cm}^3 \text{molecule}^{-1} \text{s}^{-1}$ at 298°K) [Atkinson et al. 2007, Aschmann and R. 1995, Shi and Bernhard 1996, Hooshiyar and Niki 1995]

Compound	C_0 (ppb)	k_{OH}	k_{Cl}	k_{Cl}/k_{OH}
n-Butane	55	23.6	1970	83
n-Pentane	12	38.8	1100	29
2,2-Dimethylbutane	20	22.3	1680	75
2,2,3,3-Tetramethylbutane	12	9.73	1560	160
Toluene	11	59.6	590	9.9
n-Perfluorohexane	10	0	0	-

relative humidity values and temperatures given for the experiments in this work are thus nominal values for 20°C , calculated from absolute humidities and temperatures. Before starting an experiment, by e.g. insertion of the salt sample on the pan or injection of aerosols, the chamber was cleaned by photochemistry, introducing high levels of humidity ($> 60\%$), ozone (1-2 ppm) and UV radiation of our solar simulator for 6-10 hours. Prior to each experiment, while the salt sample was already distributed on the pan, the chamber was flushed with clean air for > 12 hours.

Flame ionisation detector (FID) and the radical clock for indirect detection of OH and Cl

In order to quantify the concentration of OH- and Cl- radicals, five hydrocarbons (HC_i) and n-perfluorohexane (as inert dilution standard) are added and measured by a gas chromatograph with flame ionization detector (GC-FID, Siemens, Sichromat) with a capillary column (Al_2O_3 PLOT, Chrompack) to provide the radical clock method [Zetzsch and Behnke 1992]. Before starting the solar simulator we injected n-butane, n-pentane, 2,2-dimethylbutane, 2,2,3,3-tetramethylbutane, toluene, and n-perfluorohexane into the chamber at typical mixing ratios listed in Table 3.3. The rate constants for the reactions of the HC_i with OH and Cl and the ratios k_{Cl}/k_{OH} relevant for the radical clock method are also given in Table 3.3. Note that Br radicals only react (at room temperature) with unsaturated hydrocarbons or partly oxidized species such as aldehydes but not significantly at room temperature and below with alkanes and at a slow rate $k_{Br} = 0.1$ [Bierbach et al. 1999] with toluene.

The kinetic differential equations for the consumption of the HC_i can be written as:

$$\frac{-d[HC_i]}{dt} = k_{i,OH}[OH][HC_i] + k_{i,Cl}[Cl][HC_i] \quad (3.1)$$

Polynomials (up to 4th order) were fitted to the measured HC decays as a smoothing procedure if appropriate. Then the differential equations are solved for both

unknowns, $[OH]$ and $[Cl]$, at a time t , to calculate mean values and standard deviations for OH and Cl concentrations over the time period of the experiment and to obtain their time profiles in favorable cases. Dividing equation 3.1 by $[HC_i]$ we obtain the equation

$$\frac{-d\ln[HC_i]}{dt} = k_{i,OH}[OH] + k_{i,Cl}[Cl] \quad (3.2)$$

leading to the time integrals $\int [OH] dt$ and $\int [Cl] dt$ and time profiles of OH and Cl after separation of the variables and integration, taking the incremental slopes. For more details see [Bleicher 2012], who performed the Cl and OH calculations.

Nitrogen Oxides Injection and Detection

A chemiluminescence (CL) monitor (Ecophysics CLD-700-A1) was applied for direct monitoring of NO during the salt pan experiments. Additionally NO_x was monitored with the same instrument by reduction to NO through a molybdenum converter. During the sea salt aerosol experiments a chemiluminescence (CL) monitor (Ecophysics CLD-88p) detected NO . NO_x was reduced by a blue light converter (Ecophysics plc860). The efficiency of the blue light converter was calibrated using a reference gas mixture with known NO_2 concentration, produced via gas phase titration of NO with O_3 in the laboratory. The advantage of the blue light converter is that it particularly destroys NO_2 , whereas the molybdenum converter reduces other nitrogen oxides and acids e.g. $HONO$, as well. It will be referred which kind of converter was used, within the data shown in chapter 5. Furthermore it is well known that Teflon has the ability to store NO_x and release it under the influence of heat and UV irradiation [Carter 1999]. Therefore, NO and NO_x could not be completely removed, and this will be discussed in chapter 5. In some experiments we injected large levels of NO_2 using calibration gas from Riessner Gase, containing 101 ppm of 1.8 (98%) pure NO_2 . But NO_2 is a highly reactive gas and commercially available gas mixtures (in pressure cylinders) have a high uncertainty in the NO_2 concentration. This was not a problem during the experiments, as the NO_2 mixing ratios were monitored with both DOAS and CL.

Ozone Production and Detection

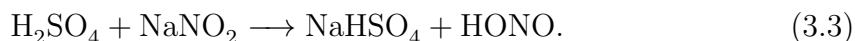
Ozone was produced by two different methods: a) O_2 (purity 99.995%) is passed through a corona discharge ozonizer (Sorbios). b) O_2 (purity 99.995%) was pre mixed in a three-necked flask, passing three Pen-Ray Lamp mercury lamps, with an emission line at 184.91 nm, to photolyse the oxygen and form ozone via reaction 2.20. The O_3 rich air is slowly flushed into the teflon chamber. Ozone was monitored by a CL ozone analyzer (Bendix-UPK8002) during the salt pan experiments. During sea salt aerosol experiments O_3 was monitored using a Thermo Scientific

Model 49i ozone analyzer, a dual-cell, UV photometric analyzer.

In some experiments, measurements of O_3 , NO and NO_x were only performed every 15-25 minutes with a gas flow of 1.4 l/min, in order to reduce dilution. The measurements were synchronized with GC-sampling. The overall dilution rate during the experiments was determined from the n-perfluorohexane data, if the HCl were injected.

HONO Production and Detection

Two LOPAP (LOng-Path AbsorPtion, QUMA Elektronik & Analytik, Wuppertal, Germany) instruments, were used for detection of nitrous acid HONO by [Sörgel 2008]. The details of the instrument are described elsewhere [Kleffmann *et al.* 2002]. The LOPAP is based on a wet chemical technique, with fast sampling of HONO as nitrite in a stripping coil and subsequent detection as an azo dye using long path absorption in 2.4m long Teflon AF tubing [Sörgel *et al.* 2011]. The external stripping coil unit is placed 1cm distance from the chamber wall, inside the chamber. The generation of the nitrous acid is based on the reaction of a sodium nitrite solution $NaNO_2$ with sulfuric acid H_2SO_4 as e.g. described by Taira and Kanda 1990:



The reaction takes place in a glass vessel with a glass frit at its base. Diluted solutions of sodium nitrite and sulfuric acid are continuously pumped into a reaction vessel and the mixture is then drawn off to waste. A carrier gas, here nitrogen, is introduced into the reagent mixture through the frit and continuously purges nitrous acid vapor from the mixture.

Particle Number and Size Distribution

The particle number and size distribution of sea salt aerosols and SOA was determined via an electrostatic classifier (EC) (TSI, 3071) and a condensation nuclei counter (CNC) (TSI, 3020). The EC consist of a sequential set-up of a bipolar diffusion charger (or traditionally named neutralizer) and a differential mobility analyzer (DMA). The aerosol particles are brought to a bipolar charge equilibrium. Positive and negative ions are produced continuously in this bipolar diffusion charger by a radioactive β -source (^{85}Kr). The DMA is built as a cylindrical capacitor. By setting different voltages in the DMA, particles of different electrical mobility are selected and their particle number concentration can be measured. The electrical particle mobility depends primarily on particle charge (proportional) and particle diameter (inversely). The smaller the particle diameter and the higher the number of charges, the larger is thus the electrical particle mobility. The Boltzmann equilibrium causes that bigger particles are double and even multiple charged, and thus counted as smaller particles. According to a characterization of the EC a charge correction is

performed (for details see [Bleicher 2012]). The particle number concentration in the sample flow is measured in the CNC, after presorting by the EC. The particles are injected into air that is supersaturated with n-butanol vapor to form larger particle droplets. Supersaturation of the air containing the particles is achieved by passing them through a higher temperature region (30°C) saturated with n-butanol. The gas/droplet stream is then cooled down to 10°C, where the alcohol vapor condenses on the nuclei to form larger droplets. The particles are counted in an absolute nuclei counter, by measuring scattered light by a photo detector. The notation CNC can be misleading, as nuclei are often connected with cloud condensation nuclei and some groups rather use the name condensation particle counter (CPC). The combination of EC (consisting of a neutralizer and DMA) and CNC (or CPC) is often referred to as DMPS (Differential Mobility Particle Sizers) or SMPS (Scanning Mobility Particle Sizers) [Wiedensohler *et al.* 2012].

3.3. Generation of Aerosols in the Chamber

Artificial Salt Aerosols

Generating sea-spray-aerosol from salt solutions was performed via an ultrasonic atomizer (Quick-Ohm, QUV-HEV FT25/16A, 35 W, 1.63 MHz). The salt solutions contained a mixture of pure NaCl (Aldrich, 99+ %, containing less than 0.01 % of bromide) and NaBr (Riedel-de-Haen, 99 %), dissolved in bidistilled water. Two different ratios were used during the present studies: a) 86.4mg/l NaBr and 1g/l NaBr, corresponding to Br/Cl ratio of 1/20, similar to the Dead Sea (Cl^- : 225-405 g/l, Br^- : 6.1-11 g/l, [Sirkes *et al.* 1997]). b) 7.6 mg/l NaBr and 1g/l NaBr, corresponding to Br/Cl ratio of 1/230, similar to sea water. The high-frequency oscillations (1.6 MHz) generate droplets which are injected by a gentle air flow from the zero air generator. The size distribution is in the order of 5-1000 nm, with a typical maximum at 300-400 nm. The respective aerosol size distributions are shown for each experiment within the results chapter. The aerosol surface is crucial for the heterogeneous exchange processes (as described below), and will be calculated assuming a spherical shape of the aerosols. Siekmann showed a detailed dependence of the aerosols size distribution from the NaBr/NaCl content within his Dissertation [2008].

SOA

Racemic α -pinene with a purity of 98% (Aldrich, 14752-4) was used for SOA formation from a terpene-type precursor. Further precursors for the SOA were catechol (Riedel-de Haen, 32101, pro analysis grade, >99% HPLC) and guaiacol (Sigma Aldrich, G5502, pro analysis grade, >99% GC). The precursor substances were injected into the chamber by evaporating the solid precursors with the help of a burner.

Inside the chamber the gas phase species form aerosols under the influence of UV-light and OH radicals. Physico chemical characterization of SOA from α -pinene has been reported by Ofner [Ofner *et al.* 2011]. SOA formation from catechol and guaiacol is described in detail by [Ofner *et al.* 2011], as well as the influence of halogen species [Ofner *et al.* 2012].

3.4. Salt Samples for the Salt Pan Experiments

Preparation of NaCl/NaBr Salt Samples

In addition to a pure sodium chloride sample (Aldrich, +99%, containing less than 0.01% of bromide), a mixture of 100 g of sodium chloride and 0.33 g of sodium bromide (Riedel-de-Haën, 99%) was dissolved in bidistilled water. This solution was concentrated and recrystallized within 24 hours at 30°C under a constant flow of purified air from a zero air generator, providing dry air with a dew point of -70 °C and containing ≈ 600 ppb of methane (quantified by purge and trap GC-FID by C.Tubesing [pers.comm.] and confirmed by Bleicher [2012]). The dry salt samples with a chloride/bromide molar ratio of 530:1, which is similar to seawater, were ground in a ball mill (Retsch MM 2) for 1 min and placed inside the chamber using a flat $0.5m^2$ Teflon sheet (FEP 200A, DuPont), as shown in figure 3.2, to simulate a natural salt pan.

Size Distribution of NaBr/NaCl Crystals on the Salt Pan

To estimate the size distribution of the salt crystal on the salt pan microscopical images of the grained salt on a black background were taken. An optical microscope (Bresser-LCD micro), with a magnification of 1:25 was used.

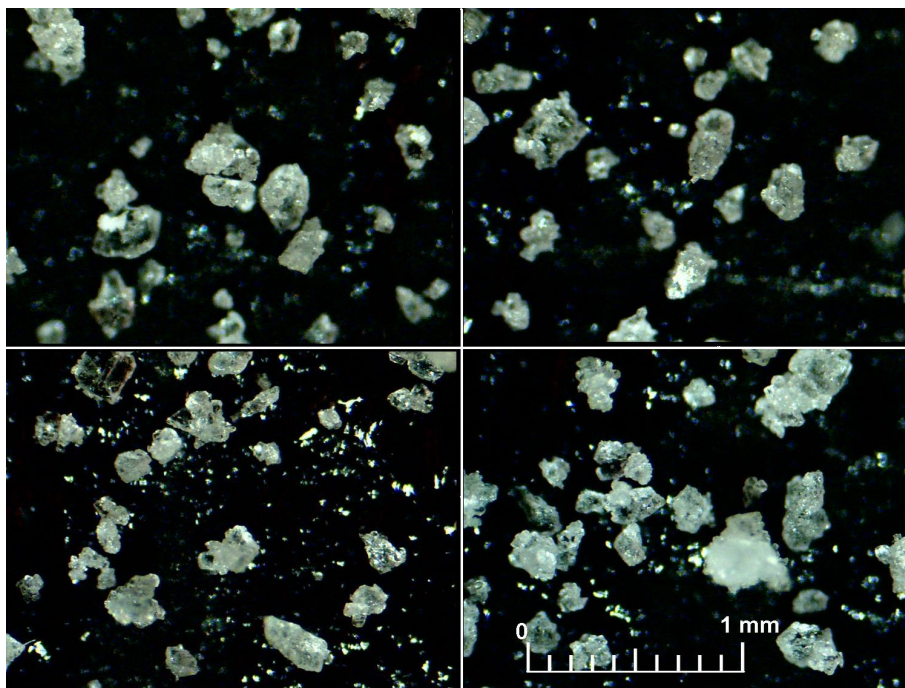


Figure 3.4.: Microscopic images of the grained salt crystals used for determination of the size distribution. Note that the density of the salt particles is smaller in these images than in the chamber experiments. This was necessary to be able to count the small particles, even they do not contribute as much to the total surface area.

Four typical images of the grained salt particles are shown in figure 3.4. For the estimation of the size distribution a HP BASIC program written by H-U. Krüger (technician, university of Bayreuth) was used. First a 1 mm unit size was defined, with $10\text{ }\mu\text{m}$ as the minimal size. For every single salt particle a line is drawn from one end to the other, saved as the diameter of one salt particle. This procedure was done for 500 particles, which leads to the particle size distribution shown in figure 3.5. More than half particles (269) have a diameter of $14 - 21\text{ }\mu\text{m}$ and 13 particles are $10\text{ }\mu\text{m}$ and smaller. Only 7 particles were counted with a size bigger than $180\text{ }\mu\text{m}$. However assuming a cubic shape of the salt crystals a total volume of 0.162 mm^3 was calculated for 500 particles. The cubic shape is justified by the cubic crystal structure of NaBr and NaCl. The molar volume of sodium chloride is known to be $27,18\text{ cm}^3/\text{mol}$, and the molar mass is $58,44\text{ g/mol}$. That means 100g NaCl are 1,711 mol or $46,5\text{ cm}^3$. Using the volume estimate of $0.162\text{ mm}^3/500$ particles the total number of the salt particles of 100g NaCl is $1.45 \cdot 10^8$ particles. With the size of the salt pan of 0.5 m^2 , this leads to $290\text{ particles/mm}^2$.

Defining one square of the diameter as a base area of a NaCl particle, the total base area (sum over square for each particle size multiplied by the number) at the measured particle size distribution gives a total area of 1.33 mm^2 for 500 particles. The biggest surface area one could imagine is five sides of the cubic shaped salt

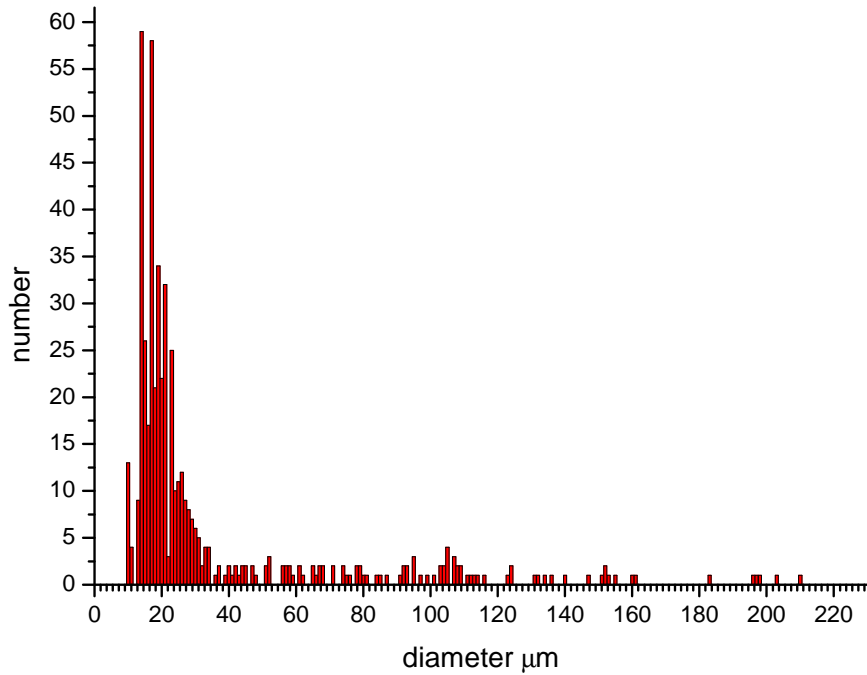


Figure 3.5.: Salt particle size distribution of the grained NaCl/NaBr mixture used in the salt pan experiments. 500 particles were counted.

cristall exposed to air. Six sides in contact with air is very unstable and therefore unlikely. That means an approximate surface area of $3,86\text{mm}^2$ for 290 particles, or $1,93\text{m}^2$ for a $0,5\text{m}^2$ salt pan containing 100g NaCl. The assumption of a cubic shape is not confirmed by the microscopical image (figure 3.4, but satisfies the purpose of estimation of an order of magnitude for a maximal surface area of 2m^2 .

3.5. Wall Effect of Ozone

In order to quantify the wall loss rate of ozone in particular, a simple set of experiments and comparison with model expectations was used [Bleicher 2012]. Ozone was injected at mixing ratios of up to 1ppm. And once the solar simulator is switched on, the ozone decay was monitored with the UV ozone monitor. Ozone is slowly photolyzed as described in chapter 2, via reaction 2.1. In the presence of water molecules the formed $\text{O}(^1D)$ produces two OH radicals, in case of collision with a water molecule (reaction 2.6). This results in an overall ozone loss, depending on O_3 photolysis and the abundance of H_2O molecules. The experiment was repeated for different relative humidities between 2%, and 85% at 20°C , and after subtract-

ing dilution, according to an exponential fit the lifetime of O_3 was calculated. The measured lifetime is compared to a model including O_3 photolysis followed by OH production as described above. The difference of the measured O_3 loss and the model gives the loss due to wall effects. This is shown in figure 3.6.

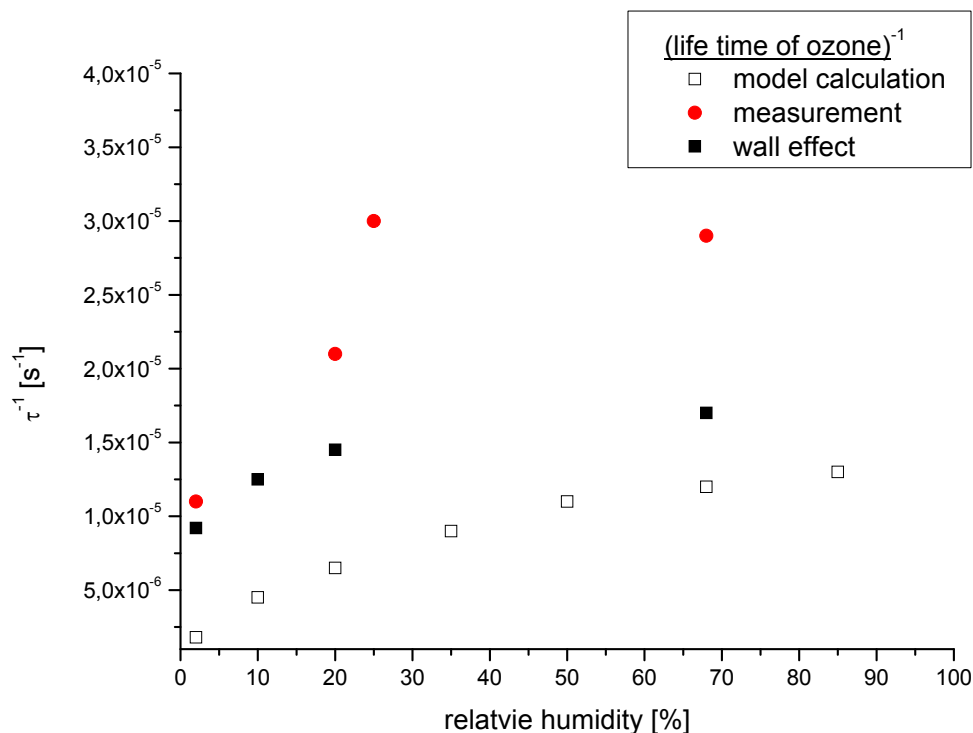


Figure 3.6.: One over life time of ozone τ^{-1} at different relative humidities in the absence of the salt pan and without aerosols. The measured life time is shown in red, a model calculation including O_3 photolysis and OH production, as well as dilution is shown in open squares. The difference between the model and measurement (black squares) reflects the wall effect. Adapted from *Bleicher* 2012.

3.6. Treatment of Heterogeneous Reactions in Smog Chambers

The aim is to parameterize heterogeneous reactions at the surface of the chamber (or at additional surfaces, like salt pans, with area A_P brought into the chamber). For that purpose the collision frequency of a constituent X (e.g. HOBr) in the chamber with the chamber wall in a smog chamber with volume V and total surface area A will be calculated in the following chapter. The following three approaches are a result of a detailed discussion with *Platt* 2012.

First Approach: Gas Kinetic Considerations

The frequency f_X/A of collisions of species X in the chamber per unit area of the chamber (inner) surface is given by:

$$\frac{f_X}{A} = \frac{1}{6} c_X \cdot v_X [\text{molec.s}^{-1}] \quad (3.4)$$

Where c_X denotes the concentration of species X (in molecules per unit volume) and v_X denotes the average molecular velocity of species X, given by $v_X = \sqrt{\frac{8k_B T}{\pi m_X}}$ (Maxwell-Boltzmann distribution), with k_B = Boltzmann constant = $1.38 \cdot 10^{-23} \text{ J/K}$, T = temperature, and m_X = mass of the molecule X. Obviously the collision frequency f_X is proportional to c_X .

In order to obtain the collision frequency of an individual molecule (of X) with the surface A, equation 3.4 is divided by the total number of molecules $n_X = c_X \cdot V$ in the chamber:

$$f_c = \frac{f_X}{c_X \cdot V} = \frac{1}{c_X \cdot V} \cdot \frac{1}{6} \cdot c_X \cdot v_X \cdot A = \frac{1}{6} v_X \cdot \frac{A}{V} [\text{s}^{-1}] \quad (3.5)$$

This reminds very much of the 'traditional' formula (e.g. [Seinfeld and Pandis 2008]) for collision frequencies of gases with aerosols $f_c = \frac{1}{4} v_X \frac{A}{V}$. The factor $\frac{1}{4}$ is the result of the cross-section to surface ratio of a spherical aerosol. In the case of wall reactions a molecule hits the wall in one out of six possible directions, which may justify the factor $\frac{1}{6}$. However, the factor is of minor importance here, as it depends on the definition of the reaction probability (see below), as well.

The numerical value of f_c for the Bayreuth chamber can be estimated by using: $\frac{A}{V} = 13, 2 \text{ m}^2/3, 5 \text{ m}^3 = 3, 8 \text{ m}^{-1}$, $v_X = 220 \text{ m/s}$. This yields $f_c = 139 \text{ s}^{-1}$ corresponding to an average time between collisions of $\tau = 1/f_c = 7 \text{ ms}$ (!). This short time appears to be much (i.e. 3 orders of magnitude) shorter than the mixing time within the chamber (estimated at 10-20 seconds).

Assuming that the reactions only take place at the surface of the salt pan the area A_P of the salt surface (see chapter 3.4) is used instead of the total inner surface area A of the chamber. Also the probability $\gamma_{upt} < 1$ that a reaction (of the type of interest) actually occurs upon collision of X with the surface A_P is introduced. Then it can be obtained for the frequency of reactive collisions:

$$f_R = \frac{1}{6} v_X \cdot \gamma_{upt} \frac{A_P}{V} [\text{s}^{-1}] \quad (3.6)$$

With $A_P \approx 0.5 \text{ m}^2$ and $\gamma_{upt} = 0.6$ [Wachsmuth et al. 2002] the result is $f_c = 15 \text{ s}^{-1}$ or $\tau = 1/f_c = 66 \text{ ms}$, still quite fast!

Second approach: Diffusion control close to the surface

The total flow of species X to the surface (area A) is given by regarding to Fick's first law:

$$F_X = \frac{dc_X}{dz} \cdot D_X \cdot A [\text{molec.s}^{-1}] \quad (3.7)$$

Where the meaning of the variables is the same as in the approach of gas kinetic considerations and D_X denotes the molecular diffusion constant of species X in air.

The assumption that the concentration c_X at the surface is zero and further diffusion control in a layer of thickness h above the surface leads to:

$$\frac{dc_X}{dz} \approx \frac{c_X}{h} \quad (3.8)$$

and obtain for F_X :

$$F_X = \frac{c_X}{h} \cdot D_X \cdot A [\text{molec.s}^{-1}] \quad (3.9)$$

In the above consideration h is the thickness of a layer, where molecular diffusion dominates the transport, while in the bulk of the volume turbulent mixing is assumed. Turbulent mixing is typically several orders of magnitude faster than mixing by molecular diffusion, however, close to the surface the eddies of the turbulent motion become smaller and smaller until their effect on mixing becomes smaller than that of molecular diffusion. From boundary layer theory [Liu *et al.* 1979] we know that h is of the order of 0.1 to 1 mm. For instance h could be derived from the Blasius formula [Blasius 1908]:

$$h \approx \sqrt{\frac{\nu^* x}{v_0}} \quad (3.10)$$

with $\nu^* = 1.5 \cdot 10^{-5} \text{ m}^2/\text{s}$ denotes the kinematic viscosity of the gas in the chamber (i.e. of air), X is the distance downstream from the beginning of the flow (X could be taken as \approx radius of the salt pan = 0.2 m at the Bayreuth chamber), and v_0 denotes the free stream velocity ($v_0 \approx 3 \text{ m/s}$ for the Bayreuth chamber). With these figures we obtain $h \approx 10^{-3} \text{ m}$ or 1 mm, which appears to be at the high end of the range.

In order to obtain the collision frequency f_{dc} of species X (as in the first approximation), equation 3.9 is divided by the total number n_X of molecules in the chamber:

$$f_{dc} = \frac{F_X}{n_X} = \frac{c_X}{c_X \cdot V} \cdot \frac{D_X}{h} \cdot A = \frac{D_X}{h} \cdot \frac{A}{V} [\text{s}^{-1}] \quad (3.11)$$

Considering that $\frac{D_X}{h}$ is some velocity, the above expression has the same structure as the one derived from the first approach.

Likewise A is replaced by A_P . Note that the reaction probability γ plays no role in this approach, since the concentration c_X is assumed to be zero at the surface:

$$f_{Rd} = \frac{D_X}{h} \cdot \frac{A_P}{V} [\text{s}^{-1}] \quad (3.12)$$

The numerical values of f_{dc} and f_{Rd} , respectively for the Bayreuth chamber can be estimated by using (as above): $\frac{A}{V} = 3.8m^{-1}$, $A_p = 0.5m^2$, $v_X = 220m/s$ and $D_X \approx 10^{-5}m^2/s$ with $h = 0.001$ m (1 mm) this leads to $D_X/h = 10^{-2}m/s$ (The diffusion coefficient for HOBr in He and H₂O were measured to be $273 \pm 1 Torr\ cm^2s^{-1}$ and $51 \pm 1 Torr\ cm^2s^{-1}$ by *Adams et al.* [2002], which justifies $D_X \approx 10^{-5}m^2/s$ for atmospheric pressure.)

This yields $f_{dc} = 0.038s^{-1}$ corresponding to an average time between collisions of $c_d = 1/f_{dc} = 26s$ and $f_{Rd} = 0.0014s^{-1}$ corresponding to $\tau_{Rd} = 700s$ (≈ 11 minutes and 40 seconds), respectively.

Obviously the diffusion approach yields collision (and reaction) frequencies which are a factor of about 3000 smaller than predicted by the gas kinetic approach.

One may obtain the small collision/reaction frequencies by inserting a very small volume V_P ($V_P \approx V/5000 = 0.4$ liter) instead of V into the expression derived from the gas kinetic approach, however it is not clear how to justify this assumption.

Third Approach: A Synthesis

Let's consider a very thin layer (thickness of the order of the length of the mean free path of the molecules under consideration) where the trace gas concentration c_{XS} is directly above the surface (see fig. 3.7). For the molecules in this layer we can assume gas kinetics as in the first approach.

The concentration gradient in the viscous layer (extending from the surface to the bulk) and the collision frequency F_X is then:

$$\frac{dc_X}{dz} \approx \frac{c_X - X_{Xs}}{h} \quad (3.13)$$

$$F_X = \frac{c_X - X_{Xs}}{h} \cdot D_X \cdot A [molec.s^{-1}] \quad (3.14)$$

Of course determination of the trace gas concentration c_{XS} directly above the surface is necessary. this can be done by inspecting the continuity relationship:

$$\frac{f_X}{A} = \frac{1}{6} \cdot c_{Xs} \cdot v_X \cdot \gamma = \frac{dc_X}{dz} D_X \approx (c_X - X_{Xs}) \frac{D_X}{h} \quad (3.15)$$

After rewriting:

$$c_{Xs} \frac{v_X \cdot \gamma}{6} + c_{Xs} \frac{D_X}{h} = c_X \frac{D_X}{h} \quad (3.16)$$

and further

$$c_{Xs} = c_X \cdot \frac{\frac{D_X}{h}}{\frac{v_X \cdot \gamma}{6} + \frac{D_X}{h}} = \frac{c_X}{\frac{v_X \cdot \gamma \cdot h}{6D_X} + 1} \quad (3.17)$$

The above formula relates the concentration c_{XS} directly at the surface to the bulk concentration c_X . Note that $c_{XS} = c_X$ for $\gamma = 0$. Putting in $h = 10^{-4}m(0.1mm)$ and

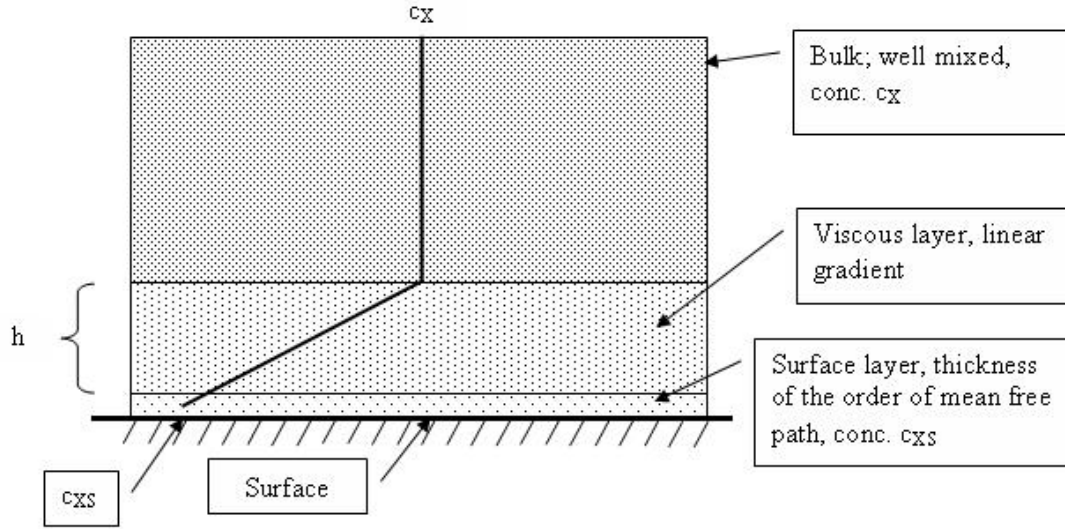


Figure 3.7.: Sketch of the near-surface layers in the smog-chamber. Three regimes can be distinguished: Bulk volume of the chamber with trace gas concentration c_X , the viscous layer (thickness h) with a linear gradient $c_X \rightarrow c_{XS}$, and the surface layer (thickness of the order of a molecule's mean free path) with concentration c_{XS} [Platt 2012].

the same choices the other parameters as above ($D_X = 10^{-5} \text{m}^2/\text{s}$, $v_X = 300 \text{m/s}$, and $\gamma = 0.6$) we obtain $c_{XS} = \frac{c_X}{300+1} \approx \frac{c_X}{300}$.

This figure can be inserted instead of c_X into the gas kinetic approach yielding time constants which are roughly (really depending on the choice of h) 300 times larger than calculated above. When using f_R from the gas kinetic approach it is important to factor in that not all molecules collide with the surface but rather the fraction c_{XS}/c_X , this leads to:

$$f_{RS} = f_R \frac{c_{XS}}{c_X} = \frac{A_p}{V} \cdot \frac{1}{\frac{h}{D_X} \frac{6}{v_X \gamma}} [\text{s}^{-1}] \quad (3.18)$$

Since $h/D_X \approx 10 \dots 100 \text{s/m}$ and $6/v_X \approx 0.02 \text{s/m}$ for high ($\gg 10^{-3}$) the equation in fact yields the diffusion approach, while for very small ($\ll 10^{-3}$) it yields the gas kinetic approach. This is illustrated in figure 3.8.

For the above number we get for $1/f_{RS} \approx 66 \text{ms} \cdot 300 = 20 \text{s}$ (which is the diffusion result for $h = 0.1 \text{mm}$). The above formula for f_{RS} can be rewritten to more clearly show the two components due to diffusion control and gas kinetic control:

$$\tau_{RS} = \frac{1}{f_{RS}} = \left(\underbrace{\frac{h}{D_X}}_{\text{Diffusion}} + \underbrace{\frac{6}{\gamma_{\text{upt}} \cdot v_X}}_{\text{gaskin.}} \right) \cdot \frac{V}{A_p} [\text{s}] \quad (3.19)$$

If we assume $f_R S$ to be a net collision frequency f_{net} including diffusion and gas kinetics, we may write:

$$f_{net} = f_R S = \left(\frac{1}{f_{dc}} + \frac{1}{f_R} \right)^{-1} = \left(\frac{h}{D} + \frac{6}{\gamma_{upt} \cdot v_X} \right)^{-1} \cdot \frac{A_p}{V} \quad (3.20)$$

The Effect of Surface Roughness

At least in the case of high $\gamma (\gg 10^{-3})$, where the transport to the surface is diffusion controlled, one should think that surface roughness with a characteristic dimension h_R should play no role as long as $h_R \ll h$ (i.e. $h_R \ll 0.1 \dots 1$ mm). This is because all molecules have to diffuse through a layer of thickness h before they reach the surface. In the case of the Bayreuth experiments, where the salt grains on the salt pan had diameters below 0.1 mm (see section 3.4, above) the surface probably can be regarded as essentially 'smooth'.

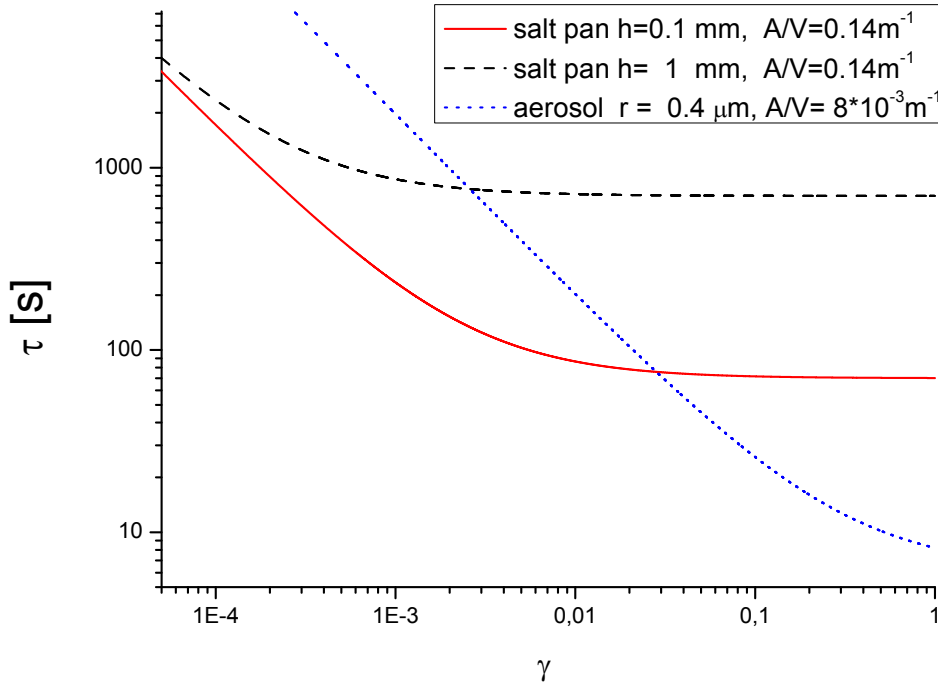


Figure 3.8.: Life time of gas phase species according to heterogeneous reactions on salt surfaces depending on the uptake coefficient γ . For a salt pan surface assuming a diffusion layer $h=0.1$ mm, diffusion is limiting for $\gamma > 0.03$. For $h=1$ mm, one is sensitive for $\gamma < 0.003$. In the case of aerosols in the smog chamber, diffusion is not the limiting process up to a $\gamma=1$.

Application to Aerosols

Similar approaches to the ones shown above for the reaction rates of heterogeneous reactions occurring on aerosol surfaces are mentioned by others before (e.g. [Hunt *et al.* 2004]). Diffusion to the surface and the actual uptake can be treated as separate processes. Then the frequencies of diffusion controlled and gas kinetic controlled uptake can be added reciprocally similar to conductances in an electrical series circuit. Alternatively, one may take the characteristic time constants (e.g. $\tau_{RS} = 1/f_{RS}$) as resistances, which have to be added. This approximation has found widespread use (e.g., [Schwartz and Freiberg [1981], Schwartz [1986], Kolb *et al.* [1995]]), and is described in detail in [Finlayson-Pitts and Pitts [2000]]. As mentioned above the factor in equation 3.4 1/6 becomes a factor 1/4, because the shape of the aerosols is assumed to be spherical. The diffusion layer thickness can be approximated to be in the order of the radius of the aerosols of about $0.4\mu\text{m}$. This leads to a life time τ_{AE} of the gas molecules according to heterogeneous reaction of τ_{AE} :

$$\tau_{AE} = \frac{1}{f_{AE}} = \left(\underbrace{\frac{r}{D_X}}_{\text{Diffusion}} + \underbrace{\frac{4}{\gamma_{upt} \cdot v_X}}_{\text{gaskin.}} \right) \cdot \frac{V}{A_{AE}} [s] \quad (3.21)$$

3.6.1. Comparison of Salt Pan and Aerosol Heterogeneous Interaction

Figure 3.8 illustrates the dependence of the life time of a gas phase species on the uptake coefficient γ for heterogeneous uptake onto a surface (here: aerosol or salt surface). In the case of aerosols, uptake for species with an uptake coefficient > 0.01 , τ is shorter than 100 s. In that case τ is also shorter than uptake onto the salt pan. For a diffusion layer height of $h=0.1$ mm uptake for $\gamma < 0.03$ is clearly diffusion controlled, with a lifetime of 70s. For a diffusion layer height of $h=1$ mm diffusion controlled uptake takes place at a life time of 700 s and for $\gamma < 0.003$. Once gas kinetic is the limiting step for uptake, the uptake onto a Salt Pan becomes faster compared to uptake on aerosols. Moreover, during salt pan experiments one is sensitive to uptake coefficients below 0.03 and 0.003 according to $h=0.1$ mm and $h=1$ mm, respectively. The shown limitations due to uptake coefficients and diffusion control is discussed in chapter 7.

4. Multi Reflection Systems used for Absorption Spectroscopy

Various trace gases (e.g. BrO, OClO, NO₂ and HCHO) are detected and quantified by the well established **Differential Optical Absorption Spectroscopy** (DOAS) technique [Perner and Platt 1979, Platt et al. 1979, Platt and Stutz 2008] using their narrow band absorption structures. In the framework of this thesis, active DOAS instruments (using an artificial light source) in combination with different kinds of multi-reflection cells as described in the following chapter are used. The first part of this chapter will give a short introduction into the DOAS technique, the underlying Lambert-Beer law and the principles of the analysis procedure. In the second part, the instrumental set-up of the White- cell system, as developed within this thesis, will be discussed. This is followed by a description of the analysis process for the trace gases of interest. In the third part, a new UV-LED-CE-DOAS instrument is described, which was also applied for measurements within this work.

4.1. Differential Optical Absorption Spectroscopy

DOAS [Platt 1978; Platt and Stutz 2008] has been used in chamber experiments [e.g. Etzkorn 1998, Volkamer et al. 2002] as well as in the troposphere and stratosphere [Platt and Stutz 2008; Solomon et al. 1987]. A large number of trace gases, absorbing light in the visible and ultraviolet wavelength range, such as OH, HONO, NO₃, OClO, BrO, IO, NO₂, NO, NH₃, OBrO, ClO, O₃, SO₂, CS₂, OIO, I₂, glyoxal, aromatics and formaldehyde, as well as methane and carbon dioxide in the near-infrared [Frankenberg et al. 2005], can be detected. Besides active DOAS measurements using artificial light sources (e.g. LEDs, Xe-arc lamps), passive DOAS, using natural light sources, e.g. scattered sunlight [Solomon et al. 1987; Wagner 1994] for the detection of trace gases from ground [e.g. Hönninger et al. 2004] as well as from air [e.g. Dorf et al. 2006] or space [e.g. Wagner et al. 2001] can be applied. Within this thesis only active DOAS instruments are used. A complete and detailed overview of the DOAS technique and its applications can be found in [Platt and Stutz 2008].

4.1.1. Basics

The DOAS technique is based on the well known Lambert-Beer-Law which describes the absorption of light in matter, following an exponential decay. For measurements in the atmosphere (or aerosol smog chambers) the Lambert-Beer law has to be expanded. The absorption structures consists of usually more than one absorber. These cross sections depend also on temperature and pressure. Furthermore one has to account for scattering by air molecules (Rayleigh) and aerosols (Mie) which also reduce the initial intensity of the light, leading to:

$$I(\lambda) = I_0(\lambda, L) \cdot \exp^{-\int_0^L (\sum_j \sigma_j(\lambda, p, T) \cdot c_j(l) + \varepsilon_R(\lambda, l) + \varepsilon_M(\lambda, l)) dl} + N(\lambda) \quad (4.1)$$

with

$I_0(\lambda, L)$: intensity of the light source

$I(\lambda)$: light intensity after passing through the atmosphere

λ : wavelength

$\sigma_j(\lambda, p, T)$: absorption cross section of the absorber j

$\varepsilon_R(\lambda, l)$: Rayleigh scattering coefficient

$\varepsilon_M(\lambda, l)$: Mie scattering coefficient

$c_j(l)$: concentration of the absorber j

p : pressure

T : temperature

L : total light path length

$N(\lambda)$: photon noise

The key in the DOAS technique is that the light reducing factors can be separated into two parts, a narrow band and a broad band part. The absorption of many trace gases show narrow band structures, caused by vibrational, rotational and electronic transitions of the molecules. The absorption caused by Rayleigh and Mie scattering, intensity fluctuations of the light source and the sensitivity of the detector is broad banded, as well as parts of the absorption structures of some molecules. Applying this idea separates the cross section into two parts:

$$\sigma_j = \sigma_{bj} + \sigma'_j \quad (4.2)$$

where σ_{bj} denotes broadband spectral features and σ'_j the differential cross section which represents narrow band spectral structures for a given trace gas j .

The logarithm $J(\lambda) = \ln I(\lambda)$ of the intensity $I(\lambda)$ can be described by:

$$J(\lambda) = J_0(\lambda) + \sum_{j=1}^m \sigma'_j \cdot S_j(\lambda) + B(\lambda) + R(\lambda) + N'(\lambda) \quad (4.3)$$

with

$\sigma'_j(\lambda)$: differential absorption structure for each trace gas species j

$B(\lambda)$: broadband absorption

$R(\lambda)$: extinction by Mie- and Rayleigh scattering

$N'(\lambda) = \ln(N(\lambda))$: caused by the detector noise and photon statistics

$S_j = \bar{c}_j \cdot L$: product of the average number densities over the light path of length L

The sum in equation 4.3 represents overlaying absorption structures of different trace gases, which can be distinguished by their characteristic absorption features. Now the average concentration of the trace gases of interest can be calculated:

$$\bar{c}_j = \frac{S_j}{L} \quad (4.4)$$

where L represents the length of the absorption path.

In reality, light of an appropriate light source passes an air mass in a chamber (or the atmosphere) and is collimated and transmitted to the entrance slit of a spectrograph-detector unit via a quartz fiber. The light is dispersed by a grating and recorded by the detector system. As the resolution of the spectrograph is limited, the spectral resolution of the spectrum $I(\lambda, L)$ is degraded, corresponding to a convolution of $I(\lambda, L)$ with the instrument function H of the spectrograph. This was done with the help of a mercury lamp (Pen-Ray Lamp), using its well defined line emission at 334.15 nm. Using a multi-channel detector, the wavelength range is mapped to n discrete pixels; the wavelength to pixel calibration was made, using the well known mercury lines (between 325-395 nm) and a 2^{nd} order polynomial. All analysis was done with the help of the software DOASIS [Kraus 2004]. The used analysis procedure combines a nonlinear Levenberg-Marquardt-Method [Levenberg 1944; Marquardt 1963] to derive a shift and squeeze for each spectrum taken into account in the fit. The shift and squeeze can result e.g. from a changing pixel to wavelength mapping and temperature drifts of the detector spectrograph unit. A standard linear least-squares fit is used [Albritton et al. 1976; Bevington 1969] to determine a_j and c_k . Detailed descriptions of the analysis procedure are given in many other works (e.g [Pöhler 2010, Seitz 2009, Kern 2009, Platt and Stutz 2008]).

From equation 4.4 it is obvious that a long light path increases the sensitivity of a DOAS measurement, if other factors (e.g. noise $N(\lambda)$), decrease by the same amount. Therefore it is attractive to fold the absorption light path in a multiple pass (or multiple reflection) cell, especially in terms of limited space like in laboratory experiments. *Platt and Stutz* 2008 gave an overview of the most widely used types of multi reflection cells. One type are Herriot cells, which are not used in this thesis and described elsewhere [Herriot et al.1964]. The other two most common types are White cells and passive resonators. As mentioned above measurements with a White- cell system, and a LED-CE-DOAS instrument were performed simultaneously. Figure 4.1 shows how the two instruments are connected to the chamber and the details will be described in the following sections.

4.2. The White-type Multi Reflection System

The set-up of the 2-m White system (WS) [*White* 1976, *White* 1942] was specially designed for the teflon smog chamber in Bayreuth, but similar instruments were used before [*Ritz et al.* 1993, [*Volkamer* 1996], *Volkamer et al.* 2002, *Hak et al.* 2005]. This set-up was optimized for the smog chamber facilities in Bayreuth including:

- A special frame for the slant attachment into the cylindric teflon chamber to achieve a long light path inside the relatively small volume of the chamber was designed and installed.
- Transfer optics were applied to adapt the incoming light to the optical parameters of the White cell and the outgoing light to the numerical aperture of the spectrograph
- Particular attention was given to prevent leaks in the chamber: The main optical components (mirrors and prisms) of the White system were mounted inside the teflon bag, the measurement light enters and exits through a quartz glass window

This is the first time that a multi reflection DOAS system is used to measure BrO, OClO and ClO simultaneously in a smog chamber. It is also possible to detect IO, NO₂, HONO, HCHO, O₃ and other trace gases absorbing in the wavelength range of the mirror reflectivities of this White system.

4.2.1. Light Propagation through the White System and Transfer Optics

The original idea of the White-type multi reflection cell was developed in the mid of 20th century [*White* 1942, *White* 1976]. The general set up is shown in figure 4.1.

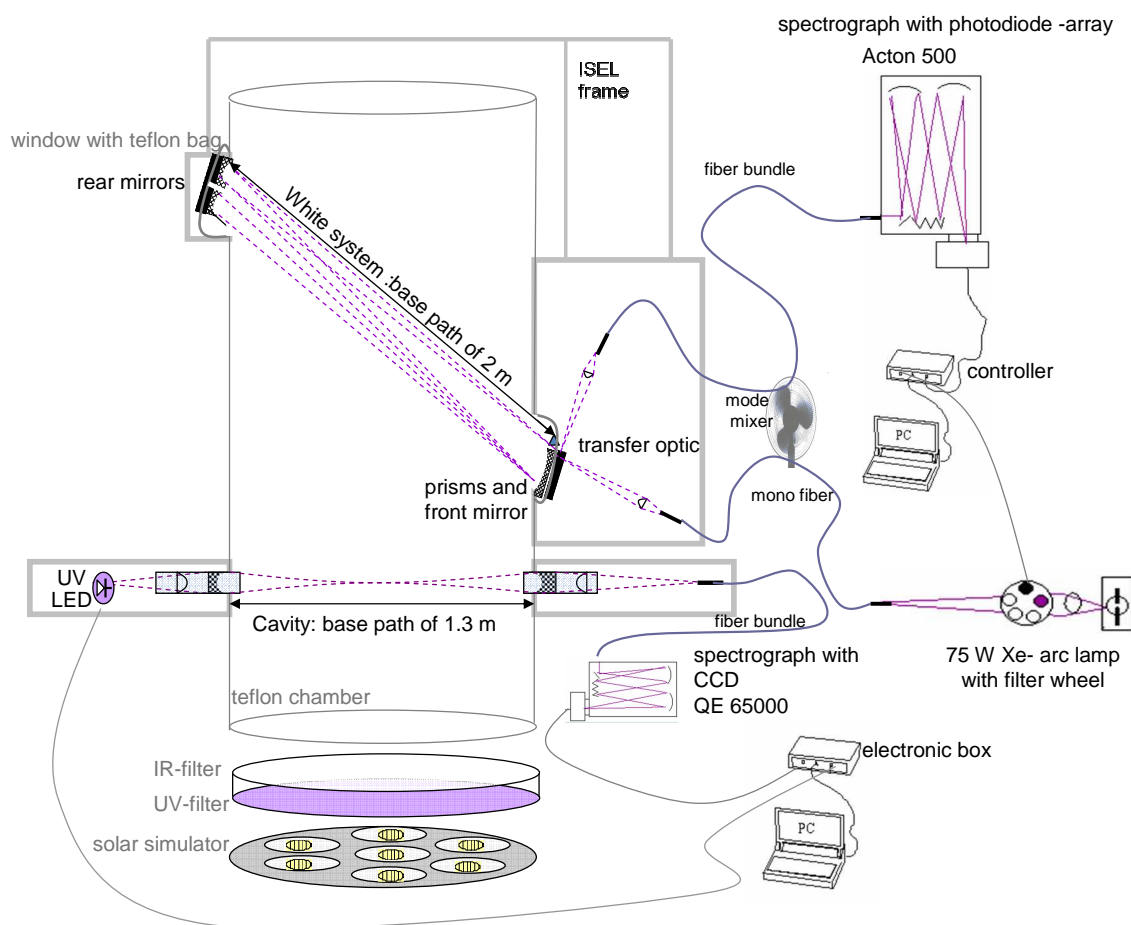


Figure 4.1.: Sketch of the multi-reflection cells used for DOAS in the teflon chamber. A White system with a base path of 2 m was installed on a diagonal frame. The mirrors and prisms of the White system were mounted inside the chamber with additional teflon bags. A maximum total light path of 320 m was achieved. The transfer optics adapts the opening aperture of the White system to the fiber and spectrograph. The BrO-cavity is mounted on a different frame, with a 1.3 cm base path, resulting in an maximal light path of about 800 m within this work (depending on the mirror reflectivity). The mirrors of the BrO-cavity are flushed with clean air constantly. The UV LED is directly coupled into the resonator via a quartz glass lens and the spectrograph QE 65000 is connected via a fiber.

One front mirror (figure 4.2) and two rear mirrors are mounted at the distance of the optical curvature, which is (for a spherically curved mirror in air) twice the focal length. Therefore a 1:1 image is drawn on the front mirror through one of the two rear mirrors leading to a characteristic pattern on the front mirror. Three prisms next to the front mirror lead to an even higher light path (optimized by *Ritz et al.*

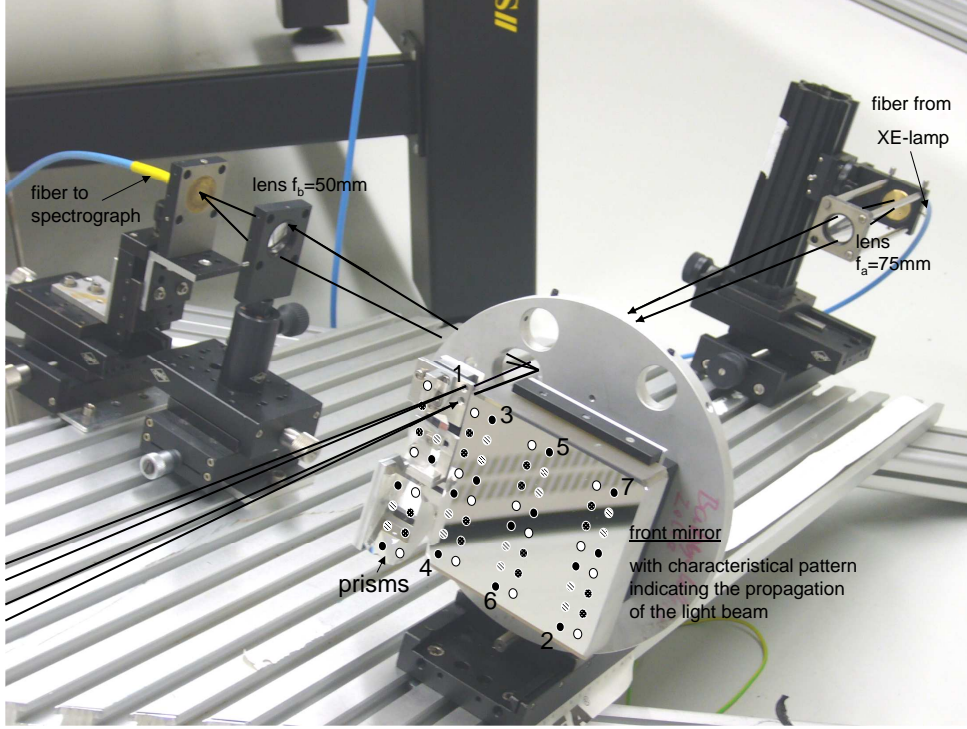


Figure 4.2.: Picture of the two telescopes for adapting the incoming light beam to the opening ratio of the WS and vis versa. The characteristic WS pattern is shown on the front mirror as well as the numbering for the first propagations. The following go on in the same scheme, until the light beam is coupled through lens f_b into the fiber to the spectrograph again.

1993). The prisms are crossed from top to bottom one, two and four times. The number of reflections used in this thesis was varied between 16, 48, 144 or 160 times, depending on the mirror set. With higher reflectivity a higher number of reflections with a reasonable integration time, in the order of 600 ms to 5 s, can be achieved. The choice of the mirror set depends on the focus of the experiment e.g. needed sensitivity for trace gases of interest or aerosol extinction. The focal length of the mirrors is 1000 mm, and therefore the distance between the incoming light beam at the side of the back mirror is 2000 mm. The rear mirrors have a diameter of 80 mm. That leads to an opening aperture (diameter of the mirror/distance between mirrors) of 0.04 or an aperture of F/25. The incoming light beam is transmitted to a fiber with a numerical aperture of 0.22. The numerical aperture NA is given by $NA = n \sin(\alpha/2)$ with n = index of refraction = 1.0 (air) and α = angular aperture (maximum cone of light that can enter or exit the optical device of interest). It can be translated to an equivalent opening ratio via $2 \cdot \tan(\arcsin NA)$, which is in the case of the used fibers 0.43. To adapt the NA of the fiber to the WS, a quartz glass lens of 75 mm focal length and 25 mm diameter was used. The distance from the

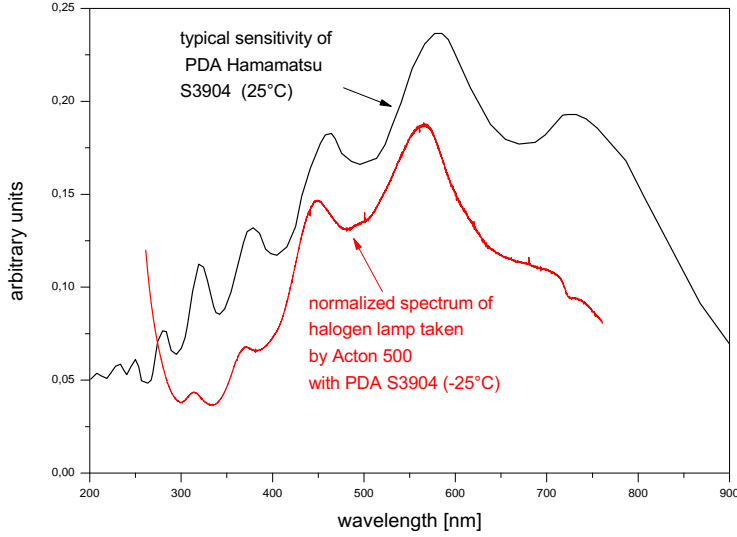


Figure 4.3.: Sensitivity of the Hamamatsu photo diode array (PDA) used in this work in the wavelength range from 200-900 nm, provided by Hamamatsu (black line). The red line indicates a measurement of a calibrated quartz- tungsten- halogen (QTH) light source (from LOT-oriel) using the set-up described in this work (Acton 500 Pro and 200 μm fiber bundle). It is normalized by the absolute spectrum provided by the LOT-Oriel group. Below 300nm the stray light from the spectrograph is dominating, whereas above the etalon structure is shown (red).

lens to the fiber is set to 85.22 mm. The distance from the lens to the WS is 625 mm. The entrance slot of the WS has a diameter of 3 mm and is located next to the smallest prism (where the light beam is coupled in) limits the magnification. The magnification is here 7.3, and a 200 μm fiber of is used. The out going light beam is focused by a 50 mm lens, to adapt the opening ratio of the WS to the optical aperture of the spectrograph (see chapter 4.2.3). The distance of the lens from the exit slot of the WS is 500 mm and from the lens to the fiber 55.5 mm. Optical adjustment to achieve maximal intensity was done previous to an experiment. This requires hours to days, but once the optimum is achieved the system is found to be stable for weeks.

4.2.2. The Xenon Lamp Radiation Source

The radiation of a high pressure short-arc xenon lamp (USHIO UXL S75XE) was collimated using a lens ($f = 25\text{ mm}$) into a 200 μm quartz fiber, matched to the F/25 optical aperture of the WS via a quartz lens, as described above (shown in figure 4.1). The UXLS75XE lamp is a 15 volt 80 watt xenon short arc lamp. It has an overall length of 88 mm and glass diameter of 13 mm. Life hours are rated by Ushio at 2,000 hrs (five times higher then UXL-75XE or Osram XBO 75 used for long path DOAS before e.g. [Pöhler *et al.* 2010]) and has a total lumens of

1,400 lm. The UXLS75XE lamp is a special type of a high pressure short-arc xenon lamp with an improved stability. This is very helpful for reducing the noise due to fluctuations of the lamp. The reference spectrum with the intensity I_0 was taken before and after an experiment, so the time gap between the reference spectrum and the measurement spectrum (intensity I) could be several hours. It was shown before [Buxmann 2008b] that higher temporal distance between I and I_0 can increase the residual structure of a DOAS, mainly caused by the detector. But lamp instabilities in the time between I and I_0 , would significantly reduce the measurement accuracy as well.

4.2.3. Spectrograph and Detector

The receiving fiber bundle (seven 200 μm quartz fibers) is connected to a spectrometer (Acton 500 pro, $f = 500$ mm, $F/6.9$, 600 gr/mm grating, thermo stated to 25°C), which disperses the radiation and projects it onto a 1024 pixel photo diode array (PDA) detector (Hamamatsu S3904-1024, cooled to -25°C). The resulting spectral resolution was 0.5 nm FWHM. The detector unit is situated in the focal plane of the spectrograph. The PDA is placed inside an evacuated camera box filled with 1-2 bar Krypton 5.0 (99.999%) to prevent freeze-out of water vapor on the PDA, which could cause a Fabry-Perot etalon effect. A detailed description is give by [Stutz 1991]. An additional Fabry-Perot etalon effect is caused by the interference of reflected light beams within the SiO_2 layer of the detector itself. This etalon effect is shown in figure 4.3. But the size of those etalon structures is in the order of 50nm. Thus they are broad banded and do not interfere with the DOAS fit procedure.

4.2.4. White System Mirror Coating

Two different kinds of mirror coatings are used in this work, an aluminum and a dielectric coating. The achievable detection limit of the different mirrors strongly depends on the length of the optical path. The aluminum coated mirrors were used for detection with low sensitivity since high amounts of halogen oxides (up to ppb range) were expected. As mentioned above with a lower reflectivity just 16 to 48 traverses through the White-system can be achieved. For an estimation of the reflectivity of the aluminum coating two different numbers of reflections through the White- system were used. The reflectivity and the number of reflections are connected via:

$$I_{long} = I_{short} \cdot R^{N_{long}-N_{short}} \quad (4.5)$$

I_{long} denotes the Intensity after N_{long} and I_{short} the Intensity after N_{short} reflections. Here the number of reflections was $N_{long} = 48$ and $N_{short} = 16$. The mean reflectivity between 325 nm and 405 nm was calculated to be 85% (figure 4.4).

This estimate neglects possible loss of intensity, due to the optical properties and alignment of the WS. Additionally the reflectivity of aluminum strongly degrades with time. The difference of the reflectivity estimate and the reflectivity curve provided by the company (Befort Wetzlar OHG) are shown in figure 4.4. An advantage of the aluminum coating is its broad band reflectivity, so that several different kinds of trace gases can be measured simultaneously.

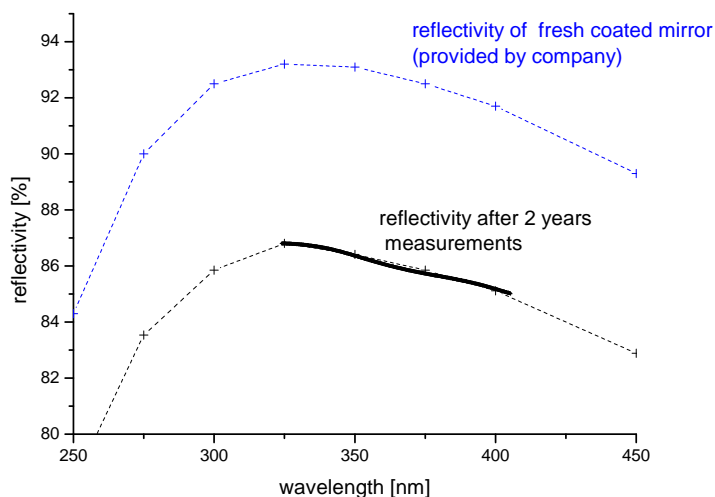


Figure 4.4.: The reflectivity of the aluminum coating degrades with time. The blue line(top) shows the reflectivity curve provided by the company (Befort Wetzlar OHG). The thick black line shows the measured reflectivity after 2 years of measurements; the dotted black line is interpolated from the original curve provided by the company.

For the detection of BrO and OClO with higher sensitivity a dielectric coating of the White system mirrors covers the wavelength range from 335-360 nm (reflectance >99.5 %). For the detection of IO an additional dielectric coating on the same mirror set can be used, which covers the wavelength range between 410nm-440nm(reflectance >99.5 %). The reflectivity curve provided by Layertec is shown in figure 4.5. These wavelength ranges contain also spectral structures of further species, which were included into the spectral analysis (see chapter 4.3).

4.2.5. Stray Light

The term stray light is used here and in general as a synonym for light reaching the detector through an irregular way. Stray light causes an additional offset in the measurement spectra and reduces therefore the optical density of the measured trace gases. This results in an error of the derived concentration. In the following the relative stray light is defined as stray light signal divided by the measurement signal.

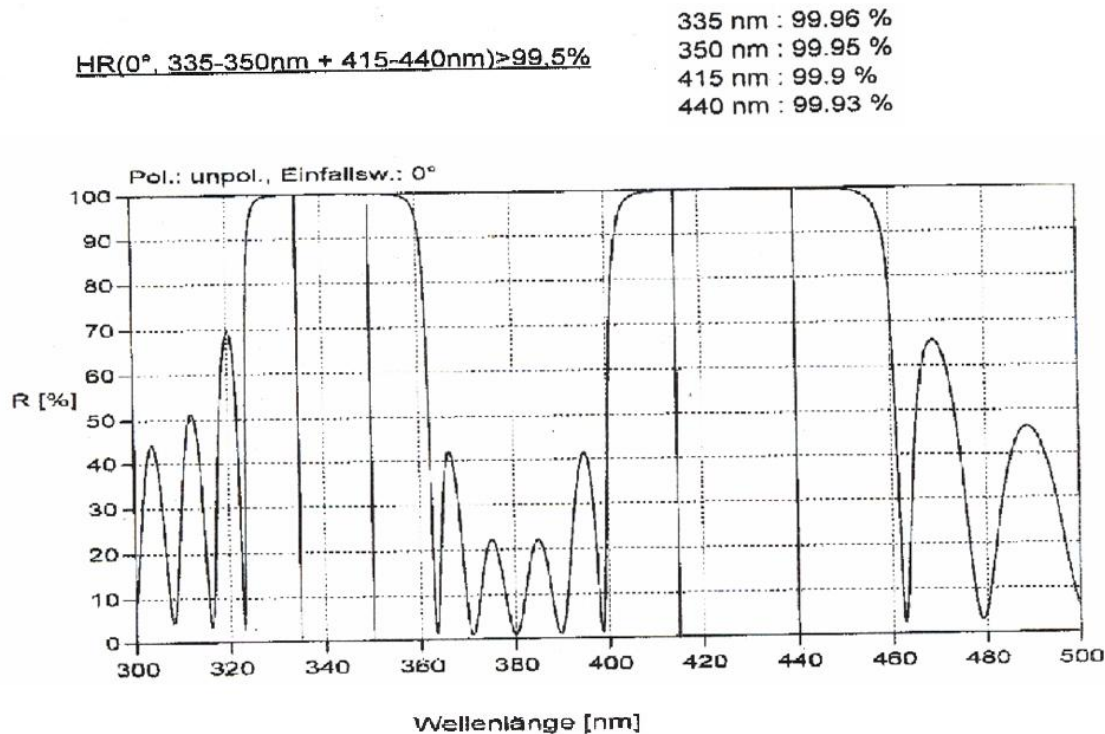


Figure 4.5.: Reflectivity curve of the dielectric coating used for high sensitivity measurements provided by Layertec GmbH Mellingen. Two ranges of high reflectivity can be used from 335nm -350nm and fom 410nm -440 nm. The coating is optimized for a 0° entrance angle between the axis of curvature and the incoming light beam.

In the case of a White system four different kinds of stray light can be distinguished:

- **Stray light of spectorgraph:** Light is reflected on surfaces in the spectrograph unit (for instance the zero order of the grating) and reaches the detector via a wrong wavelength to pixel mapping. Especially light from different orders can cause a significant contribution. This kind of stray light can be reduced with the help of an optical band pass filter, which has its transmissivity in the wavelength range of interest. The limited reflectivity to a certain part of the spectral range of dielectric coating of the mirrors reduces this kind of stray light as well. As the intensity of the light source is much lower for short wavelength (below 300nm), the relative stray light is higher in that range. The stray light of measurements with the dielectric coated mirrors (above 320nm), was <1% and therefore neglected. The stray light for measurements of ClO and O₃ (aluminum coating) was characterized using several cut off filters as shown in figure 4.6. Below 280 nm it exceeds 40 % of the total light intensity.

Using a band pass filter UG11 (figure 4.7), this stray light was reduced to less than 20% (figure 4.8). This kind of stray light was corrected by subtracting the stray light part using a WG 320nm filter as first step of the data analysis. Similar corrections have been preformed before (e.g.[*Volkamer 1996*].)

- **PDA stray light:** Light gets reflected directly at the array surface or at the window in front of the array, and causes a wrong wavelength to pixel mapping through additional reflection at the detector window. It was not possible to measure this kind of stray light directly, and as it causes $<2\%$ [*Stutz 1996*] of the overall systematical errors, it was neglected in this thesis.
- **White system stray light:** Due to Mie scattering light is scattered from one light beam of the traverses through the White system into another. It carries absorption structures of the trace gases, but reaches the detector with a not well defined light path. It can be measured by blocking the first prism. So the detected light is caused by scattering. Note that the light path of the scattered light during this measurement, is smaller than it would be without blocking the prism [*Volkamer 1996*], so that the stray light is underestimated. An example of an estimate for the stray light of the White system with aluminium coating is shown in figure 4.6. This was done with ambient aerosols concentrations (<10 particles/cm³). At different aerosol conditions, the fraction of stray light can change, but this was not characterized within this thesis.
- **Background stray light:** Scattered light from additional light sources, in this case the solar simulator, reaches the detector through the fiber coupling. This is corrected by background spectra recorded with blocked UXLS75XE lamp. An example is shown in figure 4.9

4.3. Data Analysis of the White-cell Measurements

The data evaluation was performed with DOASIS [*Kraus 2004*]. DOASIS gives the possibility to use a script language (Jscript) to automate processes of the evaluation. For the analysis a Jscript adapted from [*Pöhler 2010*] was modified for the evaluation of the White-cell measurements. Within the work of *Pöhler* [2010] several new features were introduced to the JScript evaluation like the automatic convolution of literature reference absorption spectra, which simplifies the data handling and reduces data processing time.

The spectrometer was calibrated using a mercury spectrum of known emission lines (see above). The literature absorption cross sections are reduced to the resolution of the applied spectrometer. The differential absorption cross sections summarized in table 4.2 were taken into account for the analysis of the spectra. Table

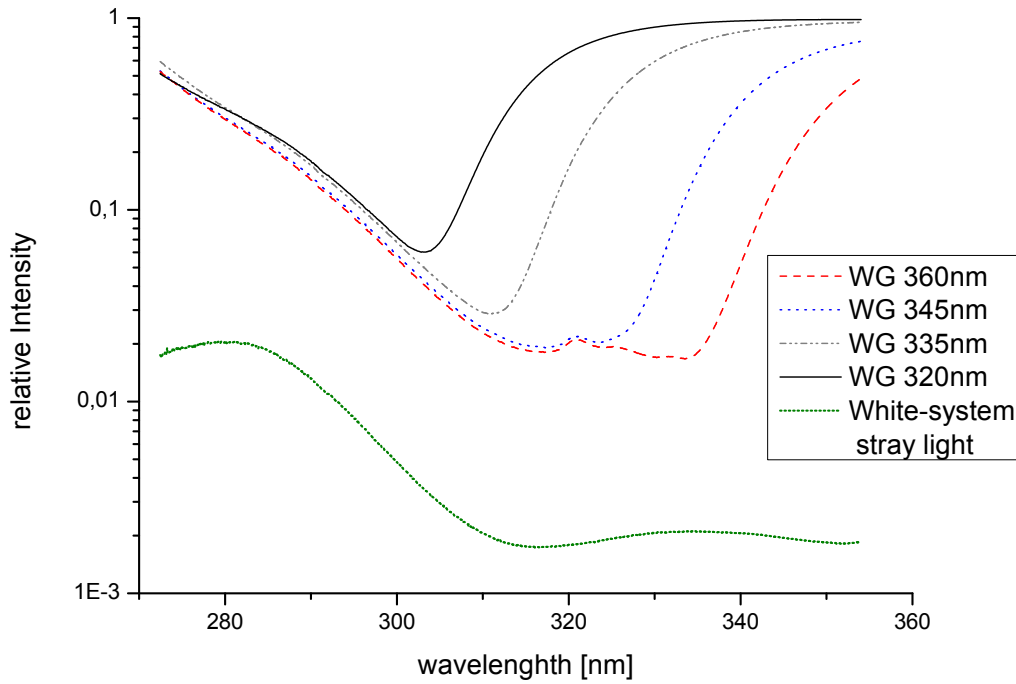


Figure 4.6.: Characterization of the stray light of the White-system with aluminum mirrors and Acton 500 spectrograph. Spectra with different cut-off filters are divided by a reference spectrum without a filter, in order to characterize the relative stray light below the cut-off wavelength of the filter. The WS stray light (stray light in the system without well defined light path) is determined by dividing a spectrum blocking off the first prism, by a measurement spectrum through the whole light path.

4.1 summarizes the different fit settings and the given name will be referred for each experiment in chapter 5.

All spectra (except the literature cross sections) were prepared by correcting for offset and background. For each wavelength range, the absorption cross sections of the species present in this range as well as a reference spectrum are fitted simultaneously to the measured spectrum, using a non-linear least-squares method (e.g., section 4.1.1). For the evaluation, a triangle high pass filter with 1,000 iterations was applied.

For each absorption cross section the mean-spectral shift was determined from a measured spectrum with strong absorption, but it turned out to be less than 0.005 nm for all trace gases included in the fit. It should be noted that the change in the O_4 concentration was low in all experiments with the White system, therefore the shift might be different at high concentrations. The shifts of the cross sections are linked together for the following measurements, and the shift of either BrO or

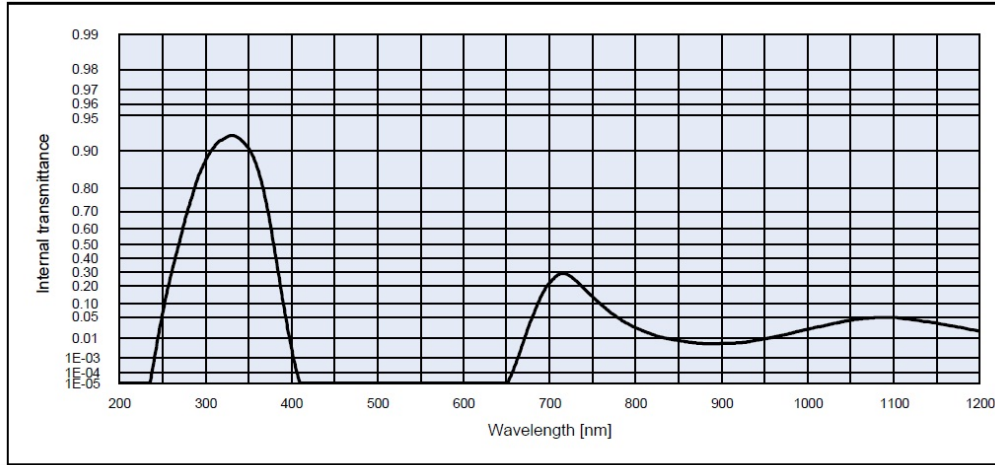


Figure 4.7.: Transmissivity of the UG11 bandpass filter provided by Schott. The filter was used to reduce the stray light from the spectrograph.

Table 4.1.: Overview of the different evaluation settings of the WS measurements used for different species and mirror coatings. The cross sections were linked together for the following evaluation. For all trace gases the following DOAS-fit settings were used: high pass filter with 1000 iterations; 3rd degree polynomial; squeeze limited to $\pm 2\%$ (of the total spectral range). The fit window, was set according to the mirror reflectivity. For the dielectric coating the reflectivity depends on the relative humidity (RH). For the aluminum coating a stray light correction (sc) was performed as described in section 4.2.5.

dielectric coating			
fit-setting	trace gases	fit range [nm]	RH [%]
DeRHh	BrO, OCIO, HONO, HCHO, O ₄ NO ₂ , O ₃ , O ₄	338-356.2	25-80
DeRhl	BrO, OCIO, HONO, HCHO, NO ₂ , O ₃ , O ₄	336-351.5	0-25
aluminum coating			
fit-setting name	trace gases	fit range [nm]	sc
AlBrO	BrO, OCIO, HONO, HCHO, NO ₂ , O ₃ , O ₄	310-340	no
AlClO	BrO, ClO O ₃ , NO ₂	279-298	GG320
AlClOU	BrO, ClO O ₃ , NO ₂	279-298	GG320+UG11

ClO was limited to ± 2 nm. The squeeze was limited to $\pm 2\%$ (of the total spectral range).

Reference spectra were recorded before starting an experiment at the same optical light path (depending on the experiments 38m, 282m or 320 m) as the measurement

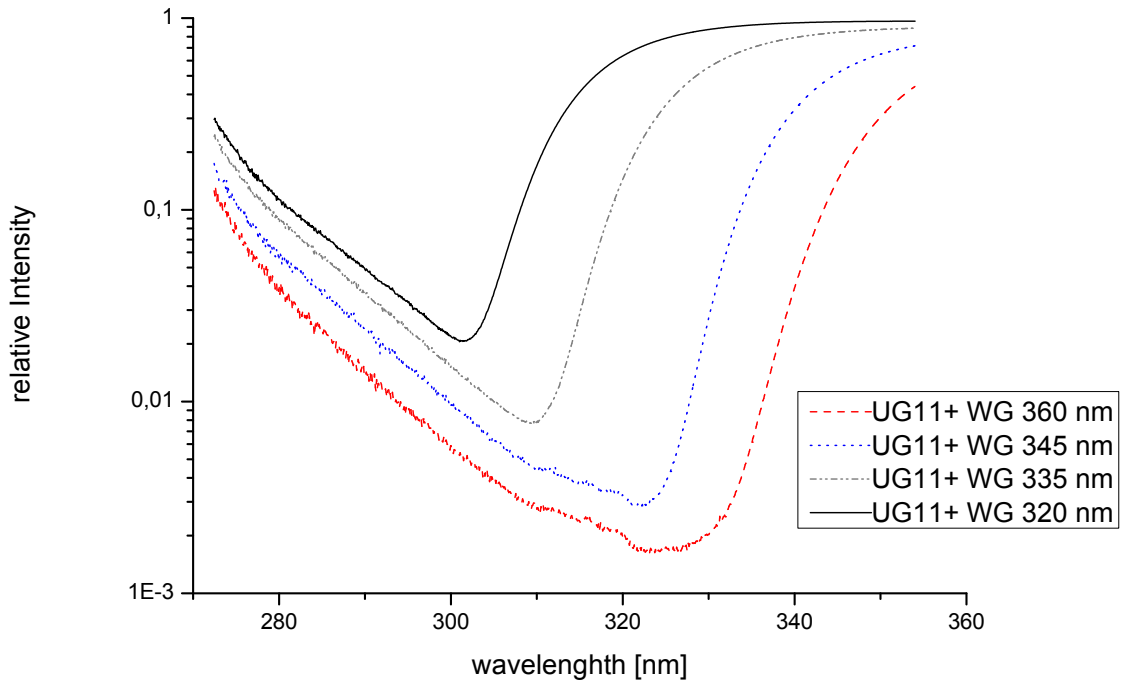


Figure 4.8.: Reduced stray light of the WS with aluminum mirrors and Acton 500 spectrograph with an additional UG11 bandpass filter. Spectra with different cut-off Filters are divided by a reference spectrum only with an UG11 filter, this characterizes the relative stray light below the cut-off wavelength of the different WG filter.

Table 4.2.: *Differential Absorption Cross Sections used for the WS DOAS analysis*

Species	Reference
BrO	<i>Wilmouth et al.</i> [1999]
O ₃	<i>Voigt et al.</i> [2001]
SO ₂	<i>Vandaele et al.</i> [1994]
HONO	<i>Stutz et al.</i> [2000]
HCHO	<i>Moortgat G.K.</i> [2000]
O ₄	<i>Greenblatt et al.</i> [1990]
NO ₂	<i>Voigt et al.</i> [2002]
ClO	<i>Sander and Friedl</i> [1989]
OCIO	<i>Kromminga et al.</i> [1999]

spectra through the White-cell system when the chamber was flushed with zero air (see chapter 3), such that no halogen oxide absorption is expected in the reference

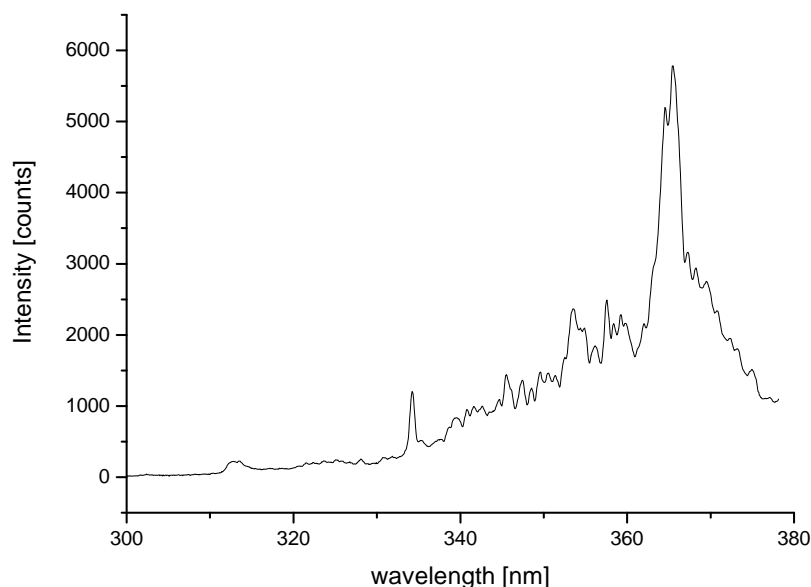


Figure 4.9.: Example of scattered light from the solar simulator. The spectrum was taken at an integration time of 10s and one scan. Mercury lines at 334.13nm and 365.44nm can be identified, which are part of the Xe lamp spectrum from the solar simulator.

spectra. Background spectra were taken after each measured series of spectra, blocking the light source and thus correcting for stray light, e.g., from the solar simulator (see section 4.2.5). In addition, a polynomial of 3rd order was included in order to account for broad band absorption structures, due to Mie and Rayleigh scattering and broad-band instrument features. Additionally, all spectra are treated with a high pass binomial filter with 1,000 iterations, as mentioned above. On the basis of *Stutz and Platt 1996* the 1σ statistical error of our analysis was doubled in order to obtain a realistic measurement error that was doubled again to obtain an estimate of detection limits. A measurement consisted of 20-50 co-added scans as a compromise between acceptable noise and time resolution. More detailed description of the settings for the different wavelength ranges as well as fit examples are given below.

4.3.1. Influence of Dielectric Coating on the Fit Range

The dielectric mirror coating limits the possible fit range, as just light of a certain wavelength range is transmitted through the White system. The direct contact of the mirror surface with the dielectric coating during the smog chamber experiments can cause problems. Dielectric coated mirrors are based on interference effects. By careful choice of the thickness and number of the layers, it is possible to tailor the reflectivity. The coating is able to store water within the layers and their thickness

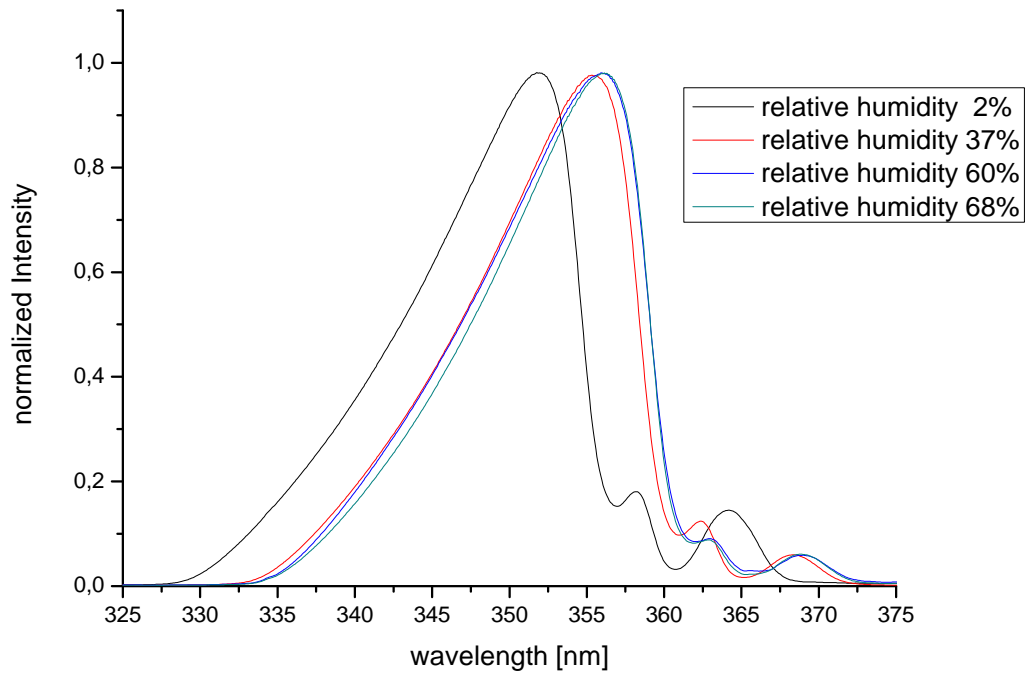


Figure 4.10.: The maximum of the dielectric mirrors varies with the relative humidity. The shown spectra are taken after 160 traverses through the White system. The intensity was normalized to the respective maximal intensity.

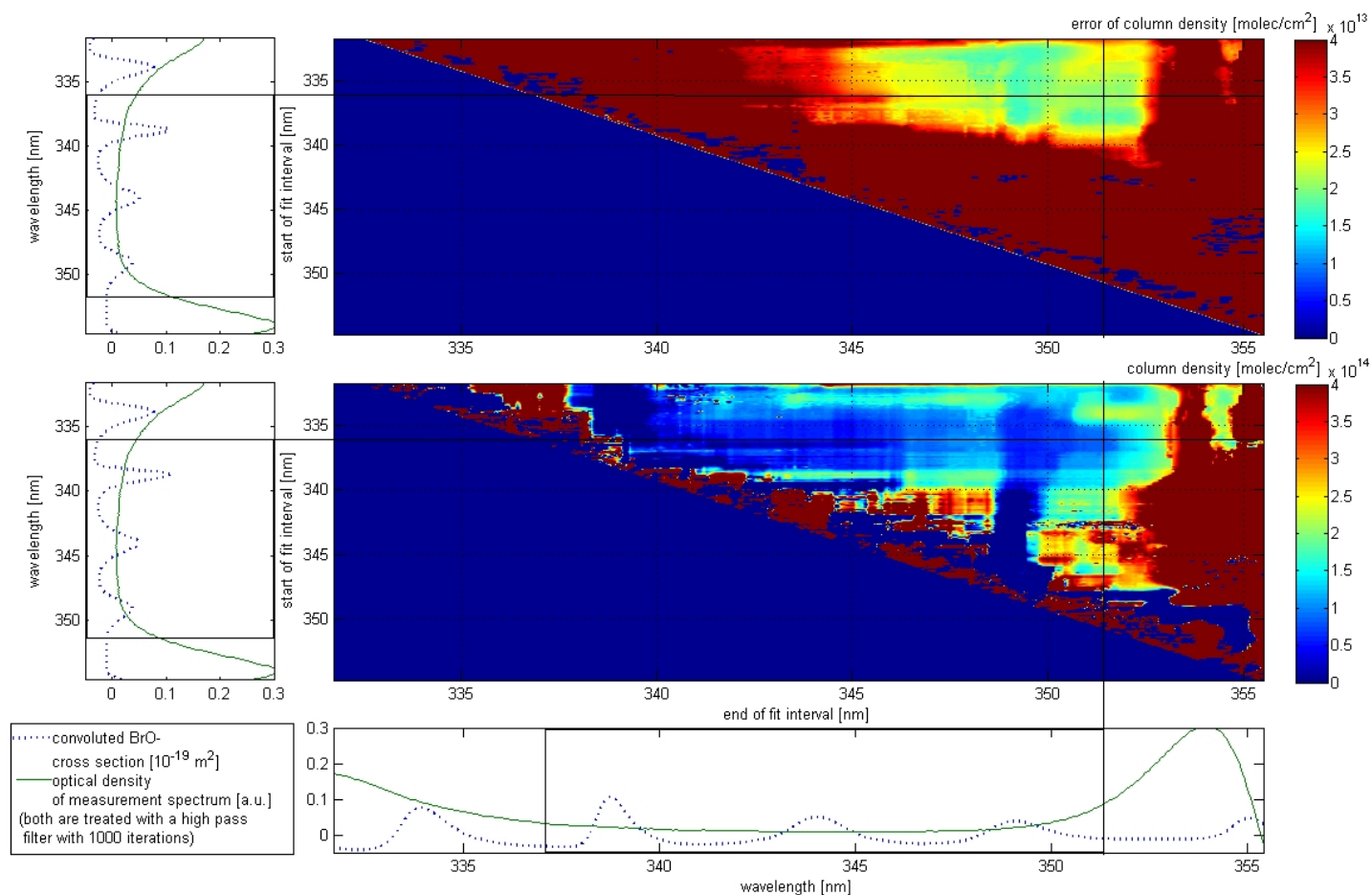


Figure 4.11.: Wavelength interval mapping of a spectrum during an experiment at 2% RH. The abscissa-axis show the lower wavelength limit of the fit interval and the ordinate-axis the upper wavelength limit. The BrO column density (cd) as well as the cd error are displayed color-coded. The convoluted BrO cross section as well as the measurement spectrum are plotted next to the axis. The black rectangles and lines indicate the chosen fit interval of 336nm-351.5nm with a BrO cd of $(1.3 \pm 0.2) \times 10^{14} \text{ molec/cm}^2$, which corresponds to a mixing ratio of $(161 \pm 25) \text{ ppt}$.

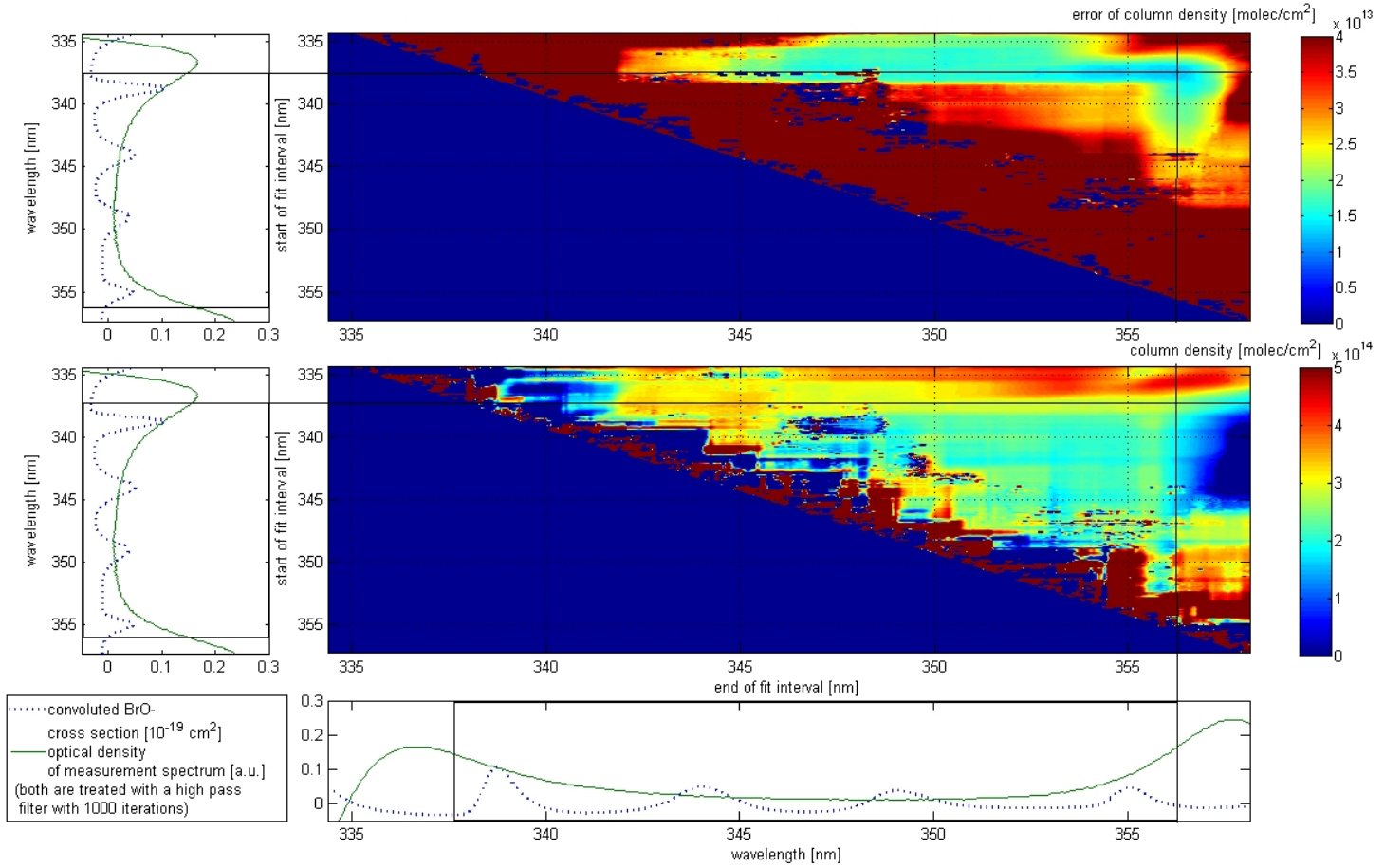


Figure 4.12.: Wavelength interval mapping of a spectrum during an experiment at 45% RH. The design here is similar to figure 4.11. The BrO cd as well as the cd error are displayed color-coded. The black rectangles and lines indicate the chosen fit interval of 338nm-356.2nm with a BrO cd of $(2.7 \pm 0.14) \times 10^{14} \text{ molec/cm}^2$, which corresponds to a mixing ratio of (336 ± 18) ppt.

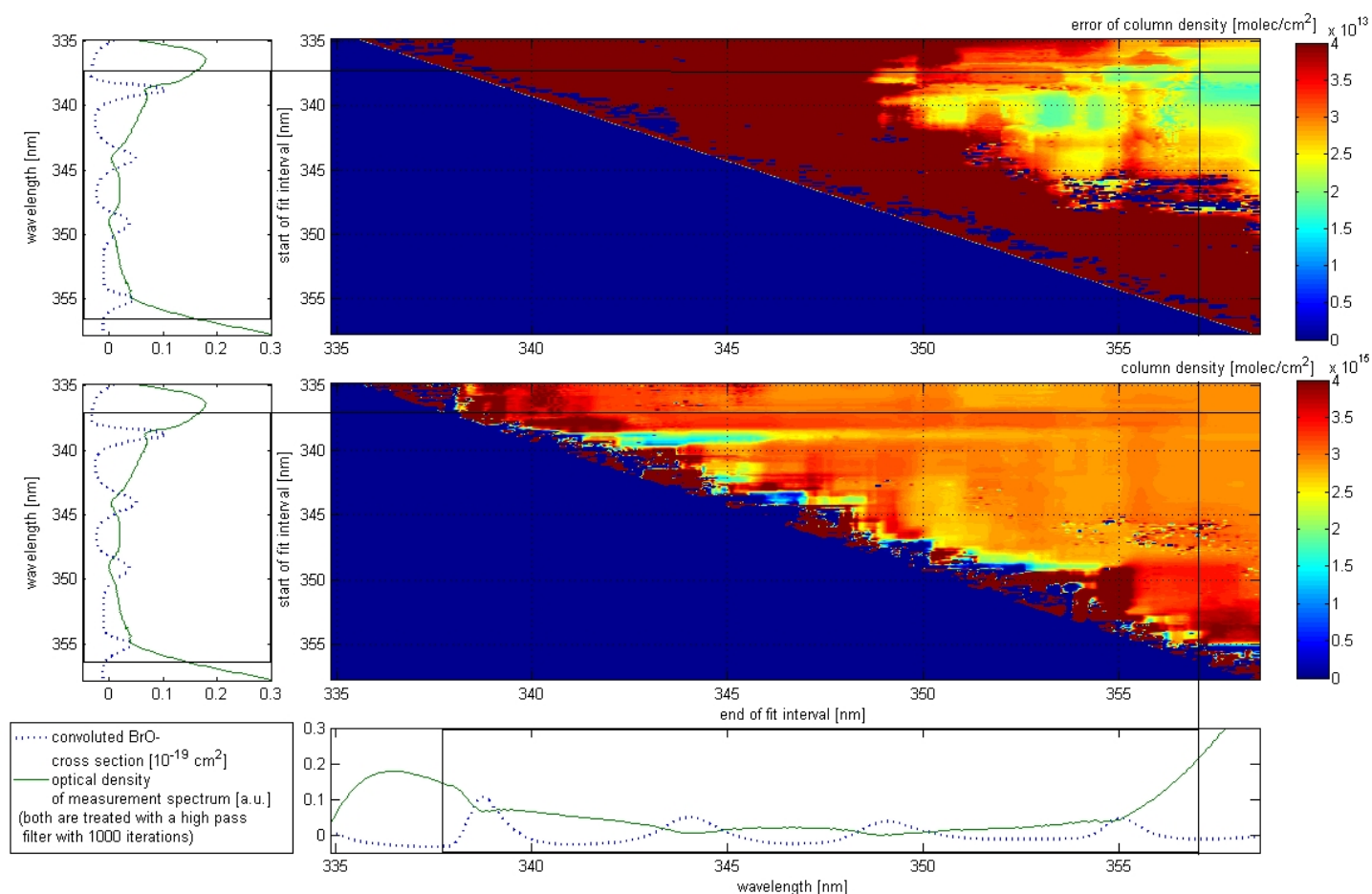


Figure 4.13.: Wavelength interval mapping of a spectrum during an experiment at 60% RH. The design here is similar to figure 4.11. The BrO cd as well as the cd error are displayed color-coded. The black rectangles and lines indicate the chosen fit interval of 338nm-356.2nm with a BrO cd of $(27 \pm 0.2) \times 10^{14} \text{ molec/cm}^2$, which corresponds to a mixing ratio of (3360 ± 27) ppt.

increases with higher relative humidity. Therefore the maximum of reflectivity can change even within one experiment. Once the relative humidity is stable the reflectivity curve is stable as well. But at changes of 10% or more the reflectivity curve can change by several nm. The spectra with 160 traverses through the White system (with the dielectric mirrors) of different relative humidities are shown in figure 4.10.

A well chosen evaluation wavelength range is crucial to the DOAS technique. It should encompass strong absorption bands of the trace gas of interest in order to maximize the sensitivity of the retrieval, while at the same time minimizing absorption structures of other trace gases and thus potential interferences. *Vogel et al.* 2012 present a novel tool to determine the optimal evaluation wavelength

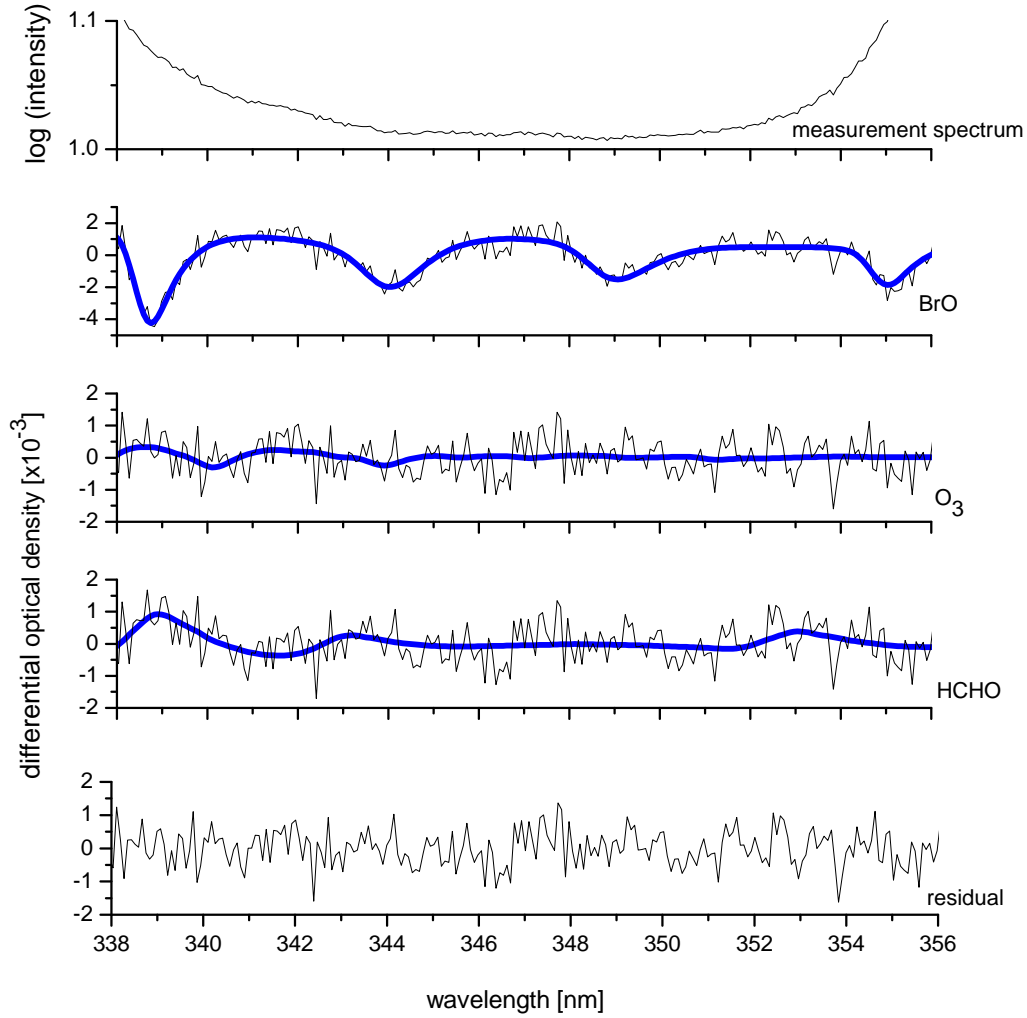


Figure 4.14.: Example for the spectral identification of BrO. The measurement spectrum was recorded at a RH of 37%. The thick blue lines indicate the fit result, the thin black lines the sum of fit result and residual. The corresponding mixing ratio for BrO is $(4.0 \pm 0.6) \cdot 10^{14} \text{ molec cm}^{-2} = 498 \pm 70 \text{ ppt}$. Structures of the Huggins bands of ozone and structures of formaldehyde could not be unambiguously identified above the respective detection limits of $4.8 \cdot 10^{17} \text{ molec cm}^{-2} = 596 \text{ ppt}$ and $4.210^{16} \text{ molec cm}^{-2} = 52 \text{ ppt}$. The residual is $2.9 \cdot 10^{-3}$ peak to peak and $5.4 \cdot 10^{-4}$ root mean square.

range. It is based on mapping retrieved values in the retrieval wavelength space and thus visualize the consequence of different choices of retrieval spectral ranges. To find the appropriate wavelength range depending on the relative humidity the evaluation range was varied. Examples are given for 2%, 45% and 60% relative

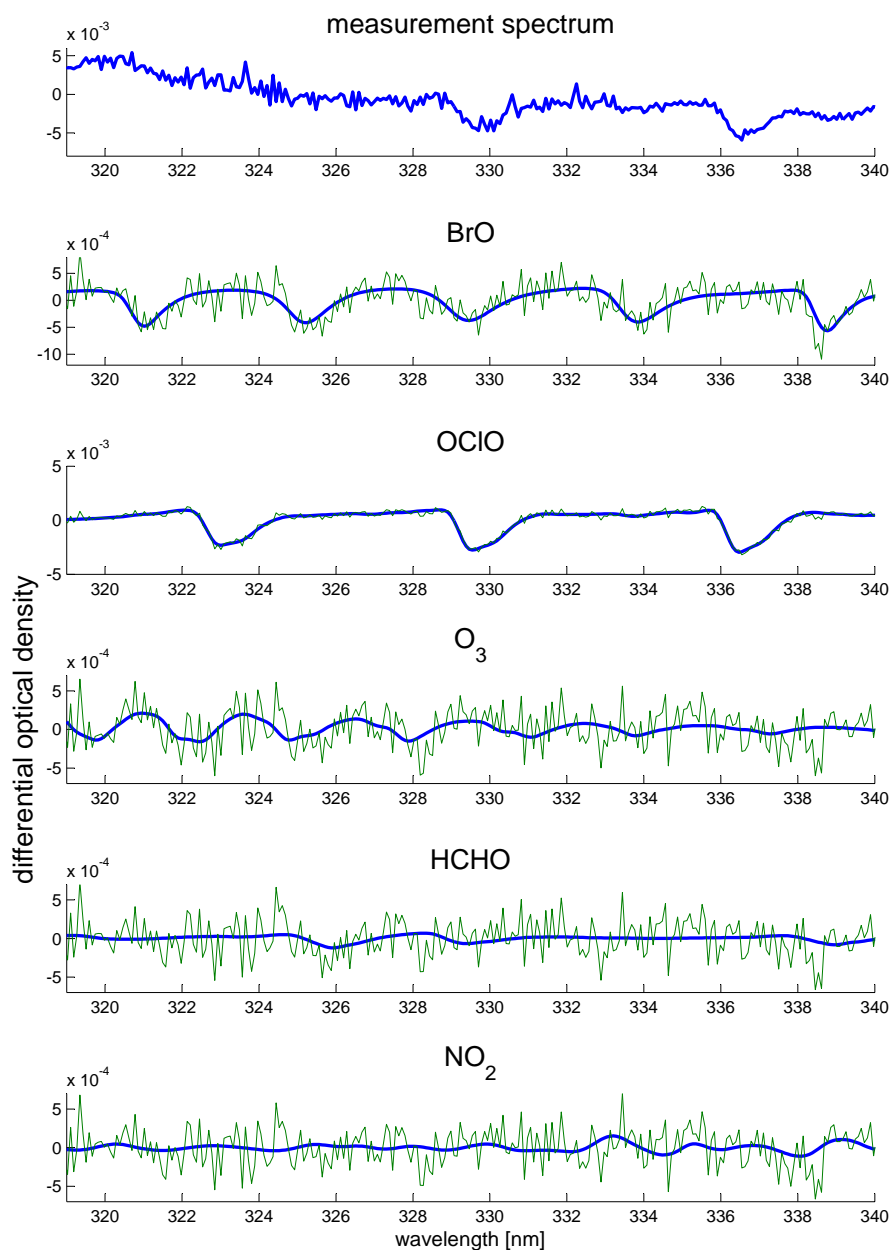


Figure 4.15.: Example for the spectral identification of BrO and OClO. The thick blue lines indicate the fit result, the thin green lines the sum of fit result and residual. The corresponding mixing ratio for BrO is $(6.4 \pm 0.8) \cdot 10^{13} \text{ molec cm}^{-2} = 797 \pm 100 \text{ ppt}$, for OClO is $(5.5 \pm 0.08) \cdot 10^{14} \text{ molec cm}^{-2} = 6903 \pm 97 \text{ ppt}$ and for ozone $(4.07 \pm 0.5) \cdot 10^{16} \text{ molec cm}^{-2} = 507 \pm 70 \text{ ppb}$. Structures of formaldehyde and nitrogendioxide could not be unambiguously identified above the respective detection limits of $2.7 \cdot 10^{15} \text{ molec cm}^{-2} = 30 \text{ ppb}$ and $9.610^{14} \text{ molec cm}^{-2} = 6 \text{ ppb}$. The residual is $1.2 \cdot 10^{-3}$ peak to peak and $2.6 \cdot 10^{-4}$ root mean square.

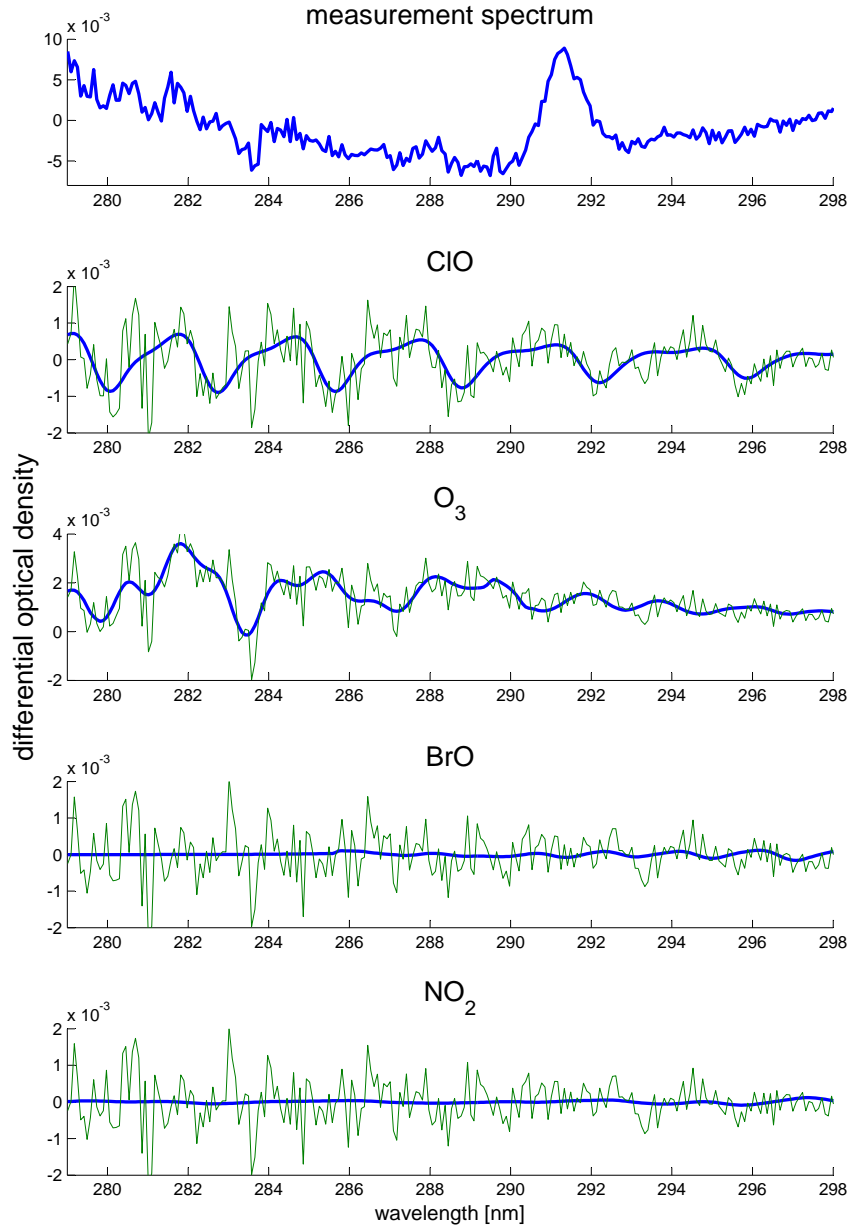


Figure 4.16.: Example for the spectral identification of ClO and O_3 . The thick blue lines indicate the fit result, the thin green lines the sum of fit result and residual. The corresponding mixing ratio for ClO is $(2.7 \pm 0.8) \cdot 10^{13} \text{ molec cm}^{-2} = 3371 \pm 1055 \text{ ppt}$, and for ozone $(3.89 \pm 0.7) \cdot 10^{16} \text{ molec cm}^{-2} = 485 \pm 50 \text{ ppb}$. Structures of BrO just exceeded the detection limit with $(7.9 \pm 3) \cdot 10^{13} \text{ molec cm}^{-2} = 990 \pm 373 \text{ ppt}$. Structures of NO_2 could not be unambiguously identified above a detection limit of $8 \cdot 10^{15} \text{ molec cm}^{-2} = 100 \text{ ppb}$. The residual is $4 \cdot 10^{-3}$ peak to peak and $6.1 \cdot 10^{-4}$ root mean square.

humidity at different BrO concentrations, resulting in different column densities (cd). The color coded plots in figure 4.11, 4.12 and 4.13 show the lower and upper limits of the retrieval wavelength. Thus each point in the plot corresponds to one particular wavelength interval. The error of the resulting cd is plotted as well, which is twice the fit error [Stutz and Platt 1996]. The resulting maps allow to readily identify retrieval wavelength intervals which are likely to lead to erroneous results [Vogel *et al.* 2012], like a very small fit interval shown along the diagonal of the plot. There is an area where the cd is fairly stable, namely along the range of high mirror reflectivity. Taking the color map of the error into account, it is obvious, that minimums of the error are connected to the differential structures of BrO. At 45% and 60% RH 4 vibrational bands of BrO were taken into account, as this fit range showed a low error and was in the stable (within the error) cd range. At 2% RH only 3 of the vibrational bands of BrO were used, as the cd was not stable using more than 3 bands.

4.3.2. BrO and OCIO

Detection of BrO and OCIO was possible with the dielectric as well as with the aluminum coated mirrors. In this wavelength range other trace gases, such as NO₂, HCHO, HONO, O₃ and O₄, can cause absorption structures as well and were taken into the fit procedure. In some measurements high amounts of O₃, NO₂, HCHO and HONO were observed (see chapter 5). For the evaluation of those species the same wavelength range as for BrO and OCIO was used. The wavelength range is limited by the dielectric coating of the mirrors. The evaluation of BrO and OCIO for the dielectric coated mirrors was performed between 338 nm and 356.2 nm where 4 vibrational bands of BrO and 3 vibrational bands of OCIO are located. However, the choice of this wavelength range provides superior BrO evaluation, since possible interferences with O₃ are reduced. In some measurements, according to the changing relative humidity as described in section 4.3.2, the fit window was reduced to 336-351.5 nm, where only 3 vibrational bands of BrO are present. The fit range was optimized using the tool of Vogel *et al.* 2012 as described before. A sample spectral fit (dielectric coating) is given in figure 4.14 for a mixing ratio of [BrO] = (498 ± 70) ppt at a RH of 37%. The O₃ mixing ratio is below the O₃-detection limit of 596 ppb.

For the aluminum coating, even more BrO absorption bands were taken into the fit window. The evaluation of BrO and OCIO was performed between 310nm-340nm where 5 vibrational bands of BrO and 3 vibrational bands of OCIO are located. An example fit of BrO and OCIO is given in figure 4.15.

4.3.3. ClO and O₃

ClO can only be detected with the aluminum coated mirrors, and with low sensitivity (detection limit of 2ppb). One reason is the low intensity of the Xe-arc lamp. Additionally, the achieved length of the light path was short with 32m, according to 16 reflections through the prisms and the first rear mirror. The used fit range was 279nm- 298nm, where 6 absorption bands of ClO and Huggins bands of ozone are present. The ozone absorption can cause interferences, which might reduce the sensitivity as well. The stray light in this wavelength range can cause up to 45% of the total light. The relative amount of stray light was determined as described above prior to each measurement. It was then multiplied with the respective measurement spectrum and subtracted. The reliability of those measurements are shown by providing a superior agreement with an ozone analyser (see chapter 5). A sample spectral fit is given in figure 4.16 for a mixing ratio of [ClO] = (3371 ± 1055) ppt. The O₃ mixing ratio was (485 ± 50) ppb.

4.4. The CE-DOAS Instrument

This chapter describes a newly developed CE -DOAS instrument for measurement in the UV (325nm-360nm) and thus for the detection of e.g. BrO, O₃ and HCHO. Details can also be found in [Hoch *et al.* 2012, Hoch *et al.* 2012], and some of the sections are similar to the paper. There are two differences: First, the LED was not pulsed during the measurements. Second, cooling and temperature stabilisation were applied (see section 4.4.4).

Figure 4.17 shows a schematic diagram of the CE-DOAS instrument (more details can be found at Hoch [2010]). The radiation of a UV-LED is imaged by lens L_1 into the resonator, consisting of two highly reflective dielectric mirrors m_1 and m_2 (focal length = 2 m). The radiation, which leaves the resonator through m_2 , is focused by the lens L_2 into a fiber bundle which can be adjusted by a x-y stage. This fiber bundle transmits the light to a temperature-stabilized spectrograph (Ocean Optics QE 65000). The moveable mirror K can redirect the light to a photomultiplier (PMT) to record a ring-down signal and thus check the quality of the resonator. F_1 and F_2 are band-pass filters. F_1 protects the PMT and F_2 reduces scattered light and LED light outside of the reflectivity range of the mirrors entering the fiber. The shutter is used to perform background measurements without radiation of the UV-LED. The electronic controller receives a constant current and creates the pulses for the UV-LED. It also controls the shutter and the mirror K.

4.4.1. The LED Radiation Source

The wavelength range (325nm to 365nm) of the LED UVTOP340 from Sensor Electronic Technology was chosen to optimize the sensitivity to BrO while minimizing

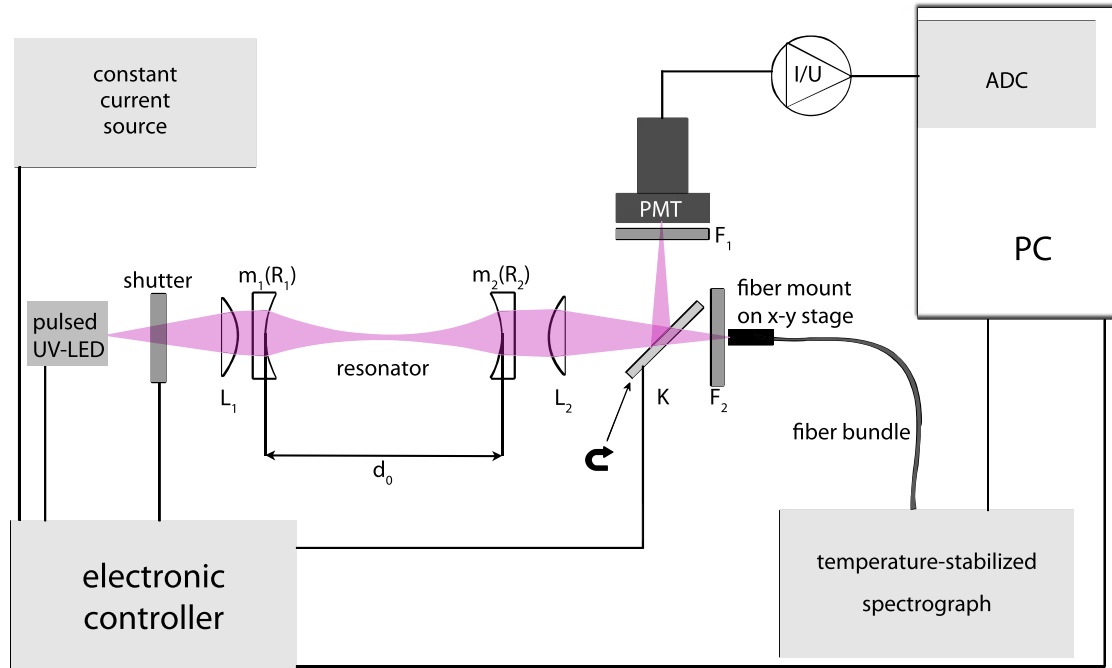


Figure 4.17.: Schematic diagram of the CE-DOAS-instrument. The resonator consists of two highly reflective dielectric mirrors m_1 and m_2 . The light beam of an UV-LED is imaged by a lens L_1 into the resonator and leaves the resonator through m_2 . Focused by the lens L_1 to a fiber bundle the light is transmitted to a temperature stabilized spectrograph (Ocean Optics QE 65000). The band-pass filter F_1 protects the PMT and F_2 the fibers from scattered light and LED radiation outside of the reflectivity range of the mirrors. The electronic controller creates the pulses for the UV-LED and controls the shutter and the mirror K . The distance d_0 was 1.33 m during the chamber measurements. It is possible to get a ring down signal with the help of moveable mirror K . K redirects the light to a photomultiplier (PMT). (adapted from [Hoch et al. 2012])

the interference due to O_3 . To minimize the known LEDs etalon structures the LED is inclined against the optical axis of the resonator at an angle of 15° [Sihler *et al.* 2009]. As no CRD-measurements were performed within this thesis, the LED was not pulsed during the measurement (in comparison to the measurements in [Hoch *et al.* 2012], where the LED was pulsed permanently).

4.4.2. Mirrors and Optics

The core of the setup is the resonator which consists of two high reflective mirrors (Fig. 4.17, m_1 and m_2). The reflectivity of the mirrors from Layertec GmbH, (Mellingen, Germany) was chosen to achieve a good compromise between optical light path length and signal to noise ratio [Fiedler *et al.* 2007]. The radiation of the UV-LED is coupled into the resonator by lens L_1 ($f_1 = 25\text{ mm}$) to use as much of the LED output as possible. The radiation which passes mirror m_2 is focused by lens L_2 ($f_2 = 100\text{ mm}$) on a fiber coupler to match the NA of the spectrometer. The fiber bundle (Loptek GmbH & Co, Berlin, Germany) consists of seven $200\text{ }\mu\text{m}$ fibers (NA of 0.22, UV solarization stabilized, 6 m long), arranged in a circular configuration on the resonators side. A slit configuration of the fibers from the bundle is coupled into the spectrometer side. The band-pass filter F_1 and F_2 , both UG11 from Schott, (Mainz, Germany, figure 4.7) have a transmission range of 270-380 nm and a thickness of 1 mm. F_1 was placed directly in front of the PMT to protect the device as much as possible against ambient light (e.g. if cover is opened). The reflectivity of the mirrors can not readily be derived from the manufacturer's data: Layertec provided transmission values (T) but not reflectivities. Since $R + T + A = 1$ ($A = \text{Absorption}$) R can not be calculated from T unless the absorption A in the dielectric mirror is negligible, which, unfortunately, is not the case in this wavelength range. In this study one set of mirrors was used with values of stated transmissivity at 340 nm :

$$M_1 : T = 0.11\%.$$

4.4.3. Spectrograph and Detector

The fiber transmits the light into a temperature stabilized (20°C) spectrograph QE65000 from Ocean Optics (Dunedin, Florida, USA). The spectrometer has a focal length of 101 mm, it is equipped with a 2400 lines/mm grating resulting in 0.62 nm spectral resolution with the column of seven $200\text{ }\mu\text{m}$ fibers (see subsection 4.4.2) acting as entrance slit.

The detector used in the QE65000 spectrometer is a scientific-grade, back-thinned, Thermo-Electrically Cooled (TEC), 1044×64 element CCD array (S7031-1006 from Hamamatsu Photonics (Naka-ku, Hamamatsu City, Shizuoka Pref., Japan)), temperature stabilized to -20°C .

4.4.4. Peltier Cooling of the LED

Several options for improvement of the system were suggested in [Hoch et al. 2012]. One aim is to increase the light intensity for a better time resolution and therefore improved detection limit. Cooling of the LED was chosen to increase the intensity, as expected from the data sheet (SET, 2010).

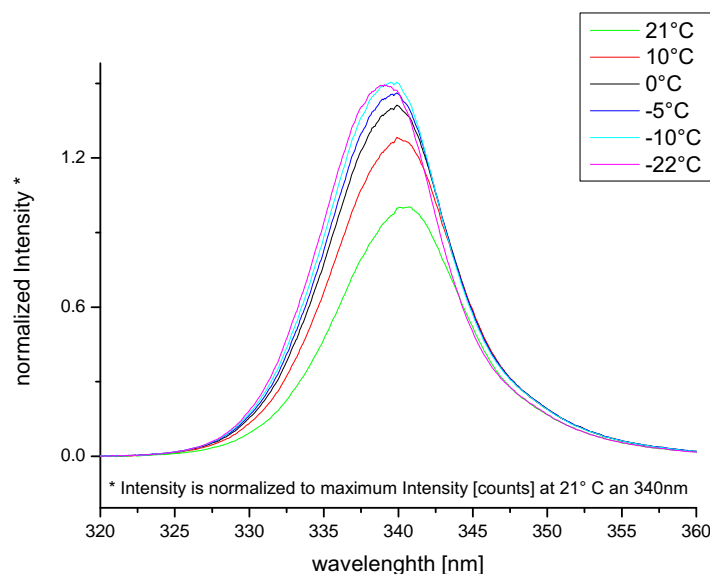


Figure 4.18.: Spectrum of the LED for different temperatures. The Intensity for 1mA LED-current was normalized to the intensity at 21°C. The intensity increases with decreasing temperature. Cooling of 30K down to -10 °C was found to increase the radiation intensity up to 46%.

The LED was cooled by a Peltier element, which was connected via an aluminum mounting directly to the LED, as well as a temperature sensor. The heat of the hot side of the Peltier element was cooled by a water flow. A water cooling system from Aquatuning GmbH was used (SLIM SINGLE 120 Radiator/XSPC X2=450 pump station). The original idea was from [Sihler 2011], who helped with the technical realization of the cooling system.

Test measurements of the relative intensity show a steep increase of up to 45% higher intensity for cooling down to -10°(shown in figure 4.18) compared to 21°C. The LED light was coupled directly into the receiving fiber of the CE-DOAS. The intensity at 30 mA (constant current during measurement) would lead to oversaturation of the detector. Therefore the current of the LED was set to a constant level of 1 mA for all temperatures. The lower the temperature the higher the energy input for the LED. That indicates an increase of the band gap between the conduction band and the valence band. This is also indicated by the shift of the maximum of

intensity in figure 4.18 to lower wavelength. However, an intensity increase of the LED light up to 45% was achieved at -10°C. Further cooling did not increase the intensity, for a current of 1 mA. It is possible that further intensity increase could be achieved at higher input current.

4.5. Cavity-Enhanced Differential Absorption Spectroscopy (CE-DOAS)

This section gives an overview of the basic idea of a CE-DOAS instrument, described in detail by *Hoch* 2010 and *Hoch et al.* 2012. The basic idea of the CE-DOAS technique is to introduce incoherent broadband radiation I_L into an optical resonator (see Fig. 4.17), consisting of two mirrors with reflectivity R (for simplicity we assume both mirrors to have the same reflectivity, if the mirrors have different reflectivities R_1, R_2 an averaged reflectivity $R = \sqrt{R_1 R_2}$ is used) ([*Platt et al.* 2009]). The distance between the mirrors is d_0 (here = 1.33 m) (see Fig. 4.17). Initially only the fraction $\rho = 1 - R$ of the radiation I_L enters the resonator. Here for simplicity I_L means only the fraction of the radiation from the LED which enters the resonator and can be used. It is obvious that not all radiation emitted by the LED is going through the lens and also passes the aperture defined by mirror m_2 . Once inside the resonator, the radiation is reflected on average about $1/(1-R)$ times (neglecting other losses). Finally, in the absence of any extinction in the resonator, half of the radiation leaves the resonator through each mirror. Each fraction has the intensity I_0 . An effective mirror reflectivity $R_0(\lambda)$ is defined to include the Rayleigh extinction coefficient $\epsilon_R(\lambda)$ of pure air:

$$R_0(\lambda) = R(\lambda) - \epsilon_R(\lambda)d_0 \quad (4.6)$$

or

$$\rho_0(\lambda) = 1 - R_0(\lambda) = 1 - R(\lambda) + \epsilon_R(\lambda)d_0 = \rho(\lambda) + \epsilon_R(\lambda)d_0 \quad (4.7)$$

In the following the index 0 always corresponds to the cavity without absorbers but including Rayleigh scattering.

4.5.1. Continuous Data Collection

DOAS techniques derive the trace gas concentration by the use of the optical density $D(\lambda)$ which requires the measurement of the intensities without ($I_0(\lambda)$) and with ($I(\lambda)$) trace gas absorption [*Platt and Stutz* 2008]. In a CE-DOAS setup the optical density D_{CE} is determined from intensity measurements with absorber free but filled

(e.g. synthetic air) resonator I_{tot0} and with sample air filled resonator I_{tot} :

$$D_{CE} = \ln \left(\frac{I_{tot0}}{I_{tot}} \right) = \ln \left(\frac{\int_0^\infty I_{in0}(n) dn}{\int_0^\infty I_{in}(n) dn} \right) = \ln \left(1 + \frac{\tau}{\rho_0} \right) \quad (4.8)$$

$I_{in0}(n)$ is the intensity after n passes through the cavity in the pure air filled cavity (without any absorbers) and $I_{in}(n)$ is the intensity after n passes through the cavity including also absorptions. The number of traverses of the photons through the cavity is n . The factor τ is given by $\tau=1$ -transmissivity of the cavity. However according to [Platt *et al.* 2009] for strong absorptions this is not equal to the optical density used in traditional DOAS application if using the average light path from section 4.5.2. Thus the corrections from section 4.5.4 have to be applied.

4.5.2. Determination of the Average Light Path

According to Platt *et al.* [2009] the average length of the light path $\bar{L}(\lambda)$ is expressed by:

$$\bar{L}(\lambda) \approx \frac{d_0}{\tau(\lambda) + \rho(\lambda)} = \frac{d_0}{\sigma(\lambda)\bar{c}d_0 + \rho_0(\lambda)} \quad (4.9)$$

where $\sigma(\lambda)$ is the absorption cross section of the trace gas and \bar{c} the average trace gas concentration in the cavity. Note that the transmission of the cavity, $\tau(\lambda)$ includes all extinction processes in the cavity i.e. aerosol absorption and Mie scattering as well as absorption by trace gases. It does not include extinction by pure air due to absorption and Rayleigh scattering. This is taken into account by using $\rho_0(\lambda)$ instead of $\rho(\lambda)$. For an air filled resonator that results in:

$$\bar{L}_0(\lambda) = \frac{d_0}{\rho_0(\lambda)} \quad (4.10)$$

In praxis this average path length $\bar{L}_0(\lambda)$ can be determined e.g. from the known Rayleigh scattering of two different gases for example He and dry zero air [Washenfelder *et al.* 2008], from a CRD decay time measurement [Meinen *et al.* 2010], or from the differential absorption of a trace gas of known concentration. In this work $\bar{L}_0(\lambda)$ was determined from the absorption band of O₄ 360.4 nm, making use of the known O₂ concentration [Ball *et al.* 2004]. This average path length has to be corrected, which is described in the following subsections.

4.5.3. Correction of the Base Path-Length

The length of the absorption medium in the resonator d is not necessarily equal to the distance between the mirrors d_0 , since at either end of the resonator a few

centimeters of the path are not filled with air due to a purge flow close to the mirrors. In this case, the effective light path has to be corrected by the factor d/d_0 .

$$\bar{L}(\lambda) = \bar{L}_0(\lambda) \frac{d}{d_0} \quad (4.11)$$

4.5.4. Correction for Light Path Reduction due to Extinction in the Cavity

Platt et al. [2009] describe in detail how the light path is reduced by extinction in the resonator. Here two out of the four ways to correct this effect presented by *Platt et al.* [2009] and *M.Horbanski* [2010] are applied. For both ways the optical density D_{CE} and the average path length $\bar{L}(\lambda)$ needs to be known.

1. Correction of the trace gas absorption cross section σ to σ_{eff} :

$$\sigma_{eff}(\lambda) = \sigma(\lambda) \times \frac{\bar{L}_{eff}(\lambda)}{\bar{L}(\lambda)} = \sigma(\lambda) \times \frac{D_{CE}}{e^{D_{CE}} - 1} \quad (4.12)$$

This σ_{eff} is used by a DOAS-fit to obtain a corrected column density. From this column density the corrected concentration is determined by dividing with $\bar{L}(\lambda)$. Equation 4.12 depends on the absolute optical density D_{CE} and thus relies on all kinds of intensity stabilities. To overcome the requirement of a stable intensity, *Horbanski* [2010] developed an iterative method, which is used for measurements with only one trace gas and without aerosols where the convoluted reference cross section σ_0 is corrected. During the first iteration a DOAS fit determines an optical density D_0 and σ_0 is corrected to σ_1 . In the next iteration step σ_1 determines a D_1 and σ_0 is corrected to σ_2 , etc:

i. iteration:

$$\sigma_i \rightarrow (cL)_i \rightarrow (cL)_i \times \sigma_i = D_i \rightarrow \sigma_0 \times \frac{D_i}{e^{D_i} - 1} = \sigma_{i+1} \quad (4.13)$$

This correction is applied in four iteration steps within this work. The same method can also be applied if several absorbers are present by extending Eq. (4.13).

2. Method 1 with Eq. (4.12) becomes very complex when using more than one absorber. In this case a second method is useful in order to correct the optical density before the fit and convert it to D_{eff} which is equal to an absorption where the light path is not reduced:

$$D_{eff} = e^{D_{CE}} - 1 = \frac{I_{0tot}}{I_{tot}} - 1 \quad (4.14)$$

In this work the second method applying Eq. (4.14) is used whenever there is more than one absorber. It needs to be considered that for this correction the intensities I_{0tot} and I_{tot} have to be successively measured. This requires an absolutely stable optical resonator and light source intensity (similar to the requirements of the BBCEAS approach).

4.5.5. Correction of the Wavelength Dependence of the Average Light Path

As described in section 4.5.2 the average light path $\bar{L}(\lambda)$ is dependent on λ because $R(\lambda)$ is dependent on λ . As described by *Venables et al.* [2006] it is possible to use differential absorption structures for the determination of the wavelength dependence of the mirror reflectivity and therefore for the calibration of the path length. This method requires an absorber of known concentration, which has several distinct absorption bands in the wavelength range of interest. In the present study, we used O_3 and HONO to estimate the relative shape of the reflection curve (compare section 4.6). Since the concentration of these gases was unknown the absorption bands of O_4 at 343.5 nm and 360.4 nm were used additionally to derive the absolute reflectivity curve of the mirrors.

4.6. Data Analysis of the CE-DOAS-measurements

The data analysis was done similar as described in [*Hoch et al.* 2012] using DOASIS ([*Kraus* 2004]). The overview in table 4.3) shows the used absorption cross-sections and analysis settings, which was adapted from [*Hoch et al.* 2012].

4.6.1. Mirror Reflectivity and Path Length Calibration

As described in section 4.5.5 it is possible to use differential absorption structures to derive the wavelength dependence of the mirror reflectivity and therefore for the determination of the wavelength dependent path length.

The relative shape of the mirror reflectivity from [*Hoch et al.* 2012] was verified as described in the following. In the paper we used O_3 and HONO for the estimation of the relative shape of the mirror reflectivity (not the absolute, as the actual concentrations were unknown). In addition absorption structures of HCHO were used within this thesis. The used fit windows are shown in figure 4.19.

Ozone was created by ionization of O_2 (*purity* = 99.995%) using a corona discharge ozonizer as described in chapter 3.

The generation of the nitrous acid is based on the reaction of a sodium nitrite solution $NaNO_2$ with sulfuric acid H_2SO_4 as described in chapter 3. The HONO

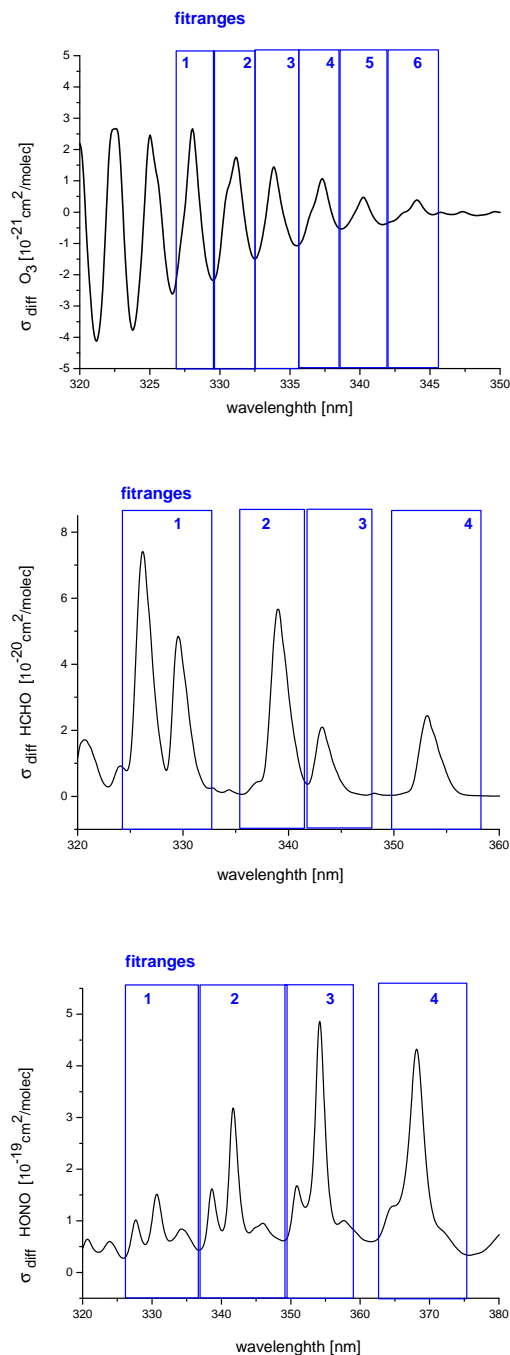


Figure 4.19.: Fit windows and differential absorption structures used for determination of the relative shape of the mirror reflectivity. For O₃ 6 fit windows (left:326.5-329.8 nm, 329.5-332.7 nm, 332.7-335.8nm, 335.8-339.2 nm, 338.9-342.7 nm and 342.4 -346.6 nm), for HONO 4 fit windows (middle:325.5-337.2 nm, 337.3-349.1 nm, 348.7-359.0 nm and 361.4-375.6 nm) and for HCHO 4 fit windows (right:324.8-333 nm, 335.4-340.8 nm, 342-348 nm and 349.8-358 nm) were included in the analysis procedure.

Table 4.3.: Overview of the literature absorption cross sections used in the CE-DOAS evaluation (adapted from [Hoch et al. 2012]): For each trace gas a mean-spectral shift was determined from a measured spectrum with strong absorption. The cross sections were corrected with these mean shift (Pre-shift) and linked together for the following measurements. For all trace gases the following DOAS-fit settings were used: fit window 325-365 nm; high pass filter with 1000 iterations; 3rd degree polynomial; squeeze limited to $\pm 2\%$ (of the total spectral range).

Trace gas	Reference	Pre-shift [nm]	Shift
BrO	[Fleischmann and Burrows 2004]	0.153	free
HCHO	[Meller and Moortgat 2000]	0.0018	linked to BrO
HONO	[Stutz et al. 2000]	0.08221	linked to BrO
O ₄	[Greenblatt et al. 1990]	0.578	linked to BrO
O ₃	Voigt et al. [2001]	0.206	linked to BrO
NO ₂	Voigt et al. [2002]	0	linked to BrO

generation depends on temperature, gas flow, NaNO₂ concentration and fluid flow. A typical concentration up to 30 ppb was accomplished.

Formaldehyde was an impurity, which occurred during some of the smog chamber experiments. The actual source is still unknown, but possible interactions with halogen release is discussed in chapter 5.

In order to determine the absolute light path in the cavity at two particular wavelengths (343.5 nm and 360.5 nm), O₄ measurements were carried out. For that purpose an additional tube was mounted in between the resonator inside the smogchamber. It was first completely filled with nitrogen and after wards completely (including mirror purge gas) with pure oxygen. Additionally barometric pressure (with a mercury barometer) and temperature were measured to determine the O₂ concentration in the resonator.

With the absorption of O₄ at 343.5nm and 360.5nm the light path at these wavelengths could be determined. The formation of O₄ is due to collision of two O₂ molecules:



Unfortunately the equilibrium constant of this second order reaction is not known. Therefore the absolute concentration and the absorption cross section of O₄ is not known. But the O₄ concentration has a quadratic dependence on the O₂ concentration and the pair absorption coefficient is introduced:

$$\alpha_{O_4}(\lambda) = \frac{\epsilon_{O_4}(\lambda)}{[O_2]^2} \text{ in } \frac{cm^5}{molec^2} \quad (4.16)$$

ϵ_{O_4} is the measured extinction coefficient.

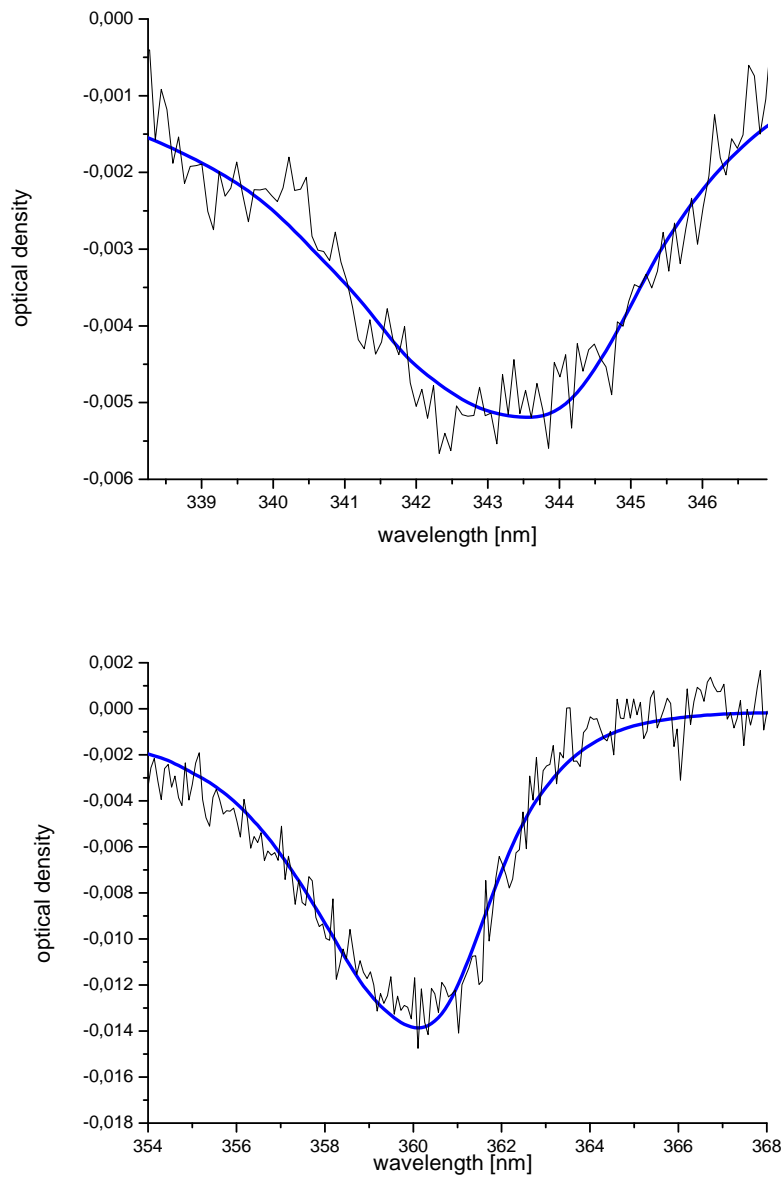


Figure 4.20.: Fit example of O_4 absorption bands at 343.5nm and 360.5nm. The fit coefficients were $(4111 \pm 1007) \cdot 10^{40} \text{ molec}^2/\text{cm}^5$ and $(3218 \pm 358) \cdot 10^{40} \text{ molec}^2/\text{cm}^5$, corresponding to a light path of $(734 \pm 180)\text{m}$ and $(575 \pm 64)\text{m}$, respectively.

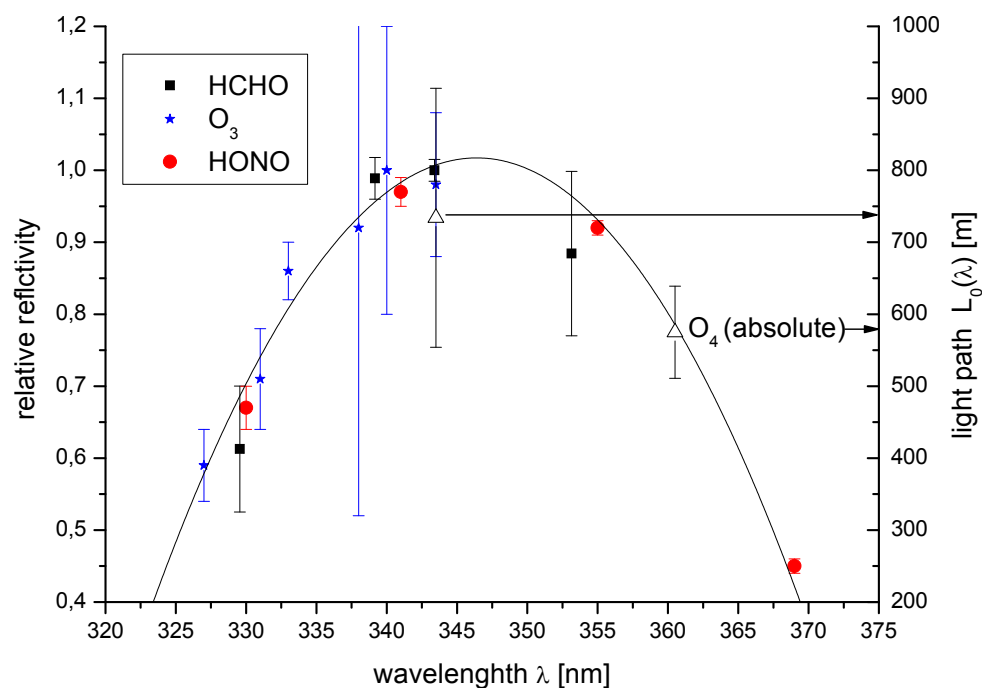


Figure 4.21.: Relative shape of reflectivity curve of the dielectric coated mirror used for the CE-DOAS instrument. The change in column density for the different fit windows for HCHO, O_3 and HONO normalized to values at 343.4 nm are shown at the respective middle of the fit window. The absolute achieved light path from the O_4 concentration is shown on the right.

An example fit of the 343.5nm and 360.5 nm absorption bands are given in figure 4.20. The fit coefficient was $[O_2]^2 \cdot L = (3218 \pm 122) \cdot 10^{40} \text{ molec}^2/\text{cm}^5$ at 360.5 nm and $(4111 \pm 839) \cdot 10^{40} \text{ molec}^2/\text{cm}^5$ at 343.5nm. This is the product of the square of oxygen concentration times light path, L. The light path is calculated, using the ideal gas law:

$$\frac{N}{V} = \text{concentration} = \frac{p}{k_b T} \quad (4.17)$$

with N=number of molecules, V=volume, p=pressure, T=temperature, k_b =Boltzmann constant= $1.381 \cdot 10^{-23} \text{ J/K}$. The pressure was p=957 hPa and the temperature T=20°C. The calculated L is then $(734 \pm 180) \text{ m}$ and $(575 \pm 64) \text{ m}$ at 343.5 nm and 360.5 nm respectively (in pure O_2). The differences do not imply a larger measurement error, but different light paths at different wavelengths. As the absorption at 360.5nm is much stronger compared to 343.5nm, the sensitivity is higher by a factor of 3. Therefore this value was used for the calculation of the wavelength dependence of the absolute path length. The optical path length was also verified by comparison of the measurement of an ozone analyser and the White system, the results are discussed in chapter 5.

The relative shape of reflectivity curve is shown in Fig. 4.21, including the relative column densities of O_3 , HONO and HCHO at the middle of the respective fit ranges. The absolute calibrated path length is shown as well. The following measurements were corrected with this reflectivity curve. A fit example for identification of BrO at a mixing ratio for BrO is $239 \pm 12 \text{ ppt}$ is given in figure 4.22.

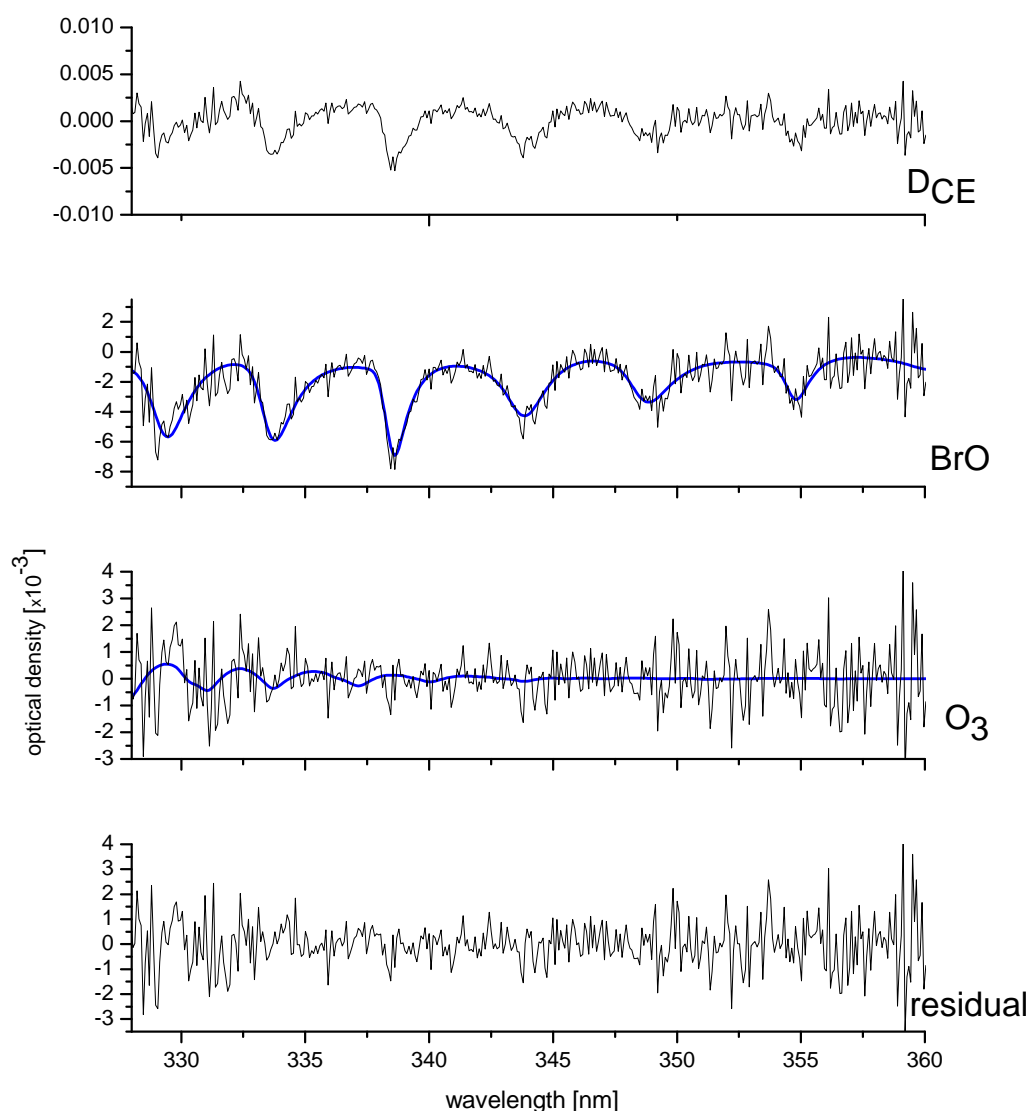


Figure 4.22.: Example for the spectral identification of BrO with the CE-DOAS set up. The thick blue lines indicate the fit result, the thin black lines the sum of fit result and residual. The corresponding mixing ratio for BrO is $239 \pm 12 ppt$. Structures of the Huggins bands of ozone were also identified with a mixing ratio of $117 \pm 42 ppb$ close to the detection limit. The residual is $4 \cdot 10^{-3}$ peak to peak. The maximal path length at 346.3 nm was 816 m.

5. Results

In the following chapter the results of the smog chamber experiments carried out within the framework of this thesis are presented. The first part shows an inter comparison of the different instruments used during the smog chamber studies. That is important for validation of the recently built instruments, as well as for showing the reliability of the established ones; possible interferences and problems are discussed. They could also show that the air in the chamber is well mixed, within the measured time of $\approx 120\text{sec}$.

In the second part, experiments using a simulated salt pan as a halogen source and the dependence of halogen chemistry on the relative humidity are shown. The experiments are the first of their kind, in terms of simulating a natural dry/semi humid salt flat, even though the chamber conditions are certainly not identical to those in nature. In the third part of this chapter, experiments with sea salt aerosols, which provide surface areas for heterogeneous halogen release processes, are shown for different initial HC and NO_x levels. At the end of this chapter, the influence of organic compounds from SOA on the halogen release from the salt pan is introduced.

5.1. Inter Comparison of the Different Instruments

During the smog chamber experiments different kinds of instruments were used. As explained in detail in chapter 4, two multi reflection systems were developed for the LOTASC teflon smog chamber in Bayreuth. They offer the possibility to measure a variety of trace gases. The smog chamber facility itself is equipped with a number of high precision instruments as described in chapter 3. In this section, the first inter comparison measurements of BrO, O₃ and formaldehyde from the WS and CE DOAS are shown. These two DOAS the instruments are further compared with the CL Ozone monitor during a salt pan experiment. Additionally, ozone mixing ratios detected by the WS using the aluminum coated mirrors are compared with those from the UV O₃ monitor during sea salt aerosol experiments. In some experiments with sea salt aerosols, large amounts of NO₂ were injected, and an inter comparison of the WS using the dielectric coated as well as the aluminum coated mirrors and a NO₂CL monitor with blue light converter was conducted. It is not possible to perform measurements using the CE DOAS instrument at high aerosol levels (see chapter 4). Furthermore, a time series of HONO is shown and the WS DOAS data is compared to a LOPAP instrument. The results of the inter comparison

Table 5.1.: *Overview of the inter comparison experiments shown in this thesis. Two different kinds of CL monitors were used: CL³=Bendix-UPK8002 for detection of O₃ and CL²=Ecophysics CLD-88p with blue light converter for detection of NO₂ were used. For details of the fit-setting of the WS see table 4.1 and for the CE table 4.3 in chapter 4. The maximal path length at 346.3 nm of the CE DOAS was 816m. For the WS 288m and 32m for dielectric (De) and aluminum (Al) coating, respectively. (*see section 5.1.4)*

experiment	instruments	trace gases compared	aerosols	fit-setting WS
SPHCHO	WS and CE CE and CL ³	BrO, HCHO, O ₃	no no	DeRHh
AeNOxh2800oz	WS and UVphotometrie	O ₃	yes	AlClOU
AeNOxh760oz	WS and CL ¹ NO ₂	NO ₂	yes	AlBrO
DNO2c	WS and CL ¹ NO ₂	NO ₂	yes	DeRHh
HONOC	WS and LOPAP	HONO	no	DeRHl*

of the different instruments demonstrate the reliability of the newly constructed instruments, as well as possible problems and interferences.

5.1.1. Comparison of White System and CE-DOAS

In this section the inter comparison during a salt pan experiment with formaldehyde (HCHO) impurity (experiment:SPHCHO) of the WS and CE DOAS of BrO, HCHO and O₃ is discussed. Both instruments are designed to fit into the special spatial and laboratory conditions at LOTASC. The CE-DOAS for detecting BrO in the ultraviolet range using an UV-LED is the first of its kind. WSs very similar to the one applied within this thesis, using a Xe arc lamp and dielectric coated mirrors, were used before. However in this case the detection of BrO is unique. For all those reasons, an inter comparison between the two instruments is very interesting. The light path calculation of the CE-DOAS includes several steps of evaluation (compare section 4). Whereas the WS light path is calculated by simply counting the number of traverses and multiplying by the distance. Additionally, the light paths of the two instruments through the chamber are different. The WS averages a diagonal light path from top to bottom (base path 2m), while the CE-DOAS light beam crosses the chamber horizontally 25cm straight above the salt pan. Concurrent measurements of BrO and O₃ during a salt pan experiment at RH of 40% are shown in figure 5.1 and 5.2. Additionally, comparison of HCHO data after the experiment during the cleaning procedure is shown in figure 5.3. No aerosols were present at the WS CE-DOAS inter comparison experiments. The maximum light path of the CE DOAS at 346.3 nm was 816 m, and of the WS system 288 m. The difference in light path is reflected in the respective errors bars shown in figures 5.1 - 5.3. The magnitude

of the error is related to the length of the light path. At a time resolution of 3 minutes per sample, the detection limits of CE-DOAS were found to be 25 ppt, 5.5 ppb, and 55 ppb for BrO, HCHO, and O₃, respectively. The White-cell has a higher detection limit at a better minimal time resolution of one minute per measurement of 40 ppt, 10 ppb, and 300 ppb for BrO, HCO, and O₃, respectively.

The BrO time series (fig. 5.1) shows a very good agreement between the two DOAS for mixing ratios from below the respective detection limits up to 400 ppt; the linear fit has a slope of 1.05 ± 0.03 and a coefficient of determination $r^2 = 0.994$.

The agreement of HCHO of the two multi reflection systems is remarkably good as well, with $r^2 = 0.998$ and a slope of the linear fit of 0.98 ± 0.01 for values up to 1ppb. HCHO is an impurity in the chamber of unknown source. The integration time as well as the measurement error for the WS slightly increased to 2 minutes and 50ppb due to misalignment of the mirrors. Nevertheless, excellent agreement between the two special Bayreuth chamber multi reflection systems measuring at different light paths, shows that the chamber was well mixed within a timescale of 120 seconds (average time resolution of the instruments). Rapid mixing is evident by the good agreement with the ozone monitor, which takes in air from a single location close to the chamber wall.

5.1.2. Comparison of White System and CE-DOAS with Ozone Monitor

During the same BrO experiment SPHCHO described in the section above, O₃ was measured as well. The ozone time series shows (fig. 5.2) a very good agreement between the CE DOAS and the Ozone CL monitor with a linear regression of 0.98 ± 0.04 and $r^2 = 0.982$. Although the detection limit of the WS is poor for O₃, the mixing ratio of ozone agrees within the measurement error and a clear decrease of O₃ during the experiment from ≈ 500 ppb to ≈ 0 ppb is shown. The mirror reflectivity is optimized for BrO, and the spectral range of the WS is smaller than that of the Cavity (see chapter 4).

During a sea salt aerosol experiment AEhNOx2 (see section 5.3.2), an intercomparison between the UV-ozone monitor and the WS was performed. During this experiment the WS used aluminum coated mirrors and had a light path of 32 m.

Below 300 nm, the relative amount of stray light compared to the measurement signal of the detector increases. A stray light correction (sc) using GG320nm or GG335nm cut off filters was performed by subtracting the stray light from the measurement spectrum prior to the fit procedure (see chapter 4). An additional cut off filter UG11 was used (see chapter 4). Without the sc correction, the ozone mixing ratios from the WS are underestimated by a factor of 0.7 compared to the ozone

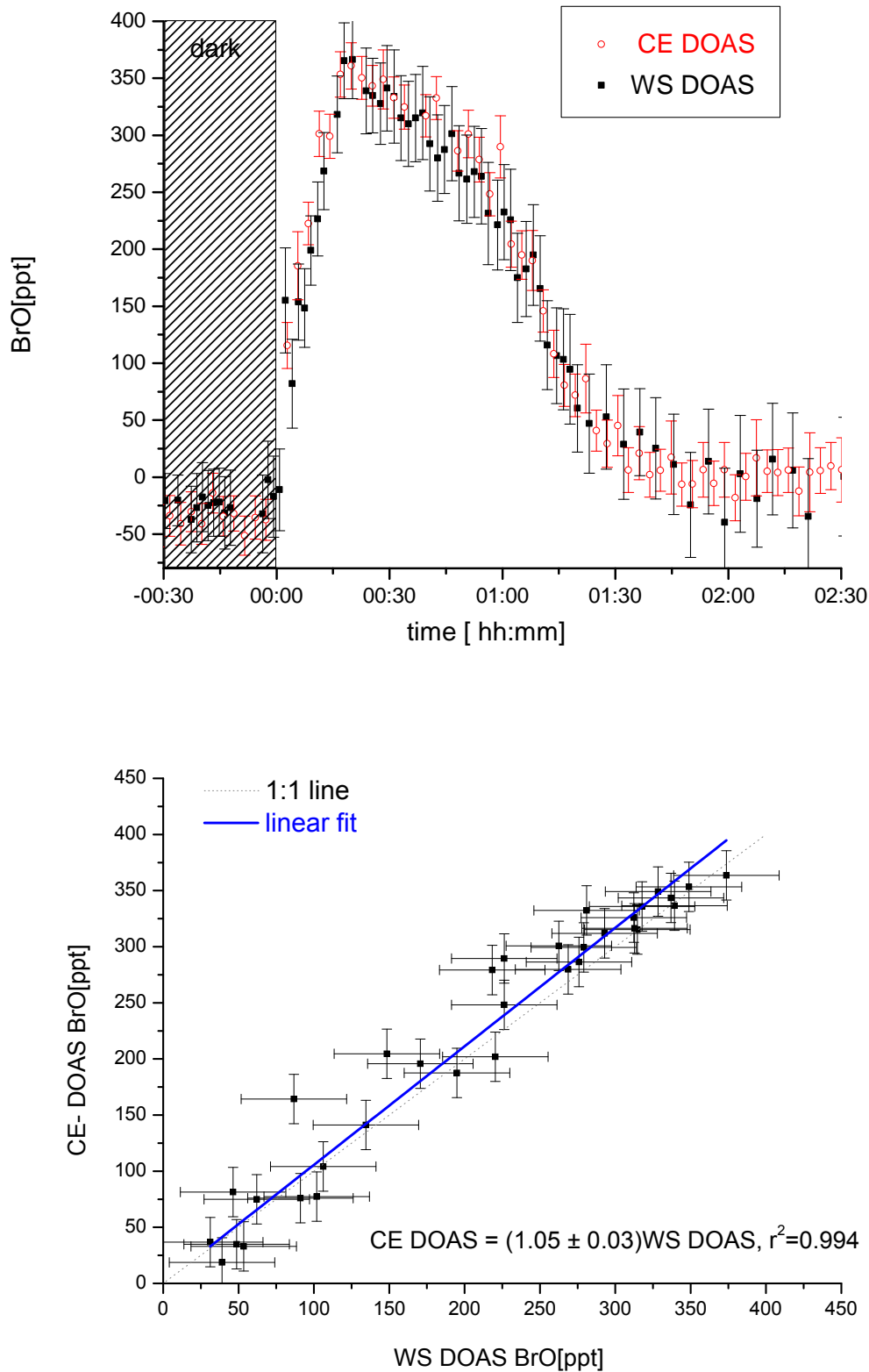


Figure 5.1.: Inter comparison of a time series for BrO detected by the WS (black squares) and CE-DOAS (red open cycles) simultaneously during a smog chamber experiment above a simulated salt pan, without injection of aerosols. Measurements from the two instruments show a very good agreement.

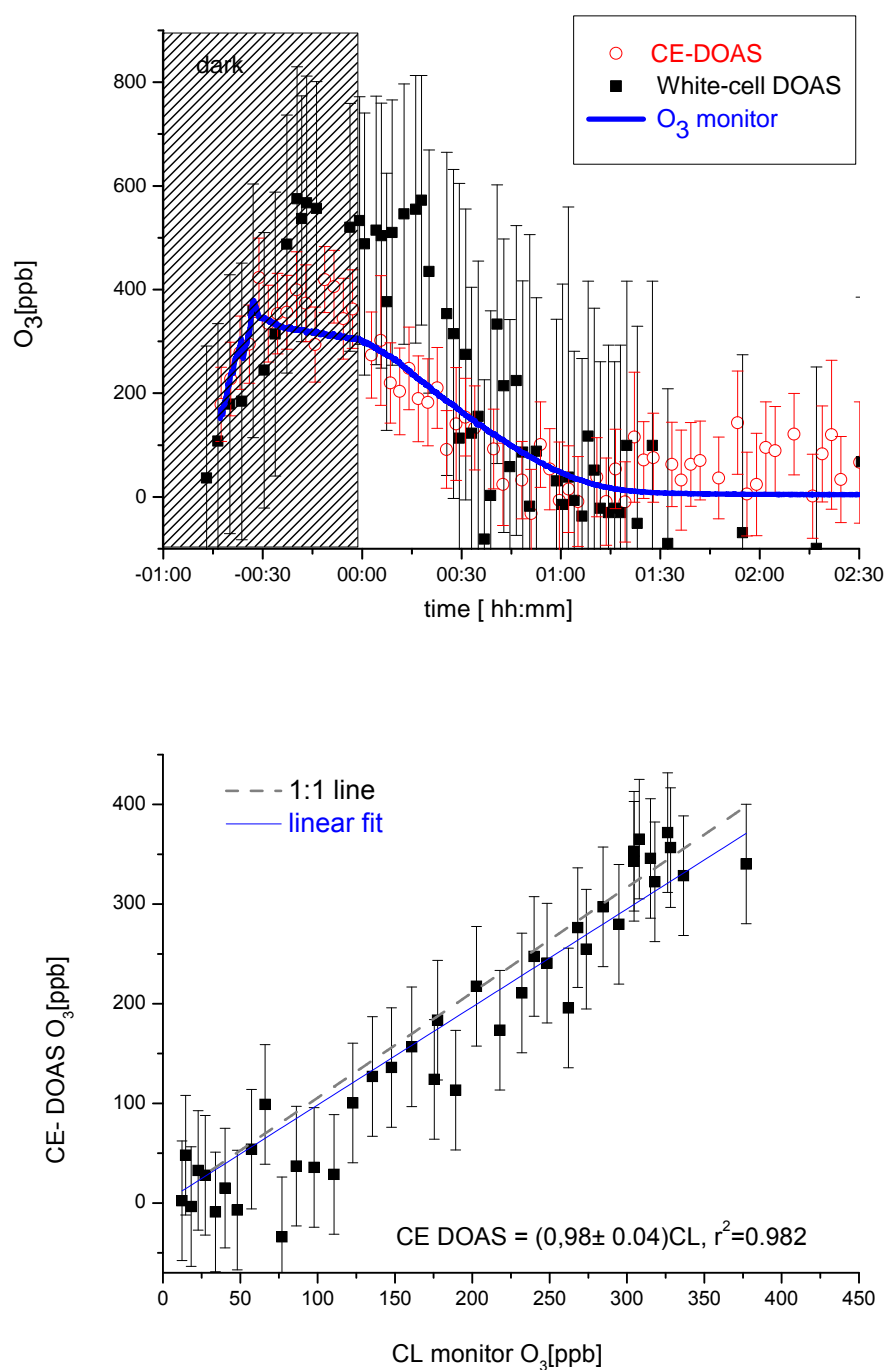


Figure 5.2.: Inter comparison of a time series (top) of O₃ detected by the WS (black squares), CE-DOAS (red open cycles) and CL (blue line) simultaneously during a smog chamber experiment above a simulated salt pan. All three instruments show reasonable good agreement measurement errors. However, the measurement accuracy of the WS is poor, as the spectral range of the dielectric mirrors is not well suited for Ozone measurements. The linear fit of the correlation between ozone monitor and CE-DOAS data (bottom) is close to one.

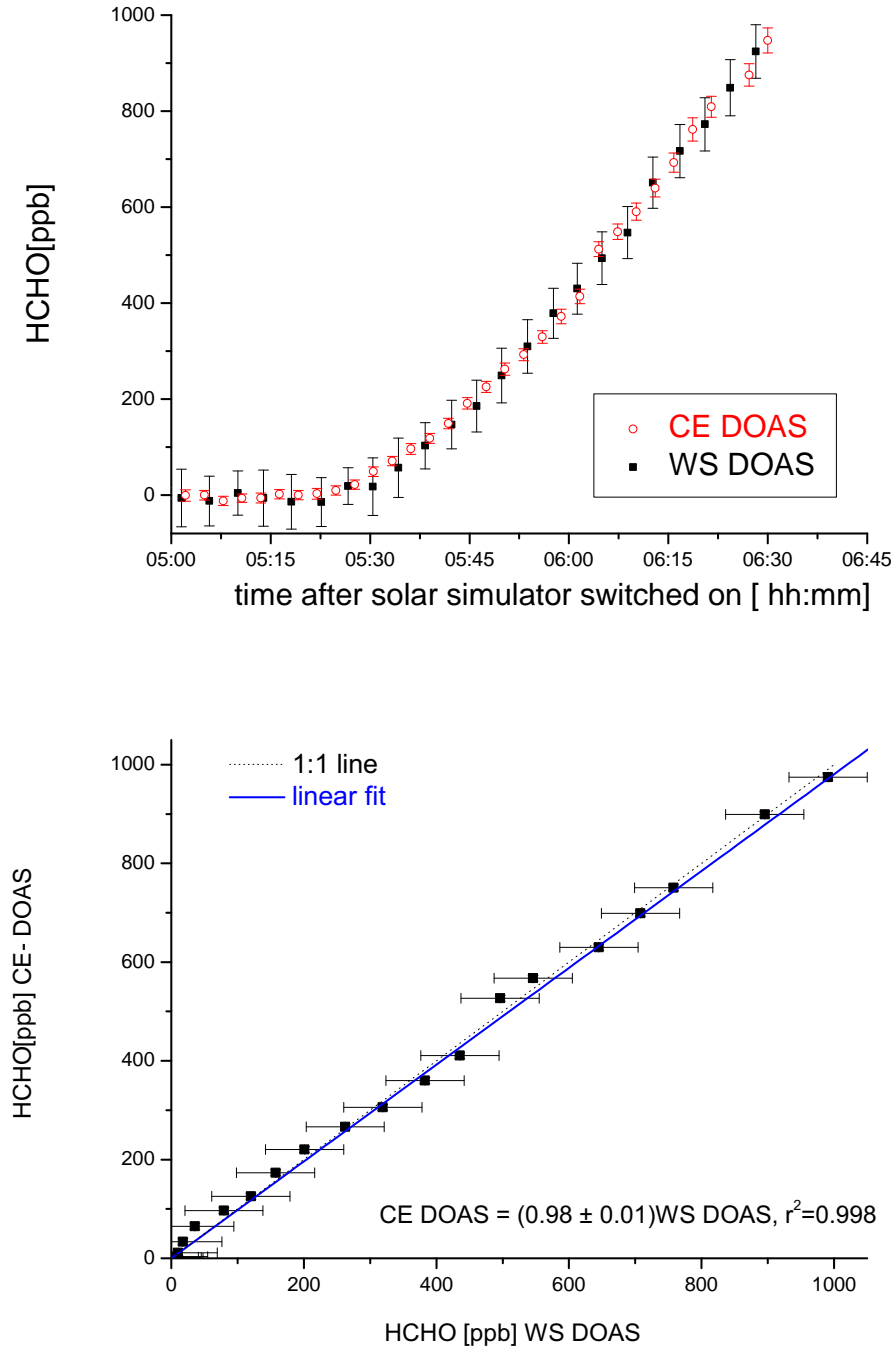


Figure 5.3.: Time series (top) of formaldehyde detected by the White-cell (red open circles) and CE-DOAS (black open squares) simultaneously in a smog chamber experiment above a simulated salt pan. The correlation of the data from the two instruments (bottom) is excellent.

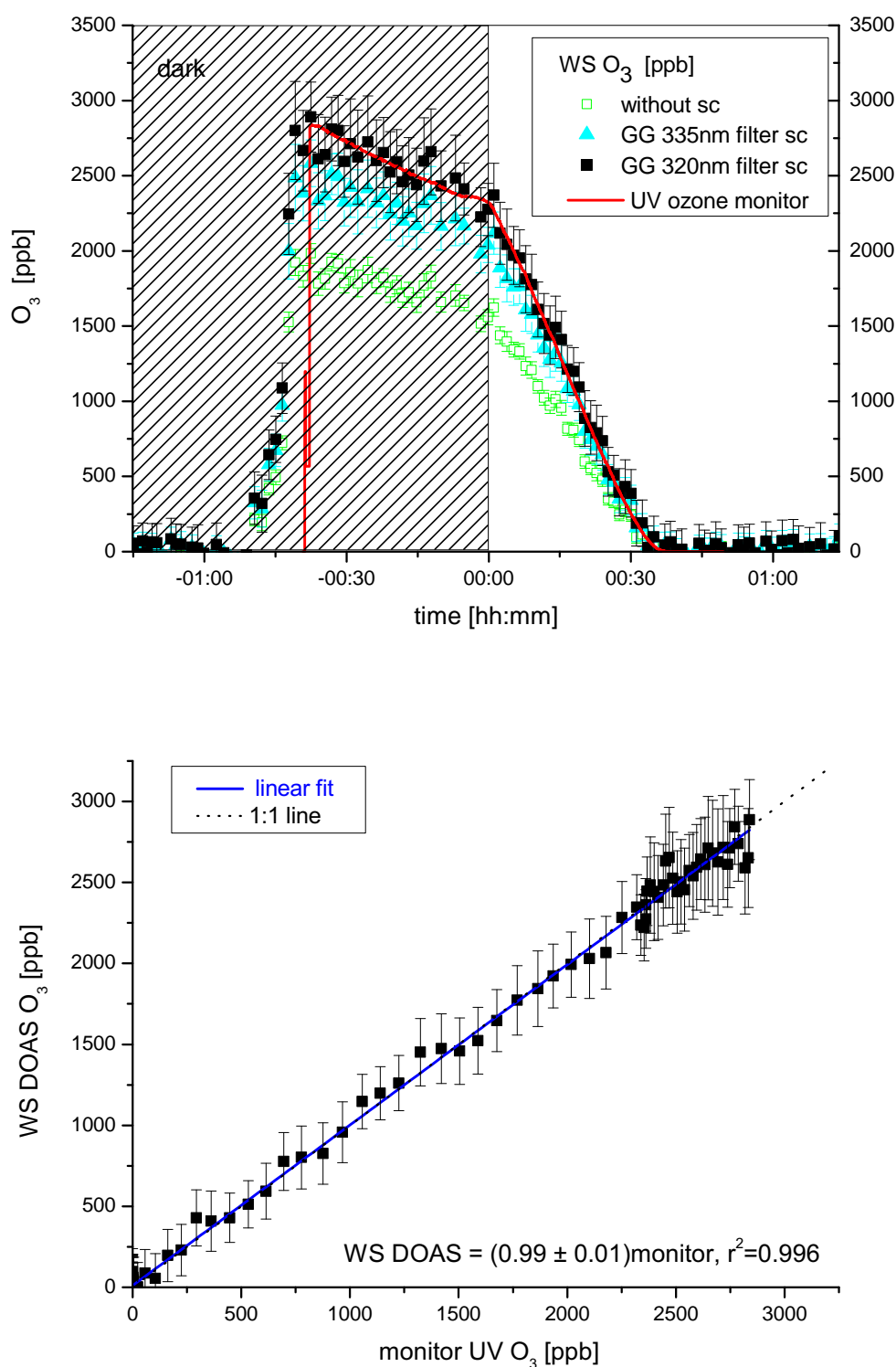


Figure 5.4.: Inter comparison of a time series of O_3 detected by the White-cell (aluminum coated mirrors) and the UV ozone monitor simultaneously during a sea salt aerosol smog chamber experiment. The UV monitor was switched on at $t=-37$ minutes. A stray light correction (sc) using different cut-off filters was applied to the White-cell data. Without sc the DOAS data underestimates the O_3 mixing ratio. Both instruments show a excellent agreement, after sc with GG 320nm in combination with UG11.

monitor, as shown in figure 5.4. Using a straylight correction with the GG335nm filter, O_3 mixing ratios are still underestimated by 11%. After the straylight correction is performed with the GG320nm, the WS DOAS shows a very good agreement with the UV ozone monitor.

5.1.3. Comparison of White System and NO_x Monitor

During some smog chamber experiments with sea salt aerosols, large amounts of NO_2 (up to 150ppb) were injected. A comparison CL with a blue light converter and the WS with aluminum coated as well as dielectric coated mirrors is shown in figure 5.5 in the form of a time series (experiment AEhNO_x2 and DNO2c). The light path of the WS is 288m and 32m with the dielectric and the aluminum coated mirrors, respectively. Both instruments show qualitatively the same decrease of NO_2 , which were caused by its reaction with O_3 and aerosol uptake. A quantitative correlation analysis of the instruments was not possible. The CL switches between NO and NO_2 (conversion to NO by photolysis), and takes a 10s running mean of the data. The analog signal was logged every second by a LabVIEW program written by S.Bleicher [2012]. The CL time series shows a step-like shape, but the response function is unknown. It is obvious that the step function is not caused by chemistry rather than software or internal hardware (e.g. a running mean) issues. Thus a direct correlation of the data is not reliable. However the time series of both instruments are in good agreement (fig. 5.5).

5.1.4. Comparison of White System and LOPAP

An experiment comparing HONO measured by a two channel LOPAP and the WS DOAS instrument was conducted (experiment:HONOC). The dielectric coated mirrors were used and a light path of 288 m was achieved. The experiment started with 4-5 ppb HONO and a RH of $(2 \pm 2)\%$. HONO was produced from the reaction of a sodium nitrite solution with sulfuric acid (as described in chapter 3). A time series and a correlation plot of measurements from the two instruments is shown in figure 5.6. The mean of the two LOPAP channels is used and the time resolution of 105s represents the average time resolution of the two instruments. The RH was kept stable for 3h and 15 minutes, and HONO decreased with $(6.6 \cdot 10^{-5})ppb/s$ mainly due to dilution. During the first 75 minutes, wall effects dominate the HONO loss. The decrease is $(2.7 \cdot 10^{-4})ppb/s$ and $(1.1 \cdot 10^{-4})ppb/s$ according to the DOAS and LOPAP data respectively, until an equilibrium is reached. The LOPAP instrument takes in air at a distance of 1 cm from the wall inside the chamber. A concentration gradient with decreasing HONO mixing ratios towards the wall are likely to cause smaller values than those measured with the DOAS instrument. The WS DOAS light path is diagonal through the chamber, and the concentration is averaged over the whole light path. It is important to note that a strong wall loss, can cause higher

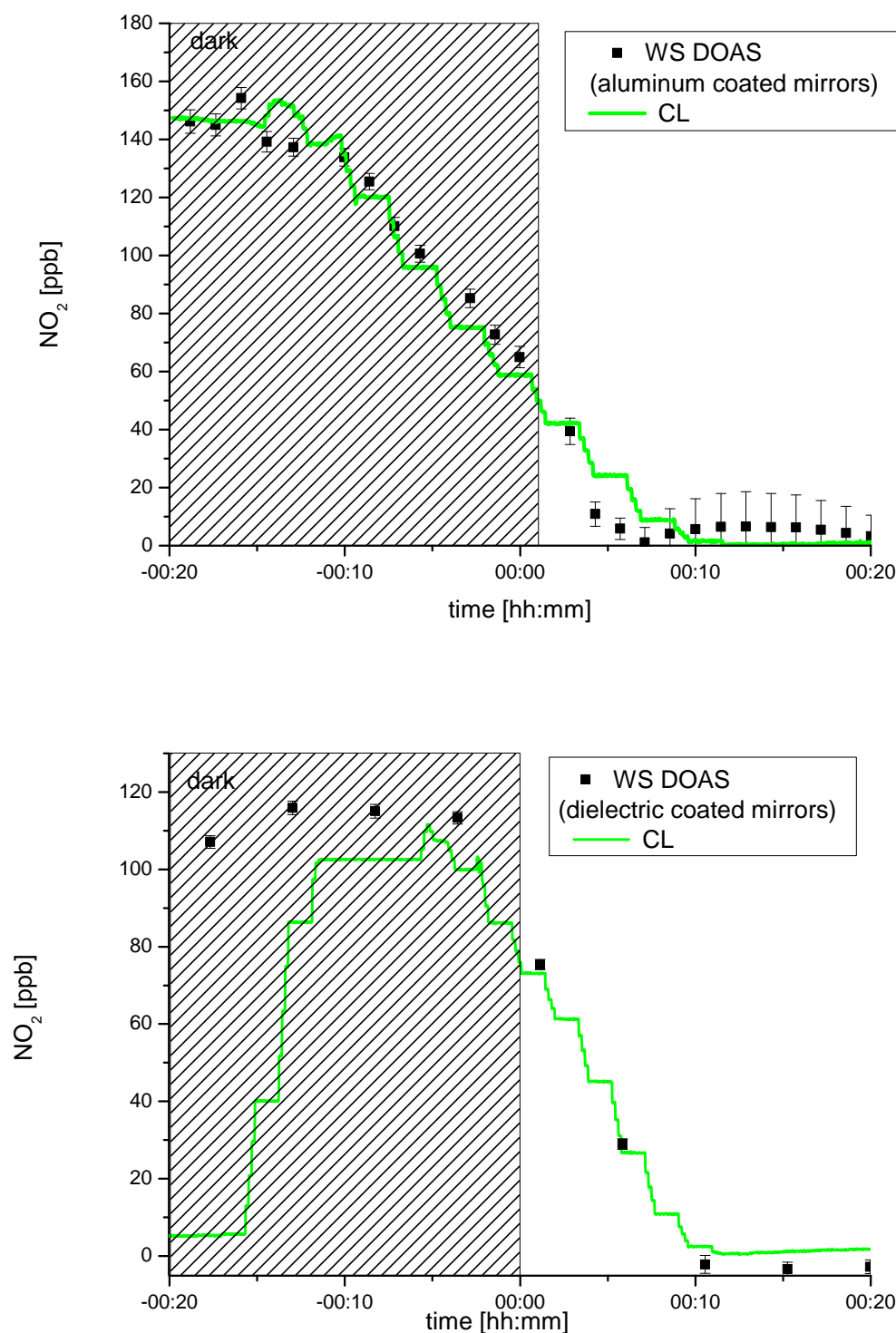


Figure 5.5.: A comparison of two time series of NO_2 during a sea salt aerosol smog chamber experiment. NO_2 was detected by a CL monitor after photolysis and the WS with aluminum coated (top) and dielectric coated (bottom) mirrors, with 32m and 288m light path, respectively. Measured NO_2 decrease from both instruments show good agreement, although a correlation was not possible due to an unknown response function of the CL.

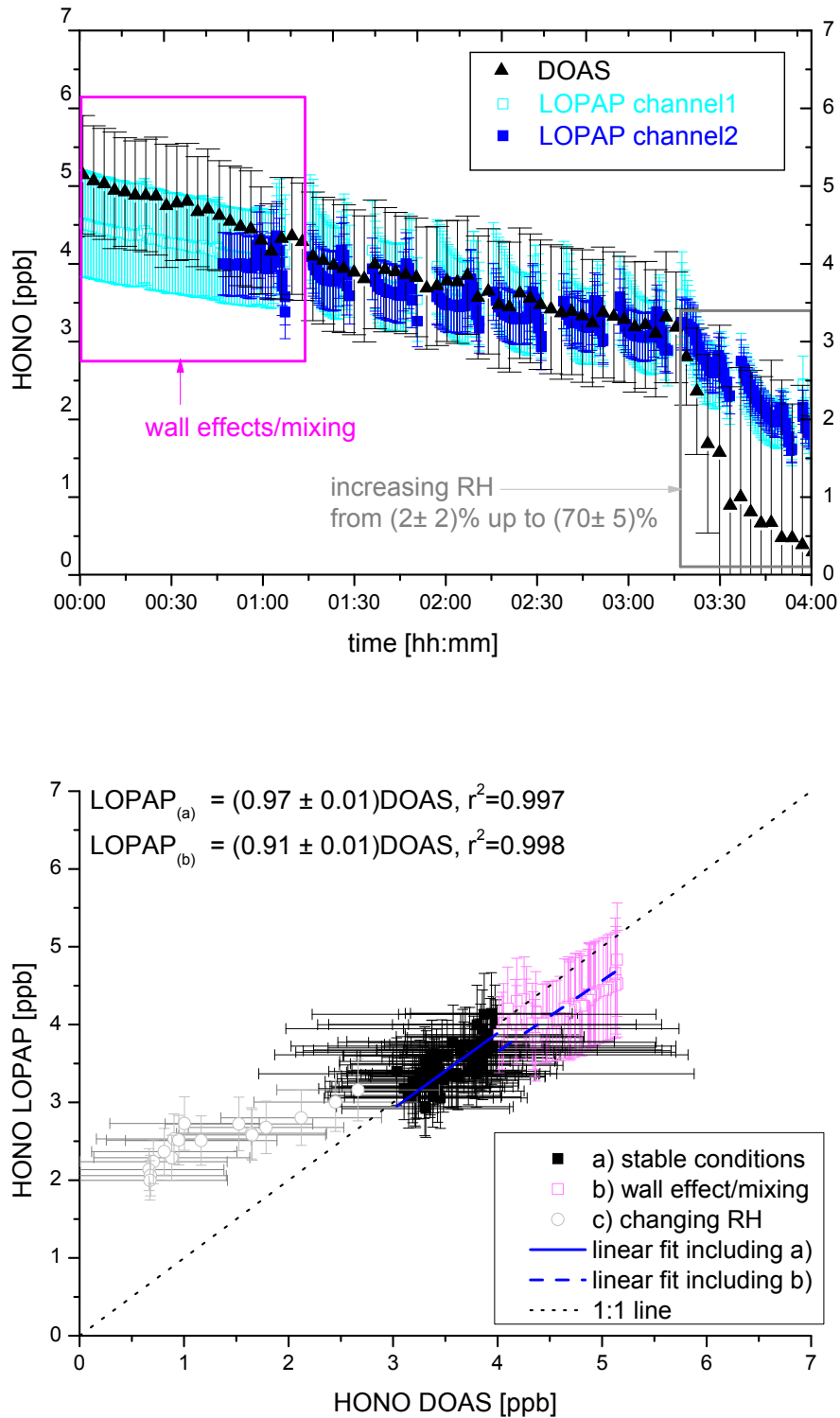


Figure 5.6.: Comparison of a time series of HONO detected by the White-cell (dielectric coated mirrors) and a LOPAP instrument simultaneously. At the beginning of the experiment, a gradient with decreasing concentrations towards the wall caused slightly lower values detected by the LOPAP (pink open squares). At stable RH of 2% – 4% (between 1:15 h and 3:15h), the instruments show a very good agreement. When the RH is increased up to $70 \pm 5\%$ (grey open circles), the DOAS fit failed, due to changing mirror reflectivity and resulting large measurement errors.

Table 5.2.: Overview of the salt pan experiments shown in this thesis. The WS system was used and no aerosols were injected. For details of the fit-setting see table 4.1 in chapter 4.

name	RH[%]	light path	fit-setting
blank	53-72	320m	DeRHh
SP2RH	2	320m	DeRHl
SP37RH	2	320m	DeRHh
SP60RH	60	320m	DeRHh
SP68RH	68	320m	DeRHh

mixing ratios (here a factor 1.17 on average) compared to a point measurement close to the chamber wall. Therefore a linear fit including values up to 75 minutes after start, has a slope of 0.91 ± 0.01 and $r^2 = 0.998$. Considering data between 75 and 195 minutes, the two instruments show a very good agreement with a slope of 0.97 ± 0.01 and $r^2 = 0.997$. This is comparable to a former intercomparison of DOAS and LOPAP instruments in the EUPHORE smog chamber [Kleffmann *et al.* 2006]. After 3 hours and 15 minutes the RH was increased from below 5% to about 70%. It was not possible to obtain a reliable fit for the WS spectra, due to humidity dependent changes in the mirror reflectivity during that time. The fit setting DeRHl, was used for all RH. Variation of the fit range for RH \geq 25%, did even increase the residual structures, as the reference spectra was taken at a low RH(\approx 5%). The data is shown here to emphasize that stable RH conditions are crucial for this kind of measurement set up. These problems can be solved in future, as now mirror coatings exist, without dependency on humidity. However the intercomparison of a LOPAP and the White-system shows good agreement under stable RH conditions and underlines the influence of occurring wall effects.

5.2. Salt Pan Experiments

The first question was whether we are able to observe a BE and how intense the explosion would be. Strong BrO signals were observed after adding 120-370 ppb O₃ and exposing the model salt pan, containing 100.3g of the NaCl/NaBr sample, to simulated sunlight. Rapid depletions of ozone were observed concurrent to the BrO release. This confirms the rapid catalytic O₃ destruction by Br and BrO (see introduction section) and underlines the important role of bromine chemistry. The content of this section is already published in [Buzmann *et al.* 2012].

5.2.1. Bromine Explosion Time Series

A blank experiment was performed, using 100 g of pure NaCl (Aldrich 99+, containing a trace impurity of 5.82 mg/kg Br according to our own analysis by ICP-MS). We observed no BrO above a mean detection limit of 54 ppt at a RH of 53% - 70%. Ozone was introduced at a level of 150 ppb, and the lifetime of ozone was calculated to be 34 hours, identical to the dilution rate of the chamber, $8.1 \cdot 10^{-6} s^{-1}$, obtained from the time profile of n-perfluorohexane, while the solar simulator was switched on.

As mentioned in section 2, the RH is supposed to have a strong influence on the BE process. The RH was varied from dry conditions of 2% to 37%, which is below the deliquescence point of NaBr of 59% [Geenspan 1977], to a set of repeated experiments at a RH of 60% and 68%, which is above the deliquescence point of NaBr but below that of NaCl (75% RH, [Tang and Munkelwitz 1993]). The BrO time series of four typical BE experiments (two of them repetitive) at different RH are shown in figures 5.7, 5.8 and 5.9 and will be discussed below. At a RH of 2% a sharp peak with a BrO mixing ratio of up to 530 ± 70 ppt 5.7 within the first minutes was followed by a rapid decrease, indicating that the halogen source is depleting rapidly. OH was close to the detection limit and Cl was below. Then a slower decrease of BrO from 230 to finally 100 ppt occurs until the solar simulator is switched off and BrO disappears.

At a RH of 37% there is an initial formation of 431 ± 65 ppt of BrO, and we observe a maximum mixing ratio of 706 ± 52 ppt 5.8 after 45 minutes. As shown in Figure 6 below, during this experiment the concentration of OH-radicals was calculated to be $3.5 \cdot 10^7 molecules cm^{-3}$. A build-up of Cl radicals with a maximum concentration of $(8 \pm 5) \cdot 10^7 molecules cm^{-3}$ within 2.5 hours was observed as shown in Figure 5.11 below. This confirms previous studies, reporting that the Br₂ release is favored [Behnke et al. 1999, Fickert et al. 1999]. As soon as the Br/Cl ratio is low enough, BrCl is formed and released into the gas phase as a source of atomic Cl.

At RHs of 68 and 60% the salt pan from the experiment at 2% RH was exposed twice each day on two subsequent days to ozone and simulated sunlight. As shown in figure 5.9, we observed a total of 4 BEs in repetition with extremely rapid depletions of O₃ and very fast build-ups of BrO where the third exposure and irradiation delivered a maximum BrO mixing ratio of 6419 ± 71 ppt after 160 seconds, corresponding to an initial rate of $\frac{d[BrO]}{dt} = 40 ppt/s$. The initial concentration of OH-radicals derived from the measured HC-decay at 68% RH was about $5 \cdot 10^7 molecules cm^{-3}$ (as obtained from not more than three gas chromatograms each during the short time span of interest). No Cl-radicals were found above a detection limit of $2 \cdot 10^4 molecules cm^{-3}$. An undesired 20 times higher injection of n-butane in the run at 60% RH interfered with a useful evaluation of OH and Cl. The maximum BrO mixing ratios at 60% and 68% RH are almost one order of magnitude higher

than at 37% RH. The frequency of O_3 determinations was too low in figure 5.9 for a proper monitoring of the rapid consumption of this species. However, in the second exposure of figure 5.9 we succeeded in observing a complete profile of O_3 in parallel to BrO by delaying and blocking the baseline check of the O_3 analyzer appropriately. A more detailed description and discussion of the behavior of O_3 and BrO is presented below in the section 'Recovery of the BrO source and behavior of O_3 '. Note that there might be a background level of BrO at the beginning (Figure 5.7-5.9, before the solar simulator was switched on), although spectral structures of BrO could not be unambiguously identified. This is a hint at a minor formation of BrO in the ozone-rich air by the analyzing Xe light source that might photolyse a bromine-containing precursor, accumulating during the initial dark phase of the experiment.

5.2.2. Recovery of the BrO Source and Behavior of O_3

The recovery of BrO formation rate after an initial strong decline within each experiment has been investigated at RHs of 60% and 68% and was illustrated in figure 5.9. In the first run, exposing the salt sample from the experiment performed at 2% RH to 68% RH, we injected 230 ppb of O_3 and reached a sharp peak of BrO of 4158 ± 57 ppt immediately (within 176 s) after switching the solar simulator on (see Figure 5a). In the following monotonic decay, BrO continued in a minor shoulder and then vanished. Ozone disappeared rapidly in the presence of simulated sunlight, but a small, significant level of O_3 remained left over. After 5400 s we switched the solar simulator off and injected 180 ppb ozone 3600 s later. After another 1920 s we switched the solar simulator on again and observed another steep rise of BrO to 1800 ± 60 ppt within 172 s but with a much more pronounced shoulder. Ozone disappeared again, down to a similar, significant level, slightly higher than after the previous light exposure. In the second run the next day (5.9, after flushing the chamber and using the same NaCl/NaBr sample again), we injected 340 ppb ozone at 60% RH and switched the solar simulator on. This time we observed a very steep increase of BrO to 6419 ± 71 ppt within 207 s, decreasing rapidly via a minor shoulder similar to the previous day. Ozone was consumed almost completely to 17 ppb within 1200 s, and after 1380 s we switched the solar simulator off. Then we replenished ozone immediately to 370 ppb, and the salt pan was left in the dark for 1500 s. Subsequently the solar simulator was switched on for another 2460 s, and O_3 decreased within 1200 s to just 34 ppb. BrO increased immediately in the presence of light to 3240 ppt within 227 s and then showed a well-separated shoulder with a maximum of 4200 ± 63 ppt. It should be noted, that the time profiles of O_3 show an unusual instability, in contrast to the smooth BrO profiles. A reason for this instability might be insufficient mixing, competing with rapid consumption of O_3 . Any inhomogeneous distribution of active bromine in the chamber may enhance the impact on the self-destruction of O_3 , even more so by the quadratic dependence of

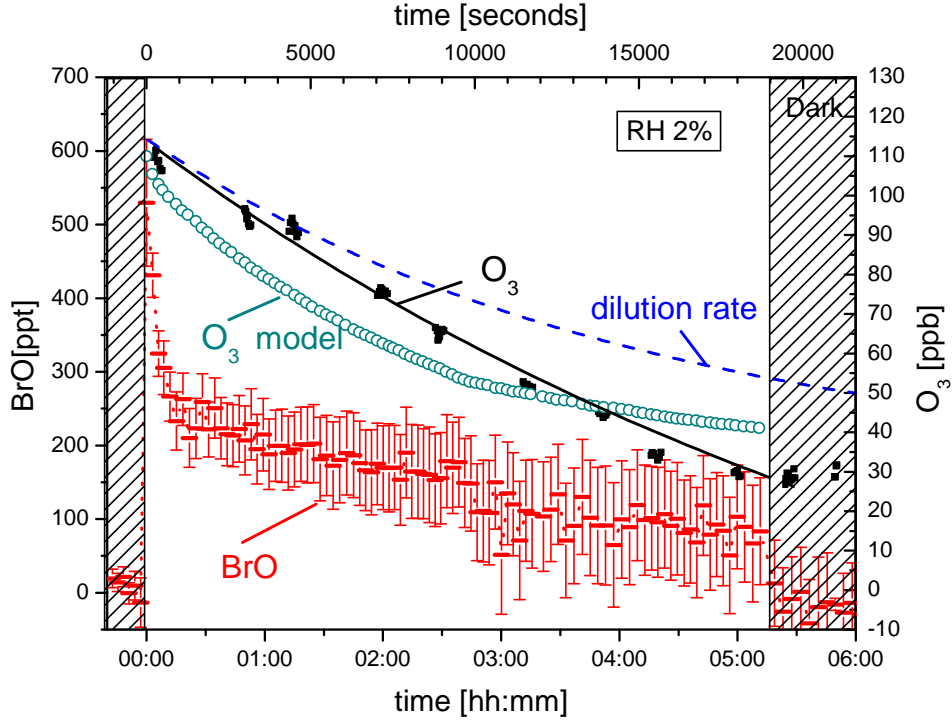


Figure 5.7.: Experiment at 2% RH: The solar simulator was switched on at $t=0$. BrO appears as an initial sharp maximum of 530 ± 70 ppt within 180 s, merges into a photostationary value of about 220 ppt, reached within 1160 s, and then decreases exponentially to about 100 ppt until the solar simulator is switched off at $t = 19000$ s. Due to a spectral shift a second reference spectrum was included in the evaluation after the solar simulator was switched off. Instead of an exponential decay (solid curve), the consumption of O_3 can be described fairly well by a constant decrease of about 0.005 ppb/s during the whole irradiation period. The ' O_3 model' is simply based on the self reaction of BrO alone (see below) and does not consider dilution. The dilution rate in this experiment was $3.6 \cdot 10^{-5} s^{-1}$. (adapted from *Burmann et al.* [2012])

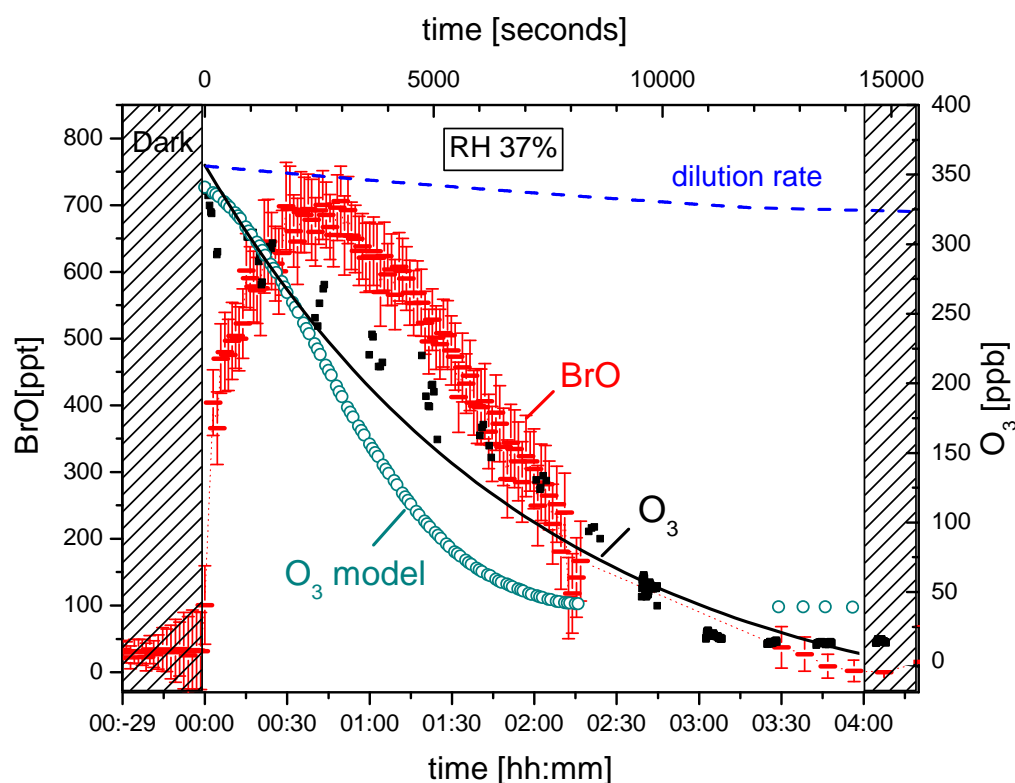


Figure 5.8.: Experiment at a RH of 37%: The solar simulator was switched on at $t=0$ and switched off at $t=14400s$. BrO is formed rapidly under irradiation (431 ± 65 ppt within 183s), reaches a maximum photostationary state of 706 ± 52 ppt within 45 min and decreases to less than 200 ppt after 2 hours. A linear decrease of O_3 by 0.03 ppb/s is observed during the irradiation by the solar simulator, and an exponential (solid curve) does not properly fit the observations. The " O_3 model" is simply based on the self reaction of BrO alone (see below) and does not include dilution. The dilution rate was $3.1 \cdot 10^{-5} s^{-1}$. (adapted from *Buzmann et al.* [2012])

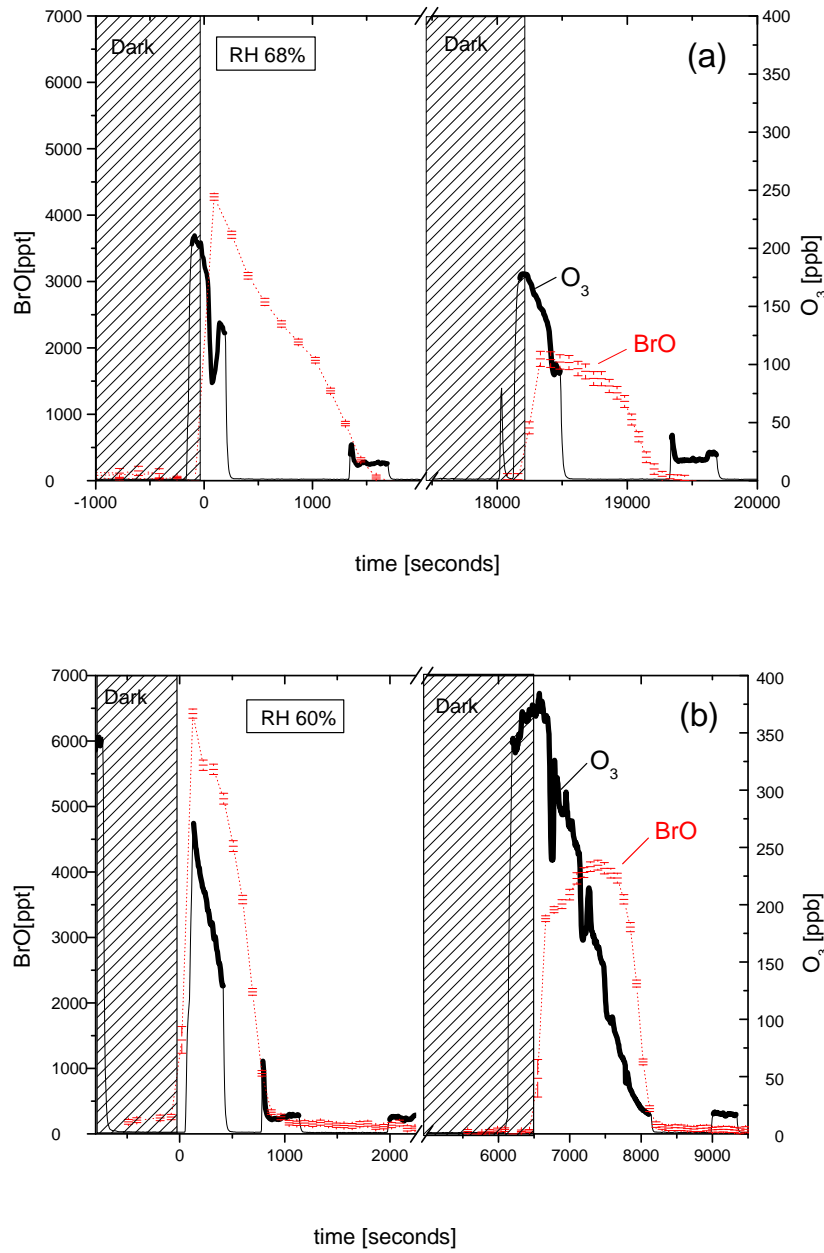


Figure 5.9.: Repeated experiments at RH of 68% (a, top) and 60% (b, bottom) on the same salt sample: A smaller amount of BrO was formed each after replenishing ozone and switching the solar simulator on a second time. Note that at 68% RH less ozone was injected (230 ppb and 180 ppb, respectively) and the solar simulator was switched off at 5400 s after the first exposure of this day. The next day, the same salt pan sample was exposed at 60% RH and 340ppb and 370 ppb ozone were injected and the solar simulator was switched off at 1260 s. In order to reduce dilution, measurements of O₃ were performed only for limited periods of time (thick black line), while purified air was measured in between (thin black line). Again the simple model cannot explain the measured ozone destruction at the detected BrO mixing ratios. (adapted from *Buxmann et al.* [2012])

BrO loss in equation 2.88. The BrO signal does not show these instabilities since it is averaged diagonally over the chamber - in contrast to the sampling tube of the ozone analyzer, localized close to the wall.

5.2.3. OH Radical Concentrations from Hydrocarbon Clock Data

As we still have trace impurities of NO_x in our chamber, OH radicals can also be formed by photolysis of HONO (photolysis frequency of $J_{HONO} = 1.3 \cdot 10^{-3} s^{-1}$) (see reaction 2.8). The CL detector showed values for $NO < 2 ppb$ and NO_x up to 10 ppb. It should be noted that the Teflon tubing between the chamber and the analyzer had a volume of about 100 ml, so NO can react with ozone within the tubing to form NO_2 before reaching the analyzer. Both NO_2 and HONO were included into the fit procedure of the DOAS analysis but were not identified above the mean detection limits of 3 ppb for NO_2 and 38 ppb for HONO. Due to reaction 2.6 and HONO production from the reaction of NO_2 with liquid water, the OH concentration is strongly influenced by the absolute H_2O concentration (number density). The H_2O concentration is proportional to RH, as our cooling system kept the temperature constant at 20°C. But the O_3 concentration still plays a major role for OH balance because of the very high initial mixing ratios of up to 340 ppb. Other possible sources are formation of OH from photolysis of formaldehyde, which is a source of HO_2 and an expected degradation product from reactions of the injected HC_i with OH. However, formaldehyde was not detected above a mean detection limit of the DOAS system of 52 ppb, and the UV spectra of other aldehydes and ketones are broad in this range [Keller-Rudek and Moortgat] and thus not appropriate for detection by DOAS.

The concentrations of OH at RH of 2%, 37% and 68% are compared in figure 5.10. At a RH of 2% the OH concentration was the smallest with an initial level of about $0.5 \cdot 10^7 molec cm^{-3}$ and a slow decrease with time in parallel with the decrease of ozone. At RH of 37% the concentration of OH increased within the first 6,000 s after the solar simulator was switched on and reached its maximum later than BrO. The rapid decrease of OH at RHs of 68% is closely correlated with the simultaneous decrease of O_3 . The initial O_3 mixing ratio was 230 ppb in the 1st exposure to light and O_3 and 180 ppb in the 2nd exposure at 68% RH, which probably explains the higher maximum OH concentration for 68% RH 1st as compared to 68% RH 2nd.

5.2.4. Chlorine Radicals

The only experiment where chlorine atoms could be detected was at 37% RH (Figures 5.8, 5.11). The time series shows an increase of up to $(8 \pm 5) \cdot 10^4$ molecules cm^{-3} , and the presence of Cl leads to the formation of ClO by the reaction with ozone via reaction 2.50.

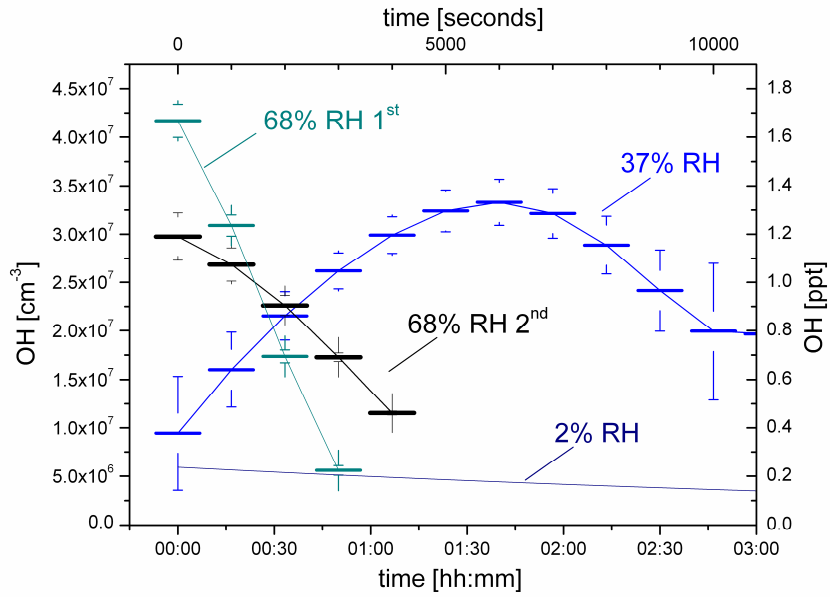


Figure 5.10.: Comparison of OH time series at RH of 2%, 37%, and 68% (for first and second exposure to light and O_3), respectively. The solar simulator was switched on at time = 0 during salt pan experiments. The length of the OH data bars represents the time between the GC-FID data of the $[\text{HC}_i]$, used for our indirect determination. The connecting lines are guides to the eyes, and the solid curve at 2% RH is the first derivative of an exponential fit to the time integrals. (adapted from *Burmann et al.* [2012])

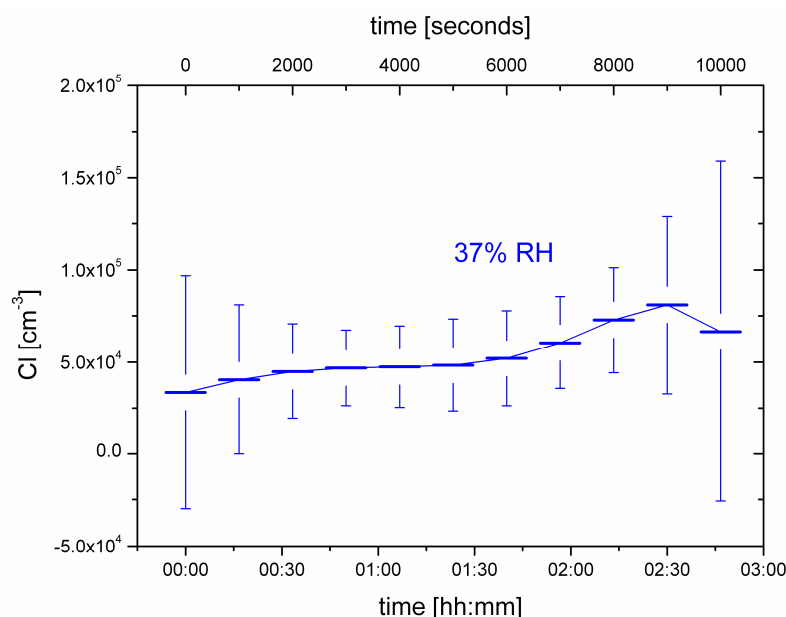


Figure 5.11.: Cl time series at RH of 37%. The solar simulator was switched on at time = 0 during a salt pan experiment. The solid line connects the data as a guide to the eye.(adapted from *Buxmann et al.* [2012])

Since ClO absorbs in the wavelength range below 310 nm, no direct detection by DOAS with the dielectric mirrors was possible during the present experiments, but an estimate of ClO can be made from the measured Cl radicals. New ozone formation as mentioned in section 2.3 can be neglected because of the small concentration of atomic Cl, considering the measured and calculated concentrations (table 5.3). According to equation 2.90, an expected ClO concentration was calculated using the initial concentrations of $[Cl] = 3.5104 \cdot \text{molecules cm}^{-3}$, $[NO] = 2 \text{ ppb}$, $[BrO] = 400 \text{ ppt}$ and $[O_3] = 290 \text{ ppb}$ observed during the 37% RH experiment. This leads to a ClO concentration of $3.3 \cdot 10^6 \text{ molecules cm}^{-3}$ (or about 0.13 ppt).

It is also possible to estimate an upper limit for the expected OClO concentration. An upper limit for the OClO mixing ratio using the maximum calculated ClO concentration according to equation 2.92 was estimated.

This relation delivers $[OClO] < 4.8 \cdot 10^6 \text{ molecules cm}^{-3}$ for maximum $[ClO] = 4 \cdot 10^6 \text{ molecules cm}^{-3}$ and $[BrO] = 400 \text{ ppt}$ (just a few seconds after the solar simulator was switched on at 37%RH), far below the mean detection limit of OClO of 90 ppt or $2.3 \cdot 10^9 \text{ molecules cm}^{-3}$ of the WS DOAS instrument. Those ClOx concentrations are more than 4 orders of magnitude lower than those of BrOx. Additionally Cl radicals react very fast with the injected HC_i . Therefore the cross reactions are less important compared to 2.26) in terms of O_3 depletion.

Table 5.3.: Overview of experiments at different RH and initial ozone concentrations, listing maximum BrO and Br mixing ratios and concentrations of OH and Cl. ^aConsidering Br alone in the light-induced ozone loss as a simplified estimate. ^bThe pre-concentrator of the GC-FID partly failed in these experiments. ^cExperiment repeated 1 day after the run at 68% RH using the same salt sample. ^d*n*-Butane was injected at 20 times higher level, perturbing the observation of other compounds. ^eSalt pan exposed a second time to ozone and simulated sunlight during the same day.

RH [%]	[O ₃ _{initial}](ppb)	[BrO] _{max} (ppt)	[Br] ^a	[Cl](cm ⁻³)	[OH](cm ⁻³)
2	120	530 ± 70	3	— ^b	0.5 · 10 ⁷
37	290	706 ± 50	22	8 · 10 ⁴	3.5 · 10 ⁷
60	340 ^c	6419 ± 71	144	— ^d	— ^d
60	370 ^{c,e}	4200 ± 63	142	— ^d	— ^d
68	230	4158 ± 57	81	< 4 · 10 ¹⁴	3 · 10 ⁷
68	180 ^e	1800 ± 60	111	< 3 · 10 ⁴	5 · 10 ⁷

5.2.5. Simple Reaction Kinetic Model for O₃

The lifetime τ of O₃ was calculated by using an exponential fit to the measured ozone time series (figures 5.7, 5.8 and 5.9). For RH of 60% and 68%, 37% and 2% τ was <500 s, 7230 s and 24030 s respectively. The loss rate of ozone can be approximated as the rate-limiting step of the BrO-BrO self-reaction (reaction 2.26) according to equation 2.88.

A time profile O₃(t) was modeled using the measured BrO and the initial O₃ mixing ratio. The results are included in figure 5.7 and figure 5.8 above for 2% RH and 37% RH, respectively. In spite of the simplicity of these calculations, neglecting the dilution completely, the agreement for 2% RH and 37% RH is surprisingly good: On the other hand, at 68% RH with [BrO]_{max} = 4158 ± 57 ppt, the simple model gives an ozone depletion rate of 2 ppb/s compared to the measured loss rate of 0.4 ppb/s and at 60% RH with [BrO]_{max} = 6419 ± 71 ppt the calculated O₃ depletion would be 5 ppb/s, which is more than six times faster than the measured O₃ loss rate of 0.8 ppb/s. This means that O₃ would have been consumed after 120 s and 70 s for 68 % and 60% RH, respectively. We have no explanation for this finding so far. One explanation could be side reactions with NO_x or hydrocarbons, which are not yet included in this simple model. It should be noted that irradiation of the Teflon chamber in blank experiments delivered photochemical ozone production rates ($J_{NO_2} = 6.3 \cdot 10^{-3} s^{-1}$) up to 30 ppb/h [Bleicher 2012], which decreased to about 10 ppb/h after the FEP material had experienced several chamber runs. These production rates are thought to arise from NO_x, stored in the material, and NO_x from outside air, permeating through the FEP film.

Table 5.4.: Overview of the sea salt aerosol experiments shown in this thesis. The WS system was used and different amount of initial nitrogen dioxide were injected, marked as $NO_{xl}=0ppb$ and $NO_{xh}=150ppb$. For details of the fit-setting see table 4.1 in chapter 4.

Experiment	RH[%]	light path	fit-setting
AeNOxl86NaBrHC	60-70	288	DeRHh
AeNOxl86NaBr	60-70	288	DeRHh
AeNOxl7.6NaBr	60	288	DeRHh
AeNOxh760oz	60	32	AlBrO, AlClO
AeNOxh2800oz	60	32	AlBrO, AlClOU

5.3. Sea Salt Aerosol Experiments

There are several factors that may affect the release of Br and Cl from sea salt aerosol. One major factor, is the concentration of Bromine and the NaBr/NaCl ratio, which was analyzed in detail by [Siekman 2008]). However, BrO molecules were never detected directly by the aforementioned authors. To further explore the importance of Br-content, two experiments at a Br concentration of 7.6 mg/l and 86.4 mg/l were compared; the NaCl concentration was 1g/l. Another question was how the HC from the radical clock method (chapter 3), which were used in the experiments before, influence the release of Br and Cl species. Therefore one experiment with injection of HC was performed. Most sea salt aerosol experiments were conducted without injecting HC, which are thought to inhibit the release of RHS.

NO_x is expected to play a further key role in RHS release. The understanding of the importance of the different path ways is not clear. Experiments with high concentrations of NO₂ (>100 ppb) at variable initial O₃ mixing ratio were undertaken, which is described in section 5.3.2. The relative humidity was of minor focus here, as the aerosols are already in an aqueous form (undergone deliquescence). To provide an aqueous surface of aerosols, the experiments were performed at relative humidities of 60-80% close to 76%, the deliquescence point of NaCl. Siekman [2008] showed that it is important to keep the RH above 39% (efflorescence point of NaCl), which is important for the release of halogenes from the salt aerosols [Siekman 2008].

5.3.1. Halogen Oxides from Sea Salt Aerosols at low NO_x

Three experiments with low mixing ratios of NO_x ($NO + NO_2 < 1ppb$) are described in this section. In one experiment, the artificial sea salt solution contained 7.6 mg/l NaBr and 1g/l NaCl (experiment: AeNOxl7.6NaBr). Two experiments were conducted using a 86 mg/l NaBr and 1g/l NaCl solution for the generation of the aerosols, one with injection of HCs and one without.

Experiment AeNOxI7.6NaBr

At a Cl/Br ratio of 100 by weight (7.6 mg/l NaBr and 1g/l NaCl), similar to seawater, a BrO peak of 150 ± 25 ppt was observed after 28 minutes of illumination. This is shown in figure 5.12. After one hour, the BrO mixing ratio dropped down to 40 ppt, followed by an increase up to 80 ppt after 90 minutes again. Ozone was injected at an initial level of 500 ppb, as discussed in more detail below. OClO was below the detection limit of 100 ppt during this experiment. No direct detection of ClO by the WS DOAS with the dielectric mirrors was possible during this experiment, as the absorption structures are below the reflectivity range of the mirrors ($< 320\text{nm}$). An upper limit for the expected ClO concentration was estimated based on the variation in the fitted OClO concentrations according to equation 2.92. This relationship yields an upper limit of $[\text{ClO}] < 200\text{ ppt}$. According to equation 2.90, an expected Cl concentration was calculated using the ClO concentration and detected O_3 . NO was assumed to be equal to the detection limit of 0.6 ppb. The maximum expected Cl concentrations were estimated to be 0.035 ppt.

Experiment AeNoxI86NaBr

Another experiment with a NaBr concentration of 86.4mg/l and NaCl of 1mg/l is shown in figure 5.13, including measured BrO, OClO, O_3 and NOx, as well as simple model calculations of ClO, Cl and O_3 (initial mixing ratio = 670 ppb). The maximum BrO mixing ratio of 450 ± 20 ppt was observed after 20 minutes. At this time, an increase in OClO mixing ratio was observed, reaching a plateau of 100 ± 35 ppt after 30 minutes, which lasted for another 30 minutes before the concentration slowly decreased. The BrO mixing ratio slowly decreased from 110 ± 30 ppt after 1 hour 40 minutes to about 90 ppt, and dropped below the detection limit again after the solar simulator was switched off at 2 hours 17 minutes.

After 1 hour 45 minutes of light exposure, OClO was below the mean detection limit of 70 ppt again. Ozone was introduced at an initial mixing ratio of 500 ppb, and an exponential decay of ozone with $\tau_{\text{O}_3\text{measured}} = 0.01\text{s}^{-1}$ was observed. Calculation the ClO mixing ratios from the observed OClO mixing ratio using equation 2.89, yields 290 ± 90 ppt in maximum. Cl mixing ratio, according to equation 2.90, remained below 0.07 ppt.

Experiment AeNoxI86NaBrHC

Another experiment using the same aerosol composition (86.4 mg/l NaBr and NaCl 1mg/l) was conducted. This time OH and Cl were measured using the hydrocarbon

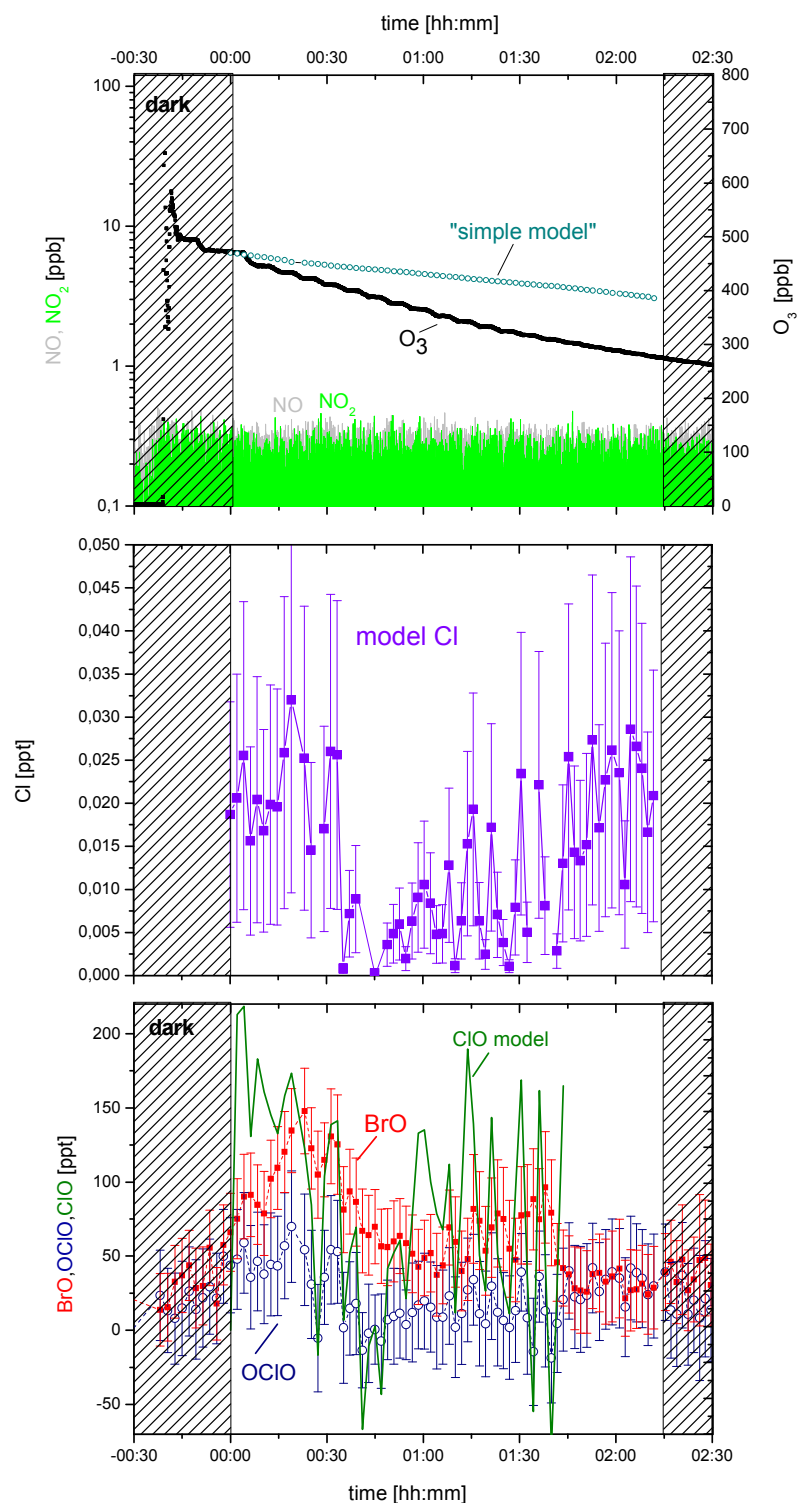


Figure 5.12.: AeNOx17.6NaBr: Sea salt aqueous aerosol experiment with 7.6 mg/l NaBr and 1g/l NaCl. Ozone, BrO and OCIO were measured. Modeled CIO and modeled Cl radicals, as well as the ozone time profile are shown. Error bars of the model CIO is not shown, for the sake of clarity.

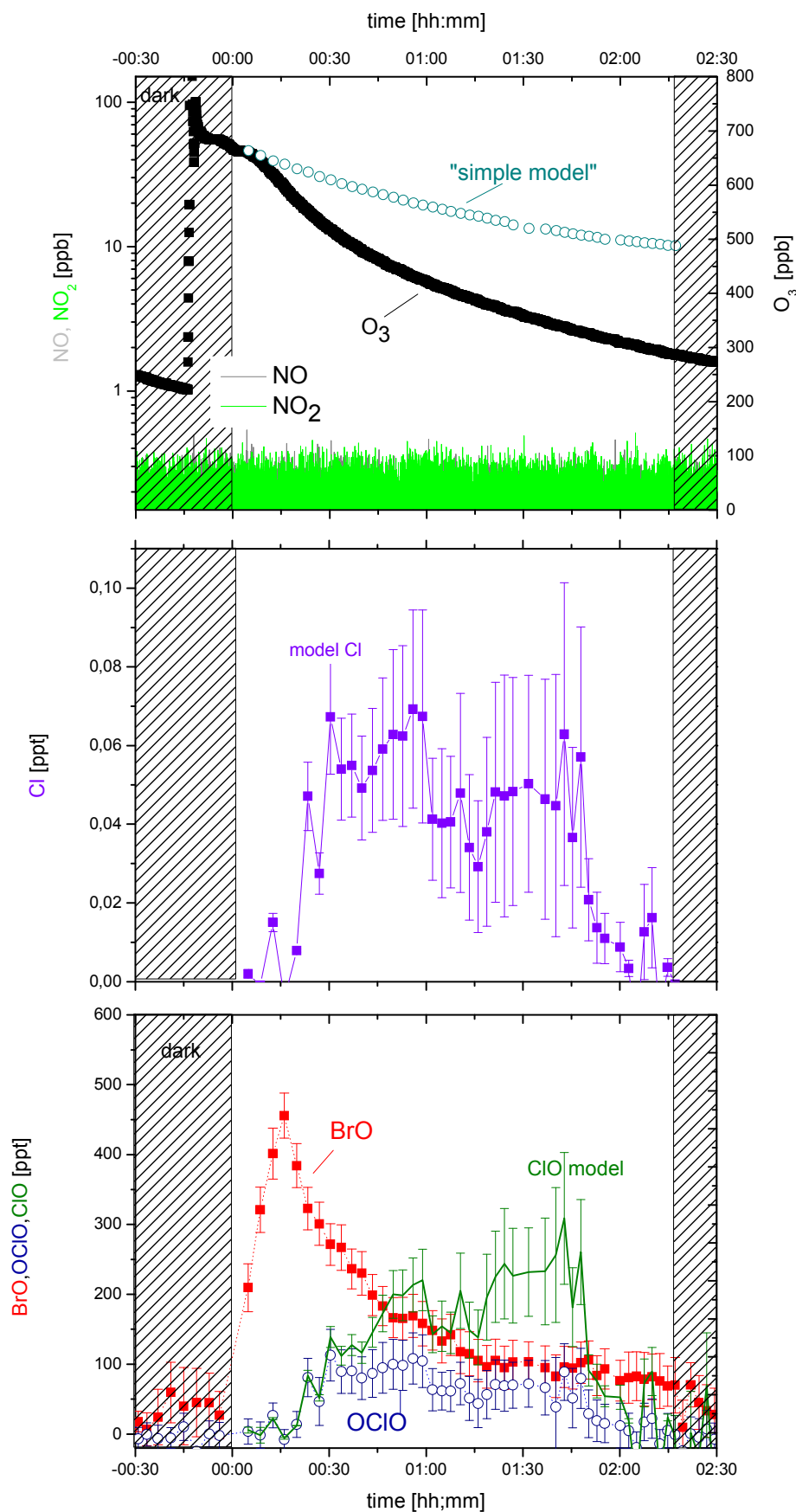


Figure 5.13.: AeNox186NaBr: Sea salt aqueous aerosol experiment with 86 mg/l NaBr and 1g/l NaCl. Ozone, BrO and OCIO were measured. Including modeled ClO and modeled Cl radicals a ozone time profile was modeled.

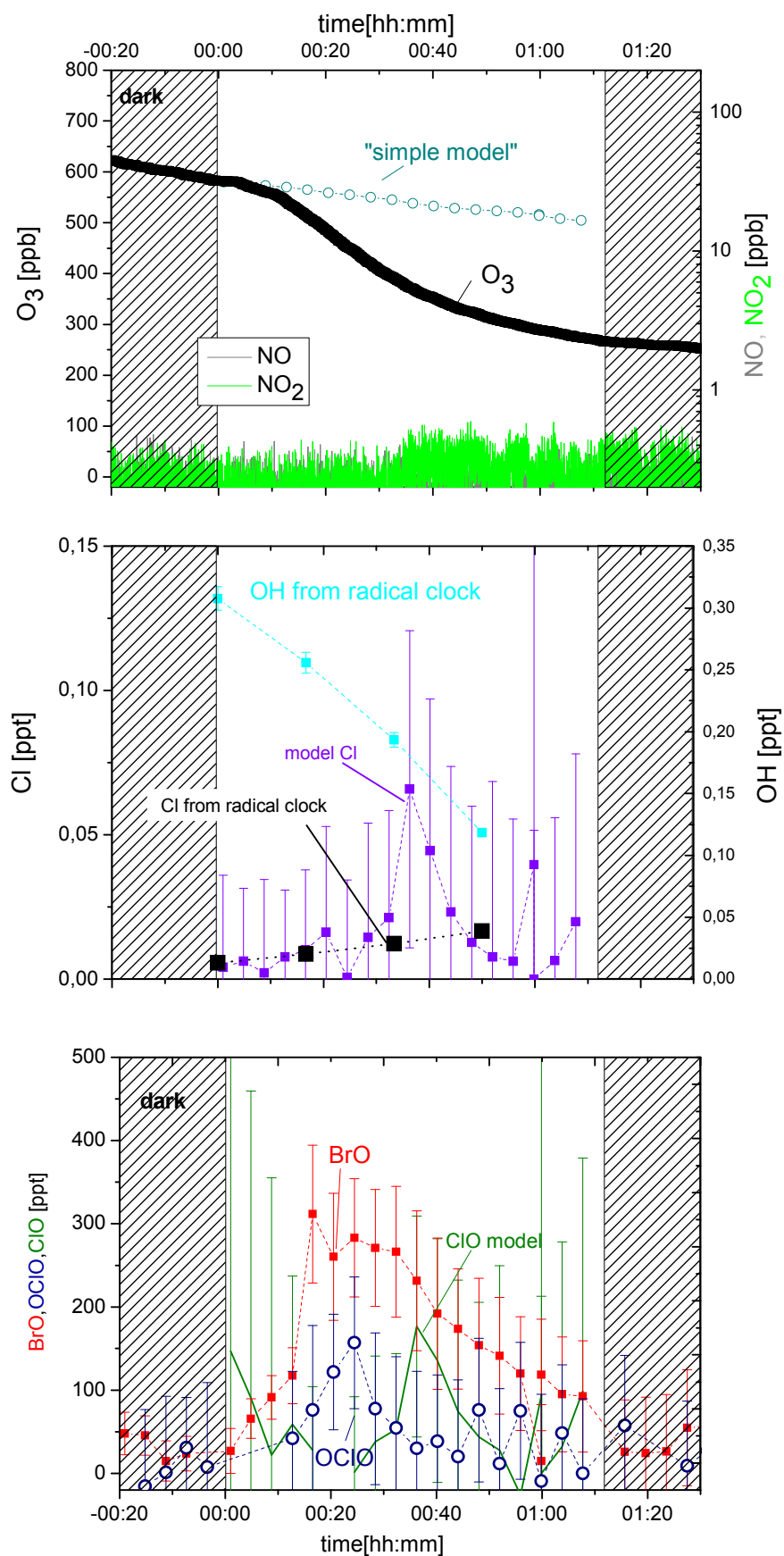


Figure 5.14.: AeNox186NaBrHC: Sea salt aqueous aerosol experiment with injected hydrocarbons at 86.4mg/l NaBr. Model Cl radical concentrations fit the measurement quite well. The simple model O_3 depletion is too slow to capture the measurement.

Table 5.5.: Overview of experiments at different initial ozone and nitrogen dioxide mixing ratios, including maximum BrO, ClO, OClO and Cl mixing ratios, as well as total aerosol surface (AS). ^a”Simple model” calculations. ^bObtained by radical clock method. ^cDetected by WS DOAS using the dielectric coated mirrors. ^dDetected by WS DOAS using the aluminum coated mirrors. ^eCNC was not operational during this experiment, due to a lack butanol.

AS ($10^{-5} \frac{cm^2}{cm^3}$)	[NO ₂] _i (ppb)	[O ₃] _i (ppb)	[ClO] _{max} (ppt)	[OClO] _{max} (ppt) ^a	[BrO] _{max} (ppt)	[Cl] _{max} (ppt)
3.1	0	500	<200 ^a	<100 ^c	150 ± 30 ^c	0.03 ± 0.01 ^a
7.5	0	670	290 ± 90 ^a	100 ± 35 ^c	450 ± 20 ^c	0.07 ± 0.03 ^b
9.8	0	600	180 ± 120 ^a	150 ± 50 ^c	340 ± 30 ^c	0.07 ± 0.04 ^b
8	150	760	4100 ± 500 ^d	6900 ± 150 ^d	833 ± 100 ^d	6 ± 1 ^a
- ^e	150	2800	17700 ± 1000 ^d	6300 ± 200 ^d	1600 ± 100 ^d	90 ± 10 ^a

clock method, as described in chapter 3. The trace gas measurements, including the simple model calculations are shown in figure 5.14. The initial O₃ mixing ratio was 600 ppb. The absolute value the maximum BrO mixing ratio of 340±25 ppt was lower in this experiment, than without HCs. However, the maximum BrO mixing ratio was observed after 20 minutes of light exposure, at a similar time as in the experiment without HC. An exponential fit yielded a life time of $\tau_{O_3measured} = 0.01s^{-1}$. From the radical clock method, it was possible to calculate the OH and Cl radicals from the decay of the HC_i . This is shown in figure 5.14. According to equation 2.89 the concentration of ClO can be calculated, which is also shown in figure 5.14. The simple model calculation leads to a mean Cl mixing ratio of 0.2±0.3 ppt. The large error results from the uncertainty in the OClO data, which was close to the detection limit of 100 ppb. The Cl radical simple model calculation, represents an upper limit. However the indirectly observed Cl radicals increased from 0.005 ppt to 0.016 ppt, which is in good agreement with the simple model. The radical clock provides integrated values with a time resolution of 1000 s (16minutes) during this experiment. Therefore it does not capture variability at a higher frequency, as indicated by the simple model.

Aerosol Distribution

The aerosol number distribution of the sea salt aerosols by size was measured by the EC-CNC (electrostatic classifier, condensation nuclei counter) combination as described in chapter 3. The charge correction for for the EC was done within the work described in *Bleicher 2012*. As explained in chapter 3, the aerosol surface area is crucial for heterogeneous release processes of halogens. The characteristic size

distributions of sea salt aerosols are shown in figure 3.4. The maximum diameter was between 300-400nm. The total particle number was 53000 for the experiments without HCs and 38000 for the experiment with HC injection. The aerosol surface area is given in units $10^{-5}\text{cm}^2/\text{cm}^3$ and the volume in $10^{-10}\text{cm}^3/\text{cm}^3$. In the experiment with a 7.6 mg/l NaBr solution, the surface area was 3.1 and the volume 1.8. In the 86.4mg/l NaBr experiment, the aerosols provided a surface area of 7.5 and a volume of 4.2. The largest surface area was observed in the experiment, where we injected HC, with a surface of 9.8 and a volume of 5.7. The influence of the surface area will be discussed in the chapter 7.

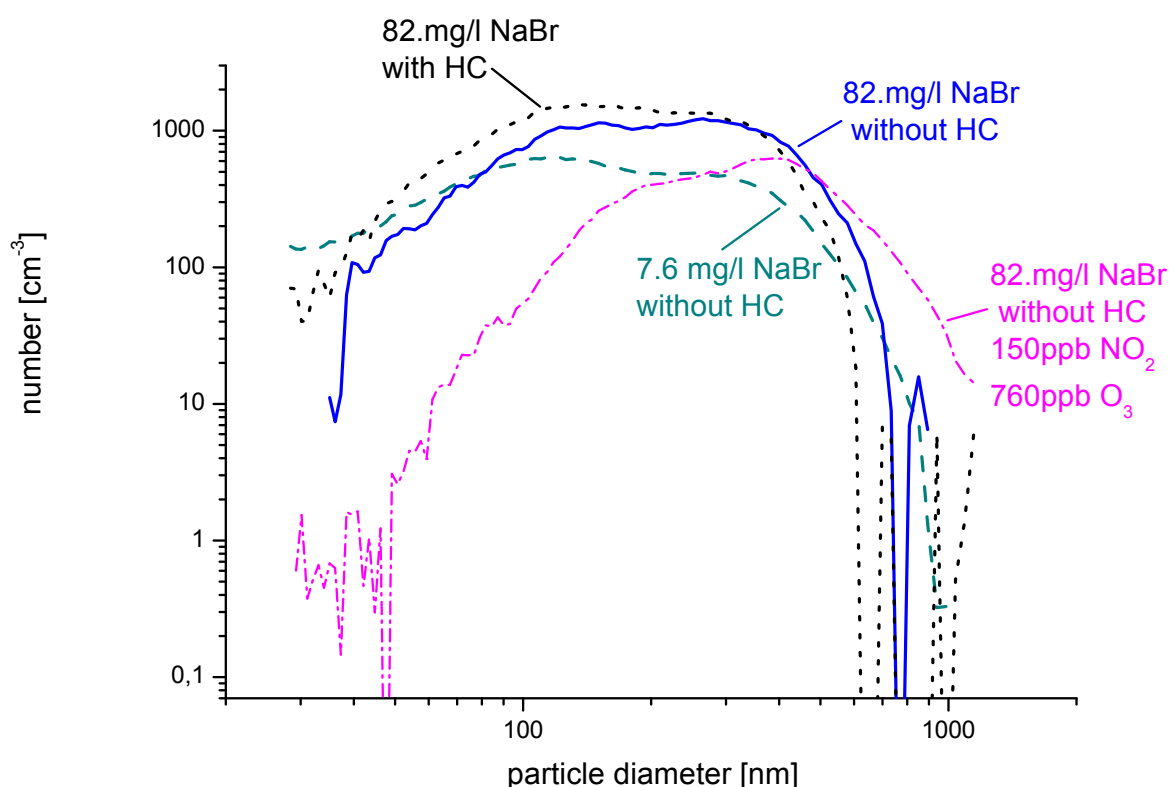


Figure 5.15.: Particle size distribution in three smog chamber experiments at low NO_x and one high NO_x experiment (760ppb O₃), at the time when the solar simulator was switched on. In the smog chamber experiment with HC the total number of 38000 particles was fewer than without HC (53000) and at high NO_x (18672), even though the total surface area and volume of all experiments were similar (compare table 5.3). Smaller particles contribute to the number, but not as much to surface and volume.

O₃ model

It is possible to calculate the contribution to ozone destruction according to the different reaction rates from known species. These approximations for ozone destruction can be summed up to generate a modeled time dependence of O₃(t). The measured ozone life time for an experiment at 75% relative humidity, including wall loss and photolysis followed by OH production with water molecules, is $2 \cdot 10^{-5} \text{s}^{-1}$ (compare section 3). The simple model calculations are included in figures 5.12, 5.13 and 5.14. During the three experiments shown with low NO_x conditions, the model ozone destruction is slower observed. On the other hand, the simple model only includes ozone depletion caused by the detected/modeled halogens, wall effects, dilution and OH-production, which is a hint for missing reactions for ozone loss. This will be discussed within chapter 6.

5.3.2. Chlorine Explosion at high NO_x

In this section the influence of high levels of NO₂ on the release of halogens from sea salt aerosols is presented. As described in section 3 up to 150 of ppb NO₂ were injected before the solar simulator was switched on. The general conditions in terms of RH and aerosol injection were similar to the experiments at low NO_x, as described in the previous section, and are summarized in table 5.5. Two different experiments with initial O₃ levels of 760 ppb and 2800ppb are described in this section (experiments AeNOxh760oz and AeNOxh2800oz). A rapid formation of BrO as well as ClO and OClO, and consequently a fast ozone depletion (fig. 5.16 and 5.17), are observed once the solar simulator was switched on. This is the first direct and simultaneous detection of ClO and OClO from 'chlorine explosions' (CE, auto catalytical chlorine formation), as well as BrO in a smog chamber. The strength of CEs strongly depends on the presence of NO₂ and initial O₃ mixing ratio. BrO, ClO, Cl and OClO are observed once NO_x values decreased from above 100 ppb to less than 1 ppb.

As described in chapter 2, simple model calculation including the measured O₃, ClO, OClO, BrO and NO are performed. The model only includes gas phase reactions, as well as ozone wall loss, and the reactions which are expected to play a major role in terms of reaction rate.

Experiment AeNOxh760oz

During experiment AeNOxh760oz shown in this section, initially 760 ppb of O₃ and 150 ppb of NO₂ were injected. In the dark, NO₂ reacts with O₃ to form NO₃. Additional loss of NO₃ and NO₂, their reaction product N₂O₅, due to aerosol uptake can occur, as well as heterogeneous formation of HONO through reaction with NO₂ and water (see reaction 2.7).

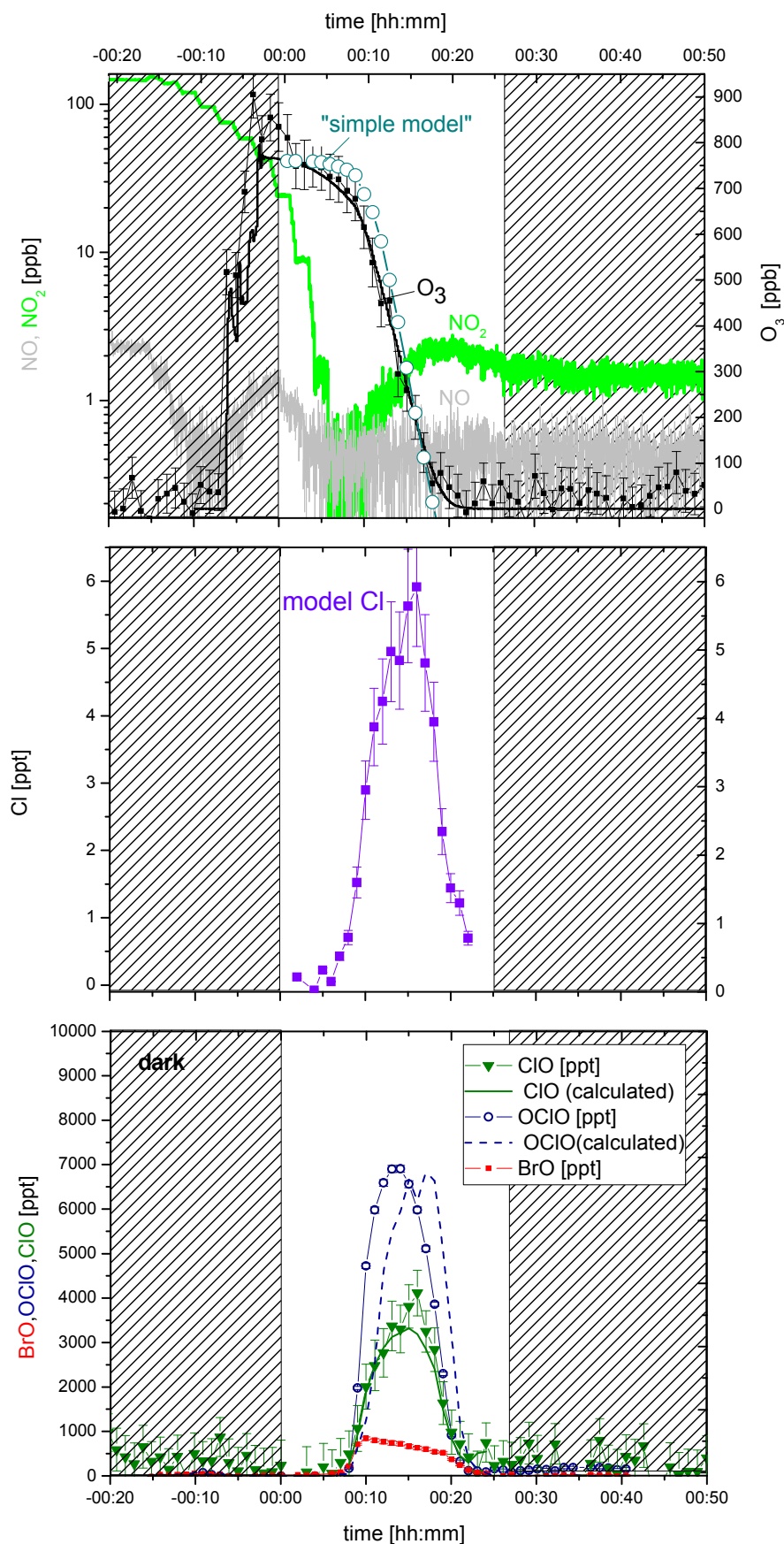


Figure 5.16.: Sea salt aqueous aerosol experiment at high initial NO_2 mixing ratios. High mixing ratios of ClO , OCIO and BrO were detected simultaneously. Error bars of the model ClO and OCIO are not shown, for the sake of clarity.

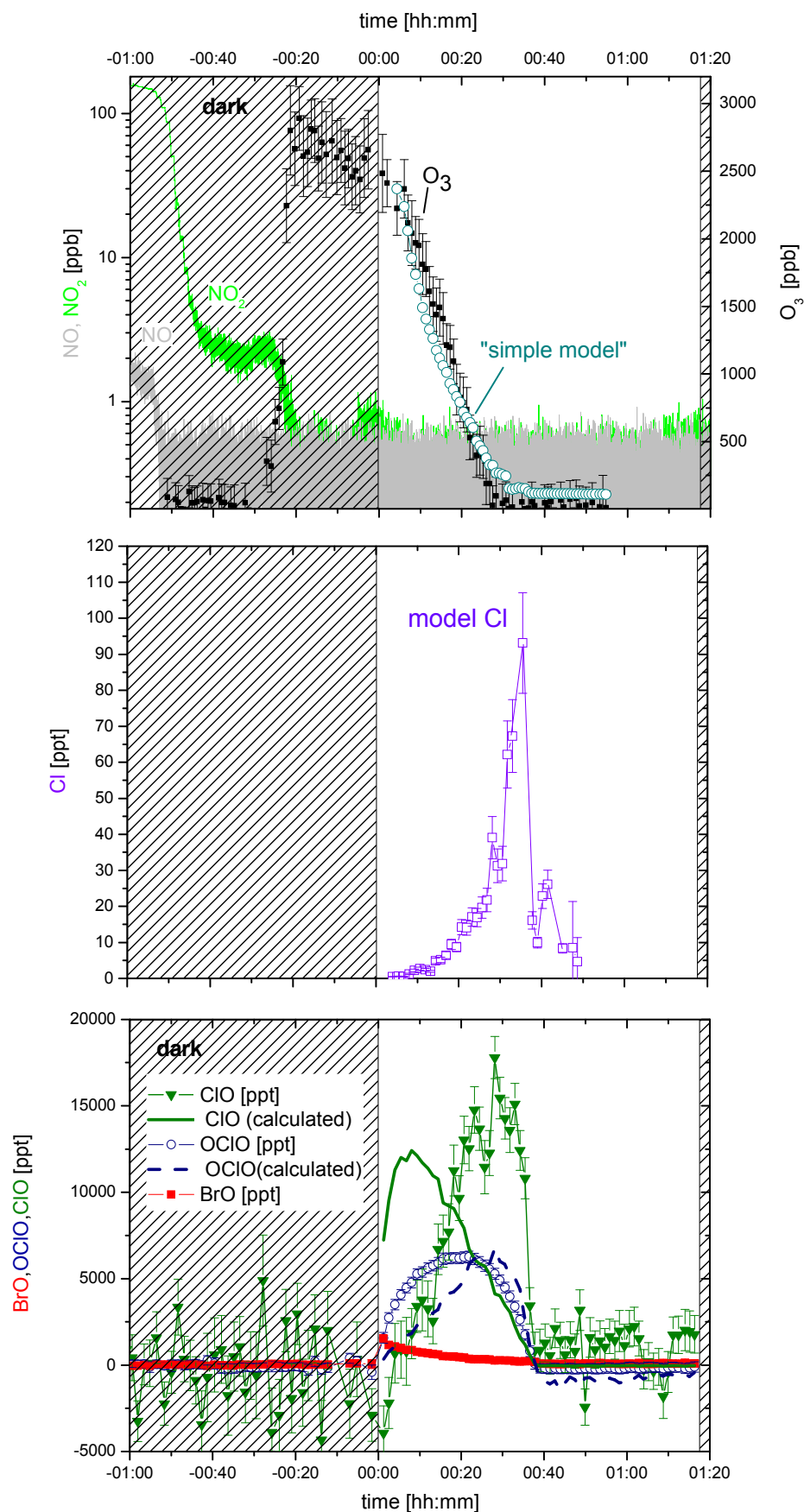


Figure 5.17.: Sea salt aqueous aerosol experiment at high initial NO_2 , mixing ratios. High amounts of ClO , OCIO and BrO were detected simultaneously. For the sake of clarity error bars of the model, except for Cl radicals, are not shown.

Light was switched on at a NO_2 level of 24 ppb and 716 ppb of ozone. 8 minutes after the solar simulator was switched on, the nitrogen dioxide level decreased below one ppb and formation of halogen oxides was detected. It is very likely that halogen radicals other than BrO, ClO and OClO (e.g. Br or Cl, from precursors e.g. Br_2 or Cl_2), could be present, before detection of the oxides. They react at a fast rate with NO_2 . OClO was formed very fast, at an initial formation rate of 39 ppt/s until it reached a maximum mixing ratio of 6900 ± 150 ppt within 5 minutes. ClO formation was observed to be slower at initially 11 ppt/s, reaching a maximum of 4100 ± 500 ppt within 8 minutes. BrO reached a maximum mixing ratio of 800 ± 100 ppt within 2 minutes after the start of halogen formation, and decreased slowly over 10 minutes to 600 ± 100 ppt. 30 minutes after the solar simulator was switched on, the halogen oxides OClO, ClO and BrO were below their respective detection limits of 300 ppt, 1000 ppt and 200 ppt again, while ozone was consumed to less than 1 ppb (detection limit of O_3 monitor). It is possible to calculate Cl radicals from the simple model, which predicts a maximum Cl radical mixing ratio of 6 ± 1 ppt. The modeled $\frac{-d[\text{O}_3]}{dt}$ seems to agree well with the observed ozone depletion for the first 10 minutes after the solar simulator was switched on. After 17 minutes still 80 ppb O_3 are observed with the DOAS system, whereas the model predicts total O_3 consumption. This will be discussed in the next chapter. Modeled ClO and OClO show a similar shape and the same quantitative values. Though the OClO maximum occurred 5 minutes earlier than predicted by the model. This is possibly because the model assumes the cross reaction of ClO and BrO to be the only source for OClO formation and photolysis the only sink. The model underestimates the ClO maximum by about 1 ppb.

Experiment AeNOxh2800oz

In experiment AeNOxh2800oz the initial NO_2 mixing ratio of 150 ppb, was similar to the first experiment described above. Ozone was injected at a higher level of 2800 ppb after NO_2 was already consumed by heterogeneous reaction on the aerosol surface (down to 3ppb). With O_3 injection NO_2 further decreased from 3ppb to <1ppb before the solar simulator was switched on. Formation of halogen oxides started immediately after the solar simulator was switched on. OClO reached a maximum mixing ratio of 6300 ± 200 ppt within 20 minutes, which is lower than during the experiment described above. BrO increased up to 1600 ± 100 ppt within 2 minutes. ClO formation was delayed compared to OClO and BrO, and reached a maximal mixing ratio of 17700 ± 1000 ppt 28 minutes after the solar simulator was switched on. Cl radical were calculated to be 90 ± 10 ppt. The modeled O_3 depletion fits the measurement. Again, modeled ClO shows a maximum before modeled OClO maximum, which is in contrast to the observations.

Surprisingly, during the sea salt aerosol experiments, higher amounts of chlorine species in forms of Cl and OClO were observed, even at low NO_x levels and a RH of 60 – 75%, compared to the salt pan experiments. At high NO_x values the formation of chlorine species was extremely high, given that 600ppb of methane were present in the clean air. This should actually lead to removal of chlorine radicals due to formation of soluble HCl. Possible reasons for the difference in concentration favored for halogen release are discussed at the end of chapter 6.

Aerosol Distribution

The aerosol number distribution of the sea salt aerosols by size is shown in figure 5.15 for the high NO_x at 2800 ppm O₃ experiment. During the high NO_x at 760ppb O₃ experiment the EC-CNC failed due to missing butanol. But the characteristic size distributions of sea salt aerosols, shown in figure 5.15, show similar maximum size and similar number. The maximum diameter was between 300-400nm. The total particle number was 18670 for the experiment at high NO_x. The total number is smaller compared to the low NO_x experiments because the aerosol was already altered. Smaller droplets coagulate, to form more big particles. Even though the aerosol surface area with $8 \cdot 10^{-5} \text{cm}^2/\text{cm}^3$ and the volume of $7 \cdot 10^{-10} \text{cm}^3/\text{cm}^3$, are similar to the low NO_x aerosols. The surface provided by the salty aerosols is crucial for halogen release, and will be discussed later.

5.4. Influence of the Presence of SOA on the Halogen Release from the Simulated Salt-Pan

The content and data of this section is already published within a paper from [Ofner *et al.* 2012], where part of my work contributed with results of the BrO measurements.

While the mechanism of halogen release from the salt pan causes a rapid ozone depletion within 20 minutes and corresponding BrO formation of up to 6ppb BrO (see above, and [Buxmann *et al.* 2012]), the organic aerosol appears to inhibit this process (figure 5.18).

Ozone depletion is slowed down, and only less than 10% of BrO of the expected values are observed during experiments with SOA formation from catechol and guaiacol. During experiments without SOA precursors the BrO formation started immediately after the solar simulator was switched on, with an initial rate of up to $d[\text{BrO}]/dt_{\text{initial}} = 40 \text{ ppt/s}$. The BrO formation in the presence of SOA was delayed: BrO exceeds the mean detection limit of 56 ppt after 18 minutes and 87 minutes with catechol and guaiacol as precursors, respectively. The mean particle diameter reached 80 nm for both precursor substances at that time (catechol SOA formation is faster, as particle formation already occurs during the dark phase) (see picture

5.18. This is a hint, that interaction of BrO precursors (e.g. Br) with the organic substances already occurs with small particles or in the gas phase, but the involved reactions were not identified so far.

Due to Mie-scattering caused by SOA formation from α -pinene, where the mean particle diameter was about 250nm, the detection limit of the DOAS instrument was poor. No BrO was observed during experiments with α -pinene above a detection limit of 200 ppt. During all salt pan experiments presented in this study, no free chlorine radicals could be found in the presence as well as in the absence of organic aerosols above a mean detection limit of $5 \cdot 10^4 \text{ molecules/cm}^3$ or 0.002 ppt of the radical clock measurements. It is well known that Br radicals mainly react with unsaturated hydrocarbons or partly oxidized species (e.g. aldehydes), whereas Cl radicals react with saturated hydrocarbons as well (compare 2). The resulting formation of HCl and HBr is most likely a sink for the RHS, as discussed in the next chapter.

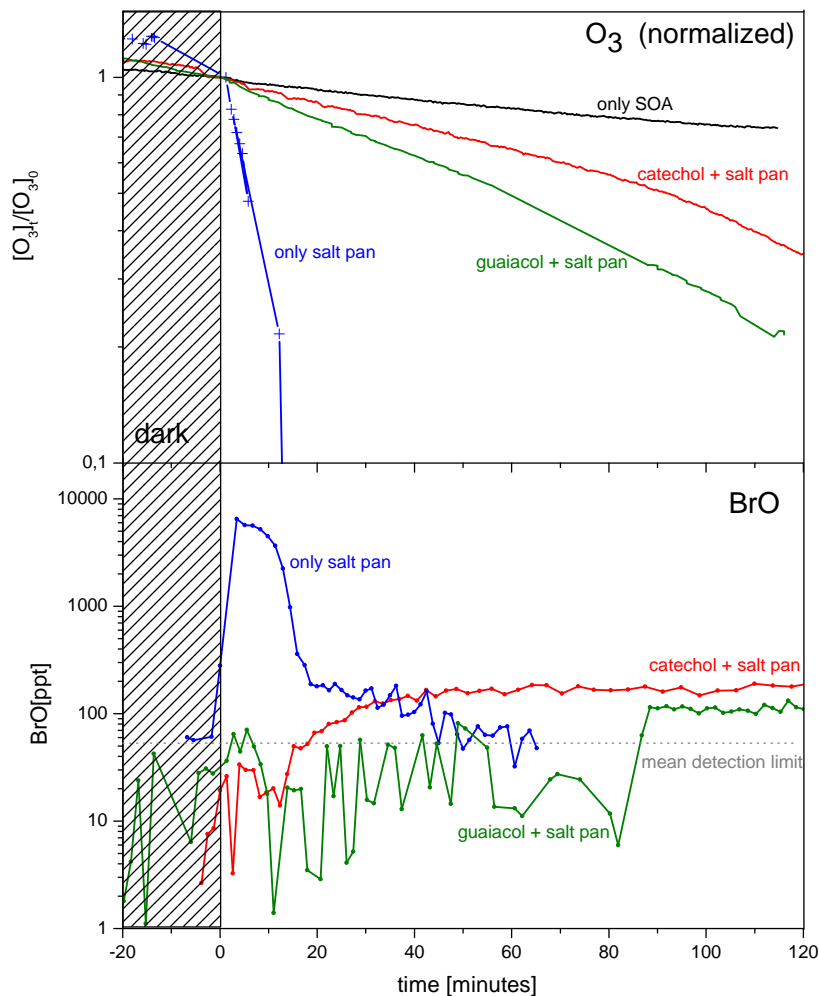


Figure 5.18.: Ozone (top) and BrO (bottom) time series show the influence of SOA from catechol and guaiacol on the release of RHS from the simulated salt-pan. Ozone values are normalized to the O₃ mixing ratios at $t=0$. The experiments were carried out at 60% RH. During an experiment, where only the salt pan without SOA precursor was exposed at simulated sunlight (blue lines, from Buxmann et al. 2012), ozone was destroyed within less than 20 minutes and more than 6 ppb BrO were formed. Measurements of O₃ were performed only for limited periods of time (indicated by crosses), to reduce dilution. During experiments with SOA precursors (indicated in red, green and black) ozone decay was much slower. BrO exceeds the mean detection limit of 57 ppt with a time delay (after the solar simulator was switched on at $t=0$) of 18 minutes for catechol and 87 minutes for guaiacol. Maximum BrO mixing ratios of less than 200 ppt BrO were observed, one order of magnitude lower than without SOA [Ofner et al. 2012].

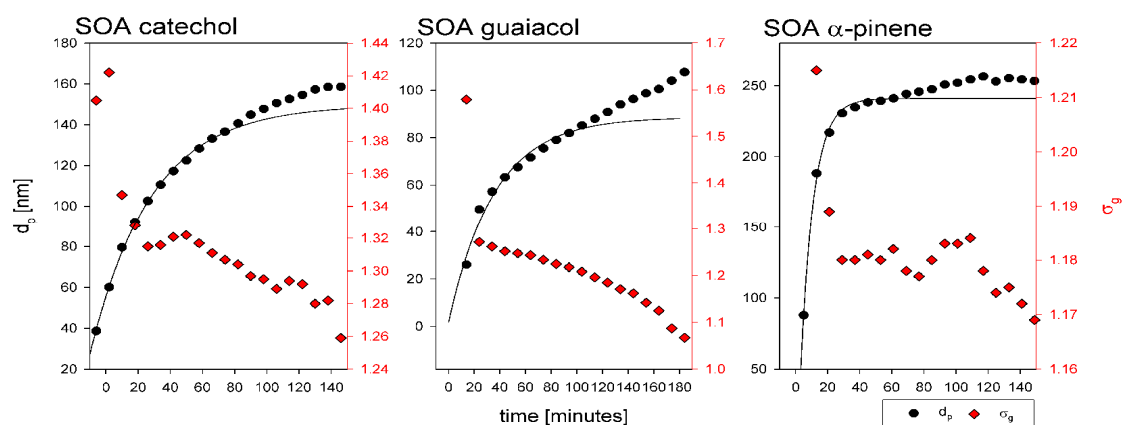


Figure 5.19.: Evolution of the mean particle diameter (d_p) and the related geometric standard deviation (σ) of SOA from the different model aerosols while interacting with RHS released from the simulated salt pan adapted from [Ofner *et al.* 2012]. Once BrO formation starts, the particle diameter changes. The thin black line should indicate particle growth without halogens being involved.

6. Discussion

6.1. White system and cavity enhanced DOAS

In this section some of the main differences between the two multi reflection cells, which were especially designed for smog chamber conditions within this thesis, are discussed.

One example is the different light path calculation of the two multi reflection systems. For the White system, it is possible to adjust the length of the light paths, with the help of the mirrors and prisms. For the CE DOAS, the light path mainly depends on the mirror reflectivity, but as well on the extinction inside the resonator (see below). For the experiments described in this thesis, 16, 48, 144 and 160 reflections in the WS were used. The number of reflections, which was chosen in the different experiments, depends on: First the coating of the mirrors, as the light intensity after traveling through the WS depends on the reflectivity of the mirrors. The reflectivity changes drastically between the dielectric (>99.9%) and the aluminum coating (80-88%) used for the WS.

Second the concentration of aerosols in the chamber, which determines the visibility (as is obvious from our daily life). Roughly, the higher the concentration of aerosols the lower the visibility. For the WS, this results in a decrease in light intensity for the measurement spectrum, which affects the integration time. A good balance between the length of light path and the integration time has to be chosen, as both determine the sensitivity of the WS DOAS (see chapter 4.)

In the atmosphere, visibility is typically given by 4 or (3.9...4.6) [*W.Roedel* 2000, *Platt and Stutz* 2008] times the extinction length L_E (with respect to the human eye). The extinction length L_E is the distance beyond which the initial light intensity decreased by a factor of e (Euler number). L_E is equal to the inverse of the extinction factor, which includes extinction due to scattering as well as to absorption. In the case of the presented aerosol smog chamber experiments, typical volume to surface ratios of 125 m were present (compare chapter 5). The cross section to surface ratio of spherical aerosols is 1/4, resulting in L_E of 500 m, or an optical density of 0.002, according to Lambert-Beer's law (chapter 4) after 1 m light path. Visibility would then be about 2 km, which should not limit the light path of the WS significantly. During the aerosol experiments with the WS, a decrease in intensity in the presence of aerosols by a factor of 2-5 of the initial intensity before the injection of aerosol at a light path of 288 m. This can be translated to an extinction

factor of $2.5 \cdot 10^{-3} m^{-1}$. Causes for intensity loss include absorption by the aerosols as well as Mie scattering, which was visible by eye as illustrated in figure 6.1. The blue color of the light beam is caused by scattering of the sea salt aerosols with a mean diameter of 300-400 nm (compare chapter 5), as well as the mirror reflectivity between 415-440 nm.

However, once the number of reflections is chosen, the light path of the WS is set, and does not change with light extinction. This is in contrast to the CE-DOAS. The light path of the CE-DOAS is directly connected to the extinction in the resonator as described in section 4.5. Therefore, the sensitivity of the CE DOAS decreases drastically in the presence of aerosols. The maximum light path achieved during the chamber measurements was 816 m at 346.5 nm. As described in chapter 4.5, the light path of the cavity is defined by:

$$\bar{L}(\lambda) \approx \frac{d_0}{\tau(\lambda) + \rho(\lambda)} \quad (6.1)$$

with $\rho(\lambda) = 1 - R(\lambda)$, where $R(\lambda)$ is the mirror reflectivity. The transmission of the cavity, $\tau(\lambda)$ includes all extinction processes in the cavity i.e. aerosol absorption and Mie scattering as well as absorption by trace gases, and is here extinction factor times $d_0 = 1.33$ m. As described above, the extinction factor due to aerosols is on the order of $3 \cdot 10^{-3} m^{-1}$. As the mirror reflectivity of the UV CE-DOAS mirrors is $>99.83\%$, the extinction due to aerosol absorption and scattering significantly reduces changes the light path from more than 800 m to about 250 m. This is comparable to the light path with the WS, but the WS time resolution is much better. Therefore the CE DOAS is less useful for aerosol experiments, whereas White-cell measurements at high aerosol levels are still possible.

In the case of salt pan experiments an analogous L_E would be 28 m, or visibility of 109 m. That would cause a strong intensity loss, imagining a comparable amount of aerosols in the chamber as halogen source. But due to the fact that the salt grains were put on a teflon sheet, that did not cause any problems. For salt pan experiments both instruments performed well. Good agreement between the CE-DOAS and WS data of HCHO and BrO was shown. During those experiments, the detection limit of CE-DOAS is much better because of longer light path and broader mirror reflectivity. However, a higher time resolution of the WS was achieved, because of higher light intensity of the Xe-arc lamp. The intensity of UV-LEDs is comparably low. High time resolution is needed in some smog chamber experiments, as a rapid halogen formation within the first 1-2 minutes was observed. One should keep in mind that, by summing up the WS measurement spectra, the detection limit could be reduced. However, a low detection limit was not the focus of this work. As UV-LEDs are being utilized for water disinfection, future improvement in the light intensity of these LEDs can be expected from further research. As stated in *Hoch et al.* [2012], mirrors with higher reflectivity can lead to an improvement of the CE-DOAS. Higher reflectivity may be achieved, e.g., by using different materials during

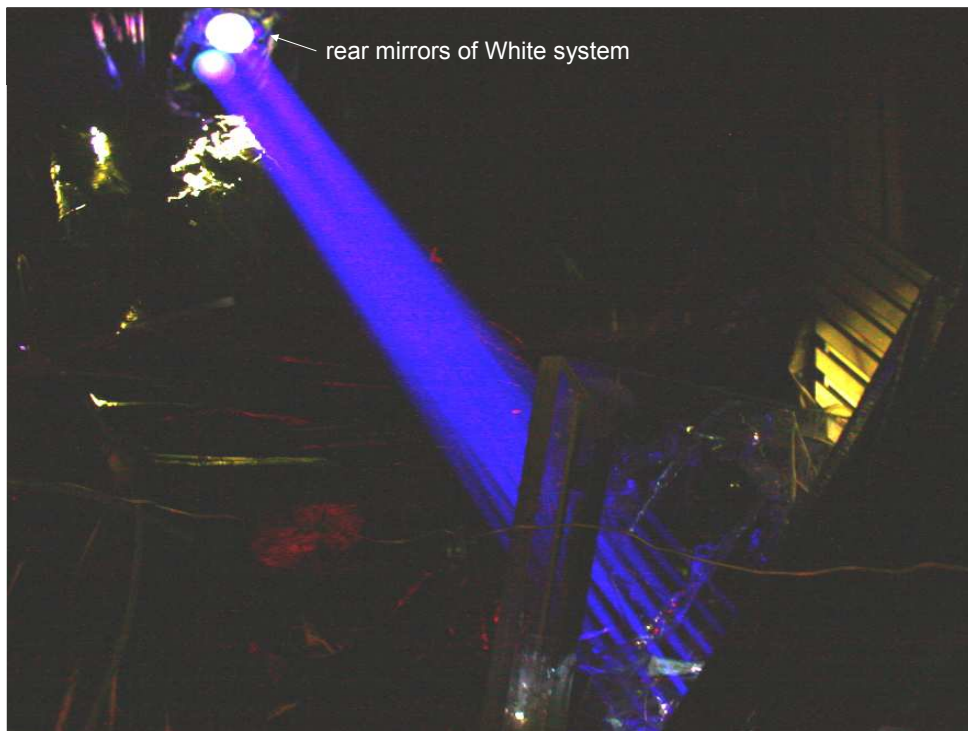


Figure 6.1.: Mie scattering within the light path of the WS system after injection of sea salt aerosols (picture taken by *Gonser* 2011).

the production process. Currently, the absorption within the mirror substrate and coating is the limiting factor here. Thus, merely by decreasing the absorption and thereby increasing reflectivity, the sensitivity of the instrument will be improved. During some of our experiments, the cooling system of the laboratory failed, and temperature changed by up to 20°. The intensity of the CE-DOAS remained stable, demonstrating a good temperature stability. In contrast the WS was not adjusted anymore. The temperature stability of CE-DOAS, looks promising for possible field measurements, where temperature changes are very common, e.g. between day and night. Some technical upgrades have to be made. Possibly high aerosol levels in the field pose a challenge, as well as the determination of wavelength dependent light path of CE-DOAS is necessary. One should note that the amount of aerosols in the chamber is extreme high, ≈ 10 higher than typical for the atmosphere. Additionally, the detection limit with at best 11 ppt for 1 hour and 20 minutes integration time [Hoch *et al.* 2012], is too high for the expected mixing ratios in many regions. Possible exceptions include some spots along the West African Coast with up to 10 ppt [Martin 2007], the Arctic [Pöhler *et al.* 2010] with up to 41 ppt, or the Dead Sea Valley [e.g. Hebestreit *et al.* 1999, Tas *et al.* 2008], where hundreds of ppt were observed.

6.2. Salt Pan Experiments

BE was observed at four different RH, showing a strong dependence with increasing maximum BrO concentrations at higher RH. The 'explosion' was very intense with up to 30ppt/s of BrO increase. Observed O₃ decrease was too slow to be explained by Br catalyzed destruction. Possible explanations and the dependence of the BE on the liquid micro layer on the surface of the sea salt crystals are discussed. Parts of the discussion of the salt pan experiments are already published in [Buxmann *et al.* 2012].

6.2.1. Recovery of the BrO Source and Behavior of O₃

As shown in figure 5.9 four BEs from the same salt sample on the teflon chamber were observed at RHs of 60% and 68%, simulating day and night, by switching on and off the solar simulator. 370-180 ppb of O₃ were injected. Two of the four experiments were performed in a row within one day. During the first light exposure, the BrO peak was larger compared to the second run on the same day. Surprisingly, however, the BrO maximum was higher by more than 6 ppb on the second day (3rd light exposure), possibly in part due to more ozone injected on the second day. The presence of precursor species from the first day in the gas phase is not a likely explanation, as the chamber was flushed with clean air for more than 6 hours. The observation of multiple BEs show that it is possible to activate the Br- source

from the salt crystals for several times. The strength of the BE depends on the recovery time between consecutive light and ozone exposures and the concentration of O_3 . Because of this apparent recovery effect for the BrO-source, the hypothesis is proposed, that the source of the bromine radicals as precursor of BrO is the liquid micro layer on the salt surface. The maximum BrO level is then limited by the source strength. Two sources of active bromine appear to exist:

- The initial source is due to precursors (e.g. Br_2 formation through heterogeneous reaction 2.81 with ozone [*Hunt et al.* 2004, *Clifford and Donaldson* 2007]) during the dark phase, causing a sharp peak of BrO during the first irradiation.
- A second source may be due to a delayed bromine release from the salt surface by the uptake of HOBr (reactions 2.76-2.78), causing the shoulder of the first BrO peak that becomes more pronounced in the second BrO peaks in figure 5.9.

Once all available bromine is released from the salt surface, BrO buildup is limited by the amount of available ozone, even though not all of the ozone has been consumed completely by the time BrO is completely depleted.

6.2.2. Bromine Release Mechanism

One may compare the dependence of BrO production rates on RH during the first minutes of each experiment. The theory of BE predicts an exponential growth in BrO concentration. However, the amount of BrO data within the first 250 s after the solar simulator was switched on is very small (<3 data points), thus an exponential fit is inappropriate. It is only possible to estimate a production rate by a linear approximation. The observations on initial production rates $d[BrO]/dt$ and BrO maxima are summarized in figure 6.2 as a function of RH. The production rates for 60% and 68% were similar at $29 \pm 2 \text{ ppt/s}$ for the first ozone injection and $12 \pm 2 \text{ ppt/s}$ for the second ozone injection. According to those very fast production rates, one should note that the uptake coefficient of $BrONO_2$ on NaCl has been determined to be very large, $\gamma_{BrONO_2} = 0.31 \pm 0.12$ [*Aguzzi and Rossi* 1999] and much larger than that of HOBr on unbuffered NaCl $\gamma_{HOBr} \cdot 10^{-3}$ [*Atkinson et al.* 2004, *Keller-Rudek and Moortgat*, *Mochida et al.* 2000]. However, γ_{HOBr} shows a strong increase with decrease in pH and can rise up to $\gamma_{HOBr} > 0.2$ for $pH < 7.2$ [*Abbatt and Waschewsky* 1998]. Additionally *Wachsmuth et al.* [2002] and coworkers found that the uptake of HOBr on NaBr deliquescent aerosol particles at low pH is clearly limited by the mass accommodation coefficient, which was calculated to be 0.6 ± 0.2 . A summary of the different uptake parameters is given by the IUPAC evaluation [*Crowley et al.* 2010], and life times of some important species are compared in table 6.1. The uptake of both bromine compounds might be one of the rate limiting steps

of BE. As mentioned above, another reason for the very fast initial BrO production could be formation of Br_2 as a precursor in the dark.

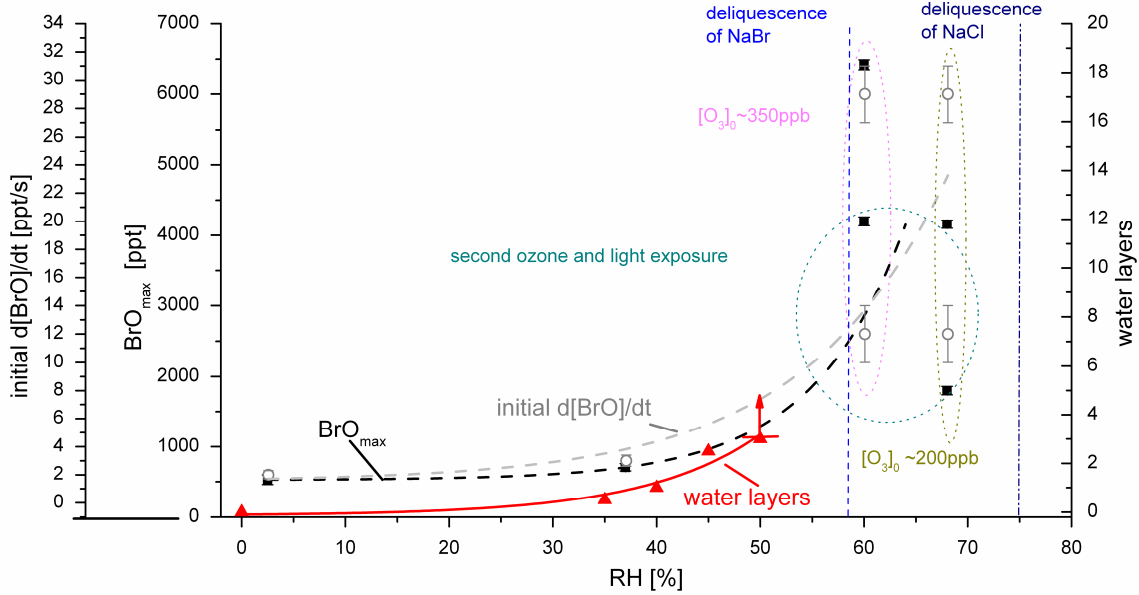
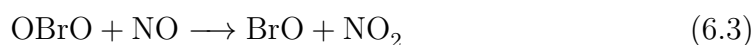


Figure 6.2.: Comparison of the maximum BrO_{max} concentration and the initial production rate $d[BrO]/dt$ observed at different RH, with the number of liquid micro layers known from literature (e.g., [Finlayson-Pitts 2003] and references therein, adapted from Burmann *et al.* [2012]).

For RHs of 2% and 37%, the initial production rates were about 2 ppt/s and 3 ppt/s respectively. In contrast, at 60% and 68% RH the initial production rates and maximum BrO concentrations were one order of magnitude higher (initial production rates ranged from 10 to 30 ppt/s at 60% and 68 % RH). A quick Br_2 pulse event during the first moment of low pressure flow reactor experiments on reaction of $Cl_2O/HOCl$ with frozen natural sea salt was observed by Pratte and Rossi [2006]. They suggested that surface adsorbed Br^- ions were consumed with high priority. On the other hand, photolysis of Br_2 and Br_2O (as the anhydride of $HOBr$) are too slow in our experiments ($J_{Br_2} = 1.7 \cdot 10^{-2} s^{-1}$, $J_{Br_2O} = 2.2 \cdot 10^{-2} s^{-1}$) to explain the steep, initial rise of BrO from the very beginning of the irradiation. The same argument may hold for the thermolabile BrO dimer, taking the absorption spectra from Harwood *et al.* 1998 or Pratte and Rossi 1993, which lead to $J_{BrOOBr} = 5 \cdot 10^{-2} s^{-1}$ in

our chamber. A thermally but extremely photolabile bromine compound is OBrO, leading to $J_{OBrO} = 0.2s^{-1}$ according to its absorption cross sections [Knight *et al.* 2000]. Formation of OBrO from HOBr is accessible by disproportionation to bromide and $HBrO_2$, followed by another disproportionating self-reaction of $HBrO_2$ to $HBrO_3 + HOBr$ and a subsequent symproportionating cross reaction of $HBrO_3$ with $HBrO_2$ [Zetzsch 2011]. This leads to the thermolabile BrO_2 dimer that dissociates rapidly to BrO_2 in the well-known oscillatory Belousov-Zhabotinskii reaction mechanism as reviewed by Field and Foersterling 1986. All these species may be formed during the dark phase of the experiments on the humidified salt surface upon acidification.

However, OBrO undergoes a null reaction cycle with respect to O_3 :



The impact of this null reaction on the system might be very limited, mostly because OBrO formation is rather slow ($k_{OBrO} = 0.7$). In addition, the reaction with NO ($k_{6.3}=18$) is comparable fast given NO concentrations of several ppb. This was just recently indicated by modeling studies of the chamber measurement [Sommariva *et al.* 2012] using the MISTRA v7.4.1 model [von Glasow *et al.* 2002]. The model calculations include reactive gas uptake on salt surface using a resistance model [Davidovits *et al.* 2006] and an estimated reactive surface area = 2 m² (compare chapter 3). Nevertheless, direct detection of OBrO at a high temporal resolution, would be very helpful, to prove or disprove OBrO as a precursor.

The model studies [Sommariva *et al.* 2012] indicate that residual levels of NO_x and high levels of HC can lead to high O_3 formation. Though during blank experiments with a pure NaCl sample, no O_3 formation was observed. But for a not well treated teflon foil (nominally cleaned by UV-light and OH radicals), NO_2 can be formed and might increase the photochemical ozone formation potential (compare [Bleicher 2012]). However, the experiments shown in this thesis were performed after carefully pretreating the chamber. Since any ozone formation partly compensate for the destruction of O_3 by bromine, to estimate the potential of ozone creation due to the presence of hydrocarbons, further model calculations are required.

The observations of BrO and simultaneous consumption of O_3 appear to be strongly connected to the number of liquid micro layers present at the salt surface. As described by Finlayson-Pitts and Pitts 2000 and references therein, the water coverage of dry NaCl powder at room temperature increases slowly with RH from zero coverage at 0% RH to ≈ 0.5 layers at 35% RH. From 35% RH to 40% RH, there is an increase in the amount of adsorbed water from half a layer to 1 layer, followed by a very steep increase to about 2.5 layers at 45% RH. At RH above 50% three or more

Table 6.1.: Overview of uptake rates for some important species for halogen release processes. The uptake coefficients for some species vary depending on the substrate and pH. A diffusion layer height of $h = 0.1\text{mm}$ and a diffusion coefficient of $D_X = 10^{-5}\text{ m}^2/\text{s}$ was taken, for reactive uptake on the salt pan surface (indicated as RS). With an effective surface of $A_p/V = 0.5\text{ m}^2/3.5\text{ m}^3 = 0.14286\text{ m}^{-1}$ this lead to $f_{dc} = 0.01429/\text{s}$ and $\tau_{dc} = 70\text{seconds}$ (compare chapter 3) for the diffusion controlled term. For uptake onto aerosols (indicated as AE) the effective surface was $8 \cdot 10^{-2}\text{ m}^{-1}$ and a radius of 400nm . The references for the uptake coefficients are ¹ [Mochida et al. 1998], ² [Abbatt and Waschewsky 1998], ³ [Wachsmuth et al. 2002], ⁴ [Frenzel et al. 1998], ⁵ [Huff and Abbatt 2000], and ⁶ [Hunt et al. 2004]. ⁷ α is the mass accommodation coefficient.

Species	v_x [m/s]	γ_{upt}	f_{RS} [s]	τ_{RS} [s ⁻¹]	f_{AE} [s]	τ_{AE} [s ⁻¹]	Substrate
HOBr	274	¹ 0.00651	96	0.01	287	0.003	NaCl, grain
	274	² 0.00152	172	0.006	1220	0.0008	NaCl aerosol, 75% RH, unbuffered
	274	² 0.22	71	0.014	15	0.07	NaCl aerosol, 75% RH, buffered
	274	³ 0.63	71	0.014	9	0.1	100nm NaBr aerosol, 37% RH, α^7
BrONO ₂	210	⁴ 0.3	71	0.014	14	0.07	solid NaCl
Cl ₂	323	¹ 0.02	76	0.01	84	0.011	synthetic sea salt
HOCl	417	⁵ 0.15	70	0.014	14	0.07	aqueous NaBr, pH 4-10
	417	⁵ 0.5	76	0.13	8	0.1	aqueous NaBr, pH 2
ClNO ₂	310	⁴ $1.4E - 4$	1037	9.6E-4	11524	8.6E-5	NaBr, HBr 0.5 and 1 mM
O ₃	390	⁶ 2E-6	54E3	1.8E-5	640E3	1.6E-6	NaCl solution

water layers are present [e.g. *Finlayson-Pitts* 2003, *Peters and Ewing* 1997]. Ewing and co-workers observed a similar dependence, using FTIR to follow the water uptake on the (100) surface of single crystals of NaCl in real time as a function of RH. Above 46% RH both Na⁺ and Cl⁻ are solvated and the ratio of Br⁻ to Cl⁻ on the surface is increased. This increases the mobility and the availability of the ions for heterogeneous processes. In contrast gas-phase conditions, such as concentrations of OH NO_x, did not change that drastically during our smog chamber experiments at different RH. Therefore it is unlikely that the observed BE is limited by gas-phase reactions, although we do observe a dependence of the maximum BrO mixing ratios on the initial ozone mixing ratios (table 5.3). However, more detailed experiments are needed to explain some of the observations.

6.3. Sea Salt Aerosol Experiments

6.3.1. Comparison with Siekmann Experiments

Chamber experiments with sea salt aerosols containing NaBr as well as NaCl had been performed previously (e.g. [Behnke et al. 1999, Zetzsch and Behnke 1992]). Many sea salt aerosol experiments were focused on the release of chlorine, from NaCl aqueous aerosol droplets or investigate the influence of NO_x (e.g. Behnke et al. 1992). The experiments of Siekmann 2008 were performed in the same smog chamber facility (LOTASC teflon smog chamber) as the experiments described in chapter 5. The author used similar aerosol compositions formed from variable mixtures of NaBr/NaCl solution of different composition. He used the radical clock method for indirect calculation of the Cl radicals. It was not possible to directly measure the halogen oxides at 2008, but he calculated an approximate BrO and ClO mixing ratio for an experiment from a solution containing 7.6 mg/l NaBr and 1g/l NaCl aerosol droplet. Therefore a comparison between his data with results from the AeNOx17.6NaBr experiment is possible. In his thesis, only the integral over the Cl radicals using the radical clock method is shown. From this the derivative of the $\int [\text{Cl}] dt$ was calculated to get $[\text{Cl}]$. The estimated Cl concentrations and Cl concentrations from [Siekmann 2008] are included in figure 6.3. The agreement is surprisingly good, given that no HC were added in the AeNOx17.6NaBr experiment and the solar simulator conditions were different (see chapter 3). Siekmann 2008 calculated expected Br radicals from O_3 depletion at a certain time according to reaction cycle 2.25-2.29. Under the assumption that Br atoms do not react with the employed HC, their concentrations can be calculated from the measured ozone degradation. A blank aerosol experiment with pure NaCl was used as a reference for estimating other ozone losses [Siekmann 2008]. This might be an underestimation of ozone destruction as additional Bromine can lead to release of chlorine species as well. He injected O_3 initial mixing ratio of 545 ppb, and observed a life time of $1.1 \cdot 10^{-4} \text{ s}^{-1}$. This is comparable to the AeNOx17.6NaBr experiment with 500 ppb initial ozone and a life time of $9 \cdot 10^{-5} \text{ s}^{-1}$. He then calculated BrO mixing ratios, from the Br radicals accounting for photolysis and reaction with HO_2 . For an experiment with sea salt aerosols at 7.6 mg/l NaBr and 1g/l NaCl, he estimated a fast BrO formation, peaking at 500 ppt followed by a decrease to 180 ppt within 3 hours. This estimated peak BrO concentration, would be higher than the BrO mixing ratios observed at the AeNOx17.6NaBr by about a factor of 3.

This inter comparison shows that the smog chamber aerosol experiments are repeatable, in terms of Cl atoms and ozone loss. In case of the high expected BrO level, the reason might be that ozone depletion, might is not only due to Br atoms. This is consistent with by the simple model calculations in chapter 5, where the model underestimates the total $d\text{O}_3/dt$ at low NO_x levels. This difference will be discussed below.

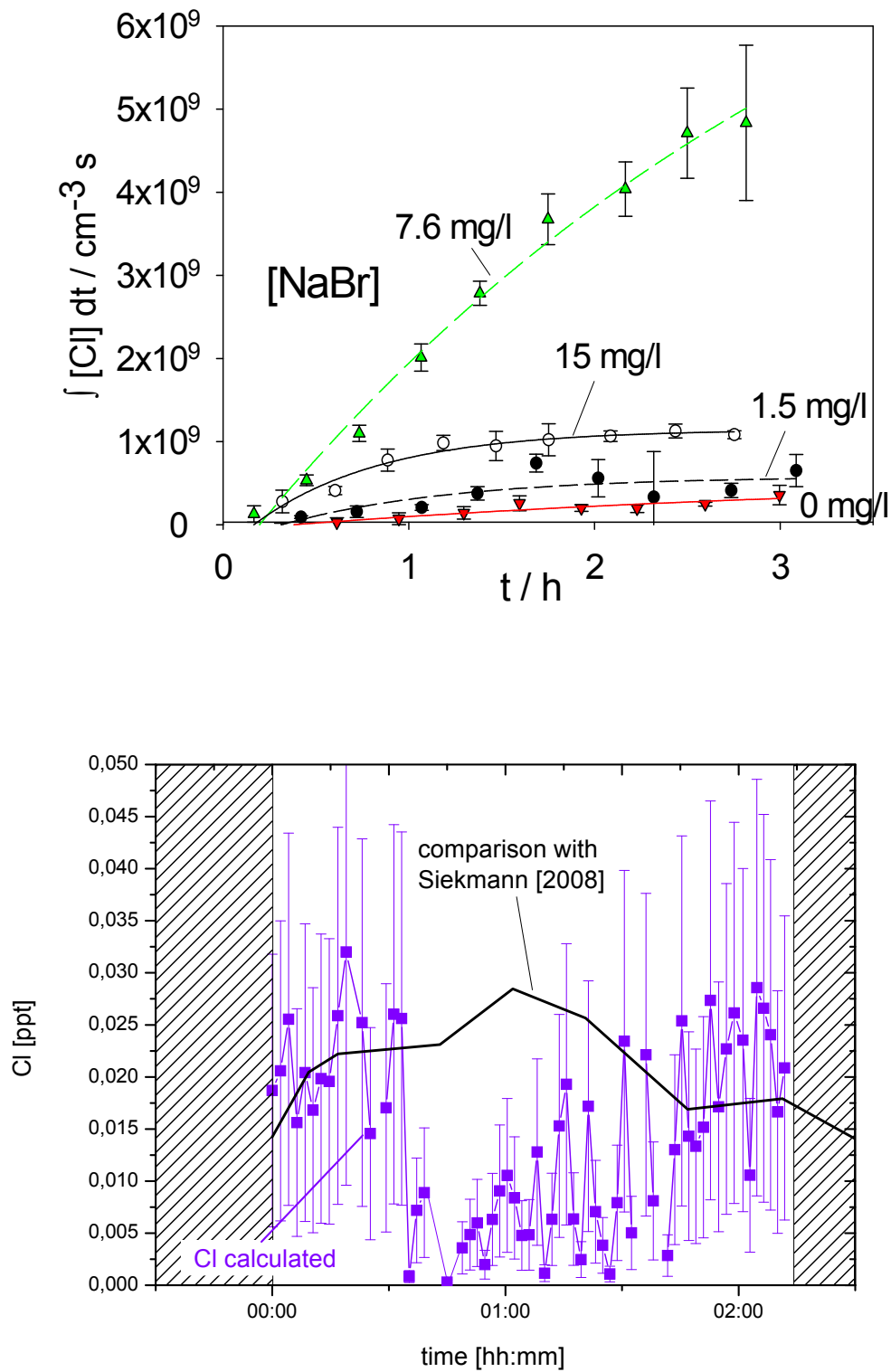


Figure 6.3.: Comparison of the AeNOx/7.6NaBr experiment (bottom, violet squares) with an experiment from Siekmann 2008 at 2.6mg/l NaBr (top, green triangles).

6.3.2. Influence of NO_x and Chlorine Explosion

It was shown in chapter 5 that the release of halogens strongly depends on the NO_x concentration. In the presence of NO_x , a fast increase of OClO followed by an increase of ClO was observed. A BE event was apparent as well. As shown by *Fickert et al.* [1999] a low pH is crucial for the BE. Acidification most likely occurs by uptake of NO_2 and formation of nitric acid (HNO_3) as well as nitrous acid (HONO) via reaction 2.7. Given the high solubility of HNO_3 in water and aerosols, it is most likely that the aerosols have been acidified. The NaBr/NaCl solution was unbuffered. Comparison of the pK_a of hypobromous acid at 8.5 and of hypochlorous acid at 7.5, shows that a similar explosion mechanism (reaction cycle 2.76-2.77) for Cl requires an even lower pH. *Fickert et al.* 1999 showed that a lower pH than expected on the pK_a is required for Br_2 release, which might be the case also for a respective chlorine cycle. Additionally, the uptake of HOBr is favored at low $\text{pH}=2$, whereas no change in uptake coefficient was observed in the 4-10 pH range (compare table 6.1). However, given the current state of knowledge, release of Br_2 is more likely than BrCl (see chapter 2). It is even more surprising though, that high ClO and OClO levels were observed. The CH_4 level was 600 ppb during our experiments, and reaction with Cl radicals, should lead to HCl . HCl is rather stable against photolysis, and given its high solubility aerosol uptake is very likely. [*Frenzel et al.* 1998] and coworkers have studied the uptake of Cl_2 on nitrite-containing aqueous solutions. The primary product was ClNO_2 , formed at a maximum yield of 50%. However, nitryl chloride, formally the anhydride of HCl and nitric acid, has a life time of 5000 s with respect to photolysis in the smog chamber. Zetzsch and co-workers have noted in the past that some experiments performed in glass aerosol chambers may be subject to heterogeneous formation of Cl_2 that apparently takes place on the walls of the chamber [*Zetzsch and Behnke* 1993]. After three sea salt aerosol experiments, without cleaning the chamber wall, a blank experiment was performed. A 600 ppb level of ozone was injected. No formation of BrO or ClO was observed above a detection limit of 90 ppt and 150ppt respectively after the solar simulator was switched on. Teflon foil might be the better choice in terms of minimizing wall reactions. *Mochida et al.* [2000] performed uptake experiments of Cl_2 on both sea salt and pure bromide and chloride substrates using a Knudsen flow reactor equipped with a mass spectrometer. They observed Br_2 as a primary product, with minor importance of BrCl . Additionally, the life time of Cl of 645 s against photolysis might be longer than the uptake onto aerosol with an estimated life time of 83s (compare table 6.1). But the fact that Cl_2 photolysis is slower compared to uptake, Cl_2 might not be sufficient as a precursor for the observed ClO and OClO mixing ratios during the chamber experiments at high NO_x . Furthermore OClO ($\approx 40\text{ppt/s}$) is formed at a faster rate than ClO ($\approx 15\text{ppt/s}$) in the experiments AeNOxh760oz and AeNOxh2800oz. The model predicts the maximum ClO concentration first, after maximum OClO concentration. The measurement indicates the opposite. This

suggests OCIO formation, possibly similar to the aforementioned OBrO formation. The life time of OCIO against photolysis is only 20s in our chamber. But an actual heterogeneous release mechanism to form OCIO (or respective OBrO), has not been confirmed yet.

6.3.3. Influence of Ozone and Ozone Model

Simple model calculations were performed on the ozone degradation. For the high NO_x case and low NO_x case the model seems to show opposite results. For low NO_x , meaning a $\text{NO}_2 + \text{NO}$ level of less than 1 ppb (which might still be high for some remote regions), the simple model underestimates O_3 loss compared to the measured $d\text{O}_3/dt$. This is shown in figure 6.4. The reactions of halogens seem to play a minor role in ozone destruction, at the levels observed during the AeNOxl86NaBrHC experiment. Uptake of ozone onto the aerosol surface has a corresponding lifetime of 640 000s (or more than 170 hours, compare table 6.1). This is considering the reaction probability for O_3 on deliquescent salt aerosols given by [Hunt *et al.* 2004] (compare reaction 2.81). Trace levels of FeCl_3 at 0.1 wt % was found to increase the O_3 uptake coefficient by four orders of magnitude to 0.033 [Sadanaga *et al.* 2001]. This would decrease the life time of O_3 to several minutes. However, the possible source of traces of iron impurities in our salt samples, is not confirmed.

In the case of high NO_x , ozone is consumed faster by the aerosols than predicted by the model. But possible reasons, as discussed above, might be reactions of HC (remaining in our clean air) and NO. Ozone is then formed via reactions 2.18, 2.19 and 2.20. This is consistent with the salt pan experiments, where the model underestimates ozone consumption as well, possibly due to high O_3 and NO_x . At the AeNOxh2800oz experiment, no NO_2 remained in the gas phase once the solar simulator was switched on. The model fits the decay very well for the AeNOxh2800oz case.

Regardless of the model performance, a strong dependence of the initially O_3 concentration on the maximum halogen oxide levels was observed for both the salt pan as well as aerosol experiments.

6.4. Interaction of RHS with Organics

It was shown that during smog chamber experiments release of BrO from a simulated salt pan was reduced by an order of magnitude in the presence of SOA. No formation of Cl radicals was observed from the radical clock data. and the particle formation from the SOA precursors was influenced. In the particulate phase chlorination was dominating over bromination of the aerosols during our studies, as shown by [Ofner *et al.* 2012]. This indicates the reaction of Cl directly with the SOA. There is growing evidence in the strong interaction of halogens with organics

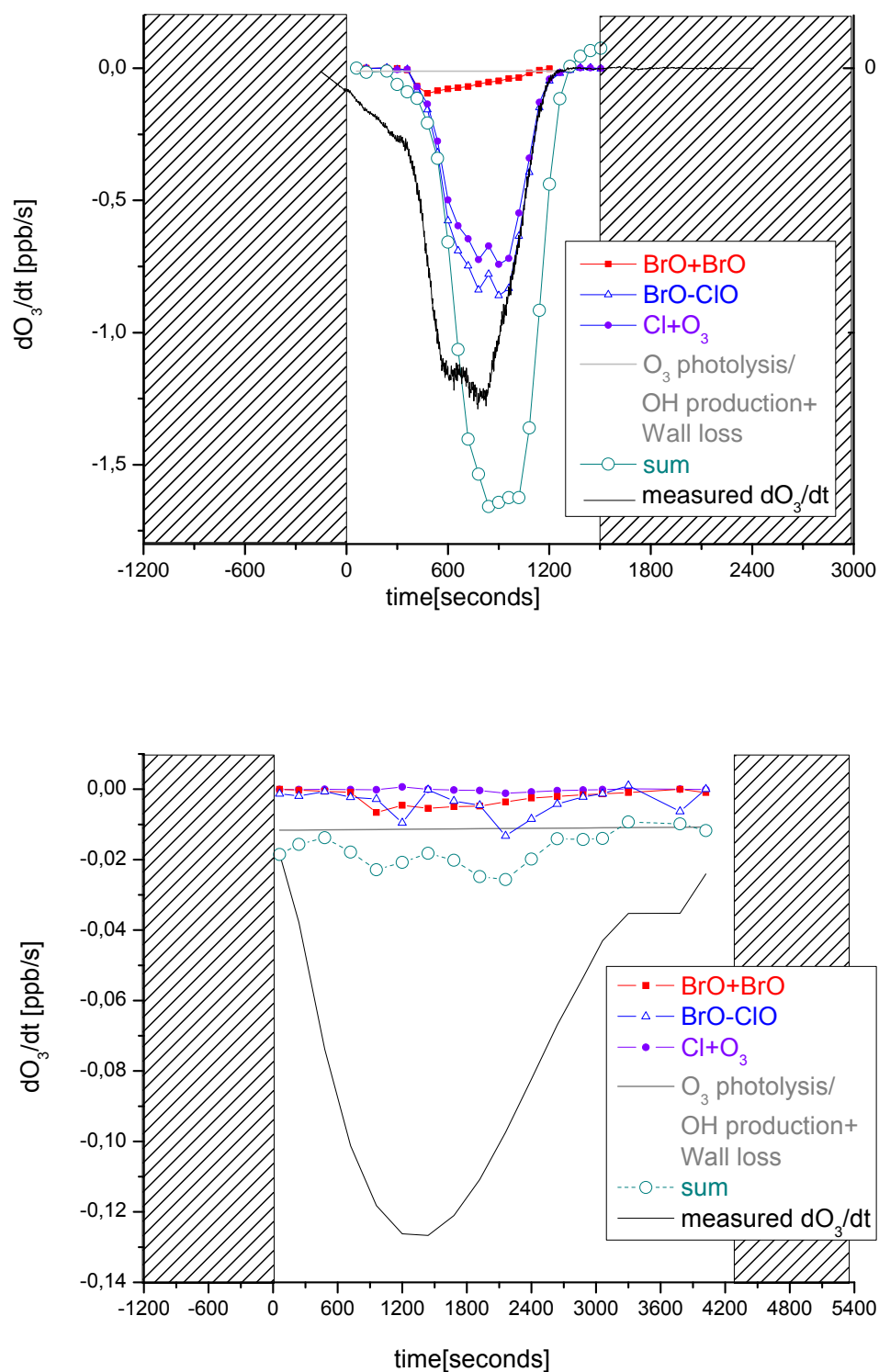


Figure 6.4.: Comparison of the simple model calculations for dO_3/dt and measured derivative of O_3 for the experiments AeNOxh760oz (top) and AeNOxl86NaBrHC (bottom).

from literature. The formation simple molecules in the atmosphere like phosgene, chloroacetone and 1,1-dichloroacetone after interaction of hydrocarbons with halogens released from NaCl aerosol was found and a detailed review on these formation pathways is given by *Zetzsch and Behnke* 2005. *Smoydzin and von Glasow* 2007 discussed the influence of organic surface films on halogen release from sea salt aerosols. Gas phase concentrations for chlorine and bromine species might have decreased due to the decreased mass transfer between gas phase and the salt pan surface. Depending on the kind of SOA and the halogen source, quite different changes in the aerosol size distribution can be observed. The chemical transformation and the related change in optical properties are indicated by the change in the color of the halogenated organic aerosols (haloSOA) [*Ofner et al.* 2012]. The formation of secondary particles from the reacted SOA is indicated (compare figure 5.19). SOA strongly influences the RHS release-mechanism, hampering the BE and causing a decrease of the ozone depletion (compare figure 5.18). However, detailed interpretation of the data sets due to high detection limit of the WS especially for α -pinene is challenging hamper. Given the indicated importance of the interaction between the organic matter and RHS, and the remaining unknown question of the exact mechanisms, more experiments are needed.

6.5. Atmospheric Relevance

One may ask the question of atmospheric relevance of the chamber experiments performed in the scope of this thesis. Temperature and relative humidity in the chamber are kept comparable to that of the atmosphere (20°C and 20-70%). The radiation of our solar simulator was improved by an UV-filter and an IR-filter compared to [*Siekmann* 2008], and is comparable to solar radiation. The salt solution contains similar amount of Br/Cl, as compared to sea water ($\approx 1:230$) or the Dead Sea ($\approx 1:20$). The salt pan experiments are the first of their kind for simulating the surface of a salt flat. However, to answer the question of atmospheric relevance, one needs to keep in mind that there are some significant differences between the smog chamber and atmospheric environments. First the concentration of O_3 was by a factor of ten higher than usually observed under tropospheric conditions. Typical values for the boundary layer height are 500 m-1.5 km. Comparing this to the aerosol volume to surface ratio of 125 m yields a factors of 4-10. One could imagine the source of halogens being located in the lower part of the troposphere close to the ground (salt flats) or ocean surface. The released halogens are then mixed up to the boundary layer height with a dilution factor of 4-10. In smog chamber experiments with salt aerosols, levels of BrO of hundreds ppt to a maximum of 1.6 ppb were observed. This would lead to tropospheric mixing ratios in the lower ppt range for low NO_x conditions, and 400 ppt to 160 ppt for high NO_x . For the salt pan, a surface/volume ratio of 0.14 m^{-1} leads to a 7 m boundary layer height equivalent,

and BrO was observed up to 6ppb. Indeed, in the Dead sea valley (with 200ppb of BrO), as well as the Great Salt lake (with 40ppb of BrO) up to ppb levels of NO₂ are present[e.g. *Matveev et al.* 2001, *Stutz et al.* 2002]. In contrast, NO₂ levels at Mauritania or Australia, or over large parts of the open ocean, remain in the several hundred ppt range and below. BrO often was found to be below the detection limit of our DOAS instruments of lower ppt range [*Holla* 2010, *Lampel* 2012]. Reactions with organics might have an influence as well, as indicated by the SOA interaction. However, NO₂ levels in polar regions are low as well, and high BrO mixing ratios were found after polar sunrise. This might be due to different conditions in terms of temperature dependence of the reaction, and meteorology (e.g. [*Pöhler* 2010, *Sihler* 2007]). Additionally, during the winter dark period, precursors such as Br₂, OBrO or even OCIO might be formed in the polar regions, which is suggested by the smog chamber experiments. Comparison of the BrO formation rates with smog chamber experiments and possible sources, such as Br₂ photolysis, could prove this assumption.

However, the discussion about atmospheric relevance shows that some of the mechanisms occurring in the atmosphere can be simulated, but should be treated carefully, as the chamber has many differences compared to the atmosphere, such as e.g. low CH₄ and comparably high O₃. So realizing the surprising formation of large amounts of Chlorine species, a question remains: Is chlorine explosion (CE) possible under atmospheric conditions? Given the results of the smog chamber experiments so far, there is a strong evidence, that the likelihood depends on the concentrations of CH₄ (or other HC), O₃ and NO₂.

7. Conclusions and Outlook

Within the scope of this thesis, the first direct observation of BrO caused by BE under laboratory conditions was observed. In addition first direct and simultaneous detection of BrO, OClO and ClO released from artificial sea salt aerosols were made. The enhanced release of these RHS under high O₃ and NO₂ conditions suggest that CE may occur in highly polluted environments. The word explosion describes the fast heterogeneous release with initial rates of 40 ppt/s for BrO and OClO, and 15 ppt/s for ClO.

The first aim of this work was to set up a compact multi reflection system in a special laboratory with very limited space. Initially, a WS was successfully installed, with a slant frame and specially designed transfer optics. The WS is capable of simultaneous detection of BrO, ClO, OClO, NO₂, O₃, HCHO and HONO. Then a CE-DOAS instrument using a UV-LED as a light source was adapted to the same smog chamber. This CE-DOAS, with low cost and low power UV-LED in comparison to the commonly used light sources, is the first of its kind. Successful inter comparison measurements of the two multi reflection systems as well as CL monitors for O₃ and NO₂, a UV photometric O₃ monitor, and a LOPAP for HONO detection, demonstrate the reliability of the instruments.

To simulate halogen release from salt surfaces such as salt deserts or salt pans, a analog salt pan was used. The experimental set-up was comparable to environmental conditions where halogen release was previously observed. During BE from the artificial salt pan, very fast initial production rates of BrO within the first minutes of our experiments were observed. During experiments with sea salt aerosols, fast rates for the formation of OClO were observed. To address the question proposed in the introduction:

What are the unknown release mechanisms not yet described by the current state of understanding of halogen chemistry?

There is strong evidence that OClO and OBrO are formed as precursors to CE and BE, possibly even during the dark phase, due to observed fast build up of BrO and ClO. Cl₂ and Br₂ are less likely precursors given their photolysis rates in comparison to OClO and OBrO. Simple model calculations using the measured OClO, BrO, ClO and O₃ mixing ratio indicate that the cross reaction of BrO and ClO, previously believed to be the primary source of OClO, is not sufficient to describe the observation. However, the initial release mechanism of these RHS is not clear yet.

A strong correlation between the maximum halogen oxide concentration and the initially injected O_3 and NO_2 concentrations was observed. This leads to the answer of the questions

What triggers the halogen release processes?

Does the concentration of NO_x significantly affect the release of bromine or chlorine species?

O_3 abundance is crucial for the strength of BE. High values of NO_2 lead to unexpectedly high formation of chlorine species, most likely caused by low pH of the aerosol phase. The pH dependence confirms previous findings [von Glasow and Sander 2001]. The heterogeneous surface reaction of O_3 was suggested as an initial source for gas phase Br_2 or other precursors (e.g. $BrCl$). A theoretical approach here shows that the heterogeneous uptake reaction on the salt pan surfaces for high uptake coefficients is mainly diffusion controlled, whereas in the case of aerosols, diffusion is negligible in importance. For small uptake probabilities such as for ozone, uptake on the salt pan is one order of magnitude faster than on the aerosols. This indicates a significant difference in RHS release between salt pans and aerosols.

Another question was

Do the relative humidity and thus the water content of the halogen source play a major role?

A strong correlation of the maximum released BrO with RH was observed. The peak BrO concentration was one order of magnitude higher at 60 % RH compared to at 37 % RH. The evolution of the OH radicals is strongly influenced by the ozone time series. This demonstrates the change in the mixing ratios in the HOx family caused by bromine-related ozone destruction. The impact of reactive bromine chemistry in the troposphere, including the effect on OH/ HO_2 ratio, has been discussed by [von Glasow and Crutzen 2007]. The total concentration of OH radicals, measured via the radical clock method, was found to be in the same range during different experiments. From this observation, we conclude that HO_2 levels, which influence the BE process, should not have varied drastically at environmentally relevant RH. It has been reported before that the number of micro layers of water on the surface of salt crystals strongly depends on RH. It can be concluded that exchange reactions at the air-water interface (with dissolved halide ions) play a key role in halogen release. A very simple model, which does not account for the heterogeneous mechanisms nor reactions of NO_x or hydrocarbons, explains the measured O_3 depletion reasonably well for 2 % RH and 37 % RH. However, there is considerable disagreement between the model and the measured O_3 destruction for 60 % RH and 68 % RH.

The experiments of SOA and RHS released from the salt pan addressed the question:

To which degree do organics possibly inhibit the release of the halogen oxides, including BrO and ClO?

Experiments with SOA show an increase in the particle diameters, as well as strongly decreased BrO formation. But due to the high aerosol concentration, the detection limit of the DOAS instruments was poor especially for experiments with α -pinene as precursor. Detailed interpretation, of the data sets is hampered. However, a strong influence BrO formation by organic aerosols and vice versa is indicated by the performed aerosol smog-chamber experiments. The interactions between BrO and SOA depend on the particular aerosol as well as on the halogen source ([Ofner *et al.* 2012]). No ClO measurements were made, as the detection limit of 1 ppb for the current aluminum mirrors would be too high given the expected mixing ratios below hundreds of ppt. A possible reason for lower BrO formation might be reactions with SOA, the precursor or intermediate in the reaction with Br. Another possibility could be an organic film on top of the salt layer. Hence, the exact mechanisms was not identified.

Overall the results of the present study on salt aerosols and salt pans may contribute to the improvement of existing models [von Glasow and Sander 2001, von Glasow *et al.* 2002]. A 0-dimensional (box-) model, including reactions of halogens, NO_x and hydrocarbons, as well as the heterogeneous phase, is under development in the Bayreuth laboratory [Bleicher 2012]. The strong dependence on RH, O_3 and NO_2 may provide important clues as to the favored conditions for BE and possibly CE events at salt lakes, as well as marine environments.

As usual in such a hot topic of ongoing research, many problems and questions remain unresolved. Further modeling studies, smog chamber experiments and field campaigns can help to improve our understanding of the highly reactive halogen species and their influence on our environment. Some ideas are listed here.

Model studies: The simple model calculations describe halogen induced ozone destruction fairly well, but many reactions are not included. Recent 0-box model studies by [Bleicher 2012] look very promising in the case of sea salt aerosols, and might give further explanations for the mechanisms involving RHS. Further modeling studies of the salt pan experiments should include an estimate of a total ozone production potential for the given amount of HC, NO_x , OH and Cl in the smog chamber. Knowing the potential O_3 production might help explaining the differences. If the measured O_3 loss is lower than predicted by the model, this indicates unknown sources of O_3 . An new possible O_3 source might play a role for tropospheric chemistry, as so far the only known source for tropospheric O_3 formation is the NO_x -HC cycle [Finlayson-Pitts and Pitts 2000].

Smog chamber experiments: The potential formation of precursor species OCIO and OBrO should be further addressed in smog chamber experiments. One possibility

is a spectral identification in the 425 nm range of OBrO with a high time resolution with the WS during salt pan experiments. A key question arose during the experiments with high NO_x , where a chlorine explosion was observed: Is Chlorine explosion possible under atmospheric conditions? The value of CH_4 in the chamber was lower than that for the atmosphere. Recent experiments with ppm range of CH_4 , resulted in a structured residual of the DOAS fit, possibly caused by an impurity in the CH_4 gas (the purity was 99.8%). Further analysis is needed. Experiments at CH_4 , O_3 and NO_x levels similar to the atmosphere, would help to address the question of the atmospheric relevance of CE. An interesting experiment would also be, instead of injecting high levels of O_3 , keeping O_3 constant over a certain amount of time. This would simulate arrival of ozone by a different air mass. The influence of SOA on RHS and vice versa, should be further investigated to address, the mechanisms, and e.g. calculate an overall reaction rate of Br with different SOA precursors at different concentrations.

Field measurements: Technical improvement of the CE-UV DOAS for field measurements is strongly recommended. There are many regions, where the location of the source is not clear. Enrichment of BrO close to the ground is very likely, given the results of the smog chamber experiments. Especially at salt lakes, the question of the discrepancy between very high and low amounts of BrO at different salt lakes is not unanswered. Volcanoes might be another region of interest as high amounts of BrO are detected in the volcanic plume, and the chemistry is not well understood [Bobrowski *et al.* 2007]. However, aerosols from the corrosive sulfuric acid and volcanic ash, might be a technical challenge. Measurements of reactive chlorine species (especially Cl, ClO, OClO) are very rare, as the measurement technique for low ppt concentrations is not developed yet [von Glasow and Salzmänn 2012]. The smog chamber provides an excellent environment for testing new development such as a CE-DOAS for the detection of ClO. Technical improvements of other kinds, such as DOAS or mass spectroscopic instruments, might be even more promising because of high sensitivity. Another possibility is outdoor chambers at potential halogen source region e.g. a salt flat, to increase RHS in a closed system. And thus investigate the chemistry directly at the place of interest.

Cooperation between different groups of researchers from different fields like in the present study, should be key in ongoing experiments, modeling and field measurements. Only if scientists from different fields like physics, chemistry and geo-ecology work together, answers to the main questions of atmosphere and environment can be found.

References

- Abbatt, J. P. D. and G. C. G. Waschewsky (1998). Heterogeneous Interactions of HOBr, HNO₃, O₃, and NO₂ with Deliquescent NaCl Aerosols at Room Temperature. *J. of Phys. Chem. A*, Vol. 102, 3719.
- Adams, J. W., N. S. Holmes, and J. N. Crowley (2002). Uptake and reaction of HOBr on frozen and dry NaCl/NaBr surfaces between 253 and 233 K. *Atmospheric Chemistry and Physics*, Vol. 2, No. 1, 79–91.
- Aguzzi, A. and M. Rossi (1999). The kinetics of the heterogeneous reaction of BrONO₂ with solid alkali halides at ambient temperature. A comparison with the interaction of ClONO₂ on NaCl and KBr. *Phys.Chem.Chem.Phys.*, Vol. 1, No. 1, 4337.
- Albritton, D. L., A. L. Schmeltekopf, and R. N. Zare (1976). An Introduction to the Least-Squares Fitting of Spectroscopic Data. In R. K. Narahari and M. W. Weldon (Eds.), *Molecular Spectroscopy: Modern Research*. Orlando, Florida, USA: Academic Press.
- Allan, W., H. Struthers, and D. C. Lowe (2007). Methane carbon isotope effects caused by atomic chlorine in the marine boundary layer: Global model results compared with Southern Hemisphere measurements. *J. Geophys. Res.D*, Vol. 112, No. D04306.
- Anderson, L. C. and D. W. Fahey (1989). Studies with ClONO₂: Thermal Dissociation and NO/O₃; Chemiluminescence Detector. *Analyt. Chem.*, Vol. 94, 644–652.
- Ariya, P. A., A. Khalizov, and A. R. Gidas (2002). Reactions of gaseous mercury with atomic and molecular halogens: Kinetics, product studies, and atmospheric implications. *Journal of Phys. Chem. A*, Vol. 106, 7310–7320.
- Aschmann, S. and A. R. (1995). Rate constants for the gas-phase reactions of alkanes with Cl atoms at 296 ± 2 K. *Int. J. Chem. Kinet.*, Vol. 27, 613.
- Atkinson, R., D. L. Baulch, R. A. Cox, J. N. Crowley, R. F. Hampson, R. G. Hynes, M. E. Jenkin, M. J. Rossi, and J. Troe (2004). Evaluated kinetic and photochemical data for atmospheric chemistry: Volume I - gas phase reactions of O_x, HO_x, NO_x and SO_x species. *Atmospheric Chemistry and Physics*, Vol. 4, No. 6, 1461–1738.

REFERENCES

- Atkinson, R., D. L. Baulch, R. A. Cox, J. N. Crowley, R. F. Hampson, R. G. Hynes, M. E. Jenkin, M. J. Rossi, and J. Troe (2007). Evaluated kinetic and photochemical data for atmospheric chemistry: Volume III – gas phase reactions of inorganic halogens. *Atmospheric Chemistry and Physics*, Vol. 7, No. 4, 981–1191.
- Ball, S., J. Langridge, and R. Jones (2004). Broadband cavity enhanced absorption spectroscopy using light emitting diodes. *Chem. Phys. Lett.*, Vol. 398, 68–74.
- Bedjanian, Y., V. Riffault, G. Poulet, and G. LeBras (2001). Kinetic Study of the Reactions of Br with HO₂ and DO₂. *J. Phys. Chem.*, Vol. 105, 573–578.
- Behnke, W., M. Elend, U. Krüger, and C. Zetzsch (1999). The Influence of NaBr/NaCl Ratio on the Br-Catalysed Production of Halogenated Radicals. *Journal of Atmospheric Chemistry*, Vol. 34, 87–99.
- Behnke, W., H. Krüger, V. Scheer, and C. Zetzsch (1992). Formation of ClNO₂ and HONO in the presence of NO₂, O₃ and wet NaCl-aerosol. *Journal of Aerosol Science*, Vol. 23, 933–936.
- Behnke, W., V. Scheer, and C. Zetzsch (1993). Formation of ClNO₂ and HNO₃ in the presence of N₂O₅ and wet pure NaCl– and wet mixed NaCl/Na₂SO₄-aerosol. *Journal of Aerosol Science*, Vol. 24, 115–116.
- Bertram, T. H., J. A. Thornton, T. P. Riedel, A. M. Middlebrook, R. Bahreini, T. S. Bates, P. K. Quinn, and D. J. Coffman (2009). Direct observations of N₂O₅ reactivity on ambient aerosol particles. *Geophys. Res. Letters*, Vol. 36, No. L19803.
- Bevington, P. (1969). *Data Reduction and Error Analysis for the Physical Sciences*. New York: McGraw-Hill.
- Bierbach, A., I. Barnes, and K. H. Becker (1999). Atmospheric Chemistry of Unsaturated Carbonyls. *Int. J. Chem. Kinet.*, Vol. 28, 565.
- Blasius, H. (1908). *Z. Math. Phys.*, Vol. 56, 1–37.
- Bleicher, S. (2012). *Halogenaktivierung im Aerosol und Salzpflanzen -Experimente und Modellierung in einer Umweltkammer*. Ph.D. thesis, Universität Bayreuth, Atmosphärische Chemie. in prep.
- Bobrowski, N., R. von Glasow, A. Aiuppa, S. Inguaggiato, I. Louban, O. Ibrahim, and U. Platt (2007). Reactive halogen chemistry in volcanic plumes. *Jgr*, Vol. 112, No. D06311.
- Boucher, O., C. Moulin, S. Belviso, O. Aumont, L. Bopp, E. Cosme, R. von Kuhlmann, M. G. Lawrence, M. Pham, M. S. Reddy, J. Sciare, and C. Venkataraman (2003). DMS atmospheric concentrations and sulphate

- aerosol indirect radiative forcing: a sensitivity study to the DMS source representation and oxidation. *Atmos. Chem. Phys.*, Vol. 3, 49–65.
- Burrows, J., A. Dehn, B. Deters, S. Himmelmann, A. Richter, S. Voigt, and J. Orphal (1998). Atmospheric Remotesensing Reference Data from GOME: Part 1. Temperature-dependent Absorption Cross Section of NO₂ in the 231–794 nm Range. *J. Quant. Spectrosc. Radiat. Transfer.*, Vol. 60, 1025–1031.
- Buxmann, J. (2008a). unpublished MAX DOAS BrO measurements in Namibia/Botswana <3 ppt.
- Buxmann, J. (2008b). *Optimierte Langpfad- DOAS Messungen von BrO und ClO an der irischen Westküste*. Diploma thesis, Institut für Umweltphysik, Universität Heidelberg.
- Buxmann, J., N. Balzer, S. Bleicher, U. Platt, and K. Zetzsch (2012). Observations of bromine explosions in smog chamber experiments above a model salt pan. *Int. J. Chem. Kinet.*, Vol. 44, 312–326.
- Carter, W. P. L. (1999). Measurement and modeling of NO_x offgasing from FEP teflon chambers. Technical report, Air Pollution Research Center and College of Engineering Center for Environmental Research and Technology, University of California.
- Chang, J. S., A. C. Baldwin, and D. M. Golden (1979). An explanation of the preferential formation of less stable isomers in three-body reactions: Cl + NO₂ + M; ClO + NO₂ + M. *Journal of Chemical Physics*, Vol. 2, No. 71, 2021–2024.
- Clifford, D. and D. J. Donaldson (2007). Direct Experimental Evidence for a Heterogeneous Reaction of Ozone with Bromide at the Air-Aqueous Interface. *Appl. Opt.*, Vol. 111, 9809.
- Crowley, J. N., M. Ammann, R. A. Cox, R. G. Hynes, M. E. Jenkin, A. Mellouki, M. J. Rossi, J. Troe, and T. J. Wallington (2010). Evaluated kinetic and photochemical data for atmospheric chemistry: Volume V: heterogeneous reactions on solid substrates. *Atmos. Chem. Phys.*, Vol. 10, No. 18, 9059–9223.
- Davidovits, P., C. E. Kolb, L. R. Williams, J. T. Jayne, and D. R. Worsnop (2006). Mass Accommodation and Chemical Reactions at Gas-Liquid Interfaces. *Chem. Rev.*, Vol. 106, No. 1323.
- DeMore, W., S. Sander, D. Golden, R. Hampson, M. Kurylo, C. Howard, A. Ravishankara, C. Kolb, and M. Molina (1994). Chemical kinetics and photochemical data for use in stratospheric modeling. *NASA JPL Publication*,, 24–26.
- DeMore, W. B., S. P. Sander, C. J. Howard, A. R. Ravishankara, D. M. Golden, C. E. Kolb, R. F. Hampson, M. J. Kurylo, and M. J. Molina (1997). Chemical Kinetics and Photochemical Data for Use in Stratospheric Modeling No. 12. Jet Propulsion Laboratory, Pasadena, Publication 97-4.

REFERENCES

- Dorf, M., J. Butler, A. Butz, C. Camy-Peyret, M. Chipperfield, L. Kritten, S. Montzka, B. Simmes, F. Weidner, and K. Pfeilsticker (2006). Long-term observations of stratospheric bromine reveal slow down in growth. *Geophys. Res. Lett.*, Vol. 33.
- Etzkorn, T. (1998). *Untersuchungen atmosphärisch relevanter Reaktionssysteme mittels Differentieller Optischer Absorptionsspektroskopie*. Ph.D. thesis, Institut für Umweltphysik, Universität Heidelberg.
- Ferracci, V., K. Hino, and D. M. Rowley (2011). Kinetic studies on the temperature dependence of the $\text{BrO} + \text{BrO}$ reaction using laser flash photolysis. *Phys. Chem. Chem. Phys.*, Vol. 13, –.
- Fickert, S., J. W. Adams, and J. N. Crowley (1999). Activation of Br_2 and BrCl via uptake of HOBr onto aqueous salt solutions. *J. Geophys. Res.*, Vol. 104, 23719.
- Fiedler, S., A. Hese, and U. Heitmann (2007). Influence of the cavity parameters on the output intensity in incoherent broadband cavity-enhanced absorption spectroscopy. *Rev. Sci. Instrum.*, Vol. 78, No. 073104, 073104.
- Field, R. J. and H. D. Foersterling (1986). On the oxybromine chemistry rate constants with cerium ions in the Field-Koeroes-Noyes mechanism of the Belousov-Zhabotinskii reaction. *J. Phys. Chem.*, Vol. 90, 5400.
- Finlayson-Pitts, B. and N. Pitts (2000). Chemistry of the Upper and Lower Atmosphere. *ACADEMIC PRESS*,, p.158 ff.
- Finlayson-Pitts, B. J. (2003). The Tropospheric Chemistry of Sea Salt: A Molecular-Level View of the Chemistry of NaCl and NaBr . *Chem. Rev.*, Vol. 103, 4801–4822.
- Finlayson-Pitts, B. J., M. J. Ezell, and J. N. Pitts (1989). Formation of chemically active chlorine compounds by reactions of atmospheric NaCl particles with gaseous N_2O_5 and ClONO_2 . *Nature*, Vol. 337, 241–244.
- Fleischmann, O. C. and J. Burrows (2004). New ultraviolet absorption cross-sections of BrO at atmospheric temperatures measured by time-windowing fourier transform spectroscopy. *J. Photochem. Photobiol. A: Chem.*, Vol. 168, 117–132.
- Frankenberg, C., U. Platt, and T. Wagner (2005). Iterative maximum a posteriori (IMAP)-DOAS for retrieval of strongly absorbing trace gases: Model studies for CH_4 and CO_2 retrieval from near infrared spectra of SCIAMACHY onboard ENVISAT. *Atmos. Chem. Phys.*, Vol. 5, 9–22.
- Frenzel, A., V. Scheer, R. Sikorski, C. George, B. W., and C. Zetzsch (1998). Heterogeneous Interconversion Reactions of BrNO_2 , ClNO_2 , Br_2 and Cl_2 . *J. Phys. Chem A*, Vol. 102, 1329–1337.

- Geenspan, L. (1977). Humidity fixed points of binary saturated aqueous solutions. *J. Res. Nat. Bur. Stand.*, Vol. 81A, 89–96.
- Gonser, S. (2011). Photograph of Mie scattering from aerosols.
- Greenblatt, G. D., J. J. Orlando, J. B. Burkholder, and A. R. Ravishankara (1990). Absorption measurements of oxygen between 330 and 1140 nm. *J. Geophys. Res.-Atmos.*, Vol. 95, 18577–18582.
- Hak, C., I. Pundt, S. Trick, C. Kern, U. Platt, J. Dommen, C. Ordonez, A. Prevot, W. Junkermann, C. Astorga-Llorens, B. Larsen, J. Mellqvist, A. Strandberg, Y. Yu, B. Galle, J. Kleffmann, J. Lorzer, G. Braathen, and R. Volkamer (2005, NOV 2). Intercomparison of four different in-situ techniques for ambient formaldehyde measurements in urban air. *Atmos. Chem. Phys.*, Vol. 5, 2881–2900.
- Harwood, M. H., D. M. Rowley, A. Cox, and L. J. Roderic (1998). Kinetics and Mechanism of the BrO Self-Reaction: Temperature- and Pressure-Dependent Studies. *J. Phys. Chem. A*, Vol. 102, 1798.
- Hebestreit, K., J. Stutz, D. Rosen, V. Matveiv, M. Peleg, M. Luria, and U. Platt (1999). DOAS measurements of tropospheric bromine oxide in mid-latitudes. *Science*, Vol. 283, 55–57.
- Hoch, D., J. Buxmann, H. Sihler, D. Pöhler, C. Zetzsch, and U. Platt (2012). Cavity-Enhanced Differential Optical Absorption Spectroscopy instrument for measurement of BrO, HCHO, HONO and O₃. *Atmos. Meas. Tech. Discuss.*, Vol. submitted.
- Hoch, D. J. (2010). *Resonator Verstärkte Differentielle Optische Absorptions Spektroskopie: Labormessungen von BrO, HCHO, HONO und O₃*. Master’s thesis, Inst. for Environmental Physics (IUP), Atmosphere and Remote Sensing, Ruprecht-Karls-Universität Heidelberg, Germany.
- Holla, R. (2010). per. comm. about MAX DOAS BrO measurements in Southern Russia and Mauritania (<2-5ppt).
- Hönninger, G., N. Bobrowski, Palenque, R. Torrez, and U. Platt (2004). Reactive bromine and sulfur emissions at Salar de Uyuni, Bolivia. *Geophys. Res. Lett.*, Vol. 31, L04101.
- Hönninger, G., C. von Friedeburg, and U. Platt (2004). Multi axis differential optical absorption spectroscopy (MAX-DOAS). *Atmos. Chem. Phys.*, Vol. 4, 231–254.
- Hooshiyar, P. A. and H. Niki (1995). Rate constants for the gas-phase reactions of Cl-atoms with C₂[BOND]C₈ alkanes at T = 296 ± 2 K. *Int. J. Chem. Kinet.*, Vol. 27, 1197.

REFERENCES

- Huff, A. and J. Abbatt (2000). Gas-Phase Br₂ Production in Heterogeneous Reactions of Cl₂, HOCl, and BrCl with Halide-Ice Surfaces. *Journal of Phys. Chem. A*, Vol. 104, 7284.
- Hunt, S. W., M. Roeselova, W. Wang, L. M. Wingen, E. M. Knipping, D. J. Tobias, D. Dabdub, and B. J. Finlayson-Pitts (2004). Formation of Molecular Bromine from the Reaction of Ozone with Deliquesced NaBr Aerosol: Evidence for Interface Chemistry. *J. Phys. Chem. A*, Vol. 108, 11559–11572.
- Keller-Rudek, H. and G. K. Moortgat. UV-VIS spectral atlas of gaseous molecules. A database of atmospherically relevant species, including numerical data and graphical presentations. www.atmosphere.mpg.de/spectral-atlas-mainz.
- Kern, C. (2009). *Spectroscopic measurements of volcanic gas emissions in the ultra-violet wavelength region*. Ph. D. thesis, University of Heidelberg, Heidelberg, Germany.
- Kleffmann, J., J. Heland, R. Kurtenbach, J. Lörzer, and P. Wiesen (2002). A new instrument (LOPAP) for the detection of nitrous acid (HONO). *Environ. Sci. Pollut. R.*, Vol. 4, 48–54.
- Kleffmann, J., J. Lörzer, P. Wiesen, C. Kern, S. Trick, R. Volkamer, M. Rodenas, and K. Wirtz (2006). Intercomparison of the DOAS and LOPAP techniques for the detection of nitrous acid (HONO). *Atmospheric Environment*, Vol. 40, 3640–3652.
- Knight, G., A. Ravishankara, and J. Burkholder (2000). Laboratory studies of OBrO. *J. Phys. Chem.*, Vol. A 104, 11121–11125.
- Kolb, C. E., D. R. Worsnop, M. S. Zahniser, P. Davidovits, L. F. Keyser, M.-T. Leu, M. J. Molina, D. R. Hanson, A. R. Ravishankara, L. R. Williams, and M. A. Tolbert (1995). Laboratory Studies of Atmospheric Heterogeneous Chemistry. in *Progress and Problems in Atmospheric Chemistry*, (J. R. Barker, Ed.), *Advanced Series in Physical Chemistry* (C.-Y. Ng, Ed.), *World Scientific, Singapore*, Vol. 3, Chap.18.
- Kraus, S. (2004). DOASIS: DOAS Intelligent Sytem. Software, copyright 2004 Stefan Kraus, Institute of Environmental Physics, University of Heidleberg, Germany. in cooperation with Hoffmann Messtechnik GmbH.
- Kromminga, H., S. Voigt, J. Orphal, and J. P. Burrows (1999). UV-visible FT spectra of OClO at atmospheric temperatures. In *Proceedings of the 1st European Symposium on Atmospheric Measurements from Space*. ESA Special Publication.
- Lampel, J. (2010-2012). unpublished MAX DOAS BrO measurements from Polarstern (research vessel).
- Leighton, P. (1961). Photochemistry of air pollution. *Academic Press, New York*,.

- Levenberg, K. (1944). A Method for the Solution of Certain Non-Linear problems in Least Squares. *Quart. Appl. Math.*, Vol. 2, 164–168.
- Liu, W. T., K. B. Katsaros, and J. A. Businger (1979). Bulk Parameterization of the Air Sea Exchange of Heat and Water Vapor Including the Molecular Constraints at the Interface. *J. Atmos. Sci.*, , No. 36, 1722–1735.
- Maric, D., J. P. Burrows, M. R., and G. K. J. Moortgat (2005). A study of the UV-visible absorption spectrum of molecular chlorine. *Bericht der Bunsen-Gesellschaft, Phys. Chem.*, Vol. 70, 2005.
- Marquardt, D. W. (1963). An Algorithm for Least Squares Estimation of Non-Linear Parameters. *Soc. Indust. Appl. Math.*, Vol. 11, 431–441.
- Martin, M. (2007). *Measurements of Halogen Oxide Radicals over the North Atlantic*. Diploma thesis, Institut für Umweltphysik, Universität Heidelberg.
- Matveev, V., M. Peleg, D. Rosen, D. S. Tov-Alper, K. Hebestreit, J. Stutz, U. Platt, D. Blake, and M. Luria (2001). Bromine oxide - ozone interaction over the Dead Sea. *J. Geophys. Res.*, Vol. 106, 10375–10387.
- McConnell, J. C., G. S. Henderson, , L. Barrie, J. Bottenheim, H. Niki, C. H. Langford, and E. M. Templeton (1992). Vol. 355, 150.
- Meinen, J., J. Thieser, U. Platt, and T. Leisner (2010). Technical Note: Using a high finesse optical resonator to provide a long light path for differential optical absorption spectroscopy: CE-DOAS. *Atmos. Chem. Phys.*, Vol. 10, 3901–3914.
- Meller, R. and G. Moortgat (2000, MAR 27). Temperature dependence of the absorption cross sections of formaldehyde between 223 and 323 K in the wavelength range 225–375 nm. *J. Geophys. Res.-Atmos.*, Vol. 105, No. D6, 7089–7101.
- Mellouki, A., R. Talukdar, and C. Howard (1994). Kinetics of the reactions of HBr with O and HO: The yield of HBr from HO + BrO. Vol. 99, D11.
- M. Horbanski (2010). *A Compact Resonator Based Instrument for DOAS Measurements of Ambient Nitrogen Dioxide*. Diploma thesis, Institut für Umweltphysik, Universität Heidelberg.
- Mochida, M., H. Akimoto, and H. van den Bergh (1998). Heterogeneous Kinetics of the Uptake of HOBr on Solid Alkali Metal Halides at Ambient Temperature. *Journal of Phys. Chem. A*, Vol. 102, 4819.
- Mochida, M., J. Hirokawa, and H. Akimoto (2000). Unexpected large uptake of O₃ on seasalts and the observed Br₂ formation. *Geophys. Res. Lett.*, Vol. 27, 2629–2632.
- Moffet, R. C., B. de Foy, L. T. Molina, M. J. Molina, and K. A. Prather (2008). Measurement of ambient aerosols in northern Mexico City by single particle

REFERENCES

- mass spectrometry. *Atmospheric Chemistry and Physics*, Vol. 8, No. 16, 4499–4516.
- Moortgat G.K., M. R. (2000). Temperature dependances of the absorption cross section HCHO between 223– 323K in the wavelength range 225– 375 nm. *J. Geophys. Res.*, Vol. 105, No. 7089–7102.
- Ofner, J., N. Balzer, J. Buxmann, H. Grothe, P. Schmitt-Kopplin, U. Platt, and C. Zetzsch (2012). Aerosol-halogen interaction: Halogenation processes of SOA. *Atmos. Chem. Phys. Discuss.*, Vol. 12, 2975–3017.
- Ofner, J., H.-U. Krüger, H. Grothe, P. Schmitt-Kopplin, K. Whitmore, and C. Zetzsch (2011). Physico-chemical characterization of SOA derived from catechol and guaiacol; a model substance for the aromatic fraction of atmospheric HULIS. *Atmospheric Chemistry and Physics*, Vol. 11, No. 1, 1–15.
- Orlando, J. and G. Tyndall (1996). Rate coefficients for the thermal decomposition of BrONO₂ and the heat of formation of BrONO₂. *J. Phys. Chem*, Vol. 100, 19398.
- Pechtl, S. and R. von Glasow (2007). Reactive chlorine in the marine boundary layer in the outflow of polluted continental air: A model study. *Geophys. Res. Letters*, Vol. 34, No. L11813.
- Perner, D. and U. Platt (1979). Detection of Nitrous Acid in the Atmosphere by Differential Optical Absorption. *Geophys. Res. Lett.*, Vol. 6, 917–920.
- Peters, S. J. and G. E. Ewing (1997). Water on Salt: An Infrared Study of Adsorbed H₂O on NaCl(100) under Ambient Conditions. *Atmospheric Chemistry and Physics*, Vol. 101.
- Platt, U. (1978). Dry Deposition of SO₂. *Atmos. Env.*, Vol. 12, 363–367.
- Platt, U. (2012). unpublished, Treatment of Heterogeneous Reactions in Chambers-V6.doc.
- Platt, U., W. Allan, and D. Lowe (2004). Hemispheric average Cl atom concentration from ¹³C/¹²C ratios in atmospheric methane. *Atmospheric Chemistry and Physics*, Vol. 4, No. 9/10, 2393–2399.
- Platt, U. and G. Hönninger (2003). The role of halogen species in the troposphere. *Chemosphere*, Vol. 52, 325–338.
- Platt, U. and C. Janssen (1995). Observation and role of the free radicals NO₃, ClO, BrO and IO in the troposphere. *Faraday Discuss.*, Vol. 100, 175–198.
- Platt, U. and C. Janssen (1996). Observation and role of the free radicals NO₃, ClO, BrO and IO in the troposphere. *Faraday Discuss. Chem. Soc.*, Vol. 100, 175–198.
- Platt, U. and E. Lehrer (1996). *Arctic Tropospheric Ozone Chemistry, ARCTOC, Final Report of the EU-Project No. EV5V-CT93-0318, Heidelberg.*

- Platt, U., J. Meinen, D. Pöhler, and T. Leisner (2009). Broadband Cavity Enhanced Differential Optical Absorption Spectroscopy (CE-DOAS) - Applicability and Corrections. *Atmos. Meas. Tech.*, Vol. 2, 713–723.
- Platt, U., D. Perner, and H. W. Pätz (1979). Simultaneous Measurement of Atmospheric CH_2O , O_3 and NO_2 by Differential Optical Absorption. *J. Geophys. Res.*, Vol. 84, 6329–6335.
- Platt, U. and J. Stutz (2008). *Differential Optical Absorption Spectroscopy: Principles and Applications, Physics of Earth and Space Environments*. Springer-Verlag Berlin Heidelberg.
- Pöhler, D. (2010). *Determination of two dimensional trace gas distributions using tomographic LP- DOAS measurements in the city of Heidelberg, Germany*. Phd thesis, University of Heidelberg, Heidelberg, Germany.
- Pöhler, D., L. Vogel, U. Frieß, and U. Platt (2010). Observation of halogen species in the Amundsen Gulf, Arctic, by active long-path differential optical absorption spectroscopy. *P. Natl. Acad. Sci. USA*, Vol. 107, 6582–6587.
- Pratte, P. and M. Rossi (1993). Kinetics and mechanism of the self-reaction of the bromine oxide radical. *J. Phys. Chem. A*, Vol. 97, 7585.
- Pratte, P. and M. Rossi (2006). *J. Phys. Chem. Chem. Phys.*, Vol. 8, 3988.
- Ritz, D., M. Hausmann, and P. U. (1993). An improved open path multi-reflection cell for the measurement of NO_2 and NO_3 . *Proc. SPIE*, Vol. 1715, 200.
- Rossi, M. J. (2003). Heterogeneous Reactions on Salts. *Chem. Rev.*, Vol. 103, 4823–4882.
- Sadanaga, Y., J. Hirokawa, and H. Akimoto (2001). Formation of molecular chlorine in dark condition: Heterogeneous reaction of ozone with sea salt in the presence of ferric ion. *Geophys. Res. Lett.*, Vol. 28.
- Sander, R. and R. Friedl (1989). Kinetics and product studies of the reaction $\text{ClO} + \text{BrO}$ using flash photolysis ultra- violet absorption. *J. Phys. Chem.*, Vol. 93, 4764–4771.
- Scheffler, D., H. Grothe, H. and Willner, A. Frenzel, and C. Zetsch (1997). Properties of Pure Nitryl Bromide. Thermal Behavior, UV/Vis and FTIR Spectra, and Photoisomerization. *Inorg. Chem.*, Vol. 36, 335.
- Schwartz, S. E. (1986). Mass-Transport Considerations Pertinent to Aqueous Phase Reactions of Gases in Liquid-Water Clouds. *NATO ASI Series, G6, 416-471 (1986)*, and in *Chemistry of Multiphase Atmospheric Systems (W. Jaeschke, Ed.)*, Springer-Verlag, 415–471.
- Schwartz, S. E. and J. E. Freiberg (1981). Mass-Transport Limitation to the Rate of Reaction of Gases in Liquid Droplets: Application to Oxidation of SO_2 in Aqueous Solutions. *Atmos. Environ.*, Vol. 15, 1129–1144.

REFERENCES

- Seinfeld, H. and N. Pandis (2008). *Atmospheric Chemistry and Physics: From Air Pollution to Climate Change*, Volume 2. John Wiley and Sons.
- Seitz, K. (2009). *The Spatial Distribution of Reactive Halogen Species at the Irish West Coast*. Ph. D. thesis, university, Heidelberg.
- Shi, J. and M. J. Bernhard (1996). Kinetic studies of Cl-atom reactions with selected aromatic compounds using the photochemical reactor-FTIR spectroscopy technique. *Int. J. chem. Kinet.*, Vol. 29, 349.
- Siekmann, F. (2008). *Freisetzung von photolabilen und reaktiven Halogenverbindungen aus salzhaltigen Aerosolen unter simulierten und troposphärischen Reinluftbedingungen in einer Aerosol-Smogkammer*. Ph. D. thesis, Universität Bayreuth.
- Sihler, H. (2007). *Light-Emitting Diodes as Light Sources in Spectroscopic Measurements of Atmospheric Trace Gases*. Diploma thesis, Institut für Umweltphysik, Universität Heidelberg.
- Sihler, H. (2011). pers.comm. and technical support with the Peltier cooling, of the UV LED.
- Sihler, H. (2012). *Halogen activation in the polar troposphere*. Ph.D. thesis, Institut für Umweltphysik, Universität Heidelberg.
- Sihler, H., C. Kern, D. Pöhler, and U. Platt (2009). Applying light-emitting diodes with narrowband emission features in differential spectroscopy. *Opt. Lett.*, Vol. 34, 3716–3718.
- Simpson, W., R. von Glasow, K. Riedel, P. Anderson, P. Ariya, J. Bottenheim, J. Burrows, L. Carpenter, U. Frieß, M. Goodsite, et al. (2007). Halogens and their role in polar boundary-layer ozone depletion. *Atmos. Chem. Phys.*, Vol. 7, No. 16, 4375–4418.
- Sinreich, R., S. Coburn, B. Dix, and R. Volkamer (2010). Ship-based detection of glyoxal over the remote tropical Pacific Ocean. *Atmospheric Chemistry and Physics*, Vol. 10, No. 23, 11359–11371.
- Sirkes, Z., F. Schirmer, H.-H. Essen, and K.-W. Gurgel (1997). Surface currents and seiches in the Dead Sea. *The Dead Sea: The Lake and Its Setting, edited by: Niemi, T., Ben-Avraham, Z., and Gat, J., Oxford Monogr. Geol. Geophys.*, , No. 36, 104–113.
- Smoydzin, L. (2008). *Modelling Gas Phase and Aerosol Phase Chemistry in the Atmospheric Boundary Layer*. Ph.D. thesis, Institut für Umweltphysik, Universität Heidelberg.
- Smoydzin, L. and R. von Glasow (2007). Do organic surface films on sea salt aerosols influence atmospheric chemistry? A model study. *Atmospheric Chemistry and Physics*, Vol. 7, No. 21, 5555–5567.

- Smoydzin, L. and R. von Glasow (2009). Modelling chemistry over the Dead Sea: bromine and ozone chemistry. *Atmospheric Chemistry and Physics*, Vol. 9, No. 14, 5057–5072.
- Solomon, S., D. Qin, M. Manning, Z. Chen, M. Marquis, K. Averyt, M. Tignor, and H. e. Miller (2007). *IPCC Fourth Assessment Report (AR4), Climate Change 2007: The Physical Science Basis*. Cambridge University Press.
- Solomon, S., A. L. Schmeltekopf, and R. W. Sanders (1987). On the interpretation of zenith sky absorption measurements. *J. Geophys. Res.*, Vol. 92, 8311–8319.
- Sommariva, R., J. Buxmann, Bleicher, U. Platt, C. Zetzsch, and R. von Glasow (2012). Model simulations of bromine explosions in a smog chamber. *SOLAS open science conference*.
- Sörgel, M. (2008). LOPAP HONO measurements.
- Sörgel, M., I. Trebs, A. Serafimovich, A. Moravek, A. Held, and C. Zetzsch (2011). Simultaneous HONO measurements in and above a forest canopy: influence of turbulent exchange on mixing ratio differences. *Atmospheric Chemistry and Physics*, Vol. 11, No. 2, 841–855.
- Stutz, J. (1991). *Charakterisierung von Photodiodenzeilen zur Messung stratosphärischer Spurenstoffe*. Diploma thesis, Institut für Umweltphysik, Universität Heidelberg.
- Stutz, J. (1996). *Messung der Konzentration troposphärischer Spurenstoffe mittels Differentieller Optischer Absorptions Spektroskopie: Eine neue Generation von Geräten und Algorithmen*. Ph. D. thesis, Institut für Umweltphysik, Universität Heidelberg.
- Stutz, J., R. Ackermann, J. D. Fast, and L. Barrie (2002). Atmospheric reactive chlorine and bromine at the Great Salt Lake, Utah. *Geophys. Res. Lett.*, Vol. 29, No. 10.
- Stutz, J., E. Kim, U. Platt, P. Bruno, C. Perrino, and A. Febo (2000). UV-visible absorption cross section of nitrous acid. *J. Geophys. Res.-Atmos.*, Vol. 105, No. D11, 14585–14592.
- Stutz, J. and U. Platt (1996, OCT 20). Numerical analysis and estimation of the statistical error of differential optical absorption spectroscopy measurements with least-squares methods. *Appl. Optics*, Vol. 35, No. 30, 6041–6053.
- Taira, M. and Y. Kanda (1990). Continuous generation system for low-concentration gaseous nitrous acid. *Anal. Chem.*, Vol. 62, 630–633.
- Tang, I. and H. Munkelwitz (1993). Composition and dependence of the deliquescence properties of hygroscopic aerosols. *Atmos. Environ.*, Vol. 27A, 467.
- Tas, E., M. Peleg, D. U. Pedersen, V. Matveev, A. P. Biazar, and M. Luria (2008). Measurement-based modeling of bromine chemistry in the Dead Sea boundary

REFERENCES

- layer - Part 2: The influence of NO₂ on bromine chemistry at mid-latitude areas. *Atmos. Chem. Phys.*, Vol. 8, 4811–4821.
- Thornton, J. A., J. P. Kercher, T. P. Riedel, N. L. Wagner, J. Cozic, J. S. Holloway, W. P. Dube, G. M. Wolfe, P. K. Quinn, A. M. Middlebrook, B. Alexander, and S. S. Brown (2010). A large atomic chlorine source inferred from mid-continental reactive nitrogen chemistry. *Nature*, Vol. 464.
- Troe, J. Z. (2000). Primary quantum yields of NO₂ photodissociation. *Phys. Chem.*, Vol. 214, 573.
- Vandaele, A. C., T. C. Simon, J. M. Goumont, C. M. Carleer, and R. Colin (1994). SO₂ Absorption Cross Section Measurement in the UV using Fourier Transform Spectrometer. *J. Geophys. Res.*, Vol. 99, 25599–25605.
- Venables, D., T. Gherman, J. Orphal, J. Wenger, and A. Ruth (2006). High sensitivity in situ monitoring of NO₃ in an atmospheric simulation chamber using incoherent broadband cavity-enhanced absorption spectroscopy. *Environ. Sci. Technol.*, Vol. 40, 6758–6763.
- Vogel, L. Sihler, H., J. Lampel, T. Wagner, and U. Platt (2012). Retrieval interval mapping, a tool to optimize the spectral retrieval range in differential optical absorption spectroscopy. *Atmos. Meas. Tech. Discuss.*, Vol. submitted.
- Vogt, R., P. J. Crutzen, and R. Sander (1996). A mechanism for halogen release from sea-salt aerosol in the remote marine boundary layer. *Nature*, Vol. 383, 327–330.
- Voigt, S., J. Orphal, K. Bogumil, and J. P. Burrows (2001). The temperature dependence (203–293 K) of the absorption cross sections of O₃ in the 230–850 nm region measured by Fourier-transform spectroscopy. *Journal of Photochemistry and Photobiology*, Vol. 143, 1–9.
- Voigt, S., J. Orphal, and J. P. Burrows (2002). The temperature and pressure dependence of the absorption cross-sections of NO₂ in the 250–800 nm region measured by Fourier-transform spectroscopy. *Journal of Photochemistry and Photobiology*, Vol. 149, 1–7.
- Volkamer, R. (1996). *Absorption von Sauerstoff im Herzberg I System und Anwendung auf Aromatenmessungen am EUROpean PHoto REactor (EUPHORE)*. Diploma thesis, Institut für Umweltphysik, Universität Heidelberg.
- Volkamer, R., W. Junkermann, K. Wirtz, and U. Platt (2002, April). Formation of formaldehyde, glyoxal and methylglyoxal from the toluene + OH reaction in the presence of NO_x. poster presented at EGS XXVII General Assembly, Nice, France.
- von Glasow, R. and P. Crutzen (2003). Tropospheric halogen chemistry. *Treatise on Geochemistry*, Vol. 4, 347.

- von Glasow, R. and P. Crutzen (2007). Tropospheric halogen chemistry. *Treatise on Geochemistry Update 1*, Vol. 4.02, 1–67.
- von Glasow, R. and E. Salzmänn (2012). Climat impact of seasalt-derived Cl atoms, discussion session. SOLAS Open Science Conference 2012.
- von Glasow, R. and R. Sander (2001). Variation of sea salt aerosol pH with relative humidity. *Geophys. Res. Lett.*, Vol. 28, 247–250.
- von Glasow, R., R. Sander, A. Bott, and P. J. Crutzen (2002). Modeling halogen chemistry in the marine boundary layer. 1. Cloud-free MBL. *J. Geophys. Res.*, Vol. 107, 4341, doi: 10.1029/2001JD000942.
- von Glasow, R., R. Sander, A. Bott, and P. J. Crutzen (2002). Modeling halogen chemistry in the marine boundary layer 2. Interactions with sulfur and the cloud-covered MBL. *J. Geophys. Res.*, Vol. 107, No. 17.
- Wachsmuth, M., H. W. Gäggeler, R. von Glasow, and M. Ammann (2002). Accommodation coefficient of HOBr on deliquescent sodium bromide aerosol particles. *Atmospheric Chemistry and Physics*, Vol. 2, No. 2, 121–131.
- Wagner, T. (1994). *Spektroskopische Messung stratosphärischer Spurenstoffe im arktischen Winter 1993/94: Abweichung von der normalen Spurenstoffzusammensetzung*. Diploma thesis, Institut für Umweltphysik, Universität Heidelberg.
- Wagner, T., C. Leue, M. Wenig, K. Pfeilsticker, and U. Platt (2001). Spatial and temporal distribution of enhanced boundary layer BrO concentrations measured by the GOME instrument aboard ERS-2. *J. Geophys. Res.*, Vol. 106, 24225–24235.
- Washenfelder, R. A., A. O. Langford, H. Fuchs, and S. S. Brown (2008). Measurement of glyoxal using an incoherent broadband cavity enhanced absorption spectrometer. *Atmos. Chem. Phys.*, Vol. 8, 7779–7793.
- Wennberg, P. (1999). Bromine explosion. *Nature*, Vol. 397, 299–300.
- Wennberg, P., T. F. Hanisco, L. Jaegle, D. J. Jacob, E. J. Hintsa, E. J. Lanzendorf, J. Anderson, R. S. Gao, E. R. Keim, S. G. Donnelly, L. A. D. Negro, D. W. Fahey, S. A. McKeen, R. J. Salawitch, C. R. Webster, R. D. May, R. L. Herman, M. H. Proffitt, J. J. Margitan, E. L. Atlas, S. M. Schauffler, F. Flocke, C. T. McElroy, and T. P. Bui (1998). Hydrogen radicals, nitrogen radicals, and the production of O₃ in the upper troposphere. *Science*, Vol. 279, 49–53.
- White, J. U. (1942). Long Paths of Large Aperture. *J. Opt. Soc. Am.*, Vol. 32, 285–288.
- White, J. U. (1976). Very long optical paths in air. *J. Opt. Soc. Am.*, Vol. 66, 411–416.

REFERENCES

- Wiedensohler, A., W. Birmili, A. Nowak, A. Sonntag, K. Weinhold, M. Merkel, B. Wehner, T. Tuch, S. Pfeifer, M. Fiebig, A. M. Fjåraa, E. Asmi, K. Sellegri, R. Depuy, H. Venzac, P. Villani, P. Laj, P. Aalto, J. A. Ogren, E. Swietlicki, P. Williams, P. Roldin, P. Quincey, C. Hüglin, R. Fierz-Schmidhauser, M. Gysel, E. Weingartner, F. Riccobono, S. Santos, C. Grüning, K. Faloon, D. Beddows, R. Harrison, C. Monahan, S. G. Jennings, C. D. O'Dowd, A. Marinoni, H.-G. Horn, L. Keck, J. Jiang, J. Scheckman, P. H. McMurry, Z. Deng, C. S. Zhao, M. Moerman, B. Henzing, G. de Leeuw, G. Löschau, and S. Bastian (2012). Mobility particle size spectrometers: harmonization of technical standards and data structure to facilitate high quality long-term observations of atmospheric particle number size distributions. *Atmospheric Measurement Techniques*, Vol. 5, No. 3, 657–685.
- Wilmouth, D. M., T. F. Hanisco, N. M. Donahue, and J. G. Anderson (1999). Fourier transform ultraviolet spectroscopy of the $A^2\Pi_{3/2} \leftarrow X^2\Pi_{3/2}$ transition of BrO. *J. Phys. Chem.*, Vol. 103, 8935–8945.
- W.Roedel (2000). *Physik unserer Umwelt, Die Atmosphäre*, Volume 3 of eds. H. Niki, H. Becker, Chapter 1, pp. 35. Berlin: Springer-Verlag.
- Yang, M. (2010). Photograph of the smogchamber.
- Zetzsch (2011). per. comm. about disproportionating self-reactions of bromine species.
- Zetzsch, C. and W. Behnke (1992). Heterogeneous photochemical sources of atomic Cl in the troposphere. *Ber. Bunsenges. Phys. Chem.*, Vol. 96, 488–493.
- Zetzsch, C. and W. Behnke (1993). In The Tropospheric Chemistry of Ozone in the Polar Regions. *Springer-Verlag: New York*,. Niki, H., Becker, K. H., Eds.; NATO ASI Series 17;.
- Zetzsch, C. and W. Behnke (2005). Formation of organohalogenes from heterogeneous atmospheric chemistry simulated in an aerosol smog chamber. *GDCh Monograph*, Vol. 34, 110–121.
- Zhang, Q., J. L. Jimenez, M. R. Canagaratna, J. D. Allan, H. Coe, I. Ulbrich, M. R. Alfarra, A. Takami, A. M. Middlebrook, Y. L. Sun, K. Dzepina, E. Dunlea, K. Docherty, P. F. DeCarlo, D. Salcedo, T. Onasch, J. T. Jayne, T. Miyoshi, A. Shimono, S. Hatakeyama, N. Takegawa, Y. Kondo, J. Schneider, F. Drewnick, S. Borrmann, S. Weimer, K. Demerjian, P. Williams, K. Bower, R. Bahreini, L. Cottrell, R. J. Griffin, J. Rautiainen, J. Y. Sun, Y. M. Zhang, , and D. R. Worsnop (2007). Ubiquity and dominance of oxygenated species in organic aerosols in anthropogenically-influenced Northern Hemisphere midlatitudes. *Geophys. Res. Letters*, Vol. 36, No. L13801.

A. Abbreviations

AE	aerosol
BE	bromine explosion
CL	Chemoluminescence
cd	column density
CE	chlorine explosion
CE-DOAS	cavity enhanced DOAS
CNC	condensation nuclei counter
DMA	differential mobility analyzer
dc	diffusion controlled
DOAS	Differential Optical Absorption Spectroscopy
EC	electrostatic classifier
FID	flame ionization detector
FEP	fluorinated ethylene propylene
EUROCHAMP	EUROpean Simulation CHAMbers for Investigating Atmospheric Processes
GC	gas chromatography
HC	hydrocarbons
HMI	hydrargyrum medium-arc iodide lamp
LOPAP	LOng-Path AbsorPtion
QTH	quartz tungsten halogen
RHS	reactive halogen species
SPHCHO	salt pan with high HCHO
STAR	system for transfer of atmospheric radiation
sc	stray light correction
UV	ultra violet
WS	White system

Acknowledgements - Danksagung

Am Anfang dieser Doktorarbeit stand die Aussage 'Es war noch nie jemand live bei einer Bromexplosion dabei.' Und nun können wir die Bromatome nach belieben auftreten lassen. Eine Smogkammer ist ein bisschen wie ein Theater der Spurengase und wir haben Regie geführt. Dabei haben viele liebe Menschen dazu beigetragen, ich möchte mich bei euch von ganzem Herzen bedanken.

*Mein grösster Dank gilt meinem Doktorvater Herr Prof. Ulrich Platt, dass er mir neben den spannenden Smogkammerexperimenten auch die Teilnahme an Feldkampagnen, sowie an internationalen Konferenzen ermöglicht hat. Es gab viele produktive Diskussion zu Ozonabbauraten oder turbulenter Diffusion. Er hat mich während meiner gesamten Promotion unterstützt, und mich sehr motiviert. Ich bewundere ihn für seinen Ideenreichtum, seine Fähigkeit schneller Kopfzurechnen, als ich in den Taschenrechner eintippen kann und seinen unendlich zu sein scheinenden Optimismus.

*Herrn Prof. Cornelius Zetzsch möchte ich danken, dafür, dass er ein Labor aufgebaut hat, zusammen mit seinen Mitarbeitern, in dem Simulation von atmosphärischen Prozessen möglich sind. Ich möchte ihm danken, dass er die direkte Beobachtung der BE erst ermöglicht hat. Seinen unermüdlichen, jedoch vorantreibenden Korrekturereifer weiss ich sehr zu schätzen.

*Vielen Dank an Herr Prof. Thomas Wagner, für die Übernahme des zweiten Gutachtens. Auf einigen Konferenzen, wie EGU und DOAS workshop, habe ich gute Ideen aus seinen Vorträgen und im Gespräch mitgenommen.

*Dankeschön Sergej Bleicher und Natalja Balzer, für die so wertvolle gemeinsame Durchführung der Experimente. Sergej es ist eine wahre Pracht, was du da aufgebaut hast; nun ist die Kammer unter Kontrolle. Dem gebührt ein grosses Lob. Natalja mit dir war es der grösste Spass, auch wenn wir manchmal am verzweifeln waren, wenn die Basislinie Achterbahn fährt oder die Kammer nur noch an einem Seil hängt. PS: Wir schaffen das!

*Danke Mingxi Yang für deine unglaubliche Unterstützung und Durchhaltevermögen, beim Korrekturlesen, in Diskussionen zur Chemie und Diffusion. Thank

火需要空气 我爱你并且 我希望 我能够与你共度余生
you so much for taking me as I am.

*Am Institut für Umweltphysik in Heidelberg gibt es so viele tolle Kollegen die mich während der gesamten Zeit unterstützt haben. Mein grösster Dank gilt hier Holger Sihler, ohne dich wäre ich wohl nie fertig geworden. Danke für die hitzigen Debatten zur Halogenchemie. Es ist schön dass es dich gibt physikalisch gesehen, aber auch als wunderbaren Freund. *Denis Pöhler möchte ich danken, dafür dass er mich überhaupt erst mit den Instrumenten vertraut gemacht hat. Ohne ihn könnte ich heute einen Spalt nicht so gut justieren. Aber auch bei Konstruktionsfragen und Auswerteschwierigkeiten war er mir eine grosse Hilfe. Und natürlich für das Korrekturlesen. *Dank gilt 'meinem' Diplomanden Daniel Hoch, der in seiner Arbeit die cavity aufgebaut und erste Messungen gemacht hat. Erst dadurch war ein Einsatz an der grossen Smog Kammer überhaupt möglich. *Danke an Johannes Lampel der mir das bunte Bilder machen beigebracht hat und einen Crashkurs in Mathlab gegeben hat. Aber natürlich auch für die leibliche Unterstützung durch den besten Schokokuchen der Welt. *Udo Friess gilt besonderer Dank für optischen Debatten zu Beginn der Arbeit, Halogenchemie Nachhilfe während der gesamten Zeit und seine unglaubliche Bereitschaft für last-minute Korrekturen.

*Meiner liebsten Katja Seitz möchte ich danken, dass sie mich auf den Irlandkampagnen überhaupt erst heiss auf Halogenchemie gemacht hat. Du bist mir eine so gute Freundin geworden, ich weiss nicht wie ich es hier ohne dich überhaupt aushalten soll!

*Neben Heidelberg ist Bayreuth meine zweite wissenschaftliche Heimat geworden.

*Und grosser Dank gilt hier Johannes Ofner für die Regie in den SOA Experimenten.

*Danke an Stefan Gonser, ohne den ich mich in Bayreuth wahrscheinlich nie zu Hause gefühlt hätte. Er hat mir grosse seelische Unterstützung gegeben, wenn ich bis spät abends im Labor war oder ein Spiegelrahmen geplatzt ist. *Für technische Unterstützung gilt besonderer Dank Ulli Krüger, der leider dieses Jahr verstorben ist. Ohne ihn wäre das Labor nicht im geringsten das was es nun ist, er war ein Genie seiner eigenen Klasse, ein besonderer Mensch. Danke auch an Andreas Held, Matthias, Agnes, Lei und Gerhardt Kufner.

*Andre Merten gilt Dank für die erste Einführung in die White-zellen justage.*Und Rainer Volkamer für seine Diplomarbeit und anregende Diskussion auf Konferenzen.

*Vielen Dank an mein wunderbarstes Büro der Welt Floh, Fiete, Claudi,Sebi. Ohne euch würde ich vielleicht noch normal werden! Ich danke noch vielen weiteren am IUP Nicole Martin, Claudi, Selami, Robert, Martin. Danke für das IUP Fussball Jörg, Michi , Stef und die restlichen Wadenbeisser.

*Vielen Dank an HALPROC. Projekte wie diese sind es die Wissenschaft verbindet, und uns auch an die entlegenen Plätze Deutschlands führt. *Ich bedanke mich für sehr interessante und Ideen-bringende Diskussion bei Roland von Glasow, Roberto

Sommariva, Wolfgang Behnke und Karsten Kotte.

*Ich bedanke mich bei meinen wunderbaren Freunden aus dem Hinterhof die immer für mich da sind. Das ist so viel wert, die kleinen Dinge sind es die uns das Leben erhellen Danke liebste Sarah und liebste Clara, danke Lotte, Doro, Susanne.

*Der Forkenhof ist mein Lieblingsort in Bayreuth, nur hier fühl ich mich richtig wohl und wie zu Hause. Danke an die Bewohner die daran nicht unschuldig sind.

*Und nun zum Schluss das wichtigste, meine absolut wundervollste Familie. Noëmie, meine liebste Schwester, von Herzen Danke, dafür, dass ich mich immer auf dich verlassen kann. Dankeschön Erika und Karlheinz, meine lieben Eltern, ihr steht immer hinter mir und bestärkt mich in dem was ich tue. Ich habe so viel von euch gelernt, und bin so froh dass es euch gibt. Dankeschön an meine Schweizer Familie Oma Lisel, Vreni, Jeannot und Renate. Es tut gut zu wissen, dass es immer einen Platz am Zürichsee gibt, and den ich mich zurück ziehen könnte!